

**STRESS AND MOTION IN DIARTHRODIAL JOINTS
USING COUPLED NONLINEAR ELASTODYNAMICS,
RIGID BODY DYNAMICS, AND
LARGE-SLIP CONTACT**

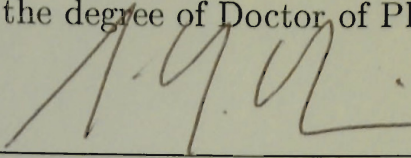
A DISSERTATION
SUBMITTED TO THE DEPARTMENT OF MECHANICAL ENGINEERING
AND THE COMMITTEE ON GRADUATE STUDIES
OF STANFORD UNIVERSITY
IN PARTIAL FULFILLMENT OF THE REQUIREMENTS
FOR THE DEGREE OF
DOCTOR OF PHILOSOPHY

CHAD B. HOVEY
AUGUST 2000

© Copyright 2000 by Chad B. Hovey

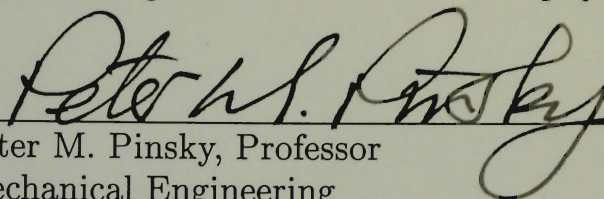
All Rights Reserved

I certify that I have read this dissertation and that in my opinion it is fully adequate, in scope and quality, as a dissertation for the degree of Doctor of Philosophy.



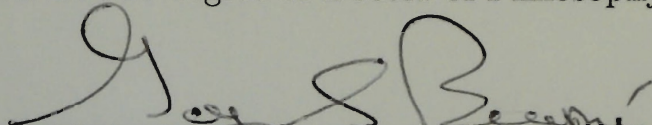
Jean H. Heegaard, Principal Advisor
Assistant Professor of Mechanical Engineering

I certify that I have read this dissertation and that in my opinion it is fully adequate, in scope and quality, as a dissertation for the degree of Doctor of Philosophy.



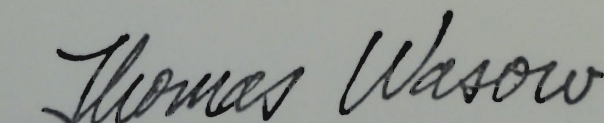
Peter M. Pinsky, Professor
Mechanical Engineering

I certify that I have read this dissertation and that in my opinion it is fully adequate, in scope and quality, as a dissertation for the degree of Doctor of Philosophy.



Gary S. Beaupré, Consulting Professor
Mechanical Engineering

Approved for the University Committee on Graduate Studies:



ABSTRACT

This thesis focuses on the formulation and implementation of coupled deformable-rigid systems, and the application of such systems to biomechanical models.

The formulation of a coupled dynamical system composed of deformable and rigid domains in the presence of equality and inequality constraints is presented. The governing, nonlinear equations of motion include finite deformation, finite rotation, and non-smooth constraints. An augmented Lagrangian formulation is used to enforce the constraints. The finite element implementation includes elements for rigid body dynamics, persistent node-on-node contact, and unilateral large-slip node-on-surface contact are developed. A rigid element that embeds the time stepping algorithm as element degrees of freedom allows the hyperbolic system to be solved in an elliptic setting.

A coupled ballistic gait model composed of rigid segments for the stance leg, swing leg, and head-arms-trunk (HAT) is developed. This model includes a total hip arthroplasty with a deformable ultra-high-molecular-weight-polyethylene liner. The effects of gait dynamics as well as muscle force on the joint stress and deformation are investigated.

The deformable and rigid domains may be successfully coupled as long as the large spread in frequency content of the two domains is addressed. Consistent linearization provides local quadratic convergence for the fully coupled system. The similarity in the dynamics of the coupled model to a purely rigid ballistic gait model indicates that joint deformation has a negligible effect on the dynamics of walking. Ground reaction forces, obtained from the Lagrange multipliers, coincide with clinical ground reaction force data for slow gait. The coupled ballistic gait model without muscles produces hip contact forces that are much lower than physiological values. This indicates that the role of muscles may

be as significant as the role of gait dynamics in the determination of joint stress.

The coupled model accounts for limb dynamics and joint deformation in a unified setting. Motion data measured in a gait analysis laboratory may now be used with this coupled framework to accurately predict the evolution of joint stress and deformation during walking.

ACKNOWLEDGEMENTS

I thank Professor Jean Heegaard for his role as my thesis advisor and for his instruction and guidance. I also thank the members of my thesis committee and people who have played a role in my thesis work. I extend gratitude to Professor Gary Beaupré and Professor Felix Zajac for advising the project and for helping me understand the practical applications of biomechanical modeling. I thank Professor Tom Andriacchi and Professor Scott Delp for their assistance with grant writing and participation in my oral defense. I thank Professor Peter Pinsky and Professor Thomas Hughes for inspiring my understanding of computational analysis. I thank Professor Alain Curnier for making my visit to The Swiss Federal Institute of Technology during the Summer of 1998 a reality.

I also gratefully acknowledge the National Science Foundation Graduate Research Fellowship and the Department of Veterans Affairs Predoctoral Fellowship for financial support.

I would like to thank my friends for their support and comradery. To avoid including a very large list of many people, and to avoid accidentally omitting someone, I have chosen not to name anyone specifically.

Finally, I extend special gratitude to my parents, who have instilled in me a love of learning and respect for education. My parents are the greatest teachers I have ever had.

CONTENTS

ABSTRACT	IV
ACKNOWLEDGEMENTS	VI
LIST OF TABLES	XII
LIST OF FIGURES	XIII
LIST OF BOXES	XX
1 INTRODUCTION	1
1.1 Clinical Relevance	1
1.2 Background	3
1.2.1 Biomechanics	3
1.2.2 Computational Mechanics	6
1.3 Goals	17
1.4 Novelty	17
1.5 Outline	19
2 FORMULATION	20
2.1 Overview	20
2.2 Deformable Body Dynamics	20
2.2.1 Local Governing Equation of Motion	21
2.2.2 Global Statement of Virtual Work	24

2.2.3	Linearization	25
2.2.4	Constitutive Laws	26
2.3	Rigid Body Dynamics	27
2.3.1	Governing Equations of Motion	28
2.3.2	Linearization	33
2.4	Equality Constraints	33
2.4.1	Methods of Constraint Enforcement	33
2.4.2	Interfaces Formulated as Equality Constraints	34
2.4.3	The Augmented Lagrangian Potential	35
2.4.4	The First Variation	35
2.4.5	The Second Variation	35
2.4.6	Specialization for Deformable-Deformable Constraints	36
2.4.7	Specialization for Deformable-Rigid Constraints	37
2.4.8	Specialization for Rigid-Rigid Constraints	40
2.4.9	Muscle Actuator Formulation	42
2.5	Inequality Constraints	47
2.5.1	Contact Mechanics Formulated as an Inequality Constraint	47
2.5.2	The Augmented Lagrangian Potential	50
2.5.3	The First Variation	50
2.5.4	The Second Variation	50
2.5.5	Specialization for Deformable-Rigid Contact	51
2.6	Formulation Summary for the Fully Coupled System	52
2.6.1	The First Variation	52
2.6.2	The Second Variation	53
3	IMPLEMENTATION	55
3.1	Overview	55
3.2	Deformable Body Dynamics	57
3.2.1	Galerkin Form	57
3.2.2	Matrix Form	57
3.2.3	Time Stepping	60

3.3	Rigid Body Dynamics	63
3.3.1	Matrix Form	64
3.3.2	Time Stepping	64
3.3.3	The Rigid Element — Version 1	65
3.3.4	Embedded Dynamics, The Rigid Element — Version 2	68
3.4	Equality Constraints	72
3.4.1	Deformable–Deformable Equality Constraint Element	72
3.4.2	Deformable–Rigid Equality Constraint Element — Version 1	74
3.4.3	Deformable–Rigid Equality Constraint Element — Version 2	76
3.4.4	Rigid–Rigid Equality Constraint Element — Version 1	77
3.4.5	Rigid–Rigid Equality Constraint Element — Version 2	79
3.4.6	Muscle Actuator Element	83
3.5	Inequality Constraints	89
3.5.1	Geometric Preliminaries	89
3.5.2	Deformable–Rigid Inequality Constraint Element — Version 1	94
3.5.3	Deformable–Rigid Inequality Constraint Element — Version 2	95
4	BIOMECHANICAL MODELS	98
4.1	Overview	98
4.2	Model Classification	99
4.3	Model Similarities	101
4.3.1	Symmetry Conditions	101
4.3.2	Initial Conditions	102
4.3.3	Anthropometric Data	105
4.3.4	Rigid Limb Segments and Associated Interfaces	105
4.4	Model Differences	105
4.4.1	Deformable Hip Joint and Associated Interfaces	106
4.4.2	Muscle Extensor and Flexor Groups	107
4.4.3	Forward Integration	112
4.5	Model Validation	114

5	RESULTS AND DISCUSSION	119
5.1	Overview	119
5.2	Results	120
5.2.1	Large Scale	120
5.2.2	The Small Scale	132
5.3	Discussion	141
6	CONCLUSIONS	152
6.1	Review	152
6.2	Limitations	155
6.3	Application	156
6.4	Future Work	157
A	FORMULATION DETAILS	158
A.1	Overview	158
A.2	Deformable Body Dynamics Details	158
A.3	Rigid Body Dynamics Details	160
A.4	Equality Constraint Details	161
A.4.1	First Variation	164
A.4.2	The Second Variation	164
A.5	Contact Mechanics Details	171
A.5.1	Some Preliminary Results	172
A.5.2	The First Variation	182
A.5.3	The Second Variation	184
A.6	Fully Coupled System Details	189
B	FINITE ELEMENT VALIDATION	192
B.1	Overview	192
B.2	Rigid Body Elements	192
B.2.1	Embedded Dynamics, The Rigid Element — Version 2	192
B.3	Equality Constraint Elements	195

B.3.1	Rigid–Rigid Equality Constraint Element — Version 2	195
B.3.2	Deformable–Rigid Equality Constraint Element — Version 2	199
B.3.3	Muscle Actuator Element	201
B.4	Inequality Constraint Elements	205
B.4.1	Deformable–Rigid Inequality Constraint Element — Version 2	205
	BIBLIOGRAPHY	210

LIST OF TABLES

3.1	Three variations of Newmark time stepping algorithm: u-type, v-type, and a-type formulations.	63
4.1	Classification of the four gait models based on the presence or absence of a deformable hip joint, and the presence or absence of muscles.	100
4.2	Initial conditions for the ballistic gait model shown in FIG. 4.2 following the convention for limb angles given in FIG. 4.4.	103
6.1	Summary of elements developed for the finite element implementation. . . .	153
A.1	Correspondence of vectors \mathbf{u} , \mathbf{p} , \mathbf{r} , and \mathbf{z} in the generalized equality constraint derivation to the special cases of deformable-deformable, deformable-rigid, and rigid-rigid.	163

LIST OF FIGURES

1.1	Total hip arthroplasty composed of the femoral component, the polyethylene liner, and the acetabular shell.	2
2.1	(a) Rigid body with two applied forces \mathbf{F}_1 and \mathbf{F}_2 applied at points \mathbf{P}_1 and \mathbf{P}_2 , respectively and with two applied torques \mathbf{T}_1 and \mathbf{T}_2 . (b) The same rigid body with an equivalent force-moment \mathbf{F}_R and \mathbf{M}_R applied at point \mathbf{P}_R	31
2.2	Generalization of constraint equation \mathbf{h} between two deformable bodies.	36
2.3	Generalization of constraint equation \mathbf{h} between a deformable and rigid body.	38
2.4	Generalization of constraint equation \mathbf{h} between two rigid bodies.	40
2.5	A simple muscle actuator group has three parallel elements. Three simple groups may be combined to create a Hill-type model by setting the actuation a , stiffness k , and damping c to zero. The Hill-type model simulates the muscle action.	43
2.6	Reference and current configurations of the muscle actuator.	44
2.7	The (a) non-penetration condition, (b) non-adhesion condition, and (c) complementarity condition.	49
2.8	The normal contact law described as the intersection of the non-penetration condition, non-adhesion condition, and complementarity condition.	49
2.9	Vector nomenclature for contact between rigid and deformable bodies.	52

3.1	Planar rigid body element with translational degrees of freedom q_1 and q_2 drawn on the body and the out-of-plane rotational degree of freedom q_3 drawn off the body.	67
3.2	Planar rigid body element with velocity and acceleration degrees of freedom embedded into the element position degrees of freedom. Translational degrees of freedom (q_1 , q_2 , and their time derivatives) are drawn on the body. The out-of-plane rotational degrees of freedom (q_3 and its time derivatives) are drawn off the body.	69
3.3	Two deformable bodies Ω_1 and Ω_2 pinned together such that point \mathbf{P}_1 and point \mathbf{P}_2 overlap for all time.	73
3.4	One deformable body Ω_1 and one rigid body Ω_2 pinned together such that point \mathbf{P}_1 and point \mathbf{P}_2 overlap for all time.	75
3.5	Two rigid bodies Ω_1 and Ω_2 pinned together such that point \mathbf{P}_1 and point \mathbf{P}_2 overlap for all time.	81
3.6	Muscle actuator element with elastic spring and actuator between two bodies. Bodies may be either deformable or rigid and in any combination.	84
3.7	Muscle actuator element with moment specified between two rigid bodies. .	85
3.8	Muscle actuator element with viscous dashpot between two rigid body elements (embedded formulation).	87
3.9	A two dimensional curve $\mathcal{C} \in \mathbb{R}^2$ parameterized by $\xi \in \mathbb{R}$. A point along that curve is located by $\mathbf{y}(\xi) \in \mathbb{R}^2$ as measured in the \mathbf{E} basis.	90
3.10	Construction of the closest point projection.	91
3.11	The target boundary between two points \mathbf{p}_1 and \mathbf{p}_2 on Γ_c use two additional points, \mathbf{p}_0 and \mathbf{p}_3 , for construction of the tangents in the Hermite interpolation. .	93
3.12	Interpolation of the target surface through points (0.5, 2.0), (1.5, 1.0), (2.5, 1.0), (3.5, 3.0) with Hermite polynomials and tangent scaling parameter α . .	94
3.13	Two-dimensional contact element.	97
4.1	One complete human gait cycle and its subdivisions into (RSW) right leg swing, (DS) double-stance, (RST) right leg single-stance, (DS) double-stance. .	99

4.2	One complete ballistic gait cycle and its subdivisions into (RST) right leg single-stance, (RSW) right leg swing.	100
4.3	Geometry and mass properties for the coupled deformable-rigid ballistic gait model. Illustration of deformable Ω_D and rigid Ω_R bodies, as well as interfaces for bilateral Γ_h and unilateral Γ_c contact.	102
4.4	Convention for limb angles: Angles are measured in the sagittal plane. The vertical E_2 axis represents zero degrees of rotation. Rotations that are counter-clock-wise from this axis are considered positive. Rotations that are clock-wise from this axis are considered negative.	103
4.5	Sagittal plane representation of the finite element mesh from [66] used to model the Johnson & Johnson total hip arthroplasty.	106
4.6	Large-scale view of a purely rigid ballistic gait model (a) without muscles and (b) with muscles.	108
4.7	Sagittal view of (a) physiological extensor and flexor muscle groups and (b) simplified extensor and flexor muscles groups.	109
4.8	Extensor muscle force magnitude required to keep HAT vertical.	112
4.9	Flexor muscle force magnitude required to keep HAT vertical.	113
4.10	Complementary extensor and flexor muscle forces magnitudes required to keep HAT vertical.	114
4.11	Comparison of (a) contact pressure and (b) maximum femoral head displacement results from Bartel [15], Maxian [78], and Kurtz [67] to the validation study.	115
4.12	Hydrostatic pressure for hip arthroplasty using Bartel's inputs: Static applied load of 3000 N, $E = 1400$ MPa, and $\nu = 0.3$	116
4.13	von Mises stress for hip arthroplasty using Bartel's inputs: Static applied load of 3000 N, $E = 1400$ MPa, and $\nu = 0.3$	117
4.14	Stress component σ_{22} for hip arthroplasty using Bartel's inputs: Static applied load of 3000 N, $E = 1400$ MPa, and $\nu = 0.3$	117
4.15	Contact pressure for hip arthroplasty using Bartel's inputs: Static applied load of 3000 N, $E = 1400$ MPa, and $\nu = 0.3$	118

4.16 Maximum and minimum strain using Bartel's inputs: Static applied load of 3000 N, $E = 1400$ MPa, and $\nu = 0.3$	118
5.1 Comparison of the coupled ballistic gait model, M2 , to the purely rigid ballistic gait model, M1 . Position and velocity data for the stance leg: (a) x position, (b) y position, (c), θ angular rotation, (d) x velocity, (e), y velocity, (f) $\dot{\theta}$ angular velocity.	121
5.2 Comparison of the coupled ballistic gait model, M2 , to the purely rigid ballistic gait model, M1 . Position and velocity data for the HAT: (a) x position, (b) y position, (c), θ angular rotation, (d) x velocity, (e), y velocity, (f) $\dot{\theta}$ angular velocity.	123
5.3 Comparison of the coupled ballistic gait model, M2 , to the purely rigid ballistic gait model, M1 . Position and velocity data for the swing leg: (a) x position, (b) y position, (c), θ angular rotation, (d) x velocity, (e), y velocity, (f) $\dot{\theta}$ angular velocity.	125
5.4 Comparison of the coupled ballistic gait model, M2 , to the purely rigid ballistic gait model, M1 . Ground reaction force between stance leg and floor: (a) horizontal reaction force, (b) vertical reaction force.	126
5.5 Comparison of the coupled ballistic gait model with muscles, M4 , to the purely rigid ballistic gait model with muscles, M3 . Position and velocity data for the stance leg: (a) x position, (b) y position, (c), θ angular rotation, (d) x velocity, (e), y velocity, (f) $\dot{\theta}$ angular velocity.	127
5.6 Comparison of the coupled ballistic gait model with muscles, M4 , to the purely rigid ballistic gait model with muscles, M3 . Position and velocity data for the HAT: (a) x position, (b) y position, (c), θ angular rotation, (d) x velocity, (e), y velocity, (f) $\dot{\theta}$ angular velocity.	129
5.7 Comparison of the coupled ballistic gait model with muscles, M4 , to the purely rigid ballistic gait model with muscles, M3 . Position and velocity data for the swing leg: (a) x position, (b) y position, (c), θ angular rotation, (d) x velocity, (e), y velocity, (f) $\dot{\theta}$ angular velocity.	131

5.8 Comparison of the coupled ballistic gait model with muscles, M4 , to the purely rigid ballistic gait model with muscles, M3 . Ground reaction force between stance leg and floor: (a) horizontal reaction force, (b) vertical reaction force.	132
5.9 Hydrostatic pressure time evolution for the coupled ballistic gait model without muscles (M2). The scale for stress values appears in FIG. 5.11.	133
5.10 von Mises stress time evolution for the coupled ballistic gait model without muscles (M2). The scale for stress values appears in FIG. 5.12.	134
5.11 Hydrostatic pressure for the coupled ballistic gait model without muscles (M2) at $t = 0.30$ s.	135
5.12 von Mises stress for the coupled ballistic gait model without muscles (M2) at $t = 0.30$ s.	135
5.13 Stress component σ_{22} for coupled ballistic gait model without muscles at $t = 0.30$ s.	136
5.14 Inner radius contact pressure, outer radius contract pressure and shear for coupled ballistic gait model without muscles at $t = 0.30$ s.	137
5.15 Maximum and minimum strain for coupled ballistic gait model without muscles at $t = 0.30$ s.	137
5.16 Hydrostatic pressure time evolution for the coupled ballistic gait model with muscles (M4). The scale for stress values appears in FIG. 5.11.	139
5.17 von Mises stress time evolution for the coupled ballistic gait model with muscles (M4). The scale for stress values appears in FIG. 5.12.	140
5.18 Comparison of vertical ground reaction force as a function of walking speed, adapted from Perry [97], to vertical ground reaction force from the ballistic gait model M1	143
5.19 Comparison of clinical thigh angle measured in a gait laboratory by Winter [117] compared to leg angle calculated from the ballistic gait model M1	146
5.20 Comparison maximum contact pressure for the coupled ballistic gait model (a) with muscles, and (b) without muscles.	148

5.21 Comparison maximum contact pressure for the coupled ballistic gait model (a) with muscles, and (b) without muscles.	149
A.1 Generalization of constraint equation \mathbf{h} between two bodies, which are either deformable or rigid, depending on the formulation type: deformable-deformable, deformable-rigid, or rigid-rigid.	162
A.2 Vector nomenclature for contact between rigid and deformable bodies.	171
B.1 Comparision of position and rotation time history, and their derivatives, using the Embedded Dynamic Rigid Element — Version 2, from TACT to closed-form solution.	194
B.2 Comparision of position and rotation time history, and their derivatives, using the Embedded Dynamic Rigid Element and Rigid–Rigid Equality Constraint Element — Version 2, from TACT to dynamic solution from SMASH. Note that SMASH does not report second derivative information, thus only the TACT data is shown for accelerations.	197
B.3 Comparision of constraint forces using the Embedded Dynamic Rigid Element and Rigid–Rigid Equality Constraint Element — Version 2, from TACT to dynamic solution from SMASH.	198
B.4 Reaction forces from the Lagrange multipliers at the deformable–rigid interface. Note that the forces sum to zero.	200
B.5 Comparison of time and velocity time history of results obtained with TACT with results obtained from integration of the equations of motion with MATLAB ODE45.	202
B.6 Comparison of angular position and velocity time history results from TACT with results from SMASH.	204
B.7 Finite element mesh used to validate the Hertz contact problem.	206
B.8 Validation of the contact implementation with the analytical contact solution. Note the FEA load is half of the analytical load because symmetry conditions in the simulation were used.	207

B.9 Position, velocity, and acceleration time history of the indentor center of mass. The vertical degree of freedom is q_2 .	209
---	-----

LIST OF BOXES

2.1	Strong Form (S) of the Initial Boundary Value Problem (IBVP) for Deformable Body Dynamics	23
2.2	Weak Form (W) of the Initial Boundary Value Problem (IBVP) for Deformable Body Dynamics	25
2.3	Lagrangian Form (L) of the Initial Value Problem (IVP) for Rigid Body Dynamics	32
3.1	Predictor/corrector time stepping algorithm applied to deformable body dynamics equations of motion.	62
3.2	Modifications to the predictor/corrector algorithm in Box 3.1 for use with rigid body dynamics equations of motion.	65
3.3	Predictor/corrector time stepping algorithm for embedded rigid body dynamics.	70
A.1	First variation of the generalized equality constraint in expanded form.	165
A.2	Second variation of the generalized equality constraint in expanded form.	170
A.3	First variation of the generalized contact constraint with contact status in expanded form.	183
A.4	First variation of the generalized contact constraint with gap status in expanded form.	183
A.5	Second variation of the generalized inequality contact constraint in tensor form.	187
A.6	Second variation of the generalized inequality contact constraint in expanded form.	188

A.7 Second variation of the generalized contact constraint with gap status in expanded form.	189
--	-----

CHAPTER 1

INTRODUCTION

This thesis focuses on the formulation and implementation of coupled deformable-rigid systems, and the application of such systems to biomechanical models. There are several compelling reasons to undertake such an investigation. The CLINICAL RELEVANCE section explains these reasons in detail. Next the BACKGROUND section explores the work of previous investigations. The GOALS section then outlines the aim and scope of this research. Finally, the OUTLINE section provides an overview of the remaining contents of the thesis.

1.1 CLINICAL RELEVANCE

Arthritis, one of the most significant musculoskeletal diseases, occurs in approximately 40 million Americans, and costs the U.S. economy \$54.6 billion in medical care and indirect costs including lost wages. By the year 2020, an estimated 59.4 million Americans will have some type of arthritis according to the Centers for Disease Control and Prevention [12, 38].

The most common of all joint diseases, osteoarthritis, is characterized by progressive degeneration of cartilage typically in the hip and knee joints. Causing pain and functional impairment, osteoarthritis currently afflicts more than 21 million adults in the United States according to the National Institute of Health (NIH). This number is expected to grow significantly since the elderly (age 65 and older) compose the fastest growing population in America and are the age-defined group of Americans most likely to suffer from osteoarthritis. Expected to exceed 68 million Americans by 2010, this elderly population will unquestion-

ably cause dramatic increases in the demand for improved treatments of this disease [90].

End-stage osteoarthritis is commonly treated with total joint replacement surgery. The NIH estimates that over 60 percent of all total joint replacement surgeries are undertaken to treat severe osteoarthritis. This treatment, in addition to adding quality of life to the patient, offers significant monetary savings. The total medical cost associated with a single total joint replacement, estimated to be \$48,000 over a 20 year implant service time, is much less than the non-operative treatment, estimated to be \$165,000 over the same time frame [90].

While beneficial to both the patient and society, total joint replacements do not represent a panacea. The components of the joint replacement are susceptible to wear and degeneration. Consider the total hip arthroplasty, shown in FIG. 1.1. The arthroplasty

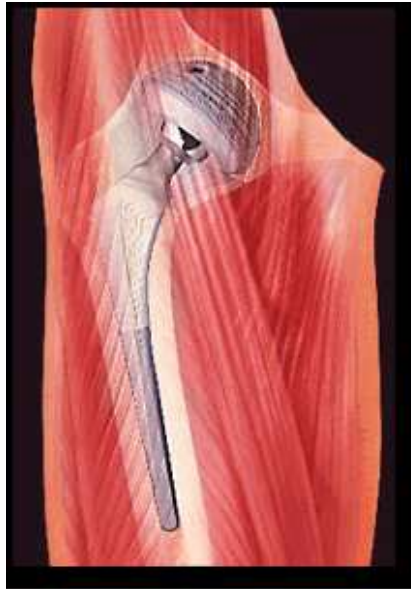


FIGURE 1.1: Total hip arthroplasty composed of the femoral component, the polyethylene liner, and the acetabular shell.

is composed of a femoral head and stem, a polyethylene liner, and an acetabular shell. The femoral component and the acetabular liner, commonly made of cobalt-chromium or a titanium alloy (Ti-6Al-4V) [27, 56, 72, 111], articulate the frontside and backside of the polyethylene liner (UHMWPE, ultra-high-molecular-weight-polyethylene). The acetabular shell is fixed rigidly into the acetabulum with bone cement, screws, or both. These compo-

nents all slide on each other during use. The relative motions over time generate particulate debris composed of metal and polyethylene.

Histological examination of tissue and the pseudomembrane surrounding the implants, near empty screw holes and the screw-shell junction, indicate the presence of metal and polyethylene debris, necrotic tissue, and tissue foreign-body giant cell reaction [56]. The debris generated from wear has been clearly identified as one of the primary causes of prosthetic loosening [1, 56, 89]. This loosening often causes more relative motion, resulting in a cascade of wear and degeneration, ultimately leading to component failure and arthroplasty revision surgery.

It is now well-accepted that the wear process is a result of the component relative motion and the stress field in the polyethylene liner [78, 77, 76, 79, 66, 67]. The relative motions and stresses emanate from movement of the body, typically during walking and other activities of daily living.

1.2 BACKGROUND

The BACKGROUND section reviews clinical, experimental, and computational contributions to the understanding of hip arthroplasty wear. The desire to improve upon the state-of-the-art in computational modeling will lead to the development of new formulations and implementations in the area of coupled finite element analysis, rigid body dynamics, time stepping, and contact mechanics. A review of the state-of-the-art in these areas will serve as a foundation from which to show the new contributions of this research.

1.2.1 BIOMECHANICS

JOINT MECHANICS — THE SMALL SCALE Efforts directed at decreasing prosthetic wear, in particular in the polyethylene acetabular cup of the hip arthroplasty, have developed in three main areas: (1) retrieval studies, (2) rocking-arm hip simulators, and (3) finite element models.

Retrieval studies of arthroplasty components offer clinically qualitative and quantitative information of wear patterns and failure modalities. Huk *et al.* performed a study

of the polyethylene liner-metal interface to examine the wear of 19 modular uncemented acetabular components having an average implant time of 22 months, retrieved during revision surgery [56]. Sychterz *et al.* quantified volumetric and linear wear rates of polyethylene with 26 components retrieved post-mortem [111]. Their study assessed wear in components not retired by virtue of component failure and therefore characterized non-pathological wear behaviors of well-functioning components. These studies, among others [13, 14, 37, 96, 115], provide a large data pool of clinically established wear rates.

There are limitations, however, to a clinical approach. Specifically, the sample size is small, the patient activity and load-history environment is largely disparate, and the manufacturer and design variability is high. These three confounding factors render the clinical approach better suited to being a retrospective rather than a predictive means for improving hip arthroplasty design.

As an alternative to the *in vivo* analysis, *in vitro* experiments offer significant insight into the wear process [28, 36, 72, 116]. **Hip simulator machines**, consisting of a rocking-arm assembly with force applied to the femoral component as it rotates in the acetabular cup, provide valuable information under known testing conditions and a well-controlled environment. While more advantageous than the clinical approach in its abilities to reduce confounding variability, such simulators do not accurately represent *in vivo* loading environments. Moreover, current mechanical simulators cost tens of thousands of dollars in combined acquisition and operations costs. Finally, the experiments can take months to complete. For example, an experiment representing a five-year *in situ* service lifetime requires 60 days, based on an assumed one million cycles per year and a walking frequency of 1 Hz. The high time and monetary costs, in conjunction with the physiologically limited loading conditions, diminish the overall appeal of the experimental approach.

In light of these limitations and shortcomings, computational biomechanical modeling using the **finite element method** offers significant advantages [78, 77, 76, 79, 65, 64, 67]. First, finite element approaches are not limited to a small number of analyses, as with clinical approaches. Second, geometric and material data may be parameterized for the purposes of design — allowing the analyst to evaluate many different design alternatives without resorting to building and physically testing each model in an experiment. Third, such models

can incorporate prescribed physiological motions and loads — a distinct advantage when compared to experimental rocking-arm simulators. Finally, the models may be evaluated in a timely and efficient manner, with analysis completed in a matter of days, in contrast to the weeks or months needed for experimental wear studies.

Computational studies predict wear rates that agree well with those observed clinically. Moreover, they serve as an invaluable tool to assist in the design of total joint replacement. However, these models rely on user-defined boundary conditions that are intended to simulate physiological loads. These prescribed loads may not reflect the loading condition arising from the dynamic limb motion during gait. Recent studies suggest that the dynamic loading experienced in the joint is not negligible [6, 7, 113].

GAIT MECHANICS — THE LARGE SCALE Analysis of human motion often uses rigid body dynamics to predict joint motion and forces. Rigid models, typically used in conjunction with a muscle model, have been used to simulate human walking [3, 80, 81, 85, 102, 122, 121], running [26, 42], jumping [95, 109], and cycling [91]. Others have used rigid body approaches to successfully identify healthy and pathological human movement [8].

While rigid body models are useful for limb motion simulations, the rigid body assumption does not allow for the determination of stress and deformation within a joint. This information is desirable to help understand the etiology of joint disease and to predict how a joint replacement will perform over time.

Since rigid body models cannot describe stress and deformation, and since deformable joint models use boundary conditions which may not reflect the physiological activity, a new model which couples the rigid body and deformable body would be a compelling approach.

When describing limb motion through rigid body dynamics, a particular length scale, typically on the order of meters, is established. When describing joint stress and deformation, a different length scale is introduced. This length scale is significantly smaller than the scale used for rigid body models. The total joint replacement geometry is typically on the order of centimeters. Therefore, any model that couples rigid and deformable bodies will need to couple bodies at significantly different length scales.

Furthermore, the motion of the rigid bodies clearly is responsible for joint loading and

hence stress and deformation of the joint. Conversely, the motion of joint, as it slides, rotates and deforms during articulation, causes the joint segments to move relative to each other and consequently has an effect on dynamics at the large scale. Thus, a model which couples rigid and deformable bodies will need to account for the dynamics and motion on both length scales as well.

When beginning to envision all the computational tools required to make a model that couples rigid and deformable domains, one might think of interfaces. The first interface occurs where the rigid and deformable domains are joined at a common boundary. This interface will be later described mathematically through equality constraints. Other types of interfaces which are described through equality constraints are connections between rigid bodies and connections between deformable bodies. These types of interfaces will be described in detail in the coming chapters. Another type of interface between rigid and deformable bodies is unilateral contact. In this case, the two bodies move freely except when in contact with each other. While in contact, the two bodies may push on each other as well as slide past one another. They may not pull on each other nor may they interpenetrate. This type of interface will be described mathematically through inequality constraints.

Before the computational tools and algorithms used to couple deformable–rigid models are examined, the state-of-the-art is reviewed.

1.2.2 COMPUTATIONAL MECHANICS

COMMERCIAL RIGID AND DEFORMABLE BODY CODES Many commercial codes exist today which can provide, in part, the coupled technology developed here. However, it appears that no single commercial code has all of the features and functionality of the coupled code developed for this research — at least not yet. The code developed for this thesis is referred to as TACT, which is an extended version of TACT written by Alain Curnier [29].

Traditionally, there are two camps of commercial codes — multi-rigid body codes and finite element codes. Recently, the traditional rigid body code developers have been adding deformable body information to their analysis engines. Several codes now allow the geometry of rigid components and the reaction forces acting on them to be output in file formats compatible with finite element codes. The geometry could then be used to create a mesh,

and the reaction forces applied, to provide stress and deformation information about the component. This type of method is sometimes referred to as a “over-the-fence”, “hand-shaking”, or “loosely coupled” approach. This philosophy is distinctly different from the approach taken here, where the equations for the rigid and deformable bodies, as well as the constraints acting between them, are solved simultaneously.

There are advantages and disadvantages to both the “loosely coupled” and the “fully coupled” approaches. The disadvantage of one approach is often the advantage of the other. The advantages of a loosely coupled approach include:

- **Smaller problem size:** Breaking the problem into a purely rigid system and a purely deformable system may allow one large problem to be replaced with two smaller, more manageable problems. This case would occur if the number of equations solved for the rigid system were on the same order as the number solved for the deformable system.

If there are significantly more deformable than rigid equations (as is the case for the models presented in this thesis), this becomes less of an advantage. This case arises when there are only a few rigid body equations, and several orders of magnitude more deformable body equations, created by the discretization of the finite element mesh.

- **More stable system with faster solution times:** The time steps used for the rigid bodies may be significantly larger than time steps for the deformable bodies. This case can arise when the rigid bodies move relatively slowly, with low frequencies, and the deformable bodies are relatively stiff, containing high frequencies. A large time step for the rigid body governing equations could lead to a shorter solution time for the rigid body part of the simulation. In a fully coupled approach, the highest frequency governs the time step size. The time step required to fully resolve the high frequency vibration of the deformable bodies may be significantly smaller than the time step required to integrate just the rigid body equations. As a result of the purely coupled approach, the rigid body equations might be evaluated and linearized several more times than necessary.

The high frequency issue may be resolved by omitting the dynamic behavior of the deformable domain, and retaining only its elastic properties. This approach, taken in

this thesis, is highly dependent on the constitutive model of the deformable system. This approach is not suitable for a highly deformable, “sloshy,” “Jello-like,” or “spaghetti-like” domain. This approach is suitable for systems with low mass, high stiffness, and small deformation.

- **Ease of implementation:** A loosely coupled approach requires less mathematical description and fewer constraint elements to be developed. One might solve the rigid body system, find the reaction forces acting on a certain component of the rigid system, then apply those reaction forces over the surface of a finite element mesh of the particular part.

While this approach is appealing, it loses its accuracy if the deformation of the component, under the reaction forces, deforms enough to move the centers of mass of the parts attached to it. In this case, the deformation of the component has a non-negligible effect on the dynamics of the entire system, and the loosely coupled approach will not provide accurate results.

The advantages of a purely coupled approach include:

- **Accuracy and Consistency:** Because the equation describing the rigid body dynamics are fully coupled to the equations describing the deformable body dynamics, there is accuracy and consistency in the simulation results. Furthermore, Lagrange and augmented Lagrange multiplier approaches exactly enforce the constraints interfacing the deformable and rigid domains — there is no approximation as a result of penalization or loosely coupling the domains.

The trade-off for accuracy and consistency comes at the price of a more complicated implementation. Constraint elements must be written and validated. The equations of constraint, when implemented with Lagrange multiplier methods, also increase the size of the equation system. Therefore, solving all equations — deformable, rigid, and constraint — can lead to greater computational storage demands and greater solution times.

- **Only one analysis required:** Solving all the deformable, rigid, and constraint equations at once provides the results for the entire system, in a single analysis.

The need for multiple programs, such as a multi-rigid body program and a separate finite element program, is obviated. The calculation and potential guess-work of how to distribute reaction forces from a rigid body dynamics simulation on to a finite element mesh is absent because the Lagrange equations of the coupled approach do this consistently and automatically. Coordination of mutliple input and output files is eliminated.

The traditional rigid body codes include

- ADAMS, by Mechanical Dynamics, Inc. [84]
- DADS, by LMS International [73]
- Madymo, by TNO [114]
- Mecano, by Samtech [103]
- visualNastran, by MSC.Working Knowledge [88]

ADAMS has an add-on finite element analysis module, which allows displacement, velocity, acceleration, and force information for components in a rigid body dynamics simulation to be output in a file usable by finite element analysis packages from other commercial vendors, including ABAQUS, ANSYS, and MSC.Nastran. DADS works in a manner similar to ADAMS.

Madymo offers some rigid and deformable body coupling. However, the software is specifically designed for the analysis of human occupant safety in cars, trains, and other vehicles. Used for accident reconstruction, automotive crash safety, and vehicle handling studies, the components of Madymo are hard-coded as a human occupant, car seats, air bags, and car frames. While such a program is useful, it is not at this time generalizable beyond the automotive safety market toward which is it geared.

Mecano can model mechanisms and rigid bodies coupled to deformable finite elements. Mecano includes many different mechanical joints and finite elements. Mecano uses standard Lagrange multipliers to enforce constraints. While Mechano uses the Newton-Raphson method for solution of nonlinear equations in the primal variables, it uses an updating pro-

cedure, similar to Uzawa's method, for updating the dual variables. The Uzawa-type methods have been shown to have convergence properties far slower than generalized Newton-Raphson procedures [50].

MSC.Working Knowledge recently released a version of visualNastran Desktop that integrates their rigid body motion analysis with the finite element analysis of MSC.Nastran. The implementation offers advantages over ADAMS and DADS because the rigid and deformable analysis is done all at once, in a single program. There is no hand-shaking between output files from one program and input files of another program. However, the current implementation is not fully coupled. The reaction forces from a rigid body analysis are used as boundary conditions to a finite element mesh of the part. The dynamics thus have an effect on the deformable body mechanics. However, with visualNastran Desktop, the deformations are not coupled back in to the analysis and thus cannot influence the rigid body dynamics. Accordingly, the finite element analysis is limited to small deformations.

Just as traditional rigid body codes are developing some compatibility with deformable body elements, the reverse is also occurring. Traditional nonlinear finite element codes include

- ABAQUS, by HKS, Inc. [53]
- ANSYS, by ANSYS, Inc. [9]
- COSMOS, by SRAC [110]
- DYNA3D and NIKE3D, by LLNL [71]
- Mecano, by Samtech [103]
- MSC.MARC, by MSC.Software [87]

Many of these codes may be used with the aforementioned rigid body codes in a hand-shaking manner to obtain stress and deformation of a component or part included in a dynamic simulation. The dynamics are run in a rigid body code, and reaction forces on a particular body in the multi-body simulation are obtained. The geometry and reaction forces are then imported into the finite element code for a stress analysis. In contrast, the

work developed here for TACT2000 allows rigid and deformable bodies to be fully coupled, and the solution to the governing equations for both domains is solved simultaneously.

Most finite element codes can now tie rigid bodies to deformable bodies. With the exception of NIKE3D and Mecano, these interactions are accomplished with a penalty or kinematic constraint. Mecano uses Lagrange multipliers while NIKE3D uses augmented Lagrange multipliers.

Both ABAQUS and DYNA3D have constraint elements and allow limited rigid-deformable coupling. ABAQUS allows rigid bodies to be defined and connections between rigid and deformable bodies. DYNA3D allows single point constraints at nodes such that the translational or rotational degrees of freedom may be specified. It is important to note that the type of rigid-deformable coupling discussed in this thesis may not be well-suited for codes, such as ABAQUS and DYNA3D, which use explicit time integration algorithms. These codes do not take advantage of Hessian information which has been shown to provide superior stability qualities, especially in the presence of coupled algebraic constraints [16, 21, 20, 40].

Holonomic coupling between rigid and deformable bodies is just one area where differences between commercial codes and the code developed in this thesis exist. Other areas include contact mechanics.

ABAQUS has two contact formulations — kinematic and penalty. ABAQUS allows bilateral contact, where the contact surfaces are defined *a priori* and the contact surface must move along the surface. ANSYS allows node-to-node, node-to-surface, and surface-to-surface contact, however, only the penalty method is available for contact enforcement. COSMOS is similar to ANSYS. DYNA3D uses either penalty or Lagrange multiplier method. NIKE3D uses either penalty or a newly implemented augmented Lagrange multiplier method. Mecano uses penalty, kinematic constraint, or Lagrange multipliers. MSC.Marc uses a kinematic enforcement of contact.

Codes that use penalty formulations to enforce contact constraints allow the constraint to be violated. Furthermore, the penalty approach is well-known to engender ill-conditioning. Kinematic enforcement “ties” or “glues” the two bodies together when the gap distance between them goes to zero. The difficulty associated with these methods is trying to find the exact time when the gap goes to zero. If two bodies are in gap status

at the first time step and then in overlap status in the second time step, the kinematic enforcement procedure rewinds the simulation to find the time between these two time steps where the two bodies instantaneously come into contact. At this time, the two bodies are then kinematically connected, and the simulation proceeds from there. The significant disadvantage to this method, though effective, is that it is often very slow and requires a large number of iterations to find the time of instantaneous contact. The number of iterations grows extensively if there are large numbers of contact zones.

The augmented Lagrangian formulation for contact resolves the issues associated with penalty and kinematic contact. Augmented Lagrange engenders no ill-conditioning to the system, and enforces the constraints exactly. Furthermore, change of status between contact and gap within a time step are handled automatically, without iterations required to find the time of instantaneous contact. More detail on the augmented Lagrangian formulation are provided in SECTION 2.4.

In addition to technology on the commercial front, the technology on the academic front should be reviewed. We look first at coupling rigid and deformable bodies through equality constraints first. Then we then review contact mechanics, enforced with inequality constraints.

EQUALITY CONSTRAINTS Ambrósio in 1996 provides a formulation for the dynamics of structures with large motions and nonlinear deformations in a multibody context [4]. He states that the limitations of DADS, ADAMS, and Mecano motivate his work. He states that DADS and ADAMS have no intrinsic flexible body behavior. That is, they can only be used in conjunction with a flexible body code, as explained previously. He notes that Mecano allows for elastic deformations and geometric nonlinearities, but disallows material nonlinearities.

The main contribution of Ambrósio's implementation is the embedding of a nonlinear finite element in part of a larger multibody system. Emphasis is on nonlinear elastic-plastic behavior of materials that occurs during crash and impact. He uses an updated Lagrangian formulation with co-rotation. A lumped mass matrix is employed. Joints between bodies of the multibody system are written as holonomic constraint equations, enforced with Lagrange multipliers.

Ambrósio demonstrates the implementation of a revolute joint between two deformable bodies. He continues with an example of geometric nonlinearity with a slender rod rotating in a plane. Finally, frontal impact of a train, with large plastic deformation, is modeled.

Anantharaman and Hiller published a paper in 1991 examining the numerical simulation of mechanical systems with differential-algebraic equations (DAEs) [5]. A mechanical system consisting of deformable and rigid bodies, joint, and actuators is examined, with emphasis given to the formulation of the system as a large sparse system of equations.

They use a linear elastic superelement, described as an element having rigid body motion superimposed upon small deformations of the body, corresponding to a small number of eigenmodes. Joints are written as constraint equations. The derivatives of these constraint equations are enforced with Lagrange multipliers, thus enforcing a velocity-type condition. Since the numerically integrated velocities will not in general satisfy the constraint equations, the authors suggest introducing another set of Lagrange multipliers to enforce the constraint equations, enforcing a position-type condition. The system is solved using Newton's method for linearization. The system of DAEs are integrated in time with linear multistep methods of variable order and time step size. The HHT- α method [52] is suggested as an alternative. A simulation of a folding antenna is shown as an example of the implementation.

Cardona, Geradin, and co-workers have contributed greatly to the field of multi-body analysis, which become mathematically represented as DAEs [21, 40, 41]. The research has developed element formulation for joints in multibody dynamics. Constraints are enforced with an augmented Lagrangian formulation. Examples of a hinge joint, a landing gear on an airplane, and a wheel capable of rolling and deforming are presented.

Like the work presented in this thesis, Cardona and co-workers enforce constraints through an augmented Lagrange formulation. They note the regularization term of the augmented form adds positive curvature to the displacement-associated submatrix of the Hessian, assists in convergence, and safeguards from encountering zero pivots during factorization.

They show that implicit time stepping algorithms perform better than explicit ones for stability reasons. They compared various time integrators including the trapezoidal rule,

Newmark- β numerical damping, HHT- α , Houbolt, and Park methods. They conclude that the Newmark trapezoidal rule should not be used in the presence of constrained dynamics because the algorithm can become unconditionally unstable. They recommend using a Newmark time integrator with a small amount of numerical damping to stabilize the constraints (Newmark algorithm with $\beta = 0.3025$ and $\gamma = 0.6$) or the HHT- α method. Examples of an articulated rod composed of five nonlinear beam elements with suddenly applied loads is given.

Bauchau *et al.*, discuss numerical integration methods for nonlinear elastic multibody schemes in their 1995 paper [16]. This appears to have its roots in the works of Simo and co-workers who developed energy preserving time integrators for beams [108] and for rigid body dynamics [107]. A Cartesian coordinate system to represent the position of each elastic body in the same inertial reference frame. Kinematic constraints are enforced using a Lagrange multiplier technique. The resulting equations of motion are stiff, nonlinear, DAEs. Integration of the equations is challenging because they claim current integration techniques can become numerically unstable. Bauchau writes,

“The time integration of the resulting equations of motion gives rise to a number of problems such as numerical instabilities and high frequency oscillations of a purely numerical origin. A thorough review of time integration schemes used in structural dynamics is found in [17]. The Newmark scheme is a widely used scheme to integrate the equations of motion resulting from finite element discretizations. Cardona and Geradin [19] have shown that this scheme presents a weak instability when applied to constrained multi-body systems. The culprit is the presence of algebraic equations which are equivalent to infinite frequencies.”

Bauchau proposes a discretization of the equations of motion so that the total energy of the elastic domain is conserved and so that the forces of constraint do no work on the system. These two features give rise to the stability of their proposed numerical integration scheme. A finite element model of a beam linked through kinematic constraints to other beams shows the efficacy of the algorithm.

It is important to note that this paper deals only with elastic bodies, not rigid bodies.

The formulation allows a single elastic body to have large rotations with respect to another elastic body. However, the elastic deformations within the body are assumed to be small. Nonetheless, Bauchau crystalizes the point of infinite frequencies arising from constraints in a multibody, dynamic setting.

More recently, Taylor and Chen investigated energy-momentum conserving algorithms for nonlinear elastic-rigid multibody systems [24]. They developed a second-order accurate time integrator which, in the presence of traction-free boundary conditions, preserves energy and momentum. They developed various joints including ball and socket, slider, and revolute interfaces. Constraints are enforced with standard Lagrange multipliers. They also advocated a modal-rigid approach which accounts for small deformations of elastic bodies with large rotation dynamics.

INEQUALITY CONSTRAINTS — CONTACT In 1881, Hertz provided some of the earliest work on contact mechanics, providing a solution solution for two elastic spheres in contact at a frictionless interface [51]. Since then, other analytical solutions have appeared, usually with standard assumptions of a simplified geometry, small deformations, and linear elasticity. The development of the field may be traced through the references contained in books written by Gladwell [43], Johnson [58], and Kikuchi and Oden [61].

Particularly significant in the history of contact was the formulation of the unilateral contact law by Signorini[105], which states that the interaction between two bodies in contact (1) does not allow interpenetration of the bodies, (2) does not allow adhesion between the bodies, and (3) must have complementarity of the first two conditions. These Signorini conditions are equivalent to the Kuhn–Tucker conditions found in optimization theory. SECTION 2.5 contains the mathematical description of thesis details. Also significant is the contribution of Moreau demonstrating that the unilateral contact law uniquely derives from a non-smooth energy potential [86].

Recent additions to the field of contact mechanics have focused on implementation into the finite element method, appearing first in the 1970’s — Chan and Tuba [23], Francavilla and Zienckiewicz [39], Hughes *et al.* [55]; and continuing into the 1980’s — Oden and Pires [93], Hallquist *et al.* [46], and Curnier and Alart [32]. Reviews by Klarbring [62] and

by Wriggers [118] examine solution methodologies for contact.

The method of constraint enforcement is a convenient way to classify contributions to the field. Perhaps the most elementary way to enforce contact constraints is through a *penalization*. Poor convergence of the penalty approach motivated Wriggers and Simo [119] to propose a *perturbed* Lagrangian method to solve moderate slip problems. An *augmented* Lagrangian formulation was advocated by Landers and Taylor [70] for bilateral (equality constrained) contact. This augmented approach was extended to unilateral contact by Glowinski *et al.* [44], Simo and Laursen [106], Alart and Curnier [2], and Heegaard and Curnier [48].

Contact in the presence of friction has been examined. Alart and Curnier proposed a mixed formulation frictional contact problems in the context of Newton solution [2]. Klarbring considered frictional contact in the context of mathematical programming [63]. Curnier *et al.* [33] discuss large deformation contact with friction. Friction in the presence of plasticity was examined by Chabrand and Dubois [22] and Pietrzak and Curnier [99, 98].

Contact with impact has also been of recent interest. Wriggers *et al.* discuss contact-impact with both large deformation and friction [120]. Taylor and Papadopoulos propose a finite element method for problems with impact [112]. Armero and Petőcz, enforcing contact through penalization, developed time stepping algorithms that conserve energy and momentum [10, 11].

Developing the continuum modeling background to discrete contact mechanics has been the focus of work by Simo and Laursen [106, 107], with emphasis given to problems with friction. The continuum framework was also emphasized in the work of Pietrzak and Curnier [98, 99].

The amount of slip between two contacting bodies is another distinguishing feature. Many contact formulations assume either no slip or small slip contact. Implementation in the finite element method takes the form of node-on-node or node-on-facet contact, respectively. Formulations such as [23, 39, 55, 93, 46, 32, 119, 70, 44, 112, 10, 11] are restricted to small slip. Large slip contact has been explicated by Heegaard and Curnier [47, 48] for frictionless contact and by Pietrzak and Curnier [98, 99] for frictional contact.

1.3 GOALS

The overriding goal of this thesis is to contribute to the understanding of joint stress and deformation during physiological activities. A better understanding of the relationship between joint stress and human motion can help improve the design of joint arthroplasty. Toward this end, a computational biomechanical model is created, accounting for finite deformation in a diarthrodial joint during human gait. The computational model relies on the following specific objectives:

- Create a method to couple deformable and rigid bodies together at interfaces in a dynamic simulation. The interfaces may describe the bodies in persistent contact with each other, or in intermittent contact.
- Use rigid bodies to describe the limb segments and HAT of human model. Couple this large-scale model with finite element model of a deformable hip. Create a forward dynamic simulation of human walking.
- Validate the computational model with clinical data of human gait. Quantify and qualify how stress and deformation of a joint evolves in relation to the gait cycle. Evaluate the significance of muscle forces on joint stress.

1.4 NOVELTY

There are several new technologies developed in this thesis which stem from the objectives stated above. The most significant is the fully coupling of rigid and deformable body analysis in a single analysis code. While other codes may enforce holonomic contact between rigid and deformable bodies, only the code developed here and NIKE3D allow that interaction to be enforced through the method of augmented Lagrange.

We have, for the first time, unilateral contact which takes into account a target surface which moves in a dynamical system. Rotation of the target surface causes a proliferation of terms in the derivation of the first and second variations (see SECTION A.5). To our knowledge, TACT is the only code at this time that allows unilateral, large-slip contact interactions between rigid and deformable bodies and enforces the non-smooth constraint

through and augmented Lagrangian method.

In addition to the enforcement method, it is important to emphasize that TACT uses the Generalized Newton-Raphson procedure for the iterative solution of the nonlinear equations in terms of both primal and dual variables. The quadratic convergence rates of Newton-type methods is superior to the linear convergence rates of Uzawa-type methods.

Embedding the time stepping algorithm into the rigid body element domain is new (see SECTION 3.3). Essentially, the method of “embedded dynamics” allows rigid body dynamics equations of motion to be combined with static nonlinear elasticity. In this way, the constraints linking the rigid and deformable bodies are stabilized, unlike previous methods, which noted time integration of these differential-algebraic type systems can lead to weak instabilities and divergence of the solution. Moreover, embedding the time stepping algorithm in the rigid body element allows the rigid hyperbolic system to be solved in an elliptic setting.

Constraints between two rigid bodies remain prone to the instabilities arising from rigid-rigid type constraints. To overcome these difficulties, we use a heavily damped Newmark method ($\beta = 0.3025$ and $\gamma = 0.6$). It is important to note, however, that the embedded dynamics approach may use any time integration scheme, as long as the first and second variations are defined and implemented properly.

Finally, we believe this is the first biomechanical model which couples rigid and deformable bodies in a single analysis. Previous large scale models have used rigid body dynamics to model the motion of human gait and movement. While beneficial, these models are unable to provide stress and deformation information because of the inherent rigid body assumption. Likewise, small scale models of joints and arthroplasties have relied on the definition of traction boundary conditions that are intended to simulate physiological loading. While this loading may be accurate for some activities, it is limited because it cannot automatically reflect changing ambulation schemes.

The biomechanical model presented here is unique because the models for the joint and limbs are fully coupled. As a result, changes in gait or locomotion are automatically reflected in stress and deformation of the joint. Similarly, joint deformations alter the position of mass centers, thus affecting the dynamic simulation. The coupled model accounts for limb

dynamics and joint deformation in a unified setting. With this model, human motion data obtained from gait analysis laboratories can be used to quantify stress in a persons joint as they walk.

1.5 OUTLINE

CHAPTER 2 provides the formulation of a coupled dynamical system composed of deformable and rigid domains in the presence of equality and inequality constraints. CHAPTER 3 details how the formulation is implemented in a finite element code, with the residual vectors and tangent matrices given for numerous element types. CHAPTER 4 discusses a biomechanical model of gait. CHAPTER 5 presents and discusses the results from the gait simulation. CHAPTER 6 makes conclusions drawn from the three aspects of the thesis work — formulation, implementation, and application of a coupled method.

CHAPTER 2

FORMULATION

2.1 OVERVIEW

This chapter provides the formulation of a mechanical system composed of deformable and rigid bodies. The bodies interact through interfaces, which will be formulated in terms of constraint equations. The formulation is the continuum basis for the discrete finite element code, discussed in CHAPTER 3. The formulation and implementation are the computational tools used to create a novel biomechanical model. This model computes stress and deformation of a human joint while simultaneously incorporating the dynamics of human gait.

The formulation of a coupled dynamical system composed of deformable and rigid domains in the presence of equality and inequality constraints is presented. The governing equations of motion and constraint equations are nonlinear, due to finite deformation, large rotation, and non-smooth constraints.

2.2 DEFORMABLE BODY DYNAMICS

The governing equations of motion for a general deformable body may be constructed from nonlinear continuum mechanics. These ideas are briefly recorded here for completeness and clarity of notation. More detail may be found in numerous texts on the subject such as Malvern [74], Gurtin [45], Marsden and Hughes [75], Ogden [94], and Ciarlet [25].

Following some definitions from continuum mechanics, the local form of the governing equations of motion is stated. This form is also called the strong form of the Initial Boundary Value Problem (IBVP). The strong form leads naturally to the equivalent weak form, which is amenable to implementation with the finite element method. This connection appears in CHAPTER 3.

2.2.1 LOCAL GOVERNING EQUATION OF MOTION

BODIES AND BOUNDARIES Let body Ω be an open, bounded subset of three-dimensional Euclidean space \mathbb{R}^3 with boundary $\partial\Omega$. The boundary is decomposed within a particular space dimension into two non-overlapping subdomains, Γ_u and Γ_T , where displacements or tractions are prescribed. Thus $\partial\Omega = \Gamma_u \cup \Gamma_T$ and $\Gamma_u \cap \Gamma_T = \emptyset$. Set closure is denoted $\bar{\Omega} = \Omega \cup \partial\Omega$. Let the body be composed of a closed set of particles with coordinates \mathbf{X} in the reference configuration. The particle has coordinates $\mathbf{X} = \langle X_1, X_2, X_3 \rangle^T$ as measured from some origin O in a dextral, orthonormal, inertial reference frame $\hat{\mathbf{E}}_1, \hat{\mathbf{E}}_2, \hat{\mathbf{E}}_3$.

MOTIONS AND DISPLACEMENTS Let the motion, a one parameter family of configurations, $\varphi : \Omega \times \mathbb{T} \mapsto \mathbb{R}^3$ map the material particle \mathbf{X} into the current configuration \mathbf{x} such that $\mathbf{x} = \varphi(\mathbf{X}, t) = \varphi_t(\mathbf{X})$. The motion occurs over a time interval defined as $\mathbb{T} \triangleq [0, T]$. A motion evaluated at a particular time $t \in \mathbb{T}$ is referred to as a configuration or placement. To each configuration, we assign a displacement field $\mathbf{u} : \Omega \mapsto \mathbb{R}^3$ such that $\mathbf{u}(\mathbf{X}, t) = \varphi(\mathbf{X}, t) - \mathbf{X}$.

To each configuration, we define a deformation gradient $\mathbf{F} : \Omega \times \mathbb{T} \mapsto \mathbb{M}_{+}^3$ such that

$$\mathbf{F} \triangleq \frac{\partial \varphi}{\partial \mathbf{X}}, \quad F_{iJ} \triangleq \frac{\partial \varphi_i}{\partial X_J}. \quad (2.1)$$

Lower case indices represent components of tensors in the current configuration whereas upper case indices represent components of tensors in the reference configuration. Real, square matrices of dimension three and positive determinants are denoted \mathbb{M}_{+}^3 .

All configurations must be admissible in the sense that the Jacobian of the deformation J must be positive

$$J \triangleq \det \mathbf{F} > 0. \quad (2.2)$$

This requirement keeps the deformations from mapping the body to a single point ($J = 0$) or turning the body “inside-out” ($J < 0$).

KINEMATICS A standard stretch measure is the Cauchy-Green strain tensor

$$\mathbf{C} \triangleq \mathbf{F}^T \mathbf{F}, \quad C_{IJ} \triangleq F_{Ii} F_{iJ}. \quad (2.3)$$

An alternative strain measure, the Green-Lagrange strain tensor, is defined

$$\mathbf{E} \triangleq \frac{1}{2}(\mathbf{C} - \mathbf{1}), \quad E_{IJ} \triangleq \frac{1}{2}(C_{IJ} - \delta_{IJ}). \quad (2.4)$$

The Green-Lagrange strain tensor is often used to define constitutive laws because the measure, when linearized about the reference configuration, coincides with the small strain tensor of linear deformation elasticity.

KINETICS The forces acting on a deformable body engender stress within the body. These forces come from external fields, such as gravity, or from tractions applied on the boundary of the body. The First Piola-Kirchhoff stress tensor $\mathbf{P} : \Omega \times \mathbb{T} \mapsto \mathbb{M}^3$ is used to describe the force vector in the current configuration, normalized by the undeformed area over which the force acts. The area is measured in the reference configuration. This stress measure is in contrast to the Cauchy (true) stress tensor $\boldsymbol{\sigma}$ (current traction vector divided by deformed area) and the second (symmetric) Piola-Kirchhoff stress tensor \mathbf{S} (the traction vector mapped back to the reference configuration divided by the undeformed area). These two stress tensors $\boldsymbol{\sigma}$ and \mathbf{S} are necessarily symmetric whereas \mathbf{P} is in general unsymmetric.

STRONG FORM Let the body force per unit volume be $\rho_0 \mathbf{B}$, where ρ_0 is the density (mass per unit volume) of the body in the undeformed configuration and the \mathbf{B} is typically a constant vector such as $\langle 0, -g, 0 \rangle^T$ arising from a gravitational field. Finally, let \mathbf{N} , in the reference configuration, be the normal vector to a surface on $\partial\Omega$ where the direction of \mathbf{N} points perpendicular to the surface and the magnitude of the vector represents the area of the surface. With these notations in hand, we state the strong form of the local momentum balance equations, subject to boundary and initial conditions, in Box 2.1. Note that in the governing equation, $\text{DIV} \mathbf{P}$ is explicitly given in indicial notation as $P_{iJ,J}$.

Box 2.1: Strong Form (**S**) of the Initial Boundary Value Problem (IBVP) for Deformable Body Dynamics

Given:	$\rho_0 \mathbf{B} : \Omega \times \mathbb{T} \mapsto \mathbb{R}^3$	(body force per unit volume)
	$\bar{\mathbf{u}} : \Gamma_u \times \mathbb{T} \mapsto \mathbb{R}^3$	(prescribed displacement)
	$\bar{\mathbf{T}} : \Gamma_T \times \mathbb{T} \mapsto \mathbb{R}^3$	(prescribed traction)
Find:	$\mathbf{u} : \bar{\Omega} \times \mathbb{T} \mapsto \mathbb{R}^3$	such that $\forall t \in \mathbb{T}$,
	$\text{DIV} \mathbf{P} + \rho_0 \mathbf{B} = \rho_0 \frac{\partial^2 \mathbf{u}}{\partial t^2}$	in $\Omega \times]0, T[$
subject to		
	$\mathbf{P} \mathbf{N} = \bar{\mathbf{T}}$	on $\Gamma_T \times]0, T[$ (natural boundary conditions)
	$\mathbf{u} = \bar{\mathbf{u}}$	on $\Gamma_u \times]0, T[$ (essential boundary conditions)
	$\mathbf{u}(\mathbf{X}, 0) = \mathbf{u}_0$	in $\bar{\Omega} \times [0]$ (initial displacement)
	$\dot{\mathbf{u}}(\mathbf{X}, 0) = \dot{\mathbf{u}}_0$	in $\bar{\Omega} \times [0]$ (initial velocity)

There are some important assumptions underlying the statement of the IBVP. First, it is assumed that the boundaries Γ_u and Γ_T are fixed on the body once-and-for-all. This means these boundaries do not evolve with time. Portions of the boundary once designated as traction boundary conditions may not, at a later instance, become displacement boundary conditions. Second, it is assumed that the prescribed initial conditions must be consistent with prescribed boundary conditions at $t = 0$. Finally, it is assumed that tractions are strictly dead loads. Pressure loads or follower loads are assumed absent.

It should be noted that the formulation has been cast in terms of unknown \mathbf{u} instead of unknown φ . An equivalent problem to that stated in Box 2.1 may be formulated in terms of placements φ , rather than the displacements \mathbf{u} . This formulation is often used in mathematical presentations of nonlinear continuum mechanics, such as Ciarlet [25], and is more economical in the sense that the unknown displacements need to be computed only if necessary ($\mathbf{u} = \varphi - \mathbf{X}$). The unknown \mathbf{u} variable as the problem unknown is retained for reasons elucidated by Curnier [31]. In many problems, the only closed-form solution available is one for linear elasticity. Validations of finite element implementations require, therefore, a linear solution. This solution is necessarily the displacement variable \mathbf{u} since the mapping φ is introduced only when generalizing linear elasticity to the nonlinear regime.

Thus, the formulation of the IVBP as in Box 2.1 readily adapts to both the linear and nonlinear contexts.

2.2.2 GLOBAL STATEMENT OF VIRTUAL WORK

SOLUTION AND VARIATIONAL SPACES Working toward the development of a variational method, we define the following solution spaces \mathcal{S} and weighting spaces \mathcal{V} such that

$$\mathcal{S} = \mathcal{S}_t = \left\{ \mathbf{u} \in H^1(\bar{\Omega} \times \mathbb{T}) \mapsto \mathbb{R}^3 \mid \mathbf{u} = \bar{\mathbf{u}} \text{ on } \Gamma_u \times]0, T[\right\}, \quad (2.5)$$

$$\mathcal{V} = \left\{ \delta \mathbf{u} \in H^1(\bar{\Omega}) \mapsto \mathbb{R}^3 \mid \delta \mathbf{u} = \mathbf{0} \text{ on } \Gamma_u \right\}. \quad (2.6)$$

Note that the trial function space is a function of time while the weighting space is not. The initial conditions, $\mathbf{u}(\mathbf{X}, 0) = \mathbf{u}_0$ and $\dot{\mathbf{u}}(\mathbf{X}, 0) = \dot{\mathbf{u}}_0$, must be members of \mathcal{S} . The notation H^1 denotes the Sobolev space with members and their gradients being square-integrable.

WEAK FORM The weak form of the IBVP is obtained from the strong form by taking the inner product of the governing equations of motion with a variation of the displacement field, integrating by parts, and invoking properties of homogeneity of the variation on the boundary. These details may be found in [30, 54]. The weak form of the IBVP is stated in Box 2.2. Note that the natural boundary conditions have already been incorporated into the weak form through the right-hand-side of the equations. Also, the essential boundary conditions have been incorporated into the weak form through construction of the solution space \mathcal{S}_t .

It is convenient to abbreviate the above statement of the variational form. Making use of the following abbreviations

$$\delta \mathbf{u} \cdot \mathbf{F}^{\text{iner}} = \int_{\Omega} \delta \mathbf{u} \cdot \rho_0 \frac{\partial^2 \mathbf{u}}{\partial t^2} d\Omega, \quad (2.7)$$

$$\delta \mathbf{u} \cdot \mathbf{F}^{\text{int}} = \int_{\Omega} \nabla \delta \mathbf{u} : \mathbf{P} d\Omega, \quad (2.8)$$

$$\delta \mathbf{u} \cdot \mathbf{F}^{\text{ext}} = \int_{\Omega} \delta \mathbf{u} \cdot \rho_0 \mathbf{B} d\Omega + \int_{\Gamma_T} \delta \mathbf{u} \cdot \bar{\mathbf{T}} d\Gamma, \quad (2.9)$$

and defining

$$\mathbf{R}_u \triangleq \mathbf{F}^{\text{ext}} - \mathbf{F}^{\text{iner}} - \mathbf{F}^{\text{int}}, \quad (2.10)$$

Box 2.2: Weak Form (**W**) of the Initial Boundary Value Problem (IBVP) for Deformable Body Dynamics

Given:	$\rho_0 \mathbf{B} : \Omega \times \mathbb{T} \mapsto \mathbb{R}^3$ (body force per unit volume)
	$\bar{\mathbf{u}} : \Gamma_u \times \mathbb{T} \mapsto \mathbb{R}^3$ (prescribed displacement)
	$\bar{\mathbf{T}} : \Gamma_T \times \mathbb{T} \mapsto \mathbb{R}^3$ (prescribed traction)
Find:	$\mathbf{u} \in \mathcal{S}_t$ such that $\forall \delta \mathbf{u} \in \mathcal{V}$,
$\int_{\Omega} \delta \mathbf{u} \cdot \rho_0 \frac{\partial^2 \mathbf{u}}{\partial t^2} d\Omega + \int_{\Omega} \nabla \delta \mathbf{u} : \mathbf{P} d\Omega$ $= \int_{\Omega} \delta \mathbf{u} \cdot \rho_0 \mathbf{B} d\Omega + \int_{\Gamma_T} \delta \mathbf{u} \cdot \bar{\mathbf{T}} d\Gamma \quad \text{in } \Omega \times]0, T[\quad (\mathbf{W})$	
subject to	
$\mathbf{u}(\mathbf{X}, 0) = \mathbf{u}_0 \quad \text{in } \bar{\Omega} \times [0] \quad (\text{initial displacement})$	
$\dot{\mathbf{u}}(\mathbf{X}, 0) = \dot{\mathbf{u}}_0 \quad \text{in } \bar{\Omega} \times [0] \quad (\text{initial velocity})$	

the variational form is written

$$-\delta \mathcal{W}_u = \delta \mathbf{u} \cdot \mathbf{R}_u = 0. \quad (2.11)$$

2.2.3 LINEARIZATION

A Taylor series expansion is used to iteratively solve the nonlinear equations \mathbf{R} which are functions of the state, defined abstractly as \mathbf{s} for now. The expansion leads to an approximation of the equation system at the new iteration, $\mathbf{R}^{(i+1)}$, as the system at the previous iteration, $\mathbf{R}^{(i)}$, plus first-order derivative information, plus higher order terms H.O.T. The expansion is written generally as

$$\mathbf{R}^{(i+1)} = \mathbf{R}^{(i)} + \frac{\partial \mathbf{R}^{(i)}}{\partial \mathbf{s}^{(i)}} \Delta \mathbf{s}^{(i)} + \text{H.O.T.} \quad (2.12)$$

Setting $\mathbf{R}^{(i+1)} = \mathbf{0}$ gives the linear system

$$-\frac{\partial \mathbf{R}^{(i)}}{\partial \mathbf{s}^{(i)}} \Delta \mathbf{s}^{(i)} = \mathbf{R}^{(i)} \quad (\text{linear system}). \quad (2.13)$$

Note that we have written only $\mathbf{R}^{(i)}$ and not $\mathbf{R}_n^{(i)}$, $\mathbf{R}_{n+1}^{(i)}$ or $\mathbf{R}_{\alpha}^{(i)}$ where n is the time step number and α is a midpoint parameter between time steps, $t_{\alpha} = \alpha t_n + (1 - \alpha) t_{n+1}$. We

have not indicated, yet, at what time step we are enforcing the equations of motion because we want the formulation to be general. Implementation of the formulation will result in enforcement of $\mathbf{R}_{n+1} = \mathbf{0}$ for a Newmark algorithm and $\mathbf{R}_\alpha = \mathbf{0}$ for a generalized midpoint rule algorithm.

For the \mathbf{R}_u residual system in Eq. (2.10), the state variables are $\mathbf{s} = \langle \mathbf{u}, \mathbf{v}, \mathbf{a} \rangle^T$, and the following are the consistent tangent stiffness, damping, and mass matrices, respectively,

$$\mathbf{K} = -\frac{\partial \mathbf{R}}{\partial \mathbf{u}} = \frac{\partial \mathbf{F}^{\text{int}}}{\partial \mathbf{u}}, \quad (2.14)$$

$$\mathbf{D} = -\frac{\partial \mathbf{R}}{\partial \mathbf{v}} = \frac{\partial \mathbf{F}^{\text{int}}}{\partial \mathbf{v}}, \quad (2.15)$$

$$\mathbf{M} = -\frac{\partial \mathbf{R}}{\partial \mathbf{a}} = \mathbf{M}. \quad (2.16)$$

2.2.4 CONSTITUTIVE LAWS

The governing equations of motion, as stated, have more unknowns than equations. To close the system, more equations must be added. These equations come in the form of constitutive equations that relate the gradients of displacements or deformations (and perhaps their time derivatives) to the stress within the body.

One of the most elementary constitutive laws for isotropic, nonlinear continuum mechanics is Kirchhoff-St.Venant, written in terms of the Green-Lagrange strain tensor \mathbf{E} , the Second Piola-Kirchhoff stress tensor \mathbf{S} , and two Lamé constants λ and μ . The stress response function is written

$$\mathbf{S}(\mathbf{E}) = [\lambda \mathbf{1} \otimes \mathbf{1} + 2\mu \mathbf{I}] : \mathbf{E}. \quad (2.17)$$

Kirchhoff-St.Venant, though widely used, is not a robust material law for finite deformation. Two features must be met for a material law to be called robust: (1) Increasing compressive strains lead to increasing compressive stresses, and (2) the tangent remains positive and monotonic for all deformation states.

To make up for the shortcomings of Kirchhoff-St.Venant in finite compression, many alternative material laws exist. We elect to use a robust material law found in Curnier [30] which has the form

$$\mathbf{S}(\mathbf{C}) = \lambda(J - 1)\mathbf{C}^{-1} + \mu(\mathbf{C} - \mathbf{1}). \quad (2.18)$$

The material law has been shown to act similarly to Kirchhoff-St.Venant for infinitesimal deformation. Unlike Krichhoff-St.Venant, however, the material law in Eq. (2.18) is robust in finite compression. Details of this law may be found in SECTION 6.6.2 of [30]. The Lamé parameters λ and μ may be used to find the modulus of elasticity E and Poisson's ratio ν through

$$E = \frac{\mu(3\lambda + 2\mu)}{\lambda + \mu}, \quad \nu = \frac{\lambda}{2(\lambda + \mu)}. \quad (2.19)$$

See Malvern [74] for additional relationships between material constants.

This robust material law has been extended to include viscoelastic effects [30, 101] and used to describe the behavior of anterior cruciate ligaments [100]. A viscoelastic stress contribution is simply added to the stress response function in the reference configuration,

$$\mathbf{S}(\mathbf{C}, \dot{\mathbf{C}}) = \underbrace{\lambda(J - 1)\mathbf{C}^{-1} + \mu(\mathbf{C} - \mathbf{1})}_{\mathbf{S}^{\text{elas}}} + \underbrace{\eta \dot{\mathbf{C}}}_{\mathbf{S}^{\text{visc}}}, \quad (2.20)$$

where \mathbf{S}^{elas} is the elastic contribution and \mathbf{S}^{visc} is the viscoelastic contribution to the second Piola-Kirchhoff stress tensor $\mathbf{S}(\mathbf{C}, \dot{\mathbf{C}})$. The material constant η controls the amount of viscoelasticity in the model. Note the robust elastic material law is recovered for $\eta = 0$.

Linearization of the governing equations of motion will require, by virtue of the chain rule, linearization of the elastic and viscoelastic material tangents. These tangents \mathbf{C} and \mathbf{V} may be found to be [30]

$$\begin{aligned} \mathbf{C}_{IJKL} &\triangleq \frac{\partial S_{IJ}}{\partial E_{KL}} = \lambda [JC_{IJ}^{-1}C_{KL}^{-1} + (1 - J)(C_{IK}^{-1}C_{JL}^{-1} + C_{IL}^{-1}C_{JK}^{-1})] \\ &\quad + \mu(\delta_{IK}\delta_{JL} + \delta_{IL}\delta_{JK}), \end{aligned} \quad (2.21)$$

$$\mathbf{V}_{IJKL} \triangleq \frac{\partial S_{IJ}}{\partial \dot{E}_{KL}} = \eta (\delta_{IK}\delta_{JL} + \delta_{IL}\delta_{JK}). \quad (2.22)$$

2.3 RIGID BODY DYNAMICS

The governing equations of motion for a rigid body or a system of rigid bodies may be constructed in many ways. Methods of forming the equations of motion for rigid body system may be found in texts such as Lanczos [68], Kane and Levinson [59], and McGill and King [82]. The two most common are the Newtonian formulation and the Lagrangian

formulation. The Lagrangian point-of-view is advantageous because (a) the minimum set of generalized coordinates may be used to fully describe the system and (b) reaction forces that do no work on the system are not brought into evidence. The number of equations necessary to describe a rigid system obtained with Lagrange's equations is often smaller than the number obtained with Newton's equations. Newton's approach, however, often produces equations that are less coupled and therefore lead to less of a proliferation of derivatives when linearized.

Regardless of which method is used to derive the equations of motion, the governing set of equations must produce the same physics. We describe the dynamical system with Lagrange's equations. However, when implemented in a finite element code, the equations will look identical to Newton's equations for a single body. See SECTION 3.3 for more details.

2.3.1 GOVERNING EQUATIONS OF MOTION

BODIES AND BOUNDARIES Since we are now considering deformable and rigid bodies, the notation for a body will be extended from simply Ω to either Ω_D or Ω_R for deformable or rigid bodies, respectively. For the case where the domain is arbitrary, either a deformable or a rigid body, Ω will be used. The boundary of Ω_R may be decomposed into two non-overlapping subdomains, Γ_q and Γ_Q where displacements and tractions are prescribed, respectively. Thus $\partial\Omega_R = \Gamma_q \cup \Gamma_Q$ and $\Gamma_q \cap \Gamma_Q = \emptyset$. Set closure is denoted $\bar{\Omega}_R = \Omega_R \cup \partial\Omega_R$. The rigid body is composed of points. The governing equations of motion for the entire rigid body may be written in terms of the evolution of the mass center. The mass center will be labeled \mathbf{r}^G and have coordinates $\mathbf{r} = \langle r_1, r_2, r_3 \rangle^T$ as measured from some origin O in the dextral, orthonormal, inertial reference frame $\hat{\mathbf{E}}_1, \hat{\mathbf{E}}_2, \hat{\mathbf{E}}_3$. A reference frame attached to a rigid body will be labeled such that the first index refers to the frame number while the second index refers to the direction. For example, $\hat{\mathbf{e}}_{11}, \hat{\mathbf{e}}_{12}, \hat{\mathbf{e}}_{13}$ refer to frame 1; $\hat{\mathbf{e}}_{31}, \hat{\mathbf{e}}_{32}, \hat{\mathbf{e}}_{33}$ refer to frame 3. The zero frame is considered to be the inertial frame with basis $\hat{\mathbf{e}}_{01}, \hat{\mathbf{e}}_{02}, \hat{\mathbf{e}}_{03}$ translated from, but not rotated with respect to, the $\hat{\mathbf{E}}_1, \hat{\mathbf{E}}_2, \hat{\mathbf{E}}_3$ frame.

MOTIONS AND DISPLACEMENTS The motion of deformable bodies was defined with the variable $\varphi(\mathbf{X}, t)$. The motion of rigid bodies will be defined with the variable $\mathbf{q}(t)$. The motion occurs over the same time interval defined for deformable bodies. The reference configuration for rigid bodies is simply $\mathbf{q}(0)$, analogous to the reference configuration for deformable bodies $\varphi(\mathbf{X}, 0) = \mathbf{X} + \mathbf{u}(\mathbf{X}, 0)$.

KINEMATICS The kinematics of a rigid body are necessary to form the kinetic energy of the system. The kinetic and potential energy of the system are then used to define a Lagrangian, from which the governing equations of motion are obtained.

Of particular importance will be the description of the velocity of two points belonging to a rigid body, moving in an inertial reference frame. Let points \mathbf{P} and \mathbf{S} belong to rigid body B moving in the inertial reference frame E . The velocity $\mathbf{v}^{S,E}$ of point \mathbf{S} measured in frame E is given by

$$\mathbf{v}^{S,E} = \mathbf{v}^{S,B} + \mathbf{v}^{P,E} + \boldsymbol{\omega}^{B,E} \times \mathbf{r}^{PS}, \quad (2.23)$$

where $\mathbf{v}^{S,B}$ is the velocity of point \mathbf{S} measured in the moving frame B , $\mathbf{v}^{P,E}$ is the velocity of point \mathbf{P} measured in the frame E , $\boldsymbol{\omega}^{B,E}$ is the angular velocity of body B measured in frame E , and \mathbf{r}^{PS} is the position vector from point \mathbf{P} to point \mathbf{S} .

ENERGY MEASURES Potential energy of a body may come from external loads or from stretch of the body, resulting in external and internal potential energy, respectively. Internal potential energy from stretching is applicable to deformable bodies but not to rigid bodies. External potential energy may be decomposed into loading throughout the body Ω or on the boundary $\partial\Omega$. Loading throughout the body will come from a gravitational field whereas loads on the boundary will be applied loads. It is often assumed that external loads are independent of the path the body takes from one configuration to the next. If a load is conservative, it is derivable from a potential and thus may be included in the external potential energy term.

For convenience, we will assume that gravity is the only conservative load known *a*

a priori. Thus the potential energy for a rigid body is written

$$V = -\mathbf{r}^G \cdot m\mathbf{g}, \quad (2.24)$$

where \mathbf{r}^G located the mass center, m is the mass of the rigid body, and \mathbf{g} is the gravity vector. Since we wish to allow the applied loads to be either conservative or non-conservative, applied loads will be included in the generalized force term \mathbf{Q} , defined in Eq. (2.27).

The kinetic energy for a rigid body Ω is defined as

$$K \triangleq \frac{1}{2} m\mathbf{v}^G \cdot \mathbf{v}^G + \frac{1}{2}\boldsymbol{\omega} \cdot \mathbf{I}\boldsymbol{\omega}, \quad (2.25)$$

where \mathbf{v}^G is the velocity of the mass center, and \mathbf{I} is the inertia tensor of the rigid body with respect to the mass center.

The definition of potential and kinetic energies leads to the Lagrangian functional, defined as

$\mathcal{L} \triangleq K - V$

(2.26)

KINETICS The applied forces and moments acting on the rigid body act with the gravitational forces to balance inertial forces. The applied forces and moments are included through the use of generalized forces \mathbf{Q} . Let the applied forces \mathbf{F}_1 , \mathbf{F}_2 , and applied torques \mathbf{T}_1 , \mathbf{T}_2 , acting on the rigid system be rewritten as an equivalent resultant force \mathbf{F}_R and resultant moment \mathbf{M}_R acting at some point $\mathbf{P}_R \in \mathbb{R}^3$ located by the vector $\mathbf{r}^{P_R}(\mathbf{q})$, as FIG. 2.1 shows.

We assume that the applied forces and moments are functions of time alone. This assumption allows the forces and moments to vary in a schedule through time without depending on the configuration of the system.

The generalized force $\mathbf{Q}(\mathbf{q}, \dot{\mathbf{q}})$ is defined as

$$\mathbf{Q} = \left[\frac{\partial \mathbf{r}^G}{\partial \mathbf{q}} \right]^T \cdot \mathbf{F}^R + \left[\frac{\partial \boldsymbol{\omega}^{B,E}}{\partial \dot{\mathbf{q}}} \right]^T \cdot \mathbf{M}^R, \quad Q_i = \frac{\partial r_k^G}{\partial q_i} F_k^R + \frac{\partial \omega_k^{B,E}}{\partial \dot{q}_i} M_k^R. \quad (2.27)$$

For the purposes of finite element implementation, it is more reasonable and convenient to have a number of forces and torques applied to the rigid body, instead of just one force-moment resultant. In this case, the generalized force \mathbf{Q} may be restated in the equivalent

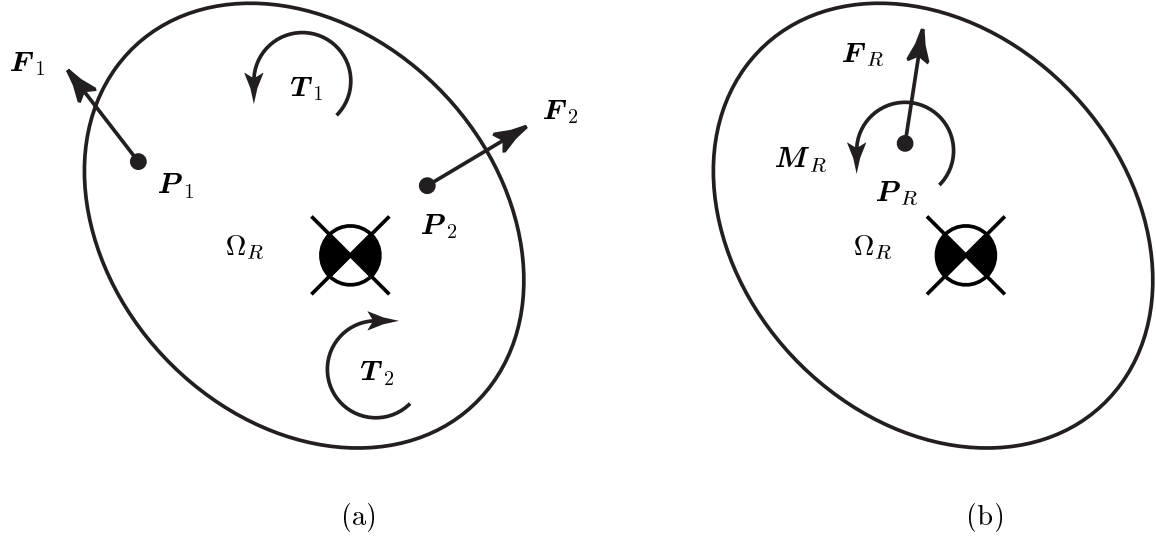


FIGURE 2.1: (a) Rigid body with two applied forces \mathbf{F}_1 and \mathbf{F}_2 applied at points P_1 and P_2 , respectively and with two applied torques \mathbf{T}_1 and \mathbf{T}_2 . (b) The same rigid body with an equivalent force-moment \mathbf{F}_R and \mathbf{M}_R applied at point P_R .

form,

$$\mathbf{Q} = \sum_{a=1}^{n_{\text{af}}} \left[\frac{\partial \mathbf{r}^{P_a}}{\partial \dot{\mathbf{q}}} \right]^T \cdot \mathbf{F}^{P_a} + \sum_{b=1}^{n_{\text{at}}} \left[\frac{\partial \boldsymbol{\omega}^{B,E}}{\partial \dot{\mathbf{q}}} \right]^T \cdot \mathbf{T}^b, \quad (2.28)$$

where n_{af} represents the number of applied forces and n_{at} represents the number of applied torques. Note that the body force vector arising from gravity is not included in applied forces (FIG. 2.1). This occurs because the effects of gravity are already included in the Lagrangian \mathcal{L} through the external potential energy V^{ext} . Note also that while only two applied forces and two applied moments are drawn in FIG. 2.1 (a), any number of forces and torques, in general, may be accounted for, as indicated by the summation in Eq. (2.28).

An alternative formulation to Eq. (2.27) may be written as

$$\mathbf{Q} = \left[\frac{\partial \mathbf{v}^{R,E}}{\partial \dot{\mathbf{q}}} \right]^T \cdot \mathbf{F}^R + \left[\frac{\partial \boldsymbol{\omega}^{B,E}}{\partial \dot{\mathbf{q}}} \right]^T \cdot \mathbf{M}^R, \quad Q_i = \frac{\partial v_k^{R,E}}{\partial \dot{q}_i} F_k^R + \frac{\partial \omega_k^{B,E}}{\partial \dot{q}_i} M_k^R, \quad (2.29)$$

where $\mathbf{v}^{R,E}$ is the velocity of point R taken in the inertial E frame. This result may be seen by considering Eqs. (A.17)–(A.22) in SECTION A.3.

Box 2.3: Lagrangian Form (**L**) of the Initial Value Problem (IVP) for Rigid Body Dynamics

Given:	$\mathcal{L} : \mathcal{C} \times \delta\mathcal{C} \mapsto \mathbb{R}$ (Lagrangian)
Find:	$\mathbf{q} \in \mathcal{C}_t$ such that $\forall \delta\mathbf{q} \in \delta\mathcal{C}$,
$\delta\mathbf{q} \cdot \left(\frac{d}{dt} \frac{\partial \mathcal{L}}{\partial \dot{\mathbf{q}}} - \frac{\partial \mathcal{L}}{\partial \mathbf{q}} - \mathbf{Q} \right) = 0 \quad \text{in } \mathbb{T}$	
subject to	
$\mathbf{q}(0) = \mathbf{q}_0 \quad \text{at } [0] \quad (\text{initial position})$	
$\dot{\mathbf{q}}(0) = \dot{\mathbf{q}}_0 \quad \text{at } [0] \quad (\text{initial velocity})$	

VARIATIONAL FORM The strong form of the IBVP for deformable body dynamics was used to obtain the equivalent weak or variational form. The analogous variational form for rigid body dynamics is obtained from the Lagrangian and the generalized forces, stated in Box 2.3. Here, the configuration space, \mathcal{C} , and the space of admissible variations, $\delta\mathcal{C}$, are respectively defined as

$$\mathcal{C} = \mathcal{C}_t = \{ \mathbf{q} : (\bar{\Omega} \times \mathbb{T}) \mapsto \mathbb{R}^q \mid \mathbf{q} = \bar{\mathbf{q}} \text{ on } \Gamma_q \times]0, T[\}, \quad (2.30)$$

$$\delta\mathcal{C} = \{ \delta\mathbf{q}(\bar{\Omega}) \mapsto \mathbb{R}^q \mid \delta\mathbf{q} = \mathbf{0} \text{ on } \Gamma_q \}, \quad (2.31)$$

where \mathbb{R}^q has dimension equal to the number of generalized coordinates.

The Lagrangian form Eq. (L) in Box 2.3 leads to a set of nonlinear equations in terms of the generalized coordinates \mathbf{q} and the time derivatives $\dot{\mathbf{q}}$ and $\ddot{\mathbf{q}}$, written compactly as

$$\delta\mathbf{q} \cdot (\mathbf{A}(\mathbf{q})\ddot{\mathbf{q}} + \mathbf{B}(\mathbf{q})\dot{\mathbf{q}}^2 - \mathbf{G}(\mathbf{q}) - \mathbf{Q}(\mathbf{q}, \dot{\mathbf{q}})) = 0. \quad (2.32)$$

The \mathbf{A} term contains generalized mass and inertia terms. The \mathbf{B} term comes from the centrifugal and Coriolis accelerations. The \mathbf{G} term comes from the gravity field. The \mathbf{Q} term comes from applied forces and torques. It is convenient to abbreviate the above variational form as follows. Making use of

$$\delta\mathbf{q} \cdot \mathbf{F}^{\text{iner}} = \delta\mathbf{q} \cdot (\mathbf{A}(\mathbf{q})\ddot{\mathbf{q}} + \mathbf{B}(\mathbf{q})\dot{\mathbf{q}}^2), \quad (2.33)$$

$$\delta\mathbf{q} \cdot \mathbf{F}^{\text{ext}} = \delta\mathbf{q} \cdot (\mathbf{G}(\mathbf{q}) + \mathbf{Q}(\mathbf{q}, \dot{\mathbf{q}})), \quad (2.34)$$

and defining

$$\mathbf{R}_{\ddot{\mathbf{q}}} \triangleq \mathbf{F}^{\text{ext}} - \mathbf{F}^{\text{int}}, \quad (2.35)$$

then the variational form may be abbreviated

$$\boxed{-\delta\mathcal{W}_q = \delta\mathbf{q} \cdot \mathbf{R}_{\ddot{\mathbf{q}}} = 0}. \quad (2.36)$$

2.3.2 LINEARIZATION

The Taylor series expansion presented in Eqs. (2.12)–(2.13) for solving nonlinear deformable body dynamics problems applies equally well for rigid body dynamics problems. For the $\mathbf{R}_{\ddot{\mathbf{q}}}$ residual system in Eq. (2.35), the state variables are $\mathbf{s} = (\mathbf{q}, \dot{\mathbf{q}}, \ddot{\mathbf{q}})^T$. The following are the consistent tangent stiffness, damping, and mass matrices, respectively,

$$\mathbf{K} = -\frac{\partial \mathbf{R}}{\partial \mathbf{q}} = \frac{\partial[\mathbf{A}(\mathbf{q})\ddot{\mathbf{q}}]}{\partial \mathbf{q}} + \frac{\partial[\mathbf{B}(\mathbf{q})\dot{\mathbf{q}}^2]}{\partial \mathbf{q}} - \frac{\partial \mathbf{G}(\mathbf{q})}{\partial \mathbf{q}} - \frac{\partial \mathbf{Q}(\mathbf{q}, \dot{\mathbf{q}})}{\partial \mathbf{q}}, \quad (2.37)$$

$$\mathbf{D} = -\frac{\partial \mathbf{R}}{\partial \dot{\mathbf{q}}} = \frac{\partial[\mathbf{B}(\mathbf{q})\dot{\mathbf{q}}^2]}{\partial \dot{\mathbf{q}}} - \frac{\partial \mathbf{Q}(\mathbf{q}, \dot{\mathbf{q}})}{\partial \dot{\mathbf{q}}}, \quad (2.38)$$

$$\mathbf{M} = -\frac{\partial \mathbf{R}}{\partial \ddot{\mathbf{q}}} = \mathbf{M}(\mathbf{q}). \quad (2.39)$$

2.4 EQUALITY CONSTRAINTS

2.4.1 METHODS OF CONSTRAINT ENFORCEMENT

Equality (and inequality) constraints may be enforced in many different ways. Perhaps the easiest enforcement method uses the penalty method. This method is advantageous because it is simple to implement and causes no increase in the problem dimension. The method is disadvantageous because it results in poor conditioning of the problem, inexact enforcement of the constraint. These disadvantages are compelling reasons to adopt an alternative method.

The Lagrange multiplier method for constraint enforcement, one possible alternative, causes the dimensionality of the problem to grow by the number of constraint equations enforced. While increased dimensionality may be disadvantageous because the computation becomes larger and more time consuming, it is also advantageous because the dual quantities required to enforce the constraint, typically reaction forces, are obtained automatically. Furthermore, Lagrange multiplier methods do not suffer from the ill-conditioning that occurs with the penalty method. Finally, Lagrange multiplier methods satisfy the constraint exactly and do not allow penetration (in the case of contact). In fact, the augmented

Lagrange multiplier method, used here, adds regularization to the standard Lagrange multiplier, which ensures the convexity of the problem. The regularization parameter r may be viewed as the penalty term appearing in the (quadratic) penalty formulation; however, r need not be large.

The augmented Lagrangian formulation is convenient because both the penalty formulation and standard Lagrange formulation may be obtained from it as special cases. Setting the regularization parameter r to zero in the augmented Lagrangian form recovers the standard Lagrangian form. Setting the r to a large value, and eliminating the Lagrange multiplier equations through the use of homogeneous essential boundary conditions in the augmented Lagrangian form, results in the standard penalty form.

The equality and inequality constraint equations are therefore developed in an augmented Lagrangian formulation. Either the standard Lagrangian or penalty formulations may be seen as a special case.

Since we will be discussing both equality and inequality constraints, it becomes necessary to distinguish between Lagrange multipliers and regularization parameters used for each case. We shall designate equality constraint equations with the letter h . The Lagrange multiplier and regularization parameter associated with h will be λ_h and r_h , respectively. Constraint equations associated with inequality constraints will be designated with the letter g . The Lagrange multiplier and regularization parameter associated with g will be λ_g and r_g . When it is clear from context what types of constraints are being discussed, we will simply use λ and r to simplify the notation.

2.4.2 INTERFACES FORMULATED AS EQUALITY CONSTRAINTS

Interactions between two bodies (or in general, a single body interacting with itself or multiple bodies) described mathematically with equations set equal to zero are referred to as bilateral constraints. These equations may be written abstractly as $\mathbf{h} = \mathbf{0}$. Bilateral constraints may describe persistent contact at joints or surfaces.

The functional form of \mathbf{h} in general depends on the motion of the bodies described for the deformable bodies through displacements \mathbf{u} and for the rigid bodies through generalized coordinates \mathbf{q} . Thus $\mathbf{h} = \mathbf{h}(\mathbf{u}, \mathbf{q})$. For the special case of a constraint involving just

deformable bodies, or just rigid bodies, the only dependent variable would be \mathbf{u} and \mathbf{q} , respectively. After writing the potential that enforces the constraint $\mathbf{h} = \mathbf{0}$, the first two variations are given. Three specific constraint types are then given, describing deformable-deformable, deformable-rigid, and rigid-rigid interfaces.

2.4.3 THE AUGMENTED LAGRANGIAN POTENTIAL

The connections between two or more bodies may be viewed as persistent (bilateral) contact, a special case of general intermittent (unilateral) contact, known to derive uniquely from a non-smooth potential Moreau [86]. The potential for equality constraints posed in the augmented Lagrangian formulation is obtained by adding the standard Lagrangian form, $\boldsymbol{\lambda} \cdot \mathbf{h}$, to a quadratic penalty-like form, $\frac{r}{2}\mathbf{h} \cdot \mathbf{h}$, to give

$$\mathcal{W}_h = \left(\boldsymbol{\lambda} + \frac{r}{2}\mathbf{h} \right) \cdot \mathbf{h}. \quad (2.40)$$

2.4.4 THE FIRST VARIATION

The first variation of the equality constraint potential is written

$$\delta\mathcal{W}_h = \begin{Bmatrix} \delta\mathbf{u} \\ \delta\mathbf{q} \\ \delta\boldsymbol{\lambda} \end{Bmatrix}^T \begin{Bmatrix} (\boldsymbol{\lambda} + r\mathbf{h}) \cdot \nabla_u \mathbf{h} \\ (\boldsymbol{\lambda} + r\mathbf{h}) \cdot \nabla_q \mathbf{h} \\ \mathbf{h} \end{Bmatrix}. \quad (2.41)$$

2.4.5 THE SECOND VARIATION

The second variation of the equality constraint potential is written

$$\Delta\delta\mathcal{W}_h = \begin{Bmatrix} \delta\mathbf{u} \\ \delta\mathbf{q} \\ \delta\boldsymbol{\lambda} \end{Bmatrix}^T \begin{bmatrix} \mathbf{T}_1 & \mathbf{T}_2 & \nabla_u \mathbf{h}^T \\ \mathbf{T}_2 & \mathbf{T}_3 & \nabla_q \mathbf{h}^T \\ \nabla_u \mathbf{h} & \nabla_q \mathbf{h} & \mathbf{0} \end{bmatrix} \begin{Bmatrix} \Delta\mathbf{u} \\ \Delta\mathbf{q} \\ \Delta\boldsymbol{\lambda} \end{Bmatrix}, \quad (2.42)$$

where

$$\mathbf{T}_1 = (\boldsymbol{\lambda} + r\mathbf{h}) \nabla_{uu}^2 \mathbf{h} + r \nabla_u \mathbf{h} \cdot \nabla_u \mathbf{h}, \quad (2.43)$$

$$\mathbf{T}_2 = (\boldsymbol{\lambda} + r\mathbf{h}) \nabla_{uq}^2 \mathbf{h} + r \nabla_u \mathbf{h} \cdot \nabla_q \mathbf{h}, \quad (2.44)$$

$$\mathbf{T}_3 = (\boldsymbol{\lambda} + r\mathbf{h}) \nabla_{qq}^2 \mathbf{h} + r \nabla_q \mathbf{h} \cdot \nabla_q \mathbf{h}. \quad (2.45)$$

2.4.6 SPECIALIZATION FOR DEFORMABLE-DEFORMABLE CONSTRAINTS

We are interested in constraining two deformable bodies, Ω_1 and Ω_2 , to move together at a point. As shown in FIG. 2.3, let P_1 be a point in $\bar{\Omega}_1$. Note that P_1 may be in the body Ω_1 or on the boundary $\partial\Omega_1$, which may be either the displacement portion Γ_u or the traction portion Γ_T . Point P_1 is located in the current configuration by the vector φ^{P_1} , which has associated displacement \mathbf{u}^{P_1} . Analogous statements may be made for body Ω_2 and its point P_2 .

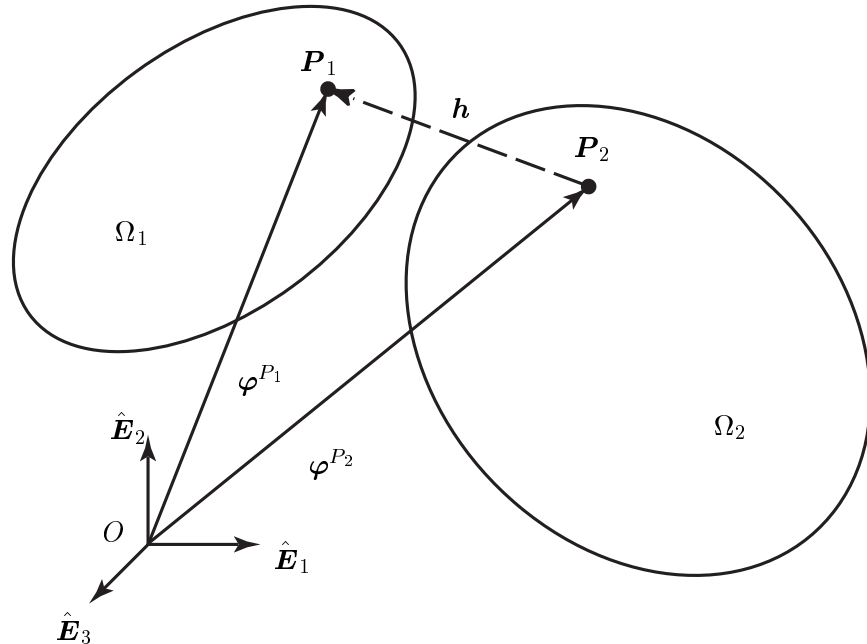


FIGURE 2.2: Generalization of constraint equation \mathbf{h} between two deformable bodies.

The constraint equation enforcing the point-wise intersection is given by $\mathbf{h} : \mathbb{R}^3 \times \mathbb{R}^3 \mapsto \mathbb{R}^3$

$$\mathbf{h}(\mathbf{u}^{P_1}, \mathbf{u}^{P_2}) = \varphi^{P_1}(\mathbf{u}^{P_1}) - \varphi^{P_2}(\mathbf{u}^{P_2}) = \mathbf{0}. \quad (2.46)$$

The first variation of the virtual work done by the constraint \mathcal{W}_h , given the particular

form of \mathbf{h} given in Eq. (2.46), may be found to be (see SECTION A.4 for the derivation)

$$\boxed{\delta \mathcal{W}_h = \begin{array}{c} \left\{ \begin{array}{c} \delta \mathbf{u}^{P_1} \\ \delta \mathbf{u}^{P_2} \\ \hline \delta \boldsymbol{\lambda} \end{array} \right\}^T \left\{ \begin{array}{c} \boldsymbol{\lambda} + r\mathbf{h} \\ -(\boldsymbol{\lambda} + r\mathbf{h}) \\ \hline \mathbf{h} \end{array} \right\} \\ \text{(D-D)} \\ \text{(1}\times\text{9)} \quad \text{(9}\times\text{1)} \end{array}} \quad (2.47)$$

Note that the (D–D) notation is used to reinforce that the specific form of \mathbf{h} involves two deformable bodies.

The second variation may be found to be (again see SECTION A.4 for the derivation)

$$\boxed{\Delta \delta \mathcal{W}_h = \begin{array}{c} \left\{ \begin{array}{c} \delta \mathbf{u}^{P_1} \\ \delta \mathbf{u}^{P_2} \\ \hline \delta \boldsymbol{\lambda} \end{array} \right\}^T \left[\begin{array}{cc|c} r\mathbf{1} & -r\mathbf{1} & \mathbf{1} \\ -r\mathbf{1} & r\mathbf{1} & -\mathbf{1} \\ \hline \mathbf{1} & -\mathbf{1} & \mathbf{0} \end{array} \right] \left\{ \begin{array}{c} \Delta \mathbf{u}^{P_1} \\ \Delta \mathbf{u}^{P_2} \\ \hline \Delta \boldsymbol{\lambda} \end{array} \right\} \\ \text{(D-D)} \\ \text{(1}\times\text{9)} \quad \text{(9}\times\text{9)} \quad \text{(9}\times\text{1)} \end{array}} \quad (2.48)$$

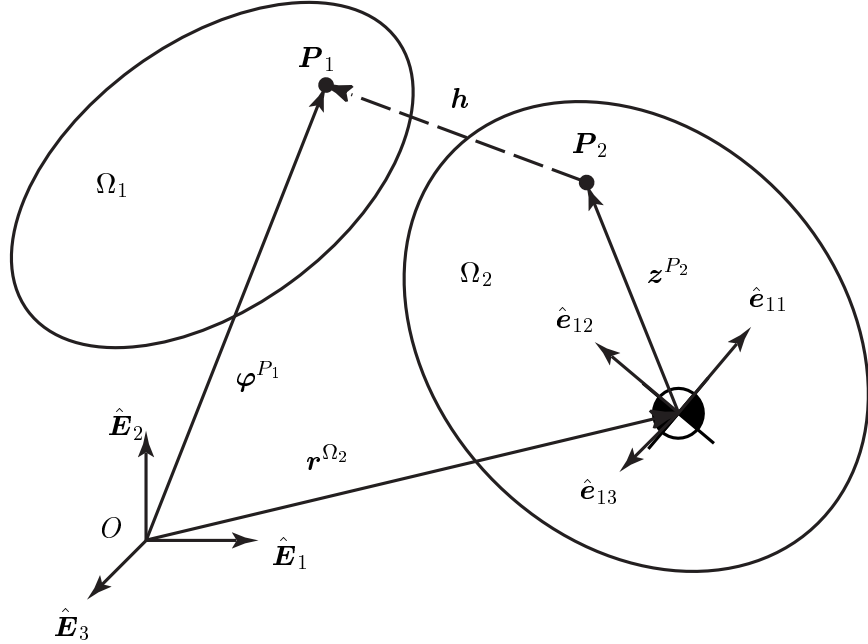
2.4.7 SPECIALIZATION FOR DEFORMABLE-RIGID CONSTRAINTS

The deformable-rigid case is similar to the deformable-deformable case with the exception of the addition of rotation variables — the distinguishing feature of constraints written to include a rigid body.

We are interested in constraining a deformable body Ω_1 and rigid body Ω_2 to move together at a point. As shown in FIG. 2.3, let \mathbf{P}_1 be a point in $\bar{\Omega}_1$, either in Ω_1 or on the boundary $\partial\Omega_1$. Point \mathbf{P}_1 is located in the current configuration by the vector $\boldsymbol{\varphi}^{P_1}$, which has associated displacements \mathbf{u}^{P_1} .

Next consider point \mathbf{P}_2 belonging to rigid body $\bar{\Omega}_2$. Motion of the rigid body is in general a function of the generalized coordinates \mathbf{q} used to parameterize the system. Formulations developed as precursors to implementation in the finite element method require the end product — a rigid body finite element — to be modular. Any number of rigid elements should be available for assembly just like their deformable finite element counterparts.

The need for modularity motivates a general rigid body finite element formulation where the generalized coordinates \mathbf{q} are selected to correspond to the three translations of the mass center $\mathbf{r}^{G_2} \in \mathbb{R}^3$, and three rotations $\boldsymbol{\theta}^{\Omega_2, E} \in \mathbb{R}^3$ of the rigid body in the inertial frame E .

FIGURE 2.3: Generalization of constraint equation \mathbf{h} between a deformable and rigid body.

Thus

$$\mathbf{q} = \begin{Bmatrix} q_1 \\ q_2 \\ q_3 \\ q_4 \\ q_5 \\ q_6 \end{Bmatrix} = \begin{Bmatrix} \mathbf{r}_1^G \\ \mathbf{r}_2^G \\ \mathbf{r}_3^G \\ \theta_1 \\ \theta_2 \\ \theta_3 \end{Bmatrix} = \begin{Bmatrix} | \\ \mathbf{r}^G_2 \\ | \\ | \\ \theta^{\Omega_2} \\ | \end{Bmatrix}. \quad (2.49)$$

The constraint equation enforcing the point-wise intersection of the two bodies is given by $\mathbf{h} : \mathbb{R}^3 \times \mathbb{R}^6 \mapsto \mathbb{R}^3$

$$\mathbf{h}(\mathbf{u}^{P_1}, \mathbf{r}^{G_2}, \boldsymbol{\theta}^{\Omega_2}) = \varphi^{P_1}(\mathbf{u}^{P_1}) - \mathbf{r}^{G_2} - \mathbf{z}^{P_2}(\boldsymbol{\theta}^{\Omega_2}) = \mathbf{0}. \quad (2.50)$$

Note that the vector \mathbf{r}^{G_2} locating the mass center of the rigid body is abbreviated simply as \mathbf{r} and the rotation of the body in the inertial frame $\boldsymbol{\theta}^{\Omega_2}$ simply as $\boldsymbol{\theta}$. The vector $\mathbf{z}^{P_2}(\boldsymbol{\theta})$ is a function of the rotation $\boldsymbol{\theta}$ of the rigid body Ω_2 . This dependence appears because the vector \mathbf{h} is resolved in the inertial basis. The \mathbf{z}^{P_2} vector is equal to the constant vector

$\mathbf{c}^{P_2, \Omega_2}$, embedded in Ω_2 , rotated by $\mathbf{R} : \mathbb{R}^3 \rightarrow \text{SO}(3)$ such that

$$\mathbf{z}^{P_2}(\boldsymbol{\theta}) = [\mathbf{R}(\theta)^T \Omega_2] \mathbf{c}^{P_2}. \quad (2.51)$$

The first variation of the virtual work done by the constraint \mathcal{W}_h , given the particular form of \mathbf{h} given in Eq. (2.50), may be found to be (see SECTION A.4 for the derivation)

$$\boxed{\delta \mathcal{W}_h}_{\text{(D-R)}} = \left\{ \begin{array}{c} \delta \mathbf{u}^{P_1} \\ \delta \mathbf{r}^{P_2} \\ \delta \boldsymbol{\theta}^{\Omega_2} \\ \hline \delta \boldsymbol{\lambda} \end{array} \right\}_{(1 \times 12)}^T \left\{ \begin{array}{c} \boldsymbol{\lambda} + r\mathbf{h} \\ -(\boldsymbol{\lambda} + r\mathbf{h}) \\ -\hat{\mathbf{Z}}(\boldsymbol{\lambda} + r\mathbf{h}) \\ \hline \mathbf{h} \end{array} \right\}_{(12 \times 1)}. \quad (2.52)$$

Note that the (D-R) notation is used to reinforce that the specific form of \mathbf{h} involves one deformable body and one rigid body. The matrix $\hat{\mathbf{Z}}$ is the skew matrix of the vector \mathbf{z} ,

$$\text{skew}(\mathbf{z}) = \hat{\mathbf{Z}} = \begin{bmatrix} 0 & -z_3 & z_2 \\ z_3 & 0 & -z_1 \\ -z_2 & z_1 & 0 \end{bmatrix}. \quad (2.53)$$

The overhat notation $\widehat{[\bullet]}$ denotes a skew matrix.

The second variation may be found to be (again see SECTION A.4 for the derivation)

$$\boxed{\Delta \delta \mathcal{W}_h}_{\text{(D-R)}} = \left\{ \begin{array}{c} \delta \mathbf{u}^{P_1} \\ \delta \mathbf{r}^{G_2} \\ \delta \boldsymbol{\theta}^{\Omega_2} \\ \hline \delta \boldsymbol{\lambda} \end{array} \right\}_{(1 \times 12)}^T \left[\begin{array}{ccc|c} r\mathbf{1} & -r\mathbf{1} & r\hat{\mathbf{Z}} & \mathbf{1} \\ -r\mathbf{1} & r\mathbf{1} & -r\hat{\mathbf{Z}} & -\mathbf{1} \\ -r\hat{\mathbf{Z}} & r\hat{\mathbf{Z}} & -[\boldsymbol{\lambda} + r\mathbf{h}] - r\hat{\mathbf{Z}} & -\hat{\mathbf{Z}} \\ \hline \mathbf{1} & -\mathbf{1} & \hat{\mathbf{Z}} & \mathbf{0} \end{array} \right]_{(12 \times 12)} \left\{ \begin{array}{c} \Delta \mathbf{u}^{P_1} \\ \Delta \mathbf{u}^{P_2} \\ \Delta \boldsymbol{\theta}^{\Omega_2} \\ \hline \Delta \boldsymbol{\lambda} \end{array} \right\}_{(12 \times 1)}. \quad (2.54)$$

Note the property of skew matrices, $\hat{\mathbf{Z}}^T = -\hat{\mathbf{Z}}$ has been used to simplify the expressions where possible to remove matrices listed as transposed. The Hessian now becomes non-symmetric due to the $\boldsymbol{\theta} \in \mathbb{R}^3$ contributions. If rotation occurs in just one plane, $\theta \in \mathbb{R}$, the Hessian regains symmetry. These details are observable from the derivation in SECTION A.4.

2.4.8 SPECIALIZATION FOR RIGID-RIGID CONSTRAINTS

Rigid-rigid constraints represent the third and final constraint member of a general holonomic, equality constraint class. The rigid-rigid case results in the largest and most general residual vector and Hessian matrix of all the three cases. In fact, the previous two cases may be seen as a special case of the rigid-rigid development by crossing out rows and columns of rotation variables where necessary.

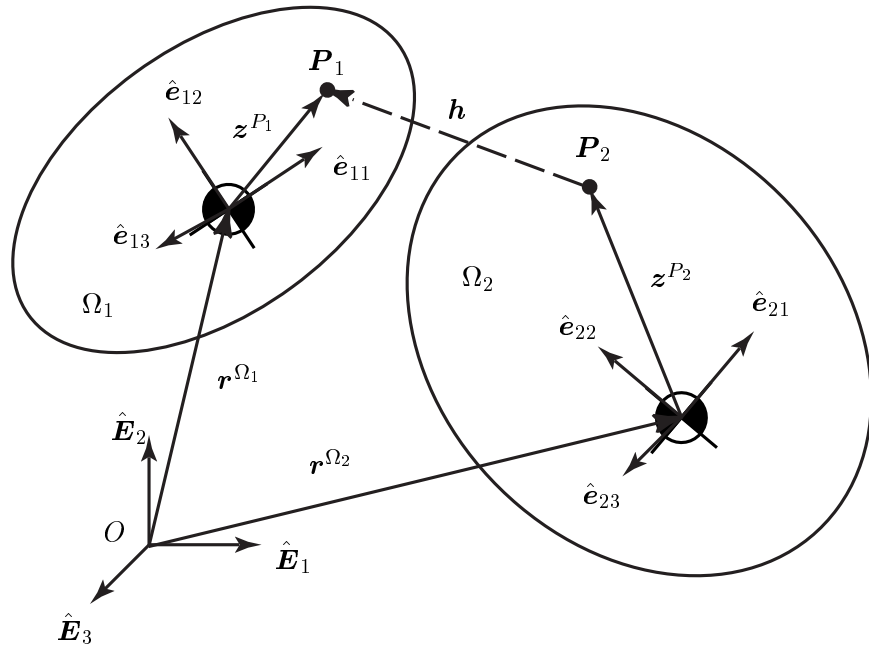


FIGURE 2.4: Generalization of constraint equation \mathbf{h} between two rigid bodies.

We have points \mathbf{P}_1 and \mathbf{P}_2 , bodies Ω_1 and Ω_2 , and position vectors \mathbf{r}^{G_1} , \mathbf{r}^{G_2} , \mathbf{z}^{P_1} , \mathbf{z}^{P_2} (see FIG. 2.4). Three translations and three rotations per body describe the parameterization of generalized coordinates in a manner similar to the description in the deformable-rigid

case. Specifically, we have

$$\mathbf{q} = \left\{ \begin{array}{c} q_1 \\ q_2 \\ q_3 \\ \hline q_4 \\ q_5 \\ q_6 \\ \hline q_7 \\ q_8 \\ q_9 \\ \hline q_{10} \\ q_{11} \\ q_{12} \end{array} \right\} = \left\{ \begin{array}{c} r_1^{G_1} \\ r_2^{G_1} \\ r_3^{G_1} \\ \hline \theta_1^{\Omega_1} \\ \theta_2^{\Omega_1} \\ \theta_3^{\Omega_1} \\ \hline r_1^{G_2} \\ r_2^{G_2} \\ r_3^{G_2} \\ \hline \theta_1^{\Omega_2} \\ \theta_2^{\Omega_2} \\ \theta_3^{\Omega_2} \end{array} \right\} = \left\{ \begin{array}{c} | \\ \mathbf{r}^{G_1} \\ | \\ | \\ | \\ | \\ | \\ \mathbf{r}^{G_2} \\ | \\ | \\ | \end{array} \right\}. \quad (2.55)$$

The constraint equation enforcing the point-wise intersection of the two bodies is given by $\mathbf{h} : \mathbb{R}^6 \times \mathbb{R}^6 \mapsto \mathbb{R}^3$

$$\mathbf{h}(\mathbf{r}^{G_1}, \mathbf{r}^{G_2}, \boldsymbol{\theta}^{\Omega_1}, \boldsymbol{\theta}^{\Omega_2}) = \mathbf{r}^{G_1} + \mathbf{z}^{P_1}(\boldsymbol{\theta}^{\Omega_1}) - \mathbf{r}^{G_2} - \mathbf{z}^{P_2}(\boldsymbol{\theta}^{\Omega_2}) = \mathbf{0}. \quad (2.56)$$

The first and second variations may be seen as extensions of the work already developed for deformable-deformable (D–D) and deformable-rigid (D–R) constraint types. Alternatively, the rigid-rigid (R–R) constraint type may be viewed as the most general of the three. In fact, the approach for obtaining the required variations for all three constraint types was obtained by first doing the most general case (R–R) and then specializing this case for the other two cases, (D–R) and (D–D). See SECTION A.4 for details.

For convenience of notation, let $\hat{\mathbf{P}} = \hat{\mathbf{Z}}(\boldsymbol{\theta}^{\Omega_1})$ and $\hat{\mathbf{Z}} = \hat{\mathbf{Z}}(\boldsymbol{\theta}^{\Omega_2})$. The first variation of

the virtual work done by the constraint \mathbf{h} is written

$$\delta\mathcal{W}_h = \left(\begin{array}{c} \delta\mathbf{r}^{G_1} \\ \delta\boldsymbol{\theta}^{\Omega_1} \\ \delta\mathbf{r}^{G_2} \\ \delta\boldsymbol{\theta}^{\Omega_2} \\ \hline \delta\boldsymbol{\lambda} \end{array} \right)_{(1 \times 15)}^T \left(\begin{array}{c} \boldsymbol{\lambda} + r\mathbf{h} \\ \hat{\mathbf{P}}(\boldsymbol{\lambda} + r\mathbf{h}) \\ -(\boldsymbol{\lambda} + r\mathbf{h}) \\ -\hat{\mathbf{Z}}(\boldsymbol{\lambda} + r\mathbf{h}) \\ \hline \mathbf{h} \end{array} \right)_{(15 \times 1)}. \quad (2.57)$$

The second variation is

$$\Delta\delta\mathcal{W}_h = \left(\begin{array}{c} \delta\mathbf{r}^{G_1} \\ \delta\boldsymbol{\theta}^{\Omega_1} \\ \delta\mathbf{r}^{G_2} \\ \delta\boldsymbol{\theta}^{\Omega_2} \\ \hline \delta\boldsymbol{\lambda} \end{array} \right)_{(1 \times 15)}^T \left[\begin{array}{cccc|c} \mathbf{r}\mathbf{1} & -r\hat{\mathbf{P}} & -r\mathbf{1} & r\hat{\mathbf{Z}} & \mathbf{1} \\ r\hat{\mathbf{P}} & \mathbf{K}_{22} & -r\hat{\mathbf{P}} & r\hat{\mathbf{P}}\hat{\mathbf{Z}} & \hat{\mathbf{P}} \\ -r\mathbf{1} & r\hat{\mathbf{P}} & r\mathbf{1} & -r\hat{\mathbf{Z}} & -\mathbf{1} \\ -r\hat{\mathbf{Z}} & r\hat{\mathbf{Z}}\hat{\mathbf{P}} & r\hat{\mathbf{Z}} & \mathbf{K}_{44} & -\hat{\mathbf{Z}} \\ \hline \mathbf{1} & -\hat{\mathbf{P}} & -\mathbf{1} & \hat{\mathbf{Z}} & \mathbf{0} \end{array} \right]_{(15 \times 15)} \left(\begin{array}{c} \Delta\mathbf{r}^{G_1} \\ \Delta\boldsymbol{\theta}^{\Omega_1} \\ \Delta\mathbf{r}^{G_2} \\ \Delta\boldsymbol{\theta}^{\Omega_2} \\ \hline \Delta\boldsymbol{\lambda} \end{array} \right)_{(15 \times 1)}, \quad (2.58)$$

where

$$\mathbf{K}_{22} = \left[\widehat{[\boldsymbol{\lambda} + r\mathbf{h}]} - r\hat{\mathbf{P}} \right] \hat{\mathbf{P}}, \quad (2.59)$$

$$\mathbf{K}_{44} = \left[-\widehat{[\boldsymbol{\lambda} + r\mathbf{h}]} - r\hat{\mathbf{Z}} \right] \hat{\mathbf{Z}}. \quad (2.60)$$

2.4.9 MUSCLE ACTUATOR FORMULATION

We are interested in forming connections between deformable and rigid bodies which are reminiscent of the equality constraints discussed in the previous section, but which play a slightly modified role. The connections between bodies discussed previously described compatibility of points or sets of points enforced with augmented Lagrange multipliers. Now, we wish to make another class of connections between points belonging to deformable and rigid domains, which simulate muscle contraction. The three constituents of the muscle actuator formulation discussed here will be an elastic contribution, a viscous contribution, and a force-producing contribution.

The fundamental form of muscle actuator, shown in FIG. 2.5, consists of a spring, a dashpot, and an actuator in parallel. Combining multiple groups of this fundamental form

can lead to traditional muscle type models, such as the Hill model, which has passive and active components.

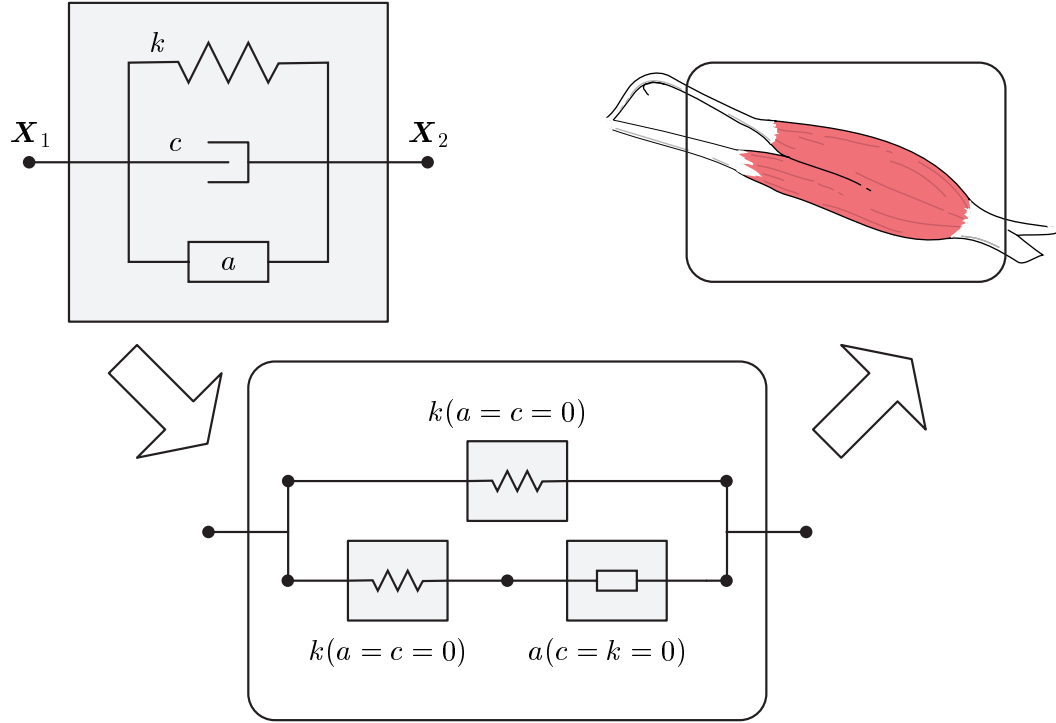


FIGURE 2.5: A simple muscle actuator group has three parallel elements. Three simple groups may be combined to create a Hill-type model by setting the actuation a , stiffness k , and damping c to zero. The Hill-type model simulates the muscle action.

ELASTIC, ROTATIONALLY NONLINEAR SPRING Let the element state vector be expressed as

$$\mathbf{s}^e = \langle \mathbf{u}_1, \mathbf{u}_2 \rangle^T, \quad (2.61)$$

which stand for the displacement of node 1 and node 2, respectively. The strain energy density for the spring is

$$\mathcal{W} = \frac{1}{2} \frac{EA}{L} e^2, \quad (2.62)$$

where E is the modulus of elasticity, A is the cross-sectional area, L is the length of the spring in the reference configuration, and e is the elongation of the spring. The elongation

is measured as the distance of the current, stretched length l from the original, unstretched length L ,

$$e = l - L > 0 \text{ for extension.} \quad (2.63)$$

The lengths L and l are obtained from the reference and current positions, respectively, of the two ends of the element

$$L = \| \mathbf{X}_2 - \mathbf{X}_1 \|, \quad (2.64)$$

$$l = \| \mathbf{x}_2 - \mathbf{x}_1 \|, \quad (2.65)$$

as shown in FIG. 2.6.

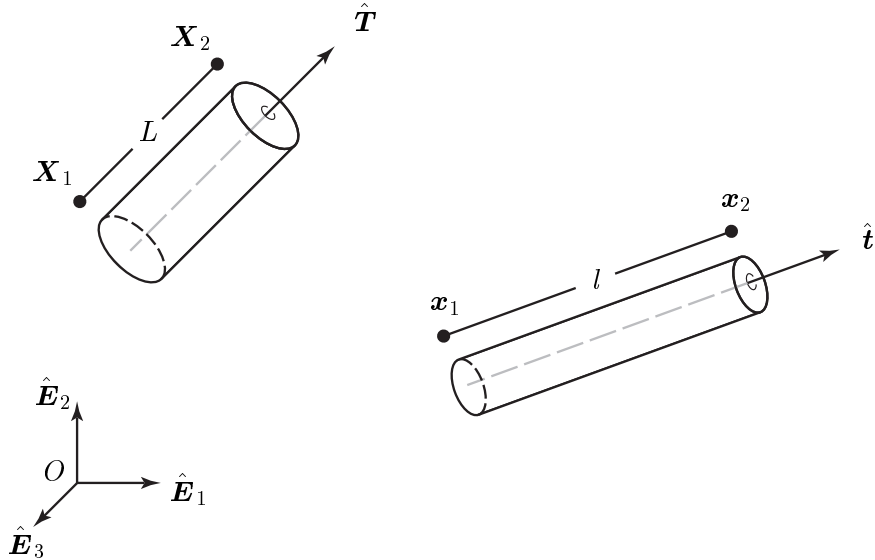


FIGURE 2.6: Reference and current configurations of the muscle actuator.

We shall abbreviate the spring constant k as

$$k = \frac{EA}{L}. \quad (2.66)$$

The virtual work of the spring is written

$$\delta\mathcal{W} = \frac{1}{2}k\delta [(l - L)^2]. \quad (2.67)$$

To find this variation in terms of $\delta\mathbf{u}_1$ and $\delta\mathbf{u}_2$, some preliminary results are helpful. First

the variation of l

$$\delta l = \delta[((\mathbf{X}_2 + \mathbf{u}_2 - \mathbf{X}_1 - \mathbf{u}_1) \cdot (\mathbf{X}_2 + \mathbf{u}_2 - \mathbf{X}_1 - \mathbf{u}_1))^{\frac{1}{2}}], \quad (2.68)$$

$$= \frac{1}{2} \frac{1}{l} 2(-\delta \mathbf{u}_1 + \delta \mathbf{u}_2) \cdot (\mathbf{x}_2 - \mathbf{x}_1), \quad (2.69)$$

$$= (-\delta \mathbf{u}_1 + \delta \mathbf{u}_2) \cdot \hat{\mathbf{t}}. \quad (2.70)$$

Here the tangent vector is determined from $\mathbf{t} = (\mathbf{x}_2 - \mathbf{x}_1)$, and l through

$$\hat{\mathbf{t}} = \frac{\mathbf{x}_2 - \mathbf{x}_1}{\|\mathbf{x}_2 - \mathbf{x}_1\|} = \frac{\mathbf{x}_2 - \mathbf{x}_1}{l}. \quad (2.71)$$

Second, the variation of $\hat{\mathbf{t}}$

$$\delta \hat{\mathbf{t}} = \delta \left(\frac{\mathbf{x}_2 - \mathbf{x}_1}{l} \right) = \delta ((\mathbf{x}_2 - \mathbf{x}_1)l^{-1}), \quad (2.72)$$

$$= \frac{1}{l} [\mathbf{1} - \hat{\mathbf{t}} \otimes \hat{\mathbf{t}}] (-\delta \mathbf{u}_1 + \delta \mathbf{u}_2). \quad (2.73)$$

The virtual work expressed in terms of the nodal displacements is then found

$$\delta \mathcal{W}^e = \frac{1}{2} k \delta[(l - L)^2], \quad (2.74)$$

$$= k(l - L)(-\delta \mathbf{u}_1 + \delta \mathbf{u}_2) \cdot \hat{\mathbf{t}}. \quad (2.75)$$

The virtual work expressed in terms of nodal displacements and the internal force vector is then

$$\boxed{\delta \mathcal{W}^e = \boldsymbol{\delta}^e \cdot \mathbf{F}^{\text{int},e} = \begin{Bmatrix} \delta \mathbf{u}_1 \\ \delta \mathbf{u}_2 \end{Bmatrix}^T k(l - L) \begin{Bmatrix} -\hat{\mathbf{t}} \\ \hat{\mathbf{t}} \end{Bmatrix}}. \quad (2.76)$$

The second variation is found through

$$\Delta(\delta \mathcal{W}) = \Delta [k(l - L)(-\delta \mathbf{u}_1 + \delta \mathbf{u}_2) \cdot \hat{\mathbf{t}}], \quad (2.77)$$

$$\begin{aligned} &= k(-\Delta \mathbf{u}_1 + \Delta \mathbf{u}_2) \cdot \hat{\mathbf{t}} (-\delta \mathbf{u}_1 + \delta \mathbf{u}_2) \cdot \hat{\mathbf{t}} \\ &\quad + k(l - L)(-\delta \mathbf{u}_1 + \delta \mathbf{u}_2)^T \frac{1}{l} [\mathbf{1} - \hat{\mathbf{t}} \otimes \hat{\mathbf{t}}] (-\Delta \mathbf{u}_1 + \Delta \mathbf{u}_2). \end{aligned} \quad (2.78)$$

This leads to the element stiffness equations

$$\boxed{\Delta \delta \mathcal{W}^e = \boldsymbol{\delta}^e \cdot \mathbf{K}^e \boldsymbol{\Delta}^e = \begin{Bmatrix} \delta \mathbf{u}_1 \\ \delta \mathbf{u}_2 \end{Bmatrix}^T \begin{bmatrix} \kappa & -\kappa \\ -\kappa & \kappa \end{bmatrix} \begin{Bmatrix} \Delta \mathbf{u}_1 \\ \Delta \mathbf{u}_2 \end{Bmatrix}}, \quad (2.79)$$

where

$$\boldsymbol{\kappa} = k \left[\hat{\mathbf{t}} \otimes \hat{\mathbf{t}} + \frac{(l - L)}{l} [\mathbf{1} - \hat{\mathbf{t}} \otimes \hat{\mathbf{t}}] \right]. \quad (2.80)$$

VISCOELASTIC, ROTATIONALLY NONLINEAR DASHPOT Let the force along the direction of the dashpot $\hat{\mathbf{t}}$ have magnitude $c \dot{l}$ where c is the viscous damping constant and \dot{l} is the time rate of change of elongation

$$\dot{l} = (-\dot{\mathbf{u}}_1 + \dot{\mathbf{u}}_2) \cdot \hat{\mathbf{t}}. \quad (2.81)$$

If the relative tangential velocity of node 2 is greater than that of node 1, the dashpot is extending in time, which means \dot{l} is positive. This leads to the internal force vector directly

$$\mathbf{F}^{\text{int},e} = c \dot{l} \begin{Bmatrix} -\hat{\mathbf{t}} \\ \hat{\mathbf{t}} \end{Bmatrix}. \quad (2.82)$$

Thus the virtual work expressed in terms of nodal displacements and the internal force vector is then

$$\boxed{\delta \mathcal{W}^e = \boldsymbol{\delta}^e \cdot \mathbf{F}^{\text{int},e} = \begin{Bmatrix} \delta \mathbf{u}_1 \\ \delta \mathbf{u}_2 \end{Bmatrix}^T c \dot{l} \begin{Bmatrix} -\hat{\mathbf{t}} \\ \hat{\mathbf{t}} \end{Bmatrix}}. \quad (2.83)$$

To find the variation of the internal force vector, it is helpful to first find the variation of \dot{l} .

$$\delta \dot{l} = \delta [(-\dot{\mathbf{u}}_1 + \dot{\mathbf{u}}_2) \cdot \hat{\mathbf{t}}], \quad (2.84)$$

$$= (-\delta \dot{\mathbf{u}}_1 + \delta \dot{\mathbf{u}}_2) \cdot \hat{\mathbf{t}} + (-\dot{\mathbf{u}}_1 + \dot{\mathbf{u}}_2)^T \frac{1}{l} [\mathbf{1} - \hat{\mathbf{t}} \otimes \hat{\mathbf{t}}] (-\delta \mathbf{u}_1 + \delta \mathbf{u}_2). \quad (2.85)$$

The second variation is found through

$$\Delta(\delta \mathcal{W}) = \Delta \left[c \dot{l} (-\delta \mathbf{u}_1 + \delta \mathbf{u}_2) \cdot \hat{\mathbf{t}} \right], \quad (2.86)$$

$$\begin{aligned} &= c (-\Delta \dot{\mathbf{u}}_1 + \Delta \dot{\mathbf{u}}_2) \cdot \hat{\mathbf{t}} (-\delta \mathbf{u}_1 + \delta \mathbf{u}_2) \cdot \hat{\mathbf{t}} \\ &\quad + c (-\dot{\mathbf{u}}_1 + \dot{\mathbf{u}}_2)^T \frac{1}{l} [\mathbf{1} - \hat{\mathbf{t}} \otimes \hat{\mathbf{t}}] (-\Delta \mathbf{u}_1 + \Delta \mathbf{u}_2) (-\delta \mathbf{u}_1 + \delta \mathbf{u}_2) \cdot \hat{\mathbf{t}} \\ &\quad + c \dot{l} (-\delta \mathbf{u}_1 + \delta \mathbf{u}_2)^T \frac{1}{l} [\mathbf{1} - \hat{\mathbf{t}} \otimes \hat{\mathbf{t}}] (-\Delta \mathbf{u}_1 + \Delta \mathbf{u}_2). \end{aligned} \quad (2.87)$$

This quantity may be simplified to give the tangent damping and stiffness matrices

$$\boxed{\Delta \delta \mathcal{W}^e = \boldsymbol{\delta}^e \cdot \mathbf{D}^e \dot{\boldsymbol{\Delta}}^e + \boldsymbol{\delta}^e \cdot \mathbf{K}^e \boldsymbol{\Delta}^e}, \quad (2.88)$$

where the tangent damping matrix may be found from

$$\delta^e \cdot D^e \dot{\Delta}^e = \begin{Bmatrix} \delta u_1 \\ \delta u_2 \end{Bmatrix}^T \begin{bmatrix} c \hat{t} \otimes \hat{t} & -c \hat{t} \otimes \hat{t} \\ -c \hat{t} \otimes \hat{t} & c \hat{t} \otimes \hat{t} \end{bmatrix} \begin{Bmatrix} \Delta \dot{u}_1 \\ \Delta \dot{u}_2 \end{Bmatrix}, \quad (2.89)$$

and the tangent stiffness matrix may be found from

$$\delta^e \cdot K^e \Delta^e = \begin{Bmatrix} \delta u_1 \\ \delta u_2 \end{Bmatrix}^T \begin{bmatrix} \beta & -\beta \\ -\beta & \beta \end{bmatrix} \begin{Bmatrix} \Delta u_1 \\ \Delta u_2 \end{Bmatrix}, \quad (2.90)$$

where

$$\beta = c \left[\frac{1}{l} [\hat{t} \otimes (-\dot{u}_1 + \dot{u}_2)] [1 - \hat{t} \otimes \hat{t}] + \frac{i}{l} [1 - \hat{t} \otimes \hat{t}] \right]. \quad (2.91)$$

NONLINEAR ACTUATOR The actuator provides a force of magnitude a along the axis of the element. The virtual work expressed in terms of nodal displacements and the internal force vector may be written directly as

$$\delta \mathcal{W}^e = \delta^e \cdot F^{\text{int},e} = \begin{Bmatrix} \delta u_1 \\ \delta u_2 \end{Bmatrix}^T (a) \begin{Bmatrix} -\hat{t} \\ \hat{t} \end{Bmatrix}. \quad (2.92)$$

The second variation is found to be

$$\Delta \delta \mathcal{W}^e = \delta^e \cdot K^e \Delta^e = \begin{Bmatrix} \delta u_1 \\ \delta u_2 \end{Bmatrix}^T \begin{bmatrix} \rho & -\rho \\ -\rho & \rho \end{bmatrix} \begin{Bmatrix} \Delta u_1 \\ \Delta u_2 \end{Bmatrix}, \quad (2.93)$$

where

$$\rho = \frac{a}{l} [1 - \hat{t} \otimes \hat{t}]. \quad (2.94)$$

2.5 INEQUALITY CONSTRAINTS

2.5.1 CONTACT MECHANICS FORMULATED AS AN INEQUALITY CONSTRAINT

Contact mechanics describes two solid bodies (or in general, one body in self-contact or multiple bodies) that cannot penetrate each other when interacting. This restriction imposes

a constraint on the governing equations of motion in terms of an inequality condition. This inequality states that the gap g_n , measuring the distance between the boundaries of two bodies, must always be non-negative during the interaction, $g_n \geq 0$. This type of constraint is formally referred to as a unilateral constraint

$$g_n(\mathbf{X}, t) \geq 0 \quad \forall \quad \mathbf{X} \in \Gamma_c, t \in \mathbb{T}. \quad (2.95)$$

This type of constraint is characterized by possible intermittent contact, wherein change-of-status between contact and gap may occur. This is in contrast to a bilateral constraint, governed by equality constraints. This type of constraint is characterized by persistent contact where no change-of-status occurs. Essential boundary conditions may also be considered bilateral constraint. In addition to non-penetration, the bodies may not pull on each other, only push. Let p be the contact pressure. The non-adhesion condition

$$p \leq 0, \quad (2.96)$$

is yet another unilateral condition for contact. Thus $p < 0 \implies$ compression.

Finally, if $g_n > 0$, then $p = 0$, and if $p < 0$, then $g_n = 0$, taken together as

$$p g_n = 0, \quad (2.97)$$

and defined as the complementarity condition. These three conditions,

$$\begin{array}{rcl} g_n & \geq & 0 \\ p & \leq & 0 \\ p g_n & = & 0 \end{array}$$

(2.98)

form the classical Kuhn-Tucker equations in nonlinear programming and are shown in FIG. 2.7.

The (normal) contact law is then defined as the union of all three Kuhn-Tucker conditions, as shown in FIG. 2.8. The contact law is inherently nonlinear because of the corner existing at the origin. The law is not a function in a strict sense because it is not a one-to-one relationship. Instead, it is a multivalued function, or a set-valued relation. Because the contact law is multivalued, it is written not as an equality but as an inclusion [31, 48].

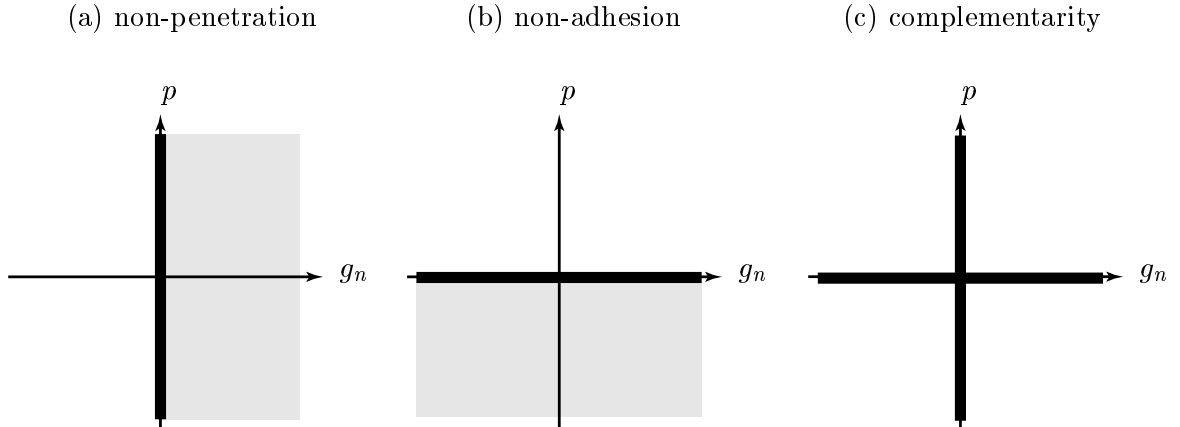


FIGURE 2.7: The (a) non-penetration condition, (b) non-adhesion condition, and (c) complementarity condition.

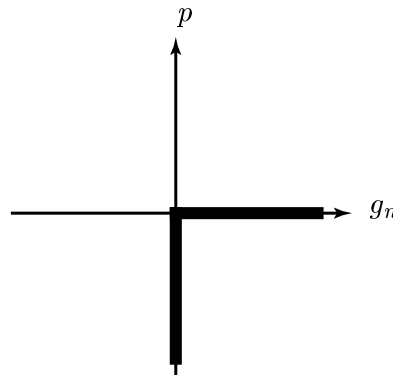


FIGURE 2.8: The normal contact law described as the intersection of the non-penetration condition, non-adhesion condition, and complementarity condition.

First the indicator function $\psi_{\mathbb{R}^+}$ is defined, such that

$$\psi_{\mathbb{R}^+}(g_n) = \begin{cases} 0 & g_n \geq 0 \\ +\infty & g_n < 0 \end{cases}. \quad (2.99)$$

The pressure is written as the subdifferential inclusion

$$p \in \partial\psi_{\mathbb{R}^+}(g_n), \quad (2.100)$$

where

$$\partial\psi(g_n) = \begin{cases} 0 & g_n > 0 \\ (-\infty, 0] & g_n = 0 \\ \emptyset & g_n < 0 \end{cases}. \quad (2.101)$$

2.5.2 THE AUGMENTED LAGRANGIAN POTENTIAL

Since (frictionless) contact is a reversible process, it would make sense that there exist a contact potential. This potential for inequality constraints posed in the augmented Lagrangian formulation takes the form [2, 32, 48]

$$\boxed{\mathcal{W}_g = -\frac{1}{2r}\lambda^2 + \frac{1}{2r}\text{dist}_{\mathbb{R}^+}^2(\lambda + rg_n)} . \quad (2.102)$$

2.5.3 THE FIRST VARIATION

The first variation of the contact potential is written as

$$\delta\mathcal{W}_g = \begin{Bmatrix} \delta\mathbf{u} \\ \delta\mathbf{q} \\ \delta\lambda \end{Bmatrix}^T \begin{Bmatrix} \text{proj}_{\mathbb{R}^-}(\lambda + rg_n)\nabla_u g_n \\ \text{proj}_{\mathbb{R}^-}(\lambda + rg_n)\nabla_q g_n \\ -\frac{1}{r}(\lambda - \text{proj}_{\mathbb{R}^-}(\lambda + rg_n)) \end{Bmatrix} . \quad (2.103)$$

All variations of the contact potential have two distinct forms, depending on whether the status is contact

$$\boxed{\delta\mathcal{W}_g_{(\text{contact})} = \begin{Bmatrix} \delta\mathbf{u} \\ \delta\mathbf{q} \\ \delta\lambda \end{Bmatrix}^T \begin{Bmatrix} (\lambda + rg_n)\nabla_u g_n \\ (\lambda + rg_n)\nabla_q g_n \\ g_n \end{Bmatrix}} , \quad (2.104)$$

or gap

$$\boxed{\delta\mathcal{W}_g_{(\text{gap})} = \begin{Bmatrix} \delta\mathbf{u} \\ \delta\mathbf{q} \\ \delta\lambda \end{Bmatrix}^T \begin{Bmatrix} \mathbf{0} \\ \mathbf{0} \\ -\frac{1}{r}\lambda \end{Bmatrix}} . \quad (2.105)$$

2.5.4 THE SECOND VARIATION

The second variation of the contact potential is obtained by taking derivatives of Eq. (2.103), which involve derivatives of the projection operator. Differentiating the projection operator gives either a zero or a one. Therefore, the second variation depends on the status of contact

$$\boxed{\Delta\delta\mathcal{W}_g_{(\text{contact})} = \begin{Bmatrix} \delta\mathbf{u} \\ \delta\mathbf{q} \\ \delta\lambda \end{Bmatrix}^T \begin{bmatrix} \mathbf{T}_1 & \mathbf{T}_2 & \nabla_u g_n^T \\ \mathbf{T}_2 & \mathbf{T}_3 & \nabla_q g_n^T \\ \nabla_u g_n & \nabla_q g_n & 0 \end{bmatrix} \begin{Bmatrix} \Delta\mathbf{u} \\ \Delta\mathbf{q} \\ \Delta\lambda \end{Bmatrix}} , \quad (2.106)$$

where

$$\mathbf{T}_1 = (\lambda + rg_n) \nabla_{uu}^2 g_n + r \nabla_u g_n \nabla_u g_n, \quad (2.107)$$

$$\mathbf{T}_2 = (\lambda + rg_n) \nabla_{uq}^2 g_n + r \nabla_q g_n \nabla_u g_n, \quad (2.108)$$

$$\mathbf{T}_3 = (\lambda + rg_n) \nabla_{qq}^2 g_n + r \nabla_q g_n \nabla_q g_n, \quad (2.109)$$

or gap

$$\boxed{\Delta\delta\mathcal{W}_g \underset{(\text{gap})}{=} \left\{ \begin{array}{c} \delta\mathbf{u} \\ \delta\mathbf{q} \\ \delta\lambda \end{array} \right\}^T \left[\begin{array}{ccc} \mathbf{0} & \mathbf{0} & \mathbf{0} \\ \mathbf{0} & \mathbf{0} & \mathbf{0} \\ \mathbf{0} & \mathbf{0} & -\frac{1}{r} \end{array} \right] \left\{ \begin{array}{c} \Delta\mathbf{u} \\ \Delta\mathbf{q} \\ \Delta\lambda \end{array} \right\}}. \quad (2.110)$$

2.5.5 SPECIALIZATION FOR DEFORMABLE-RIGID CONTACT

We formulate the first and second variation of the contact potential for contact between two bodies, one of which is deformable, the other rigid. This formulation extends the work in [49] to include the motion of rigid bodies.

Consider a deformable body Ω_D and rigid body Ω_R as shown in FIG. 2.9. A point belonging to the boundary of the deformable domain $\mathbf{X} \in \partial\Omega_D$ has current position $\varphi(\mathbf{X}, t)$. For a given point of interest \mathbf{X} , the closest point projection of $\varphi(\mathbf{X}, t)$ onto the boundary of the rigid body $\partial\Omega_D$ is given by the vector \mathbf{y} , terminating at point $C \in \partial\Omega_D$. The projector \mathbf{y} may be made from vector addition of the current particle position φ and the gap g_n . The gap vector has the special property that it is normal to the surface. The unit normal vector $\hat{\mathbf{n}}$ is co-linear with g_n . A tangent vector \mathbf{t} is constructed perpendicular to the normal. Notice that \mathbf{t} is *not* a unit vector.

The rigid body Ω_D has mass center at current time located by \mathbf{r} . The vector \mathbf{p} is directed from the mass center to the contact point C . The boundary of the rigid body $\partial\Omega_D$ is parameterized by ξ . The dependence of ξ and other variables is important to note because derivatives of these quantities will be taken as precursors to constructing the first and second variations of contact potential.

The derivation of the first and second variations for unilateral contact are very lengthy. Therefore, these derivations are not included here, but contained in SECTION A.5.

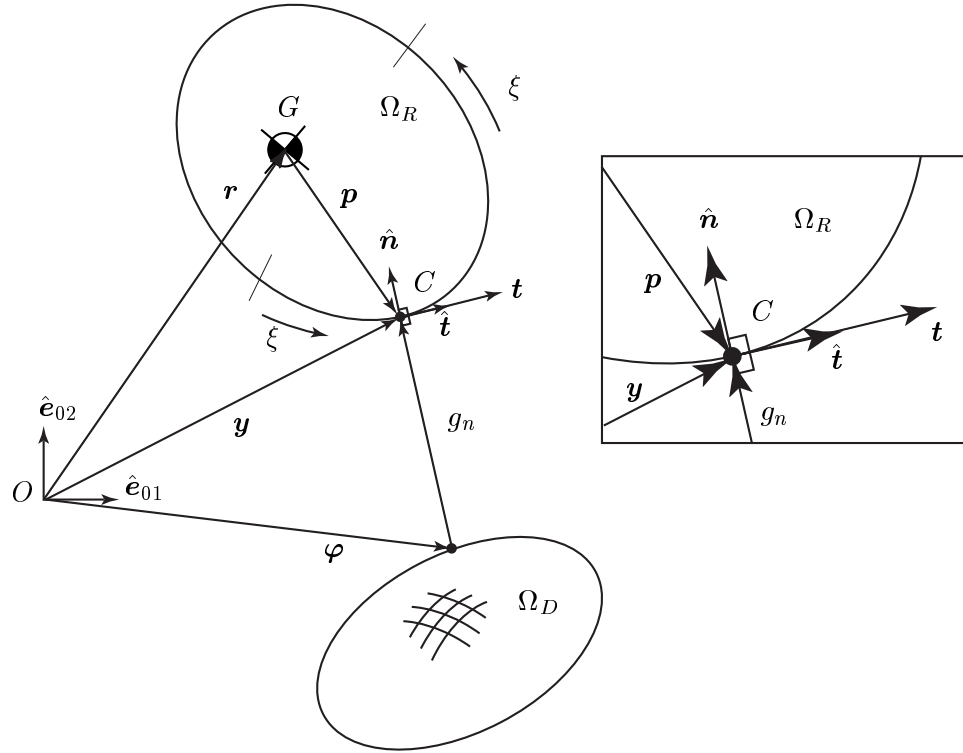


FIGURE 2.9: Vector nomenclature for contact between rigid and deformable bodies.

2.6 FORMULATION SUMMARY FOR THE FULLY COUPLED SYSTEM

2.6.1 THE FIRST VARIATION

Adding the contributions from the deformable, rigid, equality constraint, and inequality constraint variations gives

$$\delta \mathcal{W} = \delta \mathcal{W}_u + \delta \mathcal{W}_q + \delta \mathcal{W}_h + \delta \mathcal{W}_g = 0. \quad (2.111)$$

Expanded, the first variation is written

$$\delta \mathcal{W} = \left\{ \begin{array}{l} \delta \mathbf{u} \\ \delta \mathbf{q} \\ \delta \boldsymbol{\lambda}_h \\ \delta \lambda_g \end{array} \right\}^T \left\{ \begin{array}{l} -\mathbf{R}_u + (\boldsymbol{\lambda}_h + r_h \mathbf{h}) \cdot \nabla_u \mathbf{h} + \text{proj}_{\mathbb{R}^-}(\lambda_g + r_g g_n) \nabla_u g_n \\ -\mathbf{R}_{\ddot{q}} + (\boldsymbol{\lambda}_h + r_h \mathbf{h}) \cdot \nabla_q \mathbf{h} + \text{proj}_{\mathbb{R}^-}(\lambda_g + r_g g_n) \nabla_q g_n \\ \mathbf{h} \\ -\frac{1}{r_g} (\lambda_g - \text{proj}_{\mathbb{R}^-}(\lambda_g + r_g g_n)) \end{array} \right\} = 0. \quad (2.112)$$

The first variation has two distinct forms, depending on whether the status of \mathcal{W}_g is contact

$$\boxed{\delta\mathcal{W}_{(\text{contact})} = \left\{ \begin{array}{c} \delta\mathbf{u} \\ \delta\mathbf{q} \\ \delta\boldsymbol{\lambda}_h \\ \delta\lambda_g \end{array} \right\}^T \left\{ \begin{array}{c} -\mathbf{R}_u + (\boldsymbol{\lambda}_h + r_h \mathbf{h}) \cdot \nabla_u \mathbf{h} + (\lambda_g + r_g g_n) \nabla_u g_n \\ -\mathbf{R}_{\ddot{q}} + (\boldsymbol{\lambda}_h + r_h \mathbf{h}) \cdot \nabla_q \mathbf{h} + (\lambda_g + r_g g_n) \nabla_q g_n \\ \mathbf{h} \\ g_n \end{array} \right\} = 0}, \quad (2.113)$$

or gap

$$\boxed{\delta\mathcal{W}_{(\text{gap})} = \left\{ \begin{array}{c} \delta\mathbf{u} \\ \delta\mathbf{q} \\ \delta\boldsymbol{\lambda}_h \\ \delta\lambda_g \end{array} \right\}^T \left\{ \begin{array}{c} -\mathbf{R}_u + (\boldsymbol{\lambda}_h + r_h \mathbf{h}) \cdot \nabla_u \mathbf{h} \\ -\mathbf{R}_{\ddot{q}} + (\boldsymbol{\lambda}_h + r_h \mathbf{h}) \cdot \nabla_q \mathbf{h} \\ \mathbf{h} \\ -\frac{1}{r_g} \lambda_g \end{array} \right\} = 0}. \quad (2.114)$$

The first variation is expanded in indicial notation for explicitness in APPENDIX A, Eq. (A.203); the definitions for \mathbf{R}_u and $\mathbf{R}_{\ddot{q}}$ have been substituted as well.

2.6.2 THE SECOND VARIATION

The linearization of $\delta\mathcal{W}$ has contributions from the deformable, rigid, equality constraint, and inequality variations, written compactly as

$$\Delta\delta\mathcal{W} = \Delta\delta\mathcal{W}_u + \Delta\delta\mathcal{W}_q + \Delta\delta\mathcal{W}_h + \Delta\delta\mathcal{W}_g. \quad (2.115)$$

Just as the first variation, the second variation has two distinct forms depending on whether the status of \mathcal{W}_g is contact

$$\boxed{\Delta\delta\mathcal{W}_{(\text{contact})} = \left\{ \begin{array}{c} \Delta\mathbf{u} \\ \Delta\mathbf{q} \\ \Delta\boldsymbol{\lambda}_h \\ \Delta\lambda_g \end{array} \right\}^T \left[\begin{array}{cccc} \mathbf{K}_{11} & \mathbf{T}_2^h + \mathbf{T}_2^g & \nabla_u \mathbf{h}^T & \nabla_u g_n^T \\ \mathbf{T}_2^h + \mathbf{T}_2^g & \mathbf{K}_{22} & \nabla_q \mathbf{h}^T & \nabla_q g_n^T \\ \nabla_u \mathbf{h} & \nabla_q \mathbf{h} & \mathbf{0} & \mathbf{0} \\ \nabla_u g_n & \nabla_q g_n & \mathbf{0} & 0 \end{array} \right] \left\{ \begin{array}{c} \Delta\mathbf{u} \\ \Delta\mathbf{q} \\ \Delta\boldsymbol{\lambda}_h \\ \Delta\lambda_g \end{array} \right\}}, \quad (2.116)$$

where

$$\mathbf{K}_{11} = -\nabla_u \mathbf{R}_u + \mathbf{T}_1^h + \mathbf{T}_1^g, \quad (2.117)$$

$$\mathbf{K}_{22} = -\nabla_q \mathbf{R}_{\ddot{q}} + \mathbf{T}_3^h + \mathbf{T}_3^g, \quad (2.118)$$

and where

$$\mathbf{T}_1^h = (\boldsymbol{\lambda}_h + r_h \mathbf{h}) \cdot \nabla_{uu}^2 \mathbf{h} + r_h \nabla_u \mathbf{h} \cdot \nabla_u \mathbf{h}, \quad (2.119)$$

$$\mathbf{T}_2^h = (\boldsymbol{\lambda}_h + r_h \mathbf{h}) \cdot \nabla_{uq}^2 \mathbf{h} + r_h \nabla_u \mathbf{h} \cdot \nabla_q \mathbf{h}, \quad (2.120)$$

$$\mathbf{T}_3^h = (\boldsymbol{\lambda}_h + r_h \mathbf{h}) \cdot \nabla_{qq}^2 \mathbf{h} + r_h \nabla_q \mathbf{h} \cdot \nabla_q \mathbf{h}, \quad (2.121)$$

$$\mathbf{T}_1^g = (\lambda_g + r_g g_n) \nabla_{uu}^2 g_n + r_g \nabla_u g_n \nabla_u g_n, \quad (2.122)$$

$$\mathbf{T}_2^g = (\lambda_g + r_g g_n) \nabla_{uq}^2 g_n + r_g \nabla_u g_n \nabla_q g_n, \quad (2.123)$$

$$\mathbf{T}_3^g = (\lambda_g + r_g g_n) \nabla_{qq}^2 g_n + r_g \nabla_q g_n \nabla_q g_n, \quad (2.124)$$

or gap

$$\boxed{\Delta \delta \mathcal{W}_{(\text{gap})} = \left\{ \begin{array}{c} \delta \mathbf{u} \\ \delta \mathbf{q} \\ \delta \boldsymbol{\lambda}_h \\ \delta \lambda_g \end{array} \right\}^T \left[\begin{array}{cccc} -\nabla_u \mathbf{R}_u + \mathbf{T}_1^h & \mathbf{T}_2^h & \nabla_u \mathbf{h}^T & \mathbf{0} \\ \mathbf{T}_2^h & -\nabla_q \mathbf{R}_{\ddot{q}} + \mathbf{T}_3^h & \nabla_q \mathbf{h}^T & \mathbf{0} \\ \nabla_u \mathbf{h} & \nabla_q \mathbf{h} & \mathbf{0} & \mathbf{0} \\ \mathbf{0} & \mathbf{0} & \mathbf{0} & -\frac{1}{r_g} \end{array} \right] \left\{ \begin{array}{c} \Delta \mathbf{u} \\ \Delta \mathbf{q} \\ \Delta \boldsymbol{\lambda}_h \\ \Delta \lambda_g \end{array} \right\}}. \quad (2.125)$$

The second variation is expanded in indicial notation for explicitness in APPENDIX A, Eq. (A.204); the definitions for \mathbf{R}_u and $\mathbf{R}_{\ddot{q}}$ have been substituted as well.

CHAPTER 3

IMPLEMENTATION

3.1 OVERVIEW

The purpose of this chapter is to explain in detail how the formulation, developed in CHAPTER 2, is implemented in a finite element code. Element implementation of nonlinear elasticity is considered classical and therefore mentioned only very briefly for the sake of completeness. The implementations of rigid body elements and constraint elements are given more attention because they are less common than continuum elements. Particular emphasis is given to the modification of a predictor-corrector time stepping scheme, originally developed for nonlinear elastodynamics, to incorporate both rigid body and constraint elements.

Combining deformable and rigid domains into a dynamical system can become particularly more difficult than considering either of these two domains separately. The difficulty arises from the large spread of frequencies in the system. A large spread in frequencies is disadvantageous because the low frequencies typically dominate the overall behavior of the system but the high frequencies impose time step size restrictions on the time stepping algorithm. As the frequency spread grows, the time step size must decrease and the number of time steps simultaneously increase to obtain the system's response for the same time interval.

The physical system we intend to model in CHAPTER 4 is one example of such a system with a large frequency spread. The dynamics of limb segments, which have frequencies on

the order of 1 Hz, will be coupled with deformable ultra-high-molecular-weight polyethylene, which has a natural frequency approaching 1 MHz. The vibration content of the polyethylene liner is believed to be insignificant compared to the motion of the limb segments. Therefore, to avoid very large time step size restrictions imposed by a high stiffness, low density polyethylene material, we have elected to make the following assumption: Only deformation of the deformable body should be coupled to the dynamics of the large-scale model. The velocities and accelerations of the deformable body do not effect (and in fact, tend to numerically pollute) the motion of the large-scale system.

Clearly, not all mechanical systems may satisfy this assumption. Therefore, this assumption has guided certain simplifying features of the implementation. In particular, the velocity and acceleration of the deformable body mesh are “shut off” meaning that they are not computed and have no effect on the deformable-rigid coupling. Effectively, we are then coupling an elliptic, deformable body boundary value problem (BVP) with a hyperbolic, rigid body initial value problem (IVP). The boundary conditions on the deformable body BVP are therefore time-dependent, coupled to the dynamics of the rigid bodies. Similarly, the reaction forces that the rigid bodies sense through the coupling at their boundaries reflect the internal constitutive law of the deformable body.

Furthermore, we have developed a way to embed the time stepping algorithm into the rigid body as element degrees of freedom. Additional equations, similar to additional constitutive equations in coupled thermo-elasticity, are added to the nonlinear residual equations. Embedding the time stepping algorithm as element degrees of freedom allows a coupled rigid body dynamic, elastostatic solution to be obtained without an outer time stepping loop. Essentially, the solver sees only $\mathbf{F}^{\text{int}} = \mathbf{F}^{\text{ext}}$, or $\mathbf{Kd} = \mathbf{F}^{\text{ext}}$ when linearized. No extra predictor or corrector routines are necessary because they have already been embedded as element degrees of freedom. Details may be seen in SECTION 3.3.

Finally, constraint elements connecting deformable and rigid bodies will have two forms — a standard form, and a secondary form that is compatible with the “embedded dynamics” implementation. These constraint elements include holonomic interface elements, muscle actuator elements, and unilateral, large-slip contact elements.

3.2 DEFORMABLE BODY DYNAMICS

The weak form of the deformable body dynamics problem, given in Eq. **(W)** of Box 2.2 (restated here for convenience)

$$\int_{\Omega} \delta \mathbf{u} \cdot \rho_0 \frac{\partial^2 \mathbf{u}}{\partial t^2} d\Omega + \int_{\Omega} \nabla \delta \mathbf{u} : \mathbf{P} d\Omega = \int_{\Omega} \delta \mathbf{u} \cdot \rho_0 \mathbf{B} d\Omega + \int_{\Gamma_T} \delta \mathbf{u} \cdot \bar{\mathbf{T}} d\Gamma, \quad (3.1)$$

may be solved with the finite element method. The implementation is somewhat classical in the sense that finite element methods have been used successfully for decades. The details of the implementation may be found in [30, 54]. A summary is included here for completeness.

3.2.1 GALERKIN FORM

The weak form is approximated by the Galerkin form through the introduction of finite dimensional subspaces $\mathcal{S}_t^h \subset \mathcal{S}_t$ and $\mathcal{V}^h \subset \mathcal{V}$. The trial functions $\mathbf{u}^h \in \mathcal{S}_t^h$ and weighting functions $\delta \mathbf{u}^h \in \mathcal{V}^h$ are constructed and substituted into Eq. (3.1) to make the Galerkin form of the IVP,

$$\int_{\Omega} \delta \mathbf{u}^h \cdot \rho_0 \frac{\partial^2 \mathbf{u}^h}{\partial t^2} d\Omega + \int_{\Omega} \nabla \delta \mathbf{u}^h : \mathbf{P} d\Omega = \int_{\Omega} \delta \mathbf{u}^h \cdot \rho_0 \mathbf{B} d\Omega + \int_{\Gamma_T} \delta \mathbf{u}^h \cdot \bar{\mathbf{T}} d\Gamma. \quad (3.2)$$

The Galerkin form is often written in operator notation [54]

$$\mathcal{M}(\delta \mathbf{u}^h, \mathbf{u}^h) + \mathcal{N}(\delta \mathbf{u}^h; \mathbf{u}^h) = (\delta \mathbf{u}^h, \mathbf{F}) + (\delta \mathbf{u}^h, \bar{\mathbf{T}})_{\Gamma_T}. \quad (3.3)$$

The notation (\cdot, \cdot) denotes a bilinear operator. All operators appearing in Eq. (3.3) are bilinear except for the $\mathcal{N}(\cdot; \cdot)$ operator, which is in general nonlinear with respect to \mathbf{u}^h and $\dot{\mathbf{u}}^h$.

3.2.2 MATRIX FORM

The Galerkin form is amenable to many different approximate solution methods, one of which is the finite element method. The basic constituents of the finite element method include discretizing the deformable body domain Ω_D into element subdomains, such that

$$\Omega_D = \bigcup_{e=1}^{n_{\text{el}}} \Omega_D^e, \quad (3.4)$$

allowing the degrees of freedom to exist at discrete nodal points, and introducing shape functions based on interpolation of the nodal degrees of freedom. The discretized version of the Galerkin equation takes the form

$$\sum_{e=1}^{n_{\text{el}}} \left[\mathcal{M}(\delta \mathbf{u}^h, \mathbf{u}^h)^e + \mathcal{N}(\delta \mathbf{u}^h; \mathbf{u}^h)^e \right] = \sum_{e=1}^{n_{\text{el}}} \left[(\delta \mathbf{u}^h, \mathbf{F})^e + (\delta \mathbf{u}^h, \mathbf{T})_{\Gamma_T}^e \right]. \quad (3.5)$$

Trial functions and weighting functions are introduced as linear combinations of global element shape functions $N_{\text{node}}(\mathbf{X})$ such that

$$u_i^h(\mathbf{X}, t) = \sum_{B=1}^{n_{\text{en}}} N_B(\mathbf{X}) d_{Bi}^e(t), \quad (3.6)$$

$$\delta u_i^h(\mathbf{X}) = \sum_{A=1}^{n_{\text{en}}} N_A(\mathbf{X}) c_{Ai}^e. \quad (3.7)$$

Taking two time derivatives of \mathbf{u}^h gives

$$\ddot{u}_i^h(\mathbf{X}, t) = \sum_{B=1}^{n_{\text{en}}} N_B(\mathbf{X}) \ddot{d}_{Bi}^e(t). \quad (3.8)$$

Substituting the finite dimensional approximations into the discretized Galerkin form, first for the $\mathcal{M}(\cdot, \cdot)$ operator, we obtain

$$\mathcal{M}(\delta \mathbf{u}^h, \mathbf{u}^h)^e = \int_{\Omega^e} \delta u_i^h \rho_0 \ddot{u}_i^h \, d\Omega, \quad (3.9)$$

$$= \int_{\Omega^e} \sum_A N_A c_{Ai}^e \rho_0 \sum_B N_B \ddot{d}_{Bi}^e \, d\Omega, \quad (3.10)$$

$$= \int_{\Omega^e} \sum_A N_A c_{Ai}^e \rho_0 \sum_B N_B \ddot{d}_{Bk}^e \delta_{ik} \, d\Omega, \quad (3.11)$$

$$= \sum_{A,B}^{n_{\text{en}}} c_{Ai}^e \underbrace{\int_{\Omega^e} \delta_{ik} \rho_0 N_A N_B \, d\Omega}_{\mathbf{M}_{AiBk}^e} \ddot{d}_{Bk}^e. \quad (3.12)$$

For the nonlinear $\mathcal{N}(\cdot, \cdot)$ operator, we obtain

$$\mathcal{N}(\delta \mathbf{u}^h; \mathbf{u}^h)^e = \int_{\Omega^e} \left(\sum_A N_A c_{Ai}^e \right)_{,J} P_{iJ}(\mathbf{d}, \dot{\mathbf{d}}) \, d\Omega, \quad (3.13)$$

$$= \sum_{A=1}^{n_{\text{en}}} c_{Ai}^e \underbrace{\int_{\Omega^e} N_{A,J} P_{iJ}(\mathbf{d}, \dot{\mathbf{d}}) \, d\Omega}_{\mathbf{F}_{Ai}^{\text{int},e}} \quad (3.14)$$

For the (\cdot, \cdot) operator, we obtain

$$(\delta \mathbf{u}^h, \mathbf{F})^e = \int_{\Omega^e} \sum_A N_A c_{Ai}^e \rho_0 B_i^e d\Omega, \quad (3.15)$$

$$= \sum_{A=1}^{n_{en}} c_{Ai}^e \underbrace{\int_{\Omega^e} N_A \rho_0 B_i^e d\Omega}_{\mathbf{F}_{Ai}^{\text{body}, e}}. \quad (3.16)$$

Finally, for the $(\cdot, \cdot)_{\Gamma_H}$ operator, we obtain

$$(\delta \mathbf{u}^h, \bar{\mathbf{T}})_{\Gamma_H}^e = \int_{\Gamma_H^e} \sum_A N_A c_{Ai}^e T_i^e d\Gamma, \quad (3.17)$$

$$= \sum_{A=1}^{n_{en}} c_{Ai}^e \underbrace{\int_{\Gamma_H^e} N_A T_i^e d\Gamma}_{\mathbf{F}_{Ai}^{T, e}}. \quad (3.18)$$

The concept of local support allows the global shape functions

$$u_i^h(\mathbf{X}, t) = \sum_{B=1}^{n_{en}} N_B(\mathbf{X}) d_{Bi}^e(t), \quad (3.19)$$

to be rewritten as local shape functions

$$u_i^h(\boldsymbol{\xi}, t) = \sum_{B=1}^{n_{en}} N_B(\boldsymbol{\xi}) d_{Ai}^e(t), \quad (3.20)$$

because the vector \mathbf{X} is parameterized by $\boldsymbol{\xi}$ as

$$X_i(\boldsymbol{\xi}) = \sum_{B=1}^{n_{en}} N_B(\boldsymbol{\xi}) X_{Bi}^e. \quad (3.21)$$

Using the standard change of variables

$$d\Omega^e = j_0 d\Box, \quad \text{where } j_0 = \det \left[\frac{\partial \mathbf{X}}{\partial \boldsymbol{\xi}} \right], \quad (3.22)$$

the integrals over global element domains may be rewritten as integrals over \Box , the local element domains. For example, the integral in the $\mathcal{M}(\delta \mathbf{u}^h, \mathbf{u}^h)^e$ operator is changed from the global to the local domain:

$$\int_{\Omega^e} \delta_{ik} N_A(\mathbf{X}) N_B(\mathbf{X}) \rho_0 d\Omega^e = \int_{\Box} \delta_{ij} N_A(\boldsymbol{\xi}) N_B(\boldsymbol{\xi}) \rho_0 j_0(\boldsymbol{\xi}) d\Box. \quad (3.23)$$

Additional details may be found in standard textbooks on finite elements [30, 54]. With either global or local shape functions, the discrete Galerkin equation may be rewritten as

$$\mathbf{A} \sum_{e=1}^{n_{\text{el}}} \sum_{A=1}^{n_{\text{en}}} c_{Ai}^e \left[\sum_{B=1}^{n_{\text{en}}} M_{AiBk}^e \ddot{d}_{Bk}^e + F_{Ai}^{\text{int},e}(\mathbf{d}, \dot{\mathbf{d}}) - F_{Ai}^{\text{body},e} - F_{Ai}^{T,e} = 0 \right]. \quad (3.24)$$

Since Galerkin's equation must be satisfied for all $\delta \mathbf{u}^h \in \mathcal{V}^h$, each c_{Ai} is arbitrary. Equation (3.24) is true for any c_{Ai} only if

$$\underbrace{\mathbf{A} \sum_{A,B=1}^{n_{\text{en}}} M_{AiBk}^e \ddot{d}_{Bk}^e}_{\mathbf{F}^{\text{iner}}} + \underbrace{\mathbf{A} \sum_{A=1}^{n_{\text{en}}} F_{Ai}^{\text{int},e}(\mathbf{d}, \dot{\mathbf{d}})}_{\mathbf{F}^{\text{int}}} = \underbrace{\mathbf{A} \sum_{A=1}^{n_{\text{en}}} [F_{Ai}^{\text{body},e} + F_{Ai}^{T,e}]}_{\mathbf{F}^{\text{ext}}}. \quad (3.25)$$

This leads to the matrix form of the equation

$$\boxed{\mathbf{F}^{\text{iner}} + \mathbf{F}^{\text{int}} = \mathbf{F}^{\text{ext}}}, \quad (3.26)$$

which is satisfied if the residual

$$\mathbf{R}_u = \mathbf{F}^{\text{ext}} - \mathbf{F}^{\text{iner}} - \mathbf{F}^{\text{ext}}, \quad (3.27)$$

is exactly zero.

3.2.3 TIME STEPPING

The Newmark family of algorithms is selected because it is the most ubiquitous, familiar, and effective algorithm used today for structural dynamics. The following approximations are made for the time stepping algorithm. For any time step n , the displacement, velocity, and acceleration fields are approximated in time as

$$\mathbf{u}_n \approx \mathbf{d}(t_n), \quad (3.28)$$

$$\mathbf{v}_n \approx \dot{\mathbf{d}}(t_n), \quad (3.29)$$

$$\mathbf{a}_n \approx \ddot{\mathbf{d}}(t_n). \quad (3.30)$$

So we now have temporal approximations for the function $\mathbf{d}(t)$ which is continuous in time. The Newmark algorithm enforces the equations of motion at the t_{n+1} time step

$$\mathbf{R}_{n+1} = \mathbf{F}^{\text{ext}}(t_{n+1}) - \mathbf{F}^{\text{iner}}(\mathbf{a}_{n+1}) - \mathbf{F}^{\text{int}}(\mathbf{u}_{n+1}, \mathbf{v}_{n+1}), \quad (3.31)$$

subject to initial conditions $\mathbf{u}_0 = \mathbf{d}(t = 0)$ and $\mathbf{v}_0 = \dot{\mathbf{d}}(t = 0)$ and the Newmark time advancement operators

$$\mathbf{u}_{n+1} = \mathbf{u}_n + \Delta t \mathbf{v}_n + \frac{\Delta t^2}{2} [(1 - 2\beta)\mathbf{a}_n + 2\beta\mathbf{a}_{n+1}], \quad (3.32)$$

$$\mathbf{v}_{n+1} = \mathbf{v}_n + \Delta t [(1 - \gamma)\mathbf{a}_n + \gamma\mathbf{a}_{n+1}]. \quad (3.33)$$

The time evolution of the IBVP is then obtained through the implicit predictor/corrector algorithm presented in Box 3.1.

The coefficients a, b, c appearing in part (g) of Box 3.1 depend upon whether the algorithmic tangent \mathbf{T}^* is being constructed as an effective mass matrix \mathbf{M}^* , effective damping matrix \mathbf{D}^* , or effective stiffness matrix \mathbf{K}^* . These algorithms are often called a-type, v-type, and u-type, respectively, indicating accelerations, velocities, or displacements are being solved for in (f) in Box 3.1. The coefficients arise from partial differentiation of the time stepping algorithm. For example, the u-type formulation has the tangent

$$\mathbf{T}^* \stackrel{\text{u-type}}{=} \mathbf{K}^* = -\frac{\partial \mathbf{R}_{n+1}^{(i)}}{\partial \mathbf{u}_{n+1}^{(i)}} = \mathbf{M} \frac{\partial \mathbf{a}_{n+1}^{(i)}}{\partial \mathbf{u}_{n+1}^{(i)}} + \mathbf{D}_{n+1}^{(i)} \frac{\partial \mathbf{v}_{n+1}^{(i)}}{\partial \mathbf{u}_{n+1}^{(i)}} + \mathbf{K}_{n+1}^{(i)}, \quad (3.34)$$

where the Newmark algorithm advancement operators Eqs. (3.32)–(3.33) are used to find the partial derivatives (and thus the coefficients a, b, c)

$$a = \frac{\partial \mathbf{a}_{n+1}^{(i)}}{\partial \mathbf{u}_{n+1}^{(i)}} = \frac{1}{\beta \Delta t^2}, \quad b = \frac{\partial \mathbf{v}_{n+1}^{(i)}}{\partial \mathbf{u}_{n+1}^{(i)}} = \frac{\gamma}{\beta \Delta t}, \quad c = 1. \quad (3.35)$$

After solving for displacements $\Delta \mathbf{w}_{n+1}^{(i)} = \Delta \mathbf{u}_{n+1}^{(i)}$, the updates proceed using the same coefficients a, b, c . These three algorithm variations are summarized in TAB. 3.1. Note that the u-type is not available for explicit ($\beta = 0$) time stepping; either the v-type or a-type must be used instead. The u-type is mandatory for quasi-static analysis.

Explicit time stepping algorithms may be used as alternatives to implicit algorithms. Explicit approaches avoid computing and storing the tangent. However, they are only conditionally stable and therefore have a time step size limitation. Additionally, explicit methods are known to accumulate error and drift from the exact solution [54].

The Newmark parameters β and γ control the stability and accuracy of the algorithms. Second order accuracy is achieved only if $\beta = \frac{1}{2}$; first order accuracy is obtained otherwise.

Box 3.1: Predictor/corrector time stepping algorithm applied to deformable body dynamics equations of motion.

1. **Enter time step loop**, assume at t_n the state is known $\{\mathbf{u}_n, \mathbf{v}_n, \mathbf{a}_n\}$
 - (a) **Enter iteration loop** ($i = 1$)
 - (b) **Calculate**
 - $\tilde{\mathbf{u}}_{n+1} = \mathbf{u}_n + \Delta t \mathbf{v}_n + \frac{\Delta t^2}{2}(1 - 2\beta)\mathbf{a}_n$
 - $\tilde{\mathbf{v}}_{n+1} = \mathbf{v}_n + \Delta t(1 - \gamma)\mathbf{a}_n$
 - (c) **Predict**
 - $\mathbf{u}_{n+1}^{(i)} = \tilde{\mathbf{u}}_{n+1}$
 - $\mathbf{v}_{n+1}^{(i)} = \tilde{\mathbf{v}}_{n+1}$
 - $\mathbf{a}_{n+1}^{(i)} = \mathbf{0}$
 - (d) **Form residual**
 - $\mathbf{R}_{n+1}^{(i)} = \mathbf{F}^{\text{ext}}(t_{n+1}) - \mathbf{M}\mathbf{a}_{n+1}^{(i)} - \mathbf{F}^{\text{int}}(\mathbf{u}_{n+1}^{(i)}, \mathbf{v}_{n+1}^{(i)})$
 - (e) **Form algorithmic tangent** (form and factorize only as needed)
 - $\mathbf{T}^* = \frac{-\partial \mathbf{R}_{n+1}^{(i)}}{\partial \mathbf{w}_{n+1}^{(i)}} = a\mathbf{M} + b\mathbf{D}_{n+1}^{(i)} + c\mathbf{K}_{n+1}^{(i)}$
 - (f) **Equate LHS and RHS, solve linear system for $\Delta \mathbf{w}_{n+1}^{(i)}$**
 - $\mathbf{T}^* \Delta \mathbf{w}_{n+1}^{(i)} = \mathbf{R}_{n+1}^{(i)}$
 - $\Rightarrow \Delta \mathbf{w}_{n+1}^{(i)} = (\mathbf{T}^*)^{-1} \mathbf{R}_{n+1}^{(i)}$
 - (g) **Correct**
 - $\mathbf{u}_{n+1}^{(i+1)} = \mathbf{u}_{n+1}^{(i)} + c\Delta \mathbf{w}_{n+1}^{(i)}$
 - $\mathbf{v}_{n+1}^{(i+1)} = \mathbf{v}_{n+1}^{(i)} + b\Delta \mathbf{w}_{n+1}^{(i)}$
 - $\mathbf{a}_{n+1}^{(i+1)} = \mathbf{a}_{n+1}^{(i)} + a\Delta \mathbf{w}_{n+1}^{(i)}$
 - (h) **Convergence check** $\| \mathbf{R}_{n+1}^{(i+1)} \| \leq \text{TOLERANCE}$
 - NO $\Rightarrow i \leftarrow i + 1$ GOTO (d)
 - YES \Rightarrow EXIT ITERATION LOOP
2. **Update state vector** $\{\mathbf{u}_{n+1}, \mathbf{v}_{n+1}, \mathbf{a}_{n+1}\}$
 - (a) $\mathbf{a}_{n+1} = \mathbf{a}_{n+1}^{(i+1)}$
 - (b) $\mathbf{v}_{n+1} = \mathbf{v}_{n+1}^{(i+1)}$
 - (c) $\mathbf{u}_{n+1} = \mathbf{u}_{n+1}^{(i+1)}$
3. **Update time step**
 - (a) $n \leftarrow n + 1$
 - (b) RETURN to (1)

TABLE 3.1: Three variations of Newmark time stepping algorithm: u-type, v-type, and a-type formulations.

formulation	solve for	a	b	c
u-type	$\Delta\mathbf{w} = \Delta\mathbf{u}$	$\frac{1}{\beta\Delta t^2}$	$\frac{\gamma}{\beta\Delta t}$	1
v-type	$\Delta\mathbf{w} = \Delta\mathbf{v}$	$\frac{1}{\gamma\Delta t}$	1	$\frac{\beta\Delta t}{\gamma}$
a-type	$\Delta\mathbf{w} = \Delta\mathbf{a}$	1	$\gamma\Delta t$	$\beta\Delta t^2$

The algorithm is unconditionally stable for $2\beta \geq \gamma > \frac{1}{2}$ and conditionally stable for $\gamma \geq \frac{1}{2}$. These stability and accuracy results technically apply only to the *linear* elastodynamic system. Hughes has extended these ideas to nonlinear elastodynamics by offering notions of linearized stability [17]. In the nonlinear regime, even implicit methods are not guaranteed to be stable. Recent emphasis on algorithmic stability of nonlinear deformable and rigid body dynamics has been born out of energy and momentum conserving time stepping algorithms. See [107, 108] for details.

3.3 RIGID BODY DYNAMICS

In contrast to the IVP of the deformable body dynamics problem, the IVP of the rigid body dynamics problem (see Box 2.3, restated here for convenience)

$$\delta\mathbf{q} \cdot \left(\frac{d}{dt} \frac{\partial \mathcal{L}}{\partial \dot{\mathbf{q}}} - \frac{\partial \mathcal{L}}{\partial \mathbf{q}} - \mathbf{Q} \right) = 0, \quad (3.36)$$

has no spatial discretization. The effects of particles of mass making up a rigid body or rigid body system are sufficiently described by accounting for the motion of a single point — the mass center. The Galerkin projections into finite dimensional subspaces, used for deformable bodies, are therefore unnecessary for rigid bodies. The matrix equations are obtained immediately.

3.3.1 MATRIX FORM

Recalling the definitions from Eqs. (3.37)–(3.38)

$$\mathbf{F}^{\text{iner}} = \mathbf{A}(\mathbf{q})\ddot{\mathbf{q}} + \mathbf{B}(\mathbf{q})\dot{\mathbf{q}}^2, \quad (3.37)$$

$$\mathbf{F}^{\text{ext}} = \mathbf{G}(\mathbf{q}) + \mathbf{Q}(\mathbf{q}, \dot{\mathbf{q}}), \quad (3.38)$$

the matrix form of the rigid body equations is simply a balance of inertial and external forces

$$\boxed{\mathbf{F}^{\text{iner}} = \mathbf{F}^{\text{ext}}}, \quad (3.39)$$

which is satisfied if the residual

$$\mathbf{R}_{\dot{\mathbf{q}}} = \mathbf{F}^{\text{ext}} - \mathbf{F}^{\text{iner}}, \quad (3.40)$$

is exactly zero.

3.3.2 TIME STEPPING

The Newmark time stepping algorithm used for deformable body dynamics may be applied to rigid body dynamics by approximating the continuous functions of time with their discrete counterparts

$$\mathbf{q}_n \approx \mathbf{q}(t_n), \quad (3.41)$$

$$\dot{\mathbf{q}}_n \approx \dot{\mathbf{q}}(t_n), \quad (3.42)$$

$$\ddot{\mathbf{q}}_n \approx \ddot{\mathbf{q}}(t_n). \quad (3.43)$$

Note that these approximations are analogous to those appearing in Eqs. (3.28)–(3.30).

The same predictor/corrector algorithm given in Box 3.1 may be used to integrate the governing equations of motion forward in time. The \mathbf{u}_n and \mathbf{u}_{n+1} are replaced by \mathbf{q}_n and \mathbf{q}_{n+1} , respectively. Analogous replacements are made for the time derivative terms. Care must be taken to construct the residual and the tangent for the case of the rigid body dynamics equations. Comparing the residual and tangent of the deformable and rigid cases, one may notice several differences.

Box 3.2: Modifications to the predictor/corrector algorithm in Box 3.1 for use with rigid body dynamics equations of motion.

(d) Form residual

- $\mathbf{R}_{n+1}^{(i)} = \mathbf{F}^{\text{ext}}(\mathbf{q}_{n+1}^{(i)}, \dot{\mathbf{q}}_{n+1}^{(i)}) - \mathbf{F}^{\text{iner}}(\mathbf{q}_{n+1}^{(i)}, \dot{\mathbf{q}}_{n+1}^{(i)}, \ddot{\mathbf{q}}_{n+1}^{(i)})$

(e) Form algorithmic tangent (form and factorize only as needed)

- $\mathbf{T}^* = \frac{-\partial \mathbf{R}_{n+1}^{(i)}}{\partial \mathbf{w}_{n+1}^{(i)}} = a\mathbf{M}_{n+1}^{(i)} + b\mathbf{D}_{n+1}^{(i)} + c\mathbf{K}_{n+1}^{(i)}$

1. The external forces are possibly functions of position \mathbf{q} and velocity $\dot{\mathbf{q}}$ whereas in the deformable body case, the external loading was assumed to be dead loading.
2. The inertia force in the deformable body case was linear in accelerations \mathbf{a} . In the rigid body case, the inertia force is linear in the accelerations $\ddot{\mathbf{q}}$ but in general nonlinear in the positions \mathbf{q} and velocities $\dot{\mathbf{q}}$.
3. The internal force vector \mathbf{F}^{int} is absent in the rigid case.
4. The tangent mass matrix \mathbf{M} of the deformable case is assumed constant whereas for the rigid case, the mass matrix, in general, depends on the configuration $\mathbf{M}(\mathbf{q})$.

3.3.3 THE RIGID ELEMENT — VERSION 1

Implementation of elements for elasticity, heat conduction, or fluid flow may be found in many finite element textbooks, such as [30, 54]. In contrast, the implementation of rigid body elements in finite element codes is left solely to literature. Because of this, some detail on how rigid body elements are specifically implemented here is in order.

During the development of the rigid body element, it became clear that two main alternatives existed with regard to the implementation:

- (a)** Use Lagrange's equations to formulate the equations of motion for the rigid body system of interest and subsequently code an implementation of that particular system; or,
- (b)** Use Lagrange's equations to formulate the equations of motion for a single rigid body

and create the rigid body system by creating additional elements that connect individual rigid bodies.

We adopted the latter approach. The rationale is as follows. Using Lagrange's equations to describe the rigid body system, as proposed in (a), produced a compact equation system that had minimum dimensionality. The implementation led to a "Lagrangian chain element" where the number of degrees of freedom in the element equaled the number of generalized coordinates in the rigid body system. For example, a planar double pendulum would have the minimum of two generalized coordinates. Thus in a "double pendulum finite element," two degrees of freedom might be coded.

This approach soon became cumbersome because it was not known beforehand how many links might be needed in the rigid body system. With this approach, it would be necessary to write, code, debug, and validate n unique element implementations for n different "Lagrangian chain element" systems. This approach further seemed anathema to the philosophy of finite elements, where the connectivity of the finite elements and not the elements themselves define the domain. Finally, during one occasion where Lagrange's equations were used in conjunction with approach (a) to model a planar, seven-link rigid body system of the lower legs and upper body (two feet, two shanks, two thighs, and one head-arms-trunk or HAT), the choice of alternatives became very clear. The resulting equations of motion, though compact because only seven generalized coordinates were used, were excessively complicated. Furthermore, linearization of these equations — a requirement to properly construct the element tangent stiffness, damping, and mass matrices — became nearly intractable and highly error-prone.

Approach (b) seemed more manageable, particularly as the number of rigid links in the system grew. Furthermore, implementing a rigid body element in this manner seemed more like a finite element rather than one super element, composed of a rather arbitrary number of degrees of freedom representing the generalized coordinates. The modular feature of finite elements is retained with rigid elements implemented in this way. If another link is needed, the user simply adds that element to the mesh, avoiding implementation of another super element.

Two rigid body elements will be presented. Both elements are planar because they will

be used to model motion of limb segments moving during gait, which is primarily constrained to the sagittal plane. The first rigid element has three element degrees of freedom

$$\mathbf{q}^e = \langle q_1, q_2, q_3 \rangle^T, \quad (3.44)$$

where q_1 and q_2 are the translations and q_3 is the in-plane rotation (see FIG. 3.1). These three element degrees of freedom are analogous to the element degrees of freedom of a traditional, deformable finite element.

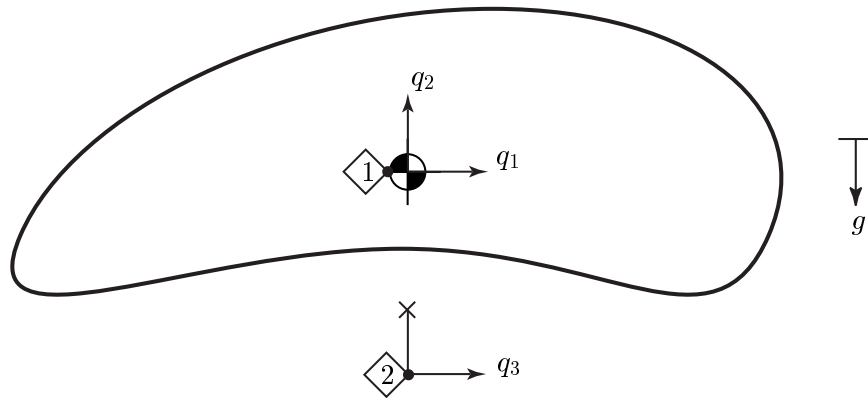


FIGURE 3.1: Planar rigid body element with translational degrees of freedom q_1 and q_2 drawn on the body and the out-of-plane rotational degree of freedom q_3 drawn off the body.

Using this particular set of generalized coordinates produces equations of motion which are identical to those obtained were Newton's equations used instead of Lagrange's equations. The element force vectors

$$\mathbf{F}^{\text{iner,e}} = \langle m \ddot{q}_1, m \ddot{q}_2, I_3 \ddot{q}_3 \rangle^T, \quad (3.45)$$

$$\mathbf{F}^{\text{ext,e}} = \langle F_1, F_2 - mg, M_3 \rangle^T, \quad (3.46)$$

$$\mathbf{F}^{\text{visc,e}} = \langle c \dot{q}_1, c \dot{q}_2, c \dot{q}_3 \rangle^T, \quad (3.47)$$

are simpler than the general form given in Eqs. (3.37)–(3.38). The mass of the rigid body is m and the principal moment of inertia of the body in the out-of-plane direction is I_3 . The viscous damping constant is c . The force resultants applied to the center of mass are F_1 and

F_2 ; the moment resultant is M_3 . The element mass and damping matrices are respectively

$$\mathbf{M}^e = \begin{bmatrix} m & 0 & 0 \\ 0 & m & 0 \\ 0 & 0 & I_3 \end{bmatrix}, \quad \text{and} \quad \mathbf{D}^e = \begin{bmatrix} c & 0 & 0 \\ 0 & c & 0 \\ 0 & 0 & c \end{bmatrix}. \quad (3.48)$$

The matrices are constant, just like traditional finite element mass and damping matrices. The element stiffness matrix is identically zero. It is important to mention that the simplicity of the element vectors and matrices comes from approach (b). In contrast, approach (a) can quickly become complicated.

Special connection elements must also be written if alternative (b) is selected. These connections have been included as a special case of generalized holonomic constraint elements which describe interactions between two deformable bodies, two rigid bodies, or one deformable and one rigid body. The implementation of these constraint elements is included in SECTION 3.4.

3.3.4 EMBEDDED DYNAMICS, THE RIGID ELEMENT — VERSION 2

As explained in the opening of this chapter, we assume the deformable domain to be an elliptic problem. When we initially ran test problems with the deformable mesh included as a hyperbolic domain, we observed erratic and large deformations. The large deformations occurred because the deformable mesh was tied via compatibility constraints to move with the deformable bodies along a common boundary. However, the large stiffness and small mass of the deformable domain caused high frequency participation to pollute the total solution and ultimately cause divergence of the system. This observation, along with the belief that the dynamics of the rigid bodies and not the deformable bodies governs the time dependent motion of the coupled system, led to the development of the embedded dynamics rigid element.

As mentioned at the beginning of this chapter, the element degrees of freedom for position as well as velocity and acceleration are contained as element degrees of freedom

$$\mathbf{s}^e = \langle \ddot{q}_1, \ddot{q}_2, \ddot{q}_3, \dot{q}_1, \dot{q}_2, \dot{q}_3, q_1, q_2, q_3 \rangle^T, \quad (3.49)$$

as shown in FIG. 3.2. These nine element degrees of freedom are analogous to the element degrees of freedom of a traditional, deformable finite element.

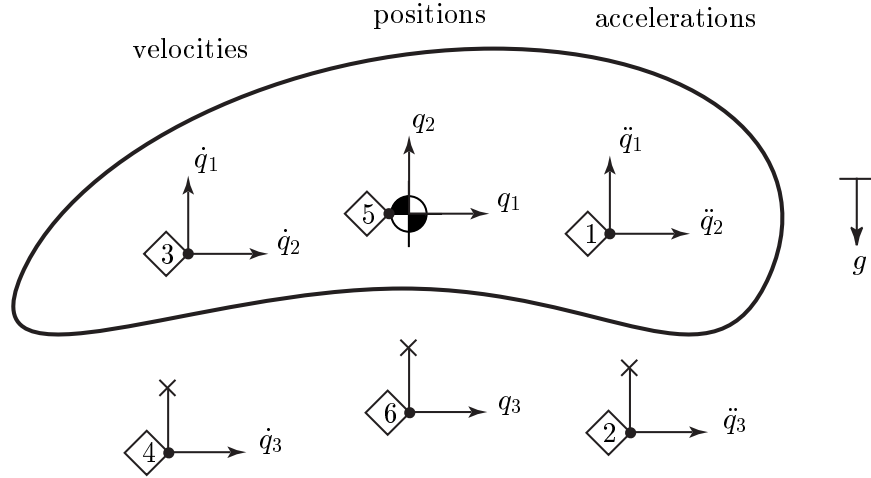


FIGURE 3.2: Planar rigid body element with velocity and acceleration degrees of freedom embedded into the element position degrees of freedom. Translational degrees of freedom (q_1 , q_2 , and their time derivatives) are drawn on the body. The out-of-plane rotational degrees of freedom (q_3 and its time derivatives) are drawn off the body.

The time stepping algorithm equations augment the standard governing equations of motion. Three residuals are defined.

$$\mathbf{R}_{n+1}^{(i)} = \begin{cases} \mathbf{R}_{n+1}^{\ddot{q}(i)} = \mathbf{F}^{\text{ext}}(t_{n+1}) - \mathbf{M}\ddot{\mathbf{q}}_{n+1}^{(i)} - \mathbf{D}\dot{\mathbf{q}}_{n+1}^{(i)}, \\ \mathbf{R}_{n+1}^{\dot{q}(i)} = \frac{-\dot{\mathbf{q}}_{n+1}^{(i)} + \dot{\mathbf{q}}_n}{\Delta t} + [(1 - \gamma)\ddot{\mathbf{q}}_n + \gamma\ddot{\mathbf{q}}_{n+1}^{(i)}], \\ \mathbf{R}_{n+1}^{q(i)} = \frac{-\mathbf{q}_{n+1}^{(i)} + \mathbf{q}_n}{\Delta t} + \left(1 - \frac{\beta}{\gamma}\right)\dot{\mathbf{q}}_n + \frac{\beta}{\gamma}\dot{\mathbf{q}}_{n+1}^{(i)} + \left(\frac{1}{2} - \frac{\beta}{\gamma}\right)\Delta t\ddot{\mathbf{q}}_n. \end{cases} \quad (3.50)$$

Linearization of these residuals is given by

$$-\frac{\partial \mathbf{R}_{n+1}^{(i)}}{\partial \mathbf{s}_{n+1}^{(i)}} \Delta \mathbf{s}_{n+1}^{(i)} = \begin{bmatrix} \mathbf{M} & \mathbf{D} & \mathbf{0} \\ -\gamma \mathbf{1} & \frac{1}{\Delta t} \mathbf{1} & \mathbf{0} \\ \mathbf{0} & -\frac{\beta}{\gamma} & \frac{1}{\Delta t} \end{bmatrix} \begin{Bmatrix} \Delta \ddot{\mathbf{q}} \\ \Delta \dot{\mathbf{q}} \\ \Delta \mathbf{q} \end{Bmatrix}. \quad (3.51)$$

Note here that the residual equations not only depend on state $n + 1$ but also on state n , which is different from the tangents developed for elastodynamics in SECTION 3.2. The predictor/corrector time stepping algorithm requires only a few minor modifications, noted in Box 3.3.

Box 3.3: Predictor/corrector time stepping algorithm for embedded rigid body dynamics.

1. **Enter time step loop**, assume at t_n the state is known $s_n = \{q_n, \dot{q}_n, \ddot{q}_n\}$
 - (a) **Enter iteration loop** ($i = 1$)
 - (b) **Form residual**
 - $\mathbf{R}_{n+1}^{(i)} = \langle \mathbf{R}_{n+1}^{\ddot{q}(i)}, \mathbf{R}_{n+1}^{\dot{q}(i)}, \mathbf{R}_{n+1}^{q(i)} \rangle^T$
 - (c) **Form algorithmic tangent** (form and factorize only as needed)
 - $\mathbf{T}^* = \frac{-\partial \mathbf{R}_{n+1}^{(i)}}{\partial s_{n+1}^{(i)}}$
 - (d) **Equate LHS and RHS, solve linear system for $\Delta s_{n+1}^{(i)}$**
 - $\mathbf{T}^* \Delta s_{n+1}^{(i)} = \mathbf{R}_{n+1}^{(i)}$
 - $\Rightarrow \Delta s_{n+1}^{(i)} = (\mathbf{T}^*)^{-1} \mathbf{R}_{n+1}^{(i)}$
 - (e) **Correct**
 - $s_{n+1}^{(i+1)} = s_{n+1}^{(i)} + \Delta s_{n+1}^{(i)}$
 - (f) **Convergence check** $\| \mathbf{R}_{n+1}^{(i+1)} \| \leq \text{TOLERANCE}$
 - NO $\Rightarrow i \leftarrow i + 1$ GOTO (b)
 - YES \Rightarrow EXIT ITERATION LOOP
2. **Update state vector** $s_{n+1} = \{q_{n+1}, \dot{q}_{n+1}, \ddot{q}_{n+1}\}$
 - (a) $s_{n+1} = s_{n+1}^{(i+1)}$
3. **Update time step**
 - (a) $n \leftarrow n + 1$
 - (b) RETURN to (1)

The element residual and tangent are implemented as a negative internal force vector and a tangent stiffness matrix, respectively.

$$\boldsymbol{\delta}^e \cdot \mathbf{F}^{int,e} = \left\{ \begin{array}{c} \delta \ddot{q}_1 \\ \delta \ddot{q}_2 \\ \hline \delta \ddot{q}_3 \\ \hline \delta \dot{q}_1 \\ \delta \dot{q}_2 \\ \hline \delta \dot{q}_3 \\ \hline \delta q_1 \\ \delta q_2 \\ \hline \delta q_3 \end{array} \right\}^T \left\{ \begin{array}{c} m \ddot{q}_1 + c \dot{q}_1 \\ m \ddot{q}_2 + c \dot{q}_2 - m g \\ \hline I_3 \ddot{q}_3 + c \dot{q}_3 \\ \hline \frac{\dot{q}_1 - \dot{q}_{1|n}}{\Delta t} - [(1-\gamma)\ddot{q}_{1|n} + \gamma \ddot{q}_1] \\ \frac{\dot{q}_2 - \dot{q}_{2|n}}{\Delta t} - [(1-\gamma)\ddot{q}_{2|n} + \gamma \ddot{q}_2] \\ \frac{\dot{q}_3 - \dot{q}_{3|n}}{\Delta t} - [(1-\gamma)\ddot{q}_{3|n} + \gamma \ddot{q}_3] \\ \hline \frac{q_1 - q_{1|n}}{\Delta t} - \left(1 - \frac{\beta}{\gamma}\right) \dot{q}_{1|n} - \frac{\beta}{\gamma} \dot{q}_1 - \left(\frac{1}{2} - \frac{\beta}{\gamma}\right) \Delta t \ddot{q}_{1|n} \\ \frac{q_2 - q_{2|n}}{\Delta t} - \left(1 - \frac{\beta}{\gamma}\right) \dot{q}_{2|n} - \frac{\beta}{\gamma} \dot{q}_2 - \left(\frac{1}{2} - \frac{\beta}{\gamma}\right) \Delta t \ddot{q}_{2|n} \\ \frac{q_3 - q_{3|n}}{\Delta t} - \left(1 - \frac{\beta}{\gamma}\right) \dot{q}_{3|n} - \frac{\beta}{\gamma} \dot{q}_3 - \left(\frac{1}{2} - \frac{\beta}{\gamma}\right) \Delta t \ddot{q}_{3|n} \end{array} \right\} \quad (3.52)$$

$$\boldsymbol{\delta}^e \cdot \mathbf{K}^e \boldsymbol{\Delta}^e = \left\{ \begin{array}{c} \delta \ddot{q}_1 \\ \delta \ddot{q}_2 \\ \hline \delta \ddot{q}_3 \\ \hline \delta \dot{q}_1 \\ \delta \dot{q}_2 \\ \hline \delta \dot{q}_3 \\ \hline \delta q_1 \\ \delta q_2 \\ \hline \delta q_3 \end{array} \right\}^T \left\{ \begin{array}{ccc|ccc|ccc} m & 0 & 0 & c & 0 & 0 & 0 & 0 & 0 & \Delta \ddot{q}_1 \\ 0 & m & 0 & 0 & c & 0 & 0 & 0 & 0 & \Delta \ddot{q}_2 \\ 0 & 0 & I_3 & 0 & 0 & c & 0 & 0 & 0 & \Delta \ddot{q}_3 \\ \hline -\gamma & 0 & 0 & \frac{1}{\Delta t} & 0 & 0 & 0 & 0 & 0 & \Delta \dot{q}_1 \\ 0 & -\gamma & 0 & 0 & \frac{1}{\Delta t} & 0 & 0 & 0 & 0 & \Delta \dot{q}_2 \\ 0 & 0 & -\gamma & 0 & 0 & \frac{1}{\Delta t} & 0 & 0 & 0 & \Delta \dot{q}_3 \\ \hline 0 & 0 & 0 & -\frac{\beta}{\gamma} & 0 & 0 & \frac{1}{\Delta t} & 0 & 0 & \Delta q_1 \\ 0 & 0 & 0 & 0 & -\frac{\beta}{\gamma} & 0 & 0 & \frac{1}{\Delta t} & 0 & \Delta q_2 \\ 0 & 0 & 0 & 0 & 0 & -\frac{\beta}{\gamma} & 0 & 0 & \frac{1}{\Delta t} & \Delta q_3 \end{array} \right\} \quad (3.53)$$

3.4 EQUALITY CONSTRAINTS

This section details three types of two dimensional equality constraints: (a) Deformable-deformable equality constraints, (b) deformable-rigid equality constraints, and (c) rigid-rigid equality constraints. All three types of constraints join two bodies together at points. These points, in the case of deformable bodies, are described as any node belonging to the finite element mesh. These points, in the case of rigid bodies, are described as any point belonging to the rigid body domain.

3.4.1 DEFORMABLE-DEFORMABLE EQUALITY CONSTRAINT ELEMENT

The purpose of this element is to constrain two planar deformable bodies to share a common point in space, throughout time, as shown in FIG. 3.3. This constraint effectively creates a pin joint between the two bodies, where relative planar translation is prohibited and relative planar rotation is allowed.

The constraint element has the element degrees of freedom

$$\boldsymbol{s}^e = \langle u_1, u_2, u_3, u_4, \lambda_1, \lambda_2 \rangle^T, \quad (3.54)$$

where

$$\boldsymbol{u}^{P_1} = \langle u_1, u_2 \rangle^T = \boldsymbol{\varphi}^{P_1} + \boldsymbol{X}^{P_1}, \quad (3.55)$$

$$\boldsymbol{u}^{P_2} = \langle u_3, u_4 \rangle^T = \boldsymbol{\varphi}^{P_2} + \boldsymbol{X}^{P_2}. \quad (3.56)$$

The constraint equation is written

$$\boldsymbol{h} = \boldsymbol{\varphi}^{P_1} - \boldsymbol{\varphi}^{P_2} = \mathbf{0}. \quad (3.57)$$

It may be shown by specialization of the derivation in SECTION A.4 that the element

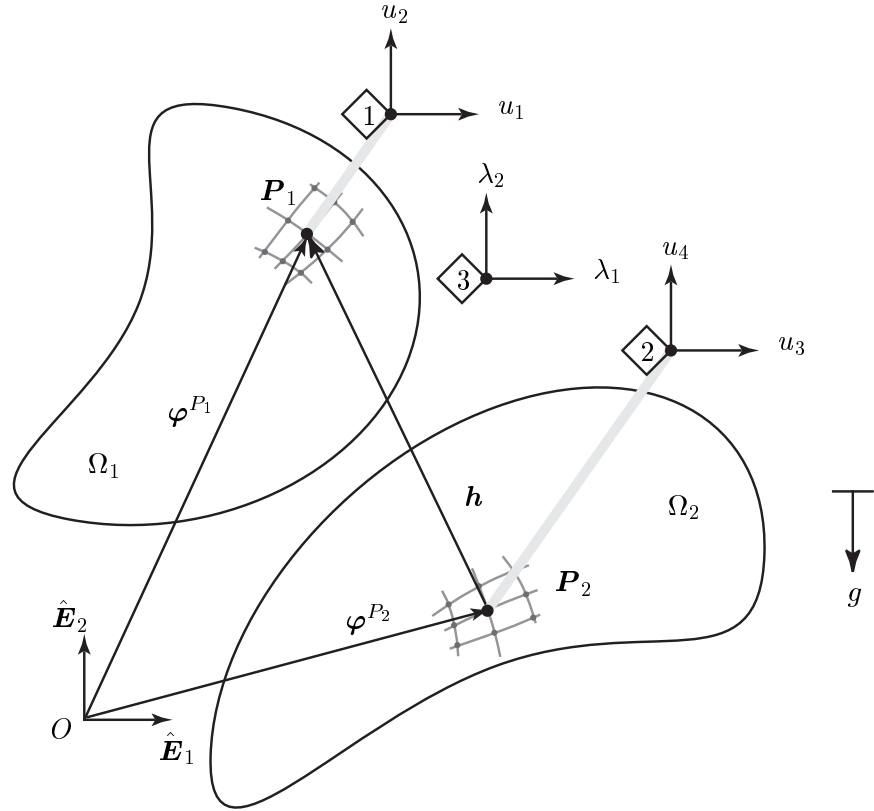


FIGURE 3.3: Two deformable bodies Ω_1 and Ω_2 pinned together such that point P_1 and point P_2 overlap for all time.

internal force vector and element tangent stiffness matrix have the following form:

$$\delta^e \cdot \mathbf{F}^{int,e} = \left\{ \begin{array}{c} \delta u_1 \\ \delta u_2 \\ \delta u_3 \\ \delta u_4 \\ \delta \lambda_1 \\ \delta \lambda_2 \end{array} \right\}^T \left\{ \begin{array}{c} \lambda_1 + rh_1 \\ \lambda_2 + rh_2 \\ -(\lambda_1 + rh_1) \\ -(\lambda_2 + rh_2) \\ h_1 \\ h_2 \end{array} \right\}, \quad (3.58)$$

$$\delta^e \cdot \mathbf{K}^e \Delta^e = \left\{ \begin{array}{c} \delta u_1 \\ \delta u_2 \\ \delta u_3 \\ \delta u_4 \\ \hline \delta \lambda_1 \\ \delta \lambda_2 \end{array} \right\}^T \left\{ \begin{array}{cc|cc|cc} r & 0 & -r & 0 & 1 & 0 \\ 0 & r & 0 & -r & 0 & 1 \\ \hline -r & 0 & r & 0 & -1 & 0 \\ 0 & -r & 0 & r & 0 & -1 \\ \hline 1 & 0 & -1 & 0 & 0 & 0 \\ 0 & 1 & 0 & -1 & 0 & 0 \end{array} \right\} \left\{ \begin{array}{c} \Delta u_1 \\ \Delta u_2 \\ \Delta u_3 \\ \Delta u_4 \\ \hline \Delta \lambda_1 \\ \Delta \lambda_2 \end{array} \right\}. \quad (3.59)$$

3.4.2 DEFORMABLE–RIGID EQUALITY CONSTRAINT ELEMENT — VERSION 1

The purpose of this element is to constrain a single planar rigid body and a planar deformable body to share a common point in space, throughout time, as shown in FIG. 3.4. This constraint effectively creates a pin joint between the two bodies, where relative planar translation is prohibited and relative planar rotation is allowed.

The constraint element has the element degrees of freedom

$$\mathbf{s}^e = \langle u_1, u_2, q_1, q_2, q_3, \lambda_1, \lambda_2 \rangle^T, \quad (3.60)$$

where $\mathbf{u}^{P_1} = \langle u_1, u_2 \rangle^T$, $\mathbf{r}^{\Omega_2} = \langle q_1, q_2 \rangle^T$, and $\mathbf{r}^{P_2} = \langle c_1^{P_2}, c_2^{P_2} \rangle^T$. The constraint equation is written

$$\mathbf{h} = \varphi^{P_1} - \mathbf{r}^{\Omega_2} - \mathbf{r}^{P_2} = \mathbf{0}. \quad (3.61)$$

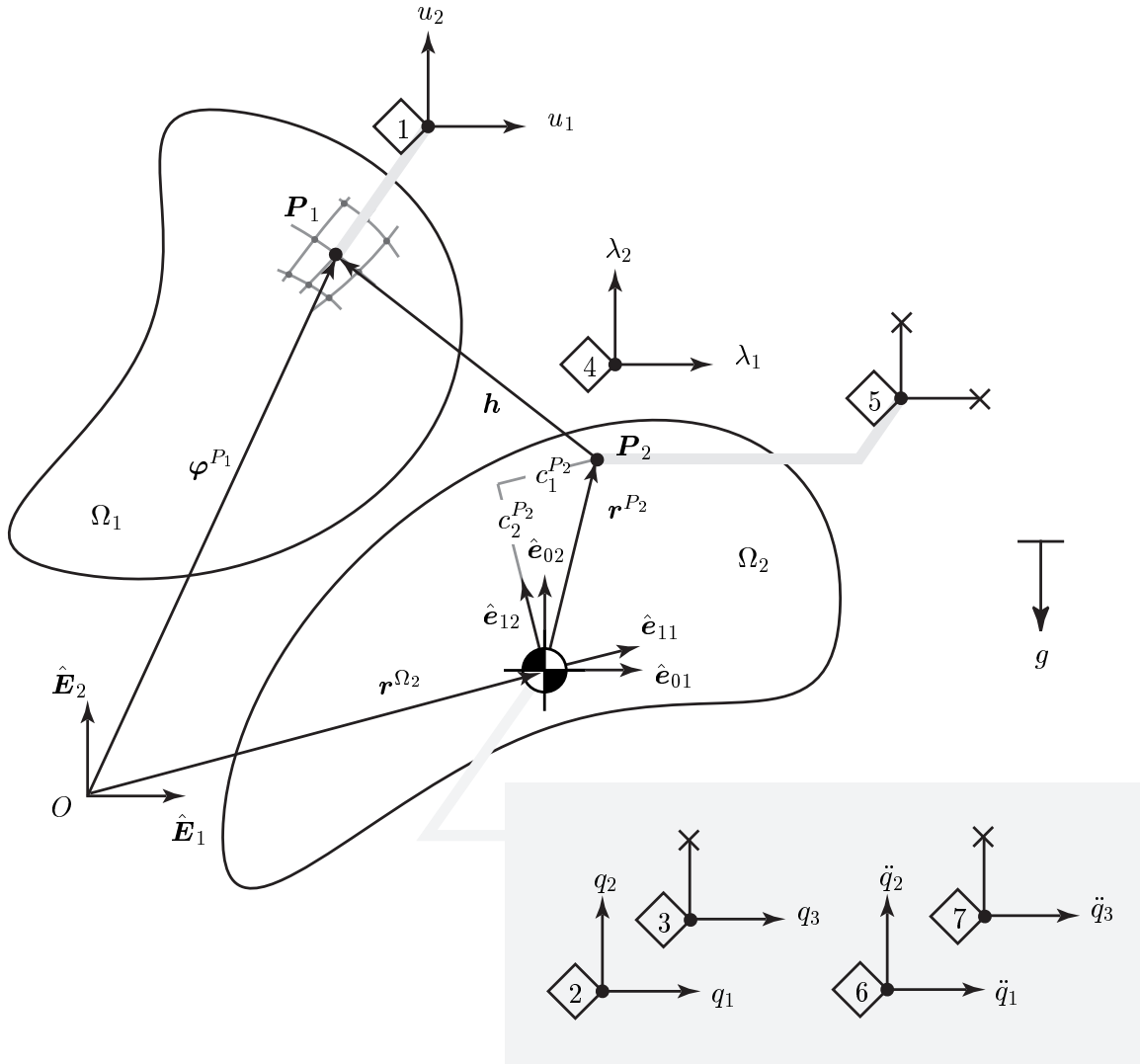


FIGURE 3.4: One deformable body Ω_1 and one rigid body Ω_2 pinned together such that point P_1 and point P_2 overlap for all time.

Let the following definitions be made:

$$z_1 = c_1^{P_2} \cos q_3 - c_2^{P_2} \sin q_3, \quad (3.62)$$

$$z_2 = c_1^{P_2} \sin q_3 + c_2^{P_2} \cos q_3. \quad (3.63)$$

It may be shown by specialization of the derivation in SECTION A.4 that the element internal force vector and element tangent stiffness matrix have the following form:

$$\boldsymbol{\delta}^e \cdot \mathbf{F}^{int,e} = \left\{ \begin{array}{c} \delta u_1 \\ \delta u_2 \\ \hline \delta q_1 \\ \delta q_2 \\ \hline \delta q_3 \\ \hline \delta \lambda_1 \\ \delta \lambda_2 \end{array} \right\}^T \left\{ \begin{array}{c} \lambda_1 + rh_1 \\ \lambda_2 + rh_2 \\ \hline -(\lambda_1 + rh_1) \\ -(\lambda_2 + rh_2) \\ \hline z_2(\lambda_1 + rh_1) - z_1(\lambda_2 + rh_2) \\ h_1 \\ h_2 \end{array} \right\}, \quad (3.64)$$

$$\boldsymbol{\delta}^e \cdot \mathbf{K}^e \Delta^e = \left\{ \begin{array}{c} \delta u_1 \\ \delta u_2 \\ \hline \delta q_1 \\ \delta q_2 \\ \hline \delta q_3 \\ \hline \delta \lambda_1 \\ \delta \lambda_2 \end{array} \right\}^T \left\{ \begin{array}{c|cc|cc|cc} r & 0 & -r & 0 & rz_2 & 1 & 0 \\ 0 & r & 0 & -r & -rz_1 & 0 & 1 \\ \hline -r & 0 & r & 0 & -rz_2 & -1 & 0 \\ 0 & -r & 0 & r & rz_1 & 0 & -1 \\ \hline rz_2 & -rz_1 & -rz_2 & rz_1 & m_{33} & z_2 & -z_1 \\ 1 & 0 & -1 & 0 & z_2 & 0 & 0 \\ 0 & 1 & 0 & -1 & -z_1 & 0 & 0 \end{array} \right\} \left\{ \begin{array}{c} \Delta u_1 \\ \Delta u_2 \\ \hline \Delta q_1 \\ \Delta q_2 \\ \hline \Delta q_3 \\ \hline \Delta \lambda_1 \\ \Delta \lambda_2 \end{array} \right\}, \quad (3.65)$$

where

$$m_{33} = (\lambda_1 + rh_1)z_1 + (\lambda_2 + rh_2)z_2 + r(z_1^2 + z_2^2). \quad (3.66)$$

3.4.3 DEFORMABLE-RIGID EQUALITY CONSTRAINT ELEMENT — VERSION 2

Embedding the time stepping algorithm into the Hessian not only causes changes to the implementation of the rigid body elements, but also causes changes to any elements that interface with the rigid elements. Accordingly, the deformable-rigid and rigid-rigid equality constraint elements take on new forms when the embedded dynamics approach is used. The constraint element has degrees of freedom similar to that defined previously, but with the addition of acceleration nodes:

$$\mathbf{s}^e = \langle u_1, u_2, q_1, q_2, q_3, \lambda_1, \lambda_2, \ddot{q}_1, \ddot{q}_2, \ddot{q}_3 \rangle^T. \quad (3.67)$$

The internal force vector for the deformable–rigid constraint element becomes

$$\delta^e \cdot \mathbf{F}^{int,e} = \left\{ \begin{array}{c} \delta u_1 \\ \delta u_2 \\ \hline \delta q_1 \\ \delta q_2 \\ \hline \delta q_3 \\ \hline \delta \lambda_1 \\ \delta \lambda_2 \\ \hline \delta \ddot{q}_1 \\ \delta \ddot{q}_2 \\ \hline \delta \ddot{q}_3 \end{array} \right\}^T \left\{ \begin{array}{c} \lambda_1 + rh_1 \\ \lambda_2 + rh_2 \\ 0 \\ 0 \\ 0 \\ h_1 \\ h_2 \\ -(\lambda_1 + rh_1) \\ -(\lambda_2 + rh_2) \\ z_2(\lambda_1 + rh_1) - z_1(\lambda_2 + rh_2) \end{array} \right\}. \quad (3.68)$$

The consistent tangent of the constraint internal force vector may be found to be

$$\delta^e \cdot \mathbf{K}^e \Delta^e = \left\{ \begin{array}{c} \delta u_1 \\ \delta u_2 \\ \hline \delta q_1 \\ \delta q_2 \\ \hline \delta q_3 \\ \hline \delta \lambda_1 \\ \delta \lambda_2 \\ \hline \delta \ddot{q}_1 \\ \delta \ddot{q}_2 \\ \hline \delta \ddot{q}_3 \end{array} \right\}^T \left[\begin{array}{ccc|ccc|ccc} r & 0 & -r & 0 & rz_2 & 1 & 0 & 0 & 0 & 0 \\ 0 & r & 0 & -r & -rz_1 & 0 & 1 & 0 & 0 & 0 \\ \hline 0 & 0 & 0 & 0 & 0 & 0 & 0 & 0 & 0 & 0 \\ 0 & 0 & 0 & 0 & 0 & 0 & 0 & 0 & 0 & 0 \\ 0 & 0 & 0 & 0 & 0 & 0 & 0 & 0 & 0 & 0 \\ \hline 1 & 0 & -1 & 0 & z_2 & 0 & 0 & 0 & 0 & 0 \\ 0 & 1 & 0 & -1 & -z_1 & 0 & 1 & 0 & 0 & 0 \\ \hline -r & 0 & r & 0 & -rz_2 & -1 & 0 & 0 & 0 & 0 \\ 0 & -r & 0 & r & rz_1 & 0 & -1 & 0 & 0 & 0 \\ rz_2 & -rz_1 & -rz_2 & rz_1 & m_{33} & z_2 & -z_1 & 0 & 0 & 0 \end{array} \right] \left\{ \begin{array}{c} \Delta u_1 \\ \Delta u_2 \\ \hline \Delta q_1 \\ \Delta q_2 \\ \hline \Delta q_3 \\ \hline \Delta \lambda_1 \\ \Delta \lambda_2 \\ \hline \Delta \ddot{q}_1 \\ \Delta \ddot{q}_2 \\ \hline \Delta \ddot{q}_3 \end{array} \right\}. \quad (3.69)$$

3.4.4 RIGID–RIGID EQUALITY CONSTRAINT ELEMENT — VERSION 1

The purpose of this element is to constrain two planar rigid bodies to share a common point in space, throughout time, as shown in FIG. 3.5. This constraint effectively creates a pin joint between the two bodies, where relative planar translation is prohibited and relative planar rotation is allowed.

The constraint element has the element degrees of freedom

$$\mathbf{s}^e = \langle q_1, q_2, q_3, q_4, q_5, q_6, \lambda_1, \lambda_2 \rangle^T, \quad (3.70)$$

where

$$\mathbf{r}^{\Omega_1} = \langle q_1, q_2 \rangle^T, \quad (3.71)$$

$$\theta_3^{\Omega_1} = q_3, \quad (3.72)$$

$$\mathbf{r}^{\Omega_2} = \langle q_4, q_5 \rangle^T, \quad (3.73)$$

$$\theta_3^{\Omega_2} = q_6, \quad (3.74)$$

$$\mathbf{r}^{P_1} = \langle c_1^{P_1}, c_2^{P_1} \rangle^T, \quad (3.75)$$

$$\mathbf{r}^{P_2} = \langle c_1^{P_2}, c_2^{P_2} \rangle^T. \quad (3.76)$$

The constraint equation is written

$$\mathbf{h} = \mathbf{r}^{\Omega_1} + \mathbf{r}^{P_1} - \mathbf{r}^{\Omega_2} - \mathbf{r}^{P_2} = \mathbf{0}. \quad (3.77)$$

Let the following definitions be made:

$$p_1 = c_1^{P_1} \cos q_3 - c_2^{P_1} \sin q_3, \quad (3.78)$$

$$p_2 = c_1^{P_1} \sin q_3 + c_2^{P_1} \cos q_3, \quad (3.79)$$

$$z_1 = c_1^{P_2} \cos q_6 - c_2^{P_2} \sin q_6, \quad (3.80)$$

$$z_2 = c_1^{P_2} \sin q_6 + c_2^{P_2} \cos q_6. \quad (3.81)$$

It may be shown by specialization of the derivation in SECTION A.4 that the element internal force vector and element tangent stiffness matrix have the following form:

$$\delta^e \cdot \mathbf{F}^{int,e} = \left\{ \begin{array}{c} \delta q_1 \\ \delta q_2 \\ \hline \delta q_3 \\ \delta q_4 \\ \delta q_5 \\ \hline \delta q_6 \\ \hline \delta \lambda_1 \\ \delta \lambda_2 \end{array} \right\}^T \left\{ \begin{array}{c} \lambda_1 + rh_1 \\ \lambda_2 + rh_2 \\ \hline -p_2(\lambda_1 + rh_1) + p_1(\lambda_2 + rh_2) \\ -(\lambda_1 + rh_1) \\ -(\lambda_2 + rh_2) \\ \hline z_2(\lambda_1 + rh_1) - z_1(\lambda_2 + rh_2) \\ h_1 \\ h_2 \end{array} \right\}, \quad (3.82)$$

$$\delta^e \cdot \mathbf{K}^e \Delta^e = \left\{ \begin{array}{c} \delta q_1 \\ \delta q_2 \\ \delta q_3 \\ \hline \delta q_4 \\ \delta q_5 \\ \delta q_6 \\ \hline \delta \lambda_1 \\ \delta \lambda_2 \end{array} \right\}^T \left\{ \begin{array}{ccc|ccc|cc} r & 0 & -rp_2 & -r & 0 & rz_2 & 1 & 0 \\ 0 & r & rp_1 & 0 & -r & -rz_1 & 0 & 1 \\ -rp_2 & rp_1 & k_{33} & rp_2 & -rp_1 & f_{33} & -p_2 & p_1 \\ \hline -r & 0 & rp_2 & r & 0 & -rz_2 & -1 & 0 \\ 0 & -r & -rp_1 & 0 & r & rz_1 & 0 & -1 \\ rz_2 & -rz_1 & f_{33} & -rz_2 & rz_1 & m_{33} & z_2 & -z_1 \\ \hline 1 & 0 & -p_2 & -1 & 0 & z_2 & 0 & 0 \\ 0 & 1 & p_1 & 0 & -1 & -z_1 & 0 & 0 \end{array} \right\} \left\{ \begin{array}{c} \Delta q_1 \\ \Delta q_2 \\ \Delta q_3 \\ \hline \Delta q_4 \\ \Delta q_5 \\ \Delta q_6 \\ \hline \Delta \lambda_1 \\ \Delta \lambda_2 \end{array} \right\}, \quad (3.83)$$

where

$$k_{33} = -(\lambda_1 + rh_1)p_1 - (\lambda_2 + rh_2)p_2 + r(p_1^2 + p_2^2), \quad (3.84)$$

$$m_{33} = (\lambda_1 + rh_1)z_1 + (\lambda_2 + rh_2)z_2 + r(z_1^2 + z_2^2), \quad (3.85)$$

$$f_{33} = -r(p_1z_1 + p_2z_2). \quad (3.86)$$

3.4.5 RIGID–RIGID EQUALITY CONSTRAINT ELEMENT — VERSION 2

This constraint element has degrees of freedom similar to that defined previously, but with the addition of acceleration nodes:

$$\mathbf{s}^e = \langle q_1, q_2, q_3, q_4, q_5, q_6, \lambda_1, \lambda_2, \ddot{q}_1, \ddot{q}_2, \ddot{q}_3, \ddot{q}_4, \ddot{q}_5, \ddot{q}_6 \rangle^T. \quad (3.87)$$

The internal force vector has the form

$$\boldsymbol{\delta}^e \cdot \mathbf{F}^{int,e} = \left\{ \begin{array}{c} \delta q_1 \\ \delta q_2 \\ \delta q_3 \\ \hline \delta q_4 \\ \delta q_5 \\ \delta q_6 \\ \hline \delta \lambda_1 \\ \delta \lambda_2 \\ \hline \delta \ddot{q}_1 \\ \delta \ddot{q}_2 \\ \delta \ddot{q}_3 \\ \hline \delta \ddot{q}_4 \\ \delta \ddot{q}_5 \\ \delta \ddot{q}_6 \end{array} \right\}^T \left\{ \begin{array}{c} 0 \\ 0 \\ 0 \\ \hline 0 \\ 0 \\ 0 \\ \hline h_1 \\ h_2 \\ \hline \lambda_1 + rh_1 \\ \lambda_2 + rh_2 \\ \hline -p_2(\lambda_1 + rh_1) + p_1(\lambda_2 + rh_2) \\ -(\lambda_1 + rh_1) \\ -(\lambda_2 + rh_2) \\ \hline z_2(\lambda_1 + rh_1) - z_1(\lambda_2 + rh_2) \end{array} \right\}. \quad (3.88)$$

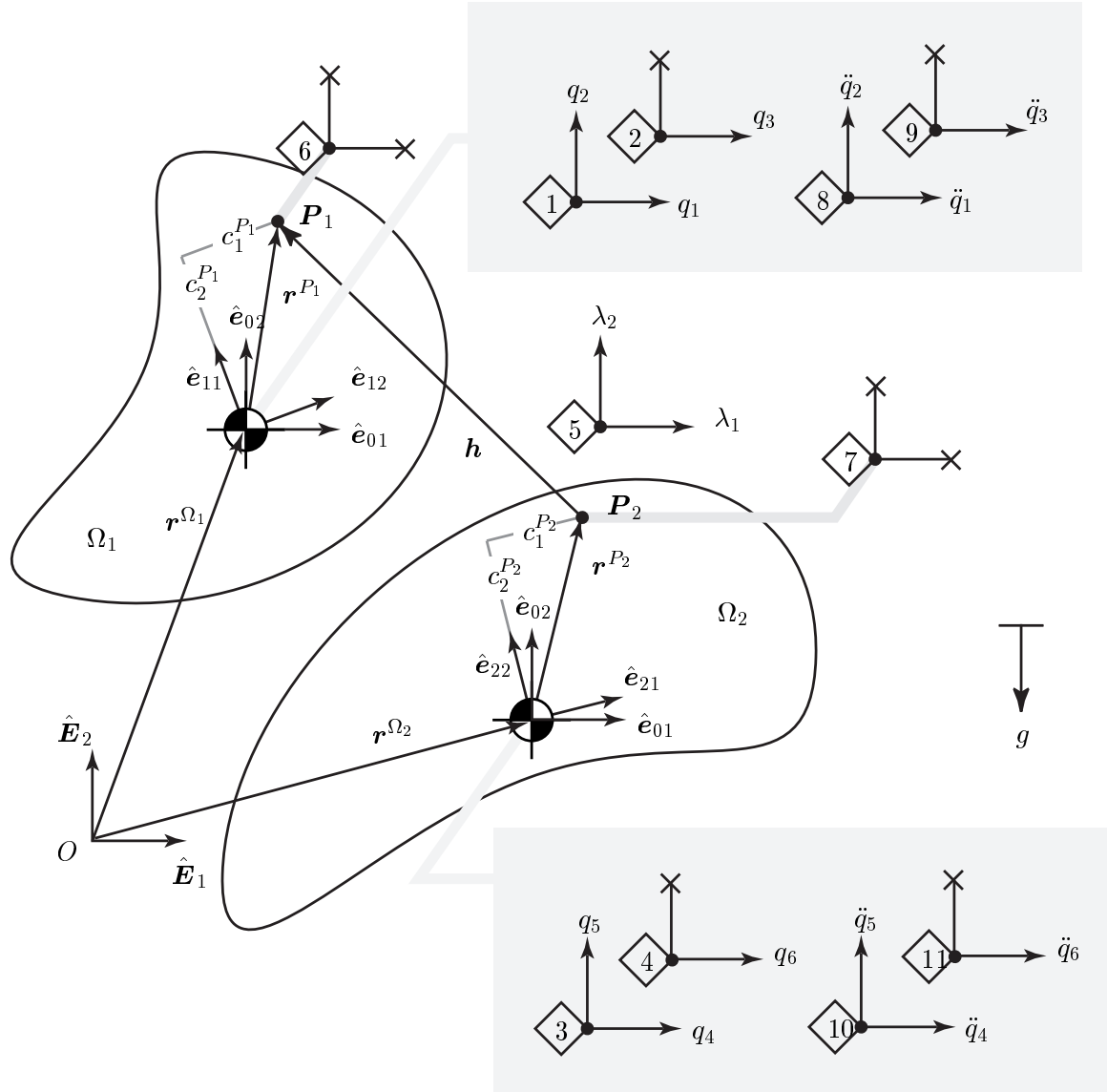


FIGURE 3.5: Two rigid bodies Ω_1 and Ω_2 pinned together such that point P_1 and point P_2 overlap for all time.

The consistent tangent has the form

$$\delta^e \cdot K^e \Delta^e = \left\{ \begin{array}{c} \delta q_1 \\ \delta q_2 \\ \delta q_3 \\ \hline \delta q_4 \\ \delta q_5 \\ \delta q_6 \\ \hline \delta \lambda_1 \\ \delta \lambda_2 \\ \hline \delta \ddot{q}_1 \\ \delta \ddot{q}_2 \\ \delta \ddot{q}_3 \\ \hline \delta \ddot{q}_4 \\ \delta \ddot{q}_5 \\ \delta \ddot{q}_6 \end{array} \right\}^T \left(\begin{array}{ccc|ccc|ccc|ccc} 0 & 0 & 0 & 0 & 0 & 0 & 0 & 0 & 0 & 0 & 0 & 0 \\ 0 & 0 & 0 & 0 & 0 & 0 & 0 & 0 & 0 & 0 & 0 & 0 \\ 0 & 0 & 0 & 0 & 0 & 0 & 0 & 0 & 0 & 0 & 0 & 0 \\ \hline 0 & 0 & 0 & 0 & 0 & 0 & 0 & 0 & 0 & 0 & 0 & 0 \\ 0 & 0 & 0 & 0 & 0 & 0 & 0 & 0 & 0 & 0 & 0 & 0 \\ 0 & 0 & 0 & 0 & 0 & 0 & 0 & 0 & 0 & 0 & 0 & 0 \\ \hline 1 & 0 & -p_2 & -1 & 0 & z_2 & 0 & 0 & 0 & 0 & 0 & 0 \\ 0 & 1 & p_1 & 0 & -1 & -z_1 & 0 & 0 & 0 & 0 & 0 & 0 \\ \hline r & 0 & -rp_2 & -r & 0 & rz_2 & 1 & 0 & 0 & 0 & 0 & 0 \\ 0 & r & rp_1 & 0 & -r & -rz_1 & 0 & 1 & 0 & 0 & 0 & 0 \\ -rp_2 & rp_1 & k_{33} & rp_2 & -rp_1 & f_{33} & -p_2 & p_1 & 0 & 0 & 0 & 0 \\ \hline -r & 0 & rp_2 & r & 0 & -rz_2 & -1 & 0 & 0 & 0 & 0 & 0 \\ 0 & -r & -rp_1 & 0 & r & rz_1 & 0 & -1 & 0 & 0 & 0 & 0 \\ rz_2 & -rz_1 & f_{33} & -rz_2 & rz_1 & m_{33} & z_2 & -z_1 & 0 & 0 & 0 & 0 \end{array} \right) \left\{ \begin{array}{c} \Delta q_1 \\ \Delta q_2 \\ \Delta q_3 \\ \hline \Delta q_4 \\ \Delta q_5 \\ \Delta q_6 \\ \hline \Delta \lambda_1 \\ \Delta \lambda_2 \\ \hline \Delta \ddot{q}_1 \\ \Delta \ddot{q}_2 \\ \Delta \ddot{q}_3 \\ \hline \Delta \ddot{q}_4 \\ \Delta \ddot{q}_5 \\ \Delta \ddot{q}_6 \end{array} \right\}. \quad (3.89)$$

3.4.6 MUSCLE ACTUATOR ELEMENT

The muscle actuator element may be used separately as either a spring or an actuator. These two subclasses share the same element connectivity, shown in FIG. 3.6. A special form of the actuator element allows moments (as opposed to forces) acting between two rigid bodies to be specified: Given a required joint moment, origin and insertion coordinates of the element, and axis about which the moment is generated, this element calculates the appropriate force a to be generated in the element, and applies the force to the two bodies at the origin and insertion. This element is shown in FIG. 3.7. Finally, a special damping element which acts between the centers of masses of two rigid bodies is developed. This damping can help to regularize the high frequencies associated with the constraint elements that serve as pin joints between rigid bodies. Since these pin constraints have “infinite frequencies” associated with them, it makes sense that some type of damping may be advantageous to controlling potential pollution and high frequency divergence of the dynamical system. The damping element is shown in FIG. 3.8.

ELASTIC, ROTATIONALLY NONLINEAR SPRING AND ACTUATOR Let the element state vector be expressed as

$$\mathbf{s}^e = \langle u_1, u_2, u_3, u_4 \rangle^T, \quad (3.90)$$

which stand for the $\hat{\mathbf{E}}_1$ and $\hat{\mathbf{E}}_2$ displacements of node 1 and node 2 (see FIG. 3.6).

By specializing the formulation in CHAPTER 2, the element force vector is found to be

$$\boxed{\delta^e \cdot \mathbf{F}^{int,e} = \left\{ \begin{array}{c} \delta u_1 \\ \delta u_2 \\ \delta u_3 \\ \delta u_4 \end{array} \right\}^T \left\{ \begin{array}{c} -[k(l - L) + a]\hat{t}_1 \\ -[k(l - L) + a]\hat{t}_2 \\ [k(l - L) + a]\hat{t}_1 \\ [k(l - L) + a]\hat{t}_2 \end{array} \right\}}, \quad (3.91)$$

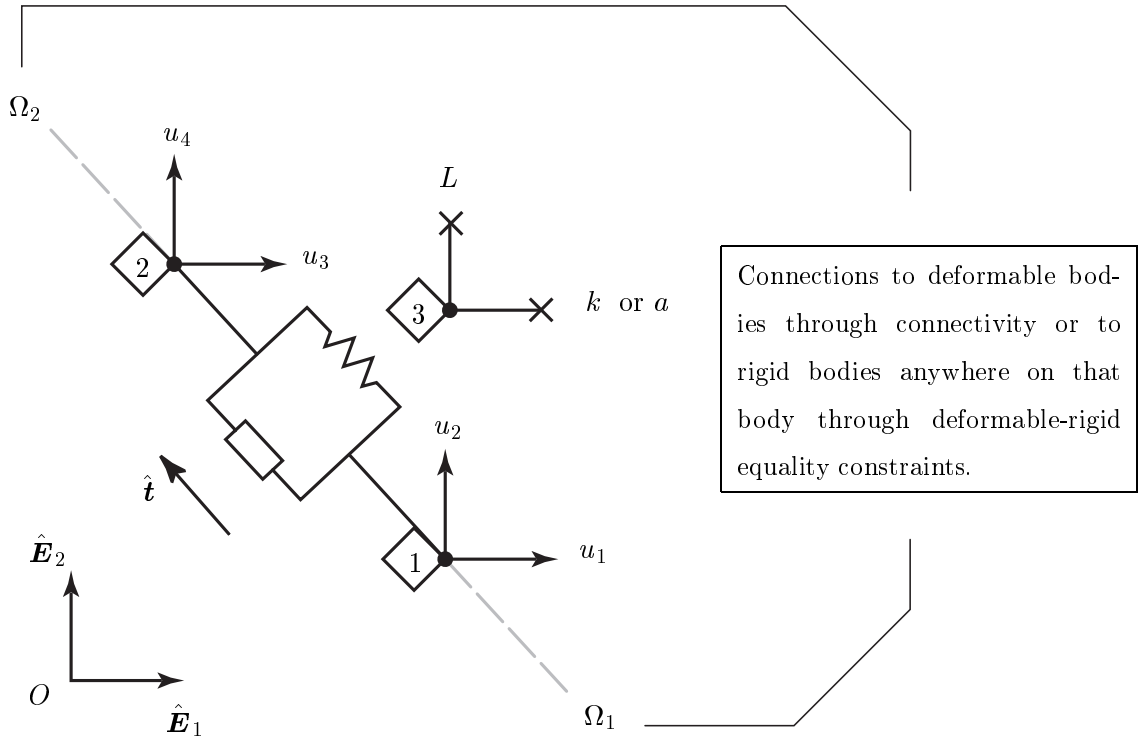


FIGURE 3.6: Muscle actuator element with elastic spring and actuator between two bodies. Bodies may be either deformable or rigid and in any combination.

and the element stiffness matrix is found to be

$$\delta^e \cdot \mathbf{K}^e \Delta^e = \left\{ \begin{array}{c} \delta u_1 \\ \delta u_2 \\ \delta u_3 \\ \delta u_4 \end{array} \right\}^T \left\{ \begin{array}{cccc} k_{11} & k_{12} & -k_{11} & -k_{12} \\ k_{21} & k_{22} & -k_{12} & -k_{22} \\ & k_{11} & k_{12} & \\ & & k_{22} & \end{array} \right\} \left\{ \begin{array}{c} \Delta u_1 \\ \Delta u_2 \\ \Delta u_3 \\ \Delta u_4 \end{array} \right\}, \quad (3.92)$$

where

$$k_{11} = k \left(\hat{t}_1 \hat{t}_1 + \frac{l-L}{l} (1 - \hat{t}_1 \hat{t}_1) \right) + \frac{a}{l} (1 - \hat{t}_1 \hat{t}_1), \quad (3.93)$$

$$k_{12} = k \left(\hat{t}_1 \hat{t}_2 - \frac{l-L}{l} (\hat{t}_1 \hat{t}_2) \right) - \frac{a}{l} (\hat{t}_1 \hat{t}_2), \quad (3.94)$$

$$k_{22} = k \left(\hat{t}_2 \hat{t}_2 + \frac{l-L}{l} (1 - \hat{t}_2 \hat{t}_2) \right) + \frac{a}{l} (1 - \hat{t}_2 \hat{t}_2). \quad (3.95)$$

MOMENT ACTUATOR Consider two rigid bodies Ω_1 and Ω_2 pinned together at point H , as shown in FIG. 3.7. We wish to be able to prescribe the moment m applied between these two

bodies. This is accomplished by specifying the moment magnitude through the prescribed essential boundary condition on node 3. Then this particular element calculates the required force needed to be supplied through the actuator element. The element connectivity allows the hinge point to be located in the reference frame local to Ω_1 through $\mathbf{r}^{\Omega_1} + \mathbf{r}^H$. The moment arm \mathbf{h} is also calculated.

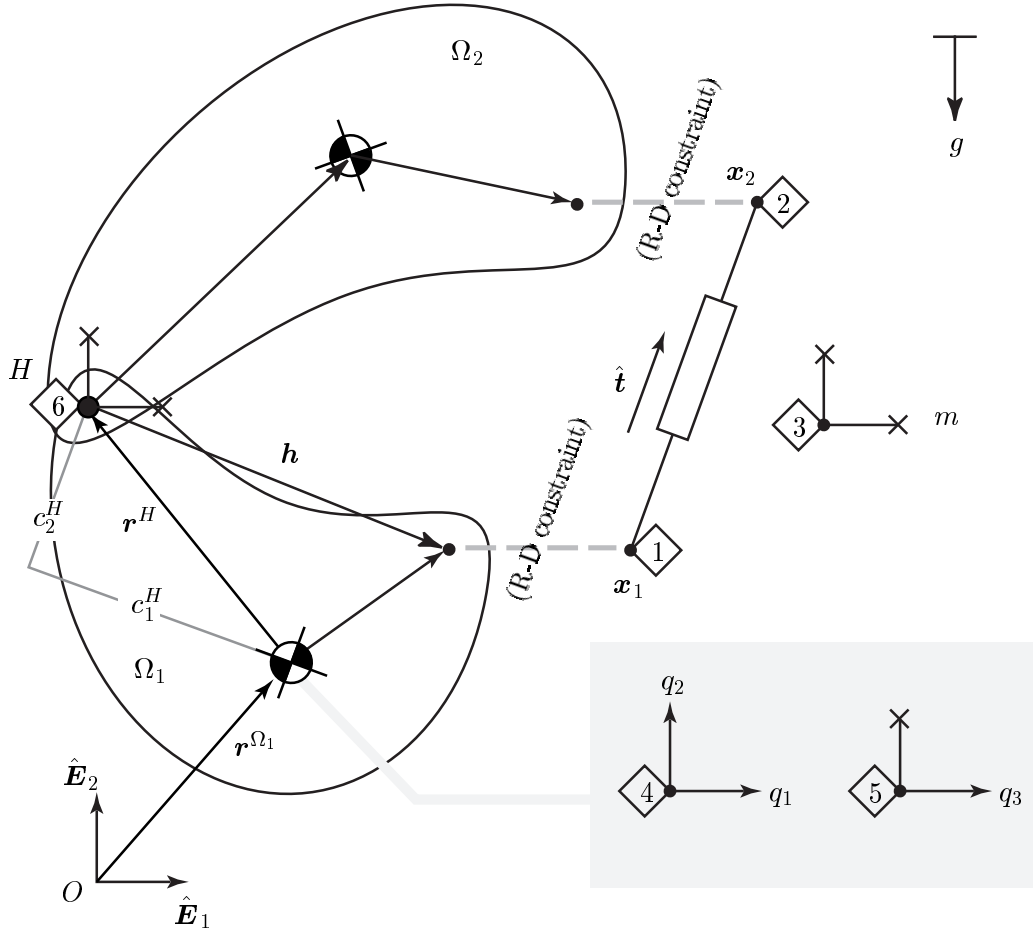


FIGURE 3.7: Muscle actuator element with moment specified between two rigid bodies.

Using the position of the origin of the actuator,

$$\mathbf{h} = \mathbf{x}_1 - \mathbf{r}^{\Omega_1} - \mathbf{r}^H, \quad (3.96)$$

the moment arm can be written in terms of the independent variables \mathbf{u} and \mathbf{q} as

$$\begin{Bmatrix} h_1 \\ h_2 \end{Bmatrix} = \begin{Bmatrix} u_1 + X_1 - q_1 - z_1 \\ u_2 + X_2 - q_2 - z_2 \end{Bmatrix}, \quad (3.97)$$

where \mathbf{z} represents the position of point H in the local Ω_1 reference frame resolved into the global $\hat{\mathbf{E}}$ reference frame through the rotation q_3 :

$$z_1 = c_1^H \cos q_3 - c_2^H \sin q_3, \quad (3.98)$$

$$z_2 = c_1^H \sin q_3 + c_2^H \cos q_3. \quad (3.99)$$

The force in the actuator at node 1 is

$$\mathbf{F} = \begin{Bmatrix} F_1 \\ F_2 \end{Bmatrix} = \begin{Bmatrix} -a\hat{t}_1 \\ -a\hat{t}_2 \end{Bmatrix}. \quad (3.100)$$

Then the moment m (in the out-of-plane direction) produced by the actuator is

$$m = -ah_1\hat{t}_2 + ah_2\hat{t}_1. \quad (3.101)$$

Since m is a prescribed quantity, the actuation level a can be obtained automatically though

$$a = \frac{m}{h_2\hat{t}_1 - h_1\hat{t}_2}.$$

(3.102)

The internal force vector and tangent matrix are then exactly what was presented in Eqs. (3.91)–(3.92).

VISCOELASTIC, ROTATIONALLY NONLINEAR DASHPOT Let the element state vector be expressed as

$$\mathbf{s}^e = \langle q_1, q_2, \dot{q}_1, \dot{q}_2, \ddot{q}_1, \ddot{q}_2, q_4, q_5, \dot{q}_4, \dot{q}_5, \ddot{q}_4, \ddot{q}_5 \rangle^T, \quad (3.103)$$

which stand for the $\hat{\mathbf{E}}_1$ and $\hat{\mathbf{E}}_2$ displacements, velocities, and accelerations of node 1 and node 2 (see FIG. 3.8).

By specializing the formulation in CHAPTER 2, the element force vector is found to be

$$\delta^e \cdot \mathbf{F}^{int,e} = \langle \delta q_1, \delta q_2, \delta \dot{q}_1, \delta \dot{q}_2, \delta \ddot{q}_1, \delta \ddot{q}_2, \mid \delta q_4, \delta q_5, \delta \dot{q}_4, \delta \dot{q}_5, \delta \ddot{q}_4, \delta \ddot{q}_5 \rangle$$

$$\langle 0, 0, 0, 0, -c \dot{l} \hat{t}_1, -c \dot{l} \hat{t}_2, \mid 0, 0, 0, 0, c \dot{l} \hat{t}_1, c \dot{l} \hat{t}_2, \rangle^T$$

(3.104)

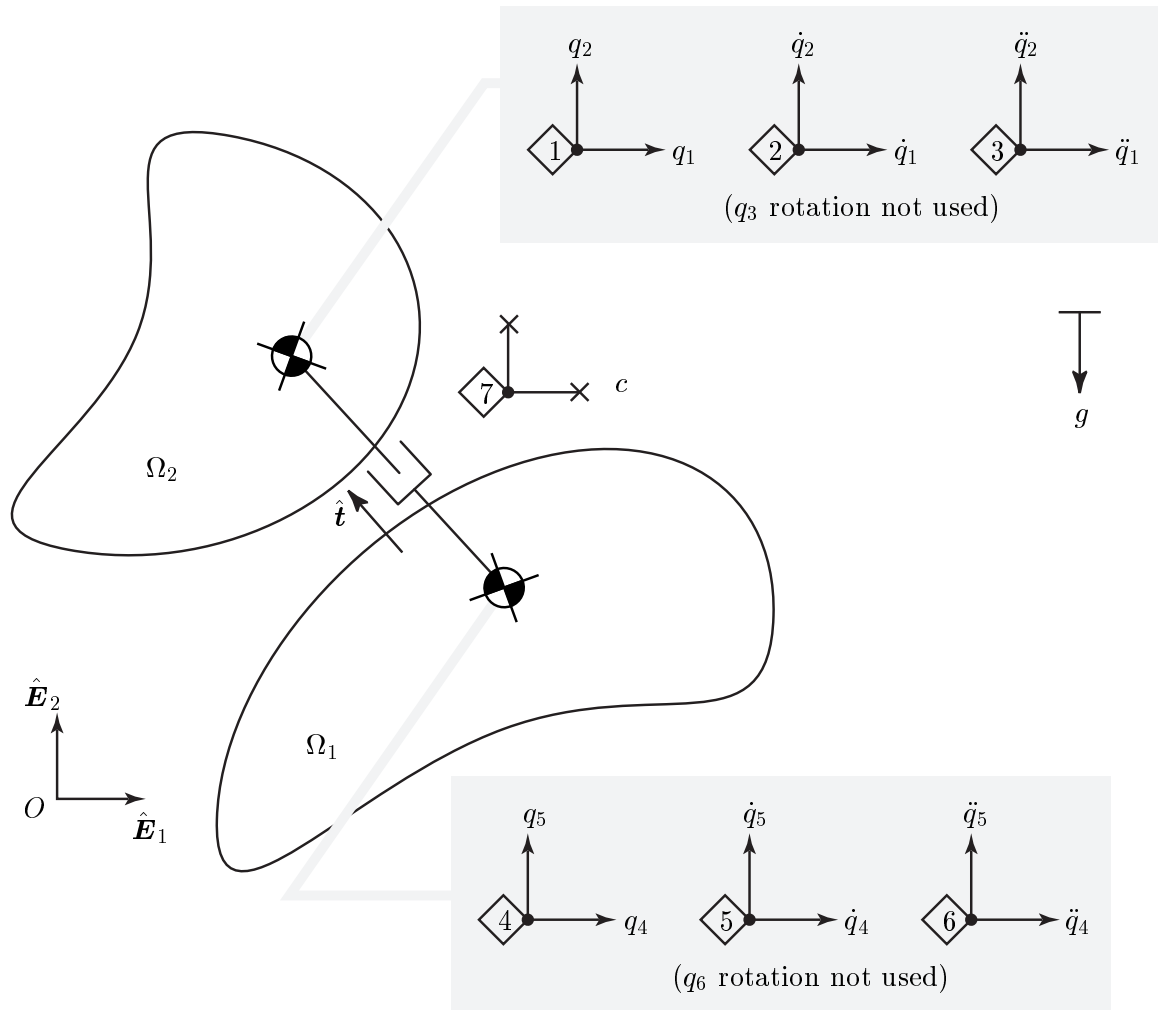


FIGURE 3.8: Muscle actuator element with viscous dashpot between two rigid body elements (embedded formulation).

The element stiffness matrix has the form

$$\delta^e \cdot \mathbf{K}^e \Delta^e = \left\{ \begin{array}{c} \delta q_1 \\ \delta q_2 \\ \delta \dot{q}_1 \\ \delta \dot{q}_2 \\ \delta \ddot{q}_1 \\ \delta \ddot{q}_2 \\ \delta q_4 \\ \delta q_5 \\ \delta \dot{q}_4 \\ \delta \dot{q}_5 \\ \delta \ddot{q}_4 \\ \delta \ddot{q}_5 \end{array} \right\}^T \left(\begin{array}{cc|cc|cc|cc|cc} 0 & 0 & 0 & 0 & 0 & 0 & 0 & 0 & 0 & 0 & 0 & 0 \\ 0 & 0 & 0 & 0 & 0 & 0 & 0 & 0 & 0 & 0 & 0 & 0 \\ 0 & 0 & 0 & 0 & 0 & 0 & 0 & 0 & 0 & 0 & 0 & 0 \\ 0 & 0 & 0 & 0 & 0 & 0 & 0 & 0 & 0 & 0 & 0 & 0 \\ \beta_{11} & \beta_{12} & \gamma_{11} & \gamma_{12} & 0 & 0 & -\beta_{11} & -\beta_{12} & -\gamma_{11} & -\gamma_{12} & 0 & 0 \\ \beta_{21} & \beta_{22} & \gamma_{21} & \gamma_{22} & 0 & 0 & -\beta_{21} & -\beta_{22} & -\gamma_{21} & -\gamma_{22} & 0 & 0 \\ \hline 0 & 0 & 0 & 0 & 0 & 0 & 0 & 0 & 0 & 0 & 0 & 0 \\ 0 & 0 & 0 & 0 & 0 & 0 & 0 & 0 & 0 & 0 & 0 & 0 \\ 0 & 0 & 0 & 0 & 0 & 0 & 0 & 0 & 0 & 0 & 0 & 0 \\ 0 & 0 & 0 & 0 & 0 & 0 & 0 & 0 & 0 & 0 & 0 & 0 \\ -\beta_{11} & -\beta_{12} & -\gamma_{11} & -\gamma_{12} & 0 & 0 & \beta_{11} & \beta_{12} & \gamma_{11} & \gamma_{12} & 0 & 0 \\ -\beta_{21} & -\beta_{22} & -\gamma_{21} & -\gamma_{22} & 0 & 0 & \beta_{21} & \beta_{22} & \gamma_{21} & \gamma_{22} & 0 & 0 \end{array} \right) \left\{ \begin{array}{c} \Delta q_1 \\ \Delta q_2 \\ \Delta \dot{q}_1 \\ \Delta \dot{q}_2 \\ \Delta \ddot{q}_1 \\ \Delta \ddot{q}_2 \\ \Delta q_4 \\ \Delta q_5 \\ \Delta \dot{q}_4 \\ \Delta \dot{q}_5 \\ \Delta \ddot{q}_4 \\ \Delta \ddot{q}_5 \end{array} \right\}, \quad (3.105)$$

where

$$[\boldsymbol{\beta}]_{(4 \times 4)} = c \left[\frac{1}{l} [\hat{\mathbf{t}} \otimes (-\dot{\mathbf{u}}_1 + \dot{\mathbf{u}}_2)] [\mathbf{1} - \hat{\mathbf{t}} \otimes \hat{\mathbf{t}}] + \frac{i}{l} [\mathbf{1} - \hat{\mathbf{t}} \otimes \hat{\mathbf{t}}] \right], \quad (3.106)$$

$$[\boldsymbol{\gamma}]_{(4 \times 4)} = c [\hat{\mathbf{t}} \otimes \hat{\mathbf{t}}]. \quad (3.107)$$

3.5 INEQUALITY CONSTRAINTS

This section discusses the interaction of deformable and rigid bodies in the presence of unilateral contact constraints, as implemented in a finite element code.

The deformable-rigid inequality constraint element is examined. The interface Γ_c , where potential contact between the deformable and rigid body may occur, represents the intersection of $\partial\Omega_D$ belonging to the deformable body and $\partial\Omega_R$ belonging to the rigid body. The surface $\partial\Omega_D$ is composed of striker nodes, which belong to the boundary of the deformable body. The surface $\partial\Omega_R$ is considered the target.

The gap distance between the two bodies is then measured discretely between each striker node and the target surface. The first and second variations of the gap distance are needed to construct the variational and linearized forms of the virtual work contributions arising from contact interactions. The internal force vector and tangent matrix are given for the particular case of a two-dimensional large slip contact element describing frictionless interactions between a deformable body and a rigid body. The rigid body, and thus its boundary, may move in time according to the dynamics of the body; or, it may be stationary.

3.5.1 GEOMETRIC PRELIMINARIES

The development of a unilateral, large-slip contact element requires additional steps not used with the holonomic constraint contact elements of SECTION 3.4 nor needed with unilateral node-on-node or node-on-surface contact elements. Much of this extra work entails the geometric description of the contact surface.

GEOMETRIC DESCRIPTION OF THE TARGET SURFACE Consider in abstraction a curve \mathcal{C} in two space dimensions and a point located along the curve $\mathbf{y} \in \mathbb{R}^2$, as shown in FIG. 3.9. The location of \mathbf{y} along the curve is parameterized by the scalar $\xi \in \mathcal{P}$ much like the shape functions of standard finite elements. The curve may be viewed as a mapping such that $\mathbf{y} : \mathcal{P} \subset \mathbb{R} \mapsto \mathcal{C} \subset \mathbb{R}^2$. For any point located by \mathbf{y} , a tangent $\mathbf{t}(\xi)$ and unit normal vector $\hat{\mathbf{n}}(\xi)$ may be defined.

From geometric considerations, the tangent vector \mathbf{t} is the derivative of the projection

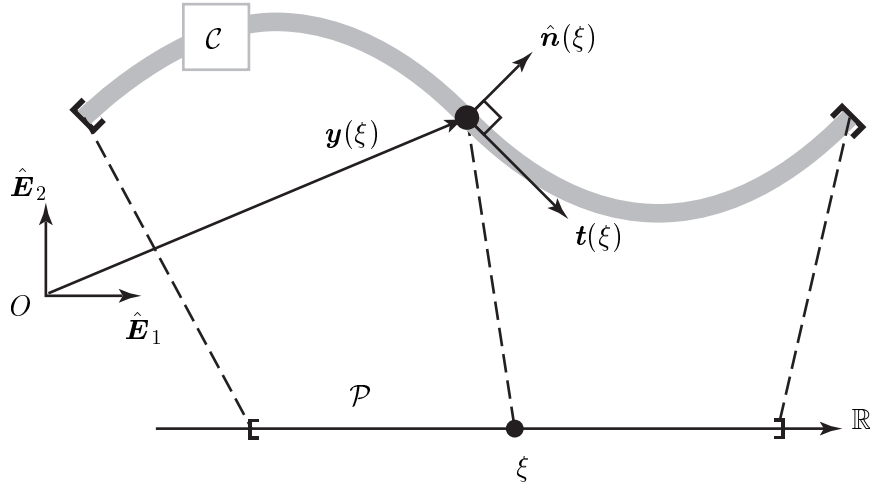


FIGURE 3.9: A two dimensional curve $\mathcal{C} \in \mathbb{R}^2$ parameterized by $\xi \in \mathbb{R}$. A point along that curve is located by $\mathbf{y}(\xi) \in \mathbb{R}^2$ as measured in the \mathbf{E} basis.

with respect to the ξ parameter,

$$\mathbf{t}(\xi) = \frac{\partial \mathbf{y}(\xi)}{\partial \xi}. \quad (3.108)$$

The unit normal vector $\hat{\mathbf{n}}$ is constructed from

$$\hat{\mathbf{n}}(\xi) = \frac{\hat{\mathbf{e}}_3 \times \mathbf{t}(\xi)}{\| \hat{\mathbf{e}}_3 \times \mathbf{t}(\xi) \|}, \quad (3.109)$$

where $\hat{\mathbf{e}}_3$ is the out-of-plane unit normal vector (sometimes called the bi-normal vector).

CLOSEST POINT PROJECTION Consider now a point $\varphi_s \in \mathbb{R}^2$, later to be called the striker node when the contact finite element is discussed, shown in FIG. 3.10. We are interested in finding the value of ξ such that the projection of the stiker node on the curve \mathcal{C} , called $\mathbf{y}_c(\xi)$, is minimized, *viz.*,

$$\xi_c(\varphi_s) = \underset{\xi \in \mathcal{P}}{\operatorname{argmin}} \| \mathbf{y}_c(\xi) - \varphi_s \|, \quad (3.110)$$

which locates the position on \mathcal{C} at ξ_c from φ_s .

This relationship, given a particular point φ_s of interest, is used in determining where φ_s will first touch the contact surface \mathcal{C} . In general, a closed-form solution to Eq. (3.110) does not exist. As a consequence, the solution must be found numerically. Toward this end,

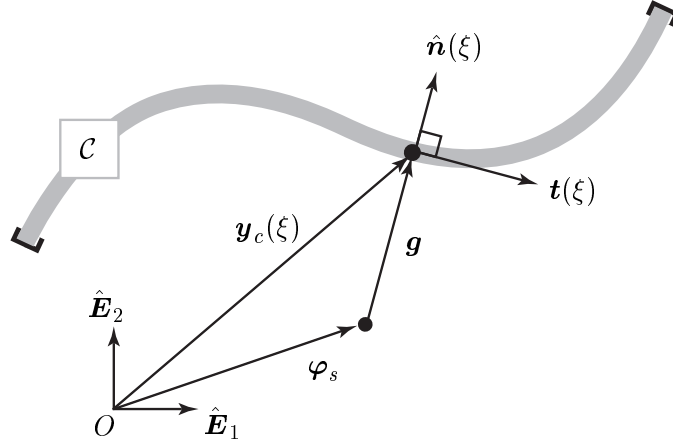


FIGURE 3.10: Construction of the closest point projection.

a gap vector \mathbf{g} is defined,

$$\mathbf{g} = \mathbf{g}(\varphi_s, \xi) = \mathbf{y}_c - \varphi_s = \mathbf{y}(\xi_c(\varphi_s)) - \varphi_s. \quad (3.111)$$

An equivalent problem to Eq. (3.110) is then stated

$$\xi_c(\varphi_s) = \min_{\xi \in \mathcal{P}} \left(\frac{1}{2} \| \mathbf{g} \|^2 \right) = \min_{\xi \in \mathcal{P}} \left(\frac{1}{2} g_n^2 \right). \quad (3.112)$$

The squared norm of the gap vector (of the square of its length) is related to the signed contact distance g_n through

$$g_n = g_n(\varphi, \xi) = \mathbf{g}(\xi_c(\varphi_s)) \cdot \hat{\mathbf{n}}(\xi_c(\varphi_s)). \quad (3.113)$$

The problem in Eq. (3.112) has a minimum when the first derivative is equal to zero

$$\frac{1}{2} \nabla_\xi \| \mathbf{g}(\xi) \|^2 = 0, \quad (3.114)$$

and the second derivative is greater than zero

$$\frac{1}{2} \nabla_\xi^2 \| \mathbf{g}(\xi) \|^2 > 0. \quad (3.115)$$

Equivalent forms of these two foregoing expressions may be found to be [47]

$$\frac{1}{2} \nabla_\xi \| \mathbf{g}(\xi) \|^2 = \mathbf{t} \cdot \mathbf{g}, \quad (3.116)$$

$$\frac{1}{2} \nabla_\xi^2 \| \mathbf{g}(\xi) \|^2 = \mathbf{t}_{,\xi} \cdot \mathbf{g} + \mathbf{t} \cdot \mathbf{t}. \quad (3.117)$$

A Newton-Raphson procedure is used to iteratively find the value of ξ_c such that Eq. (3.112) is satisfied. Let (k) represent the iteration number. Then we search for values of $\xi^{(k+1)}$ such that Eq. (3.114) is equal to zero, *viz.*,

$$\underbrace{\nabla_\xi \frac{1}{2} \| \mathbf{g}(\xi^{(k+1)}) \|^2}_{\text{set}=0} = \nabla_\xi \frac{1}{2} \| \mathbf{g}(\xi^{(k)}) \|^2 + \nabla_\xi^2 \frac{1}{2} \| \mathbf{g}(\xi^{(k)}) \|^2 \Delta\xi^{(k)} + \text{H.O.T.} \quad (3.118)$$

Solving for $\Delta\xi^{(k)}$ gives

$$\Delta\xi^{(k)} = \xi^{(k+1)} - \xi^{(k)} = \frac{1}{2} \left[\nabla_\xi^2 \| \mathbf{g}(\xi^{(k)}) \|^2 \right]^{-1} \left(\frac{1}{2} \nabla_\xi \| \mathbf{g}(\xi^{(k)}) \|^2 \right). \quad (3.119)$$

Rearranging and substituting Eqs. (3.116)–(3.117) gives

$$\xi^{(k+1)} = \xi^{(k)} - \frac{\mathbf{t} \cdot \mathbf{g}}{\mathbf{t}_{,\xi} \cdot \mathbf{g} + \mathbf{t} \cdot \mathbf{t}}. \quad (3.120)$$

This update is continued until the first derivative in Eq. (3.116) is equal to zero to within some small tolerance. The converged value of $\xi^{(k+1)}$ is then set equal to ξ_c . In practice, the Newton-Raphson scheme for finding ξ_c works well. It is possible in theory, however, for this approach to find the maximum rather than the minimum projection. An example is discussed in [47].

INTERPOLATION OF THE TARGET SURFACE We define a curve \mathbf{s} interpolated with parameter ξ weighted by coefficients $\mathbf{a}_0, \mathbf{a}_1, \mathbf{a}_2, \mathbf{a}_3$ such that

$$\mathbf{s}(\xi) = \mathbf{a}_0 + \mathbf{a}_1 \xi + \mathbf{a}_2 \xi^2 + \mathbf{a}_3 \xi^3 \in \mathbb{R}^2. \quad (3.121)$$

We want to find values of \mathbf{a}_i such that the curve \mathbf{s} goes through four points $\mathbf{p}_0, \mathbf{p}_1, \mathbf{p}_2, \mathbf{p}_3$, as shown in FIG. 3.11.

To accomplish this interpolation, the following four boundary conditions are set on \mathbf{s}

$$\mathbf{s}(\xi = 0) = \mathbf{a}_0 \stackrel{\text{set}}{=} \mathbf{p}_1, \quad (3.122)$$

$$\mathbf{s}(\xi = 1) = \mathbf{a}_0 + \mathbf{a}_1 + \mathbf{a}_2 + \mathbf{a}_3 \stackrel{\text{set}}{=} \mathbf{p}_2, \quad (3.123)$$

$$\mathbf{s}'(\xi = 0) = \mathbf{a}_1 \stackrel{\text{set}}{=} \alpha(\mathbf{p}_2 - \mathbf{p}_0), \quad (3.124)$$

$$\mathbf{s}'(\xi = 1) = \mathbf{a}_1 + 2\mathbf{a}_2 + 3\mathbf{a}_3 \stackrel{\text{set}}{=} \alpha(\mathbf{p}_3 - \mathbf{p}_1). \quad (3.125)$$

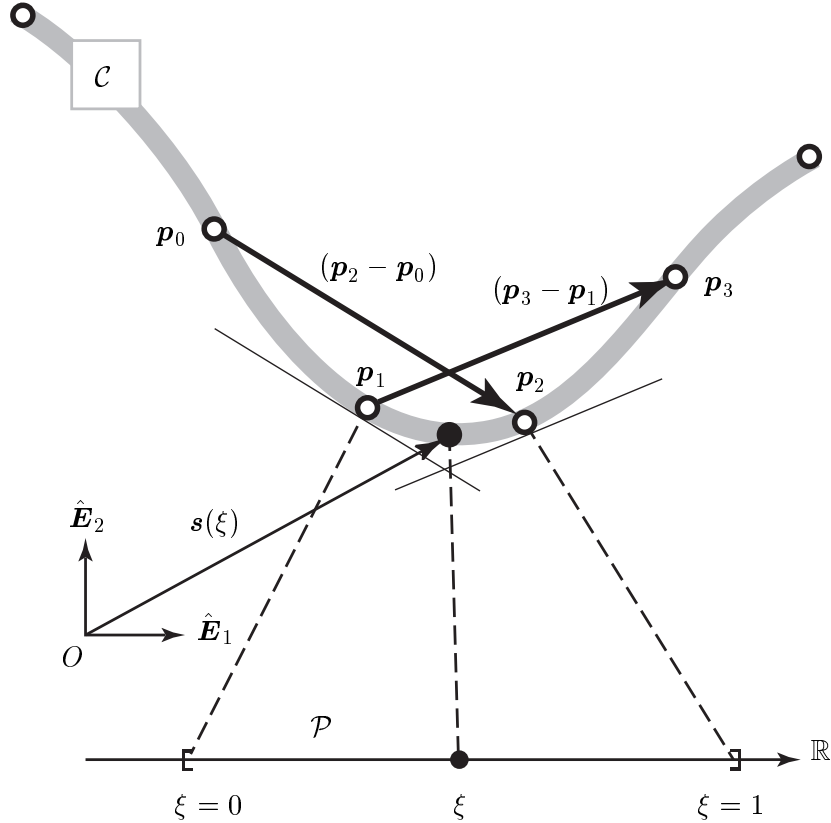


FIGURE 3.11: The target boundary between two points \mathbf{p}_1 and \mathbf{p}_2 on Γ_c use two additional points, \mathbf{p}_0 and \mathbf{p}_3 , for construction of the tangents in the Hermite interpolation.

The constant $\alpha \in (0, 1]$ is used to scale the tangent, causing the line connecting points \mathbf{p}_1 and \mathbf{p}_2 to vary from flattened to pointed, respectively, as shown in FIG. 3.12. Solving for the \mathbf{a}_i coefficients in terms of the \mathbf{p}_i points gives the following result

$$\left\{ \begin{array}{c} \mathbf{a}_0 \\ \mathbf{a}_1 \\ \mathbf{a}_2 \\ \mathbf{a}_3 \end{array} \right\} = \left[\begin{array}{cccc} \mathbf{0} & \mathbf{1} & \mathbf{0} & \mathbf{0} \\ -\alpha\mathbf{1} & \mathbf{0} & \alpha\mathbf{1} & \mathbf{0} \\ 2\alpha\mathbf{1} & (-3 + \alpha)\mathbf{1} & (3 - 2\alpha)\mathbf{1} & -\alpha\mathbf{1} \\ -\alpha\mathbf{1} & (2 - \alpha)\mathbf{1} & (-2 + \alpha)\mathbf{1} & \alpha\mathbf{1} \end{array} \right] \left\{ \begin{array}{c} \mathbf{p}_0 \\ \mathbf{p}_1 \\ \mathbf{p}_2 \\ \mathbf{p}_3 \end{array} \right\}. \quad (3.126)$$

This matrix is necessary during finite element implementation to construct \mathbf{s} in Eq. (3.121) from known points \mathbf{p}_i along the boundary Γ_c .

It may be shown, for example in [47, 48], that the Hermite interpolation used to construct \mathbf{s} results in curves which have first derivatives (tangents) that are continuous at any

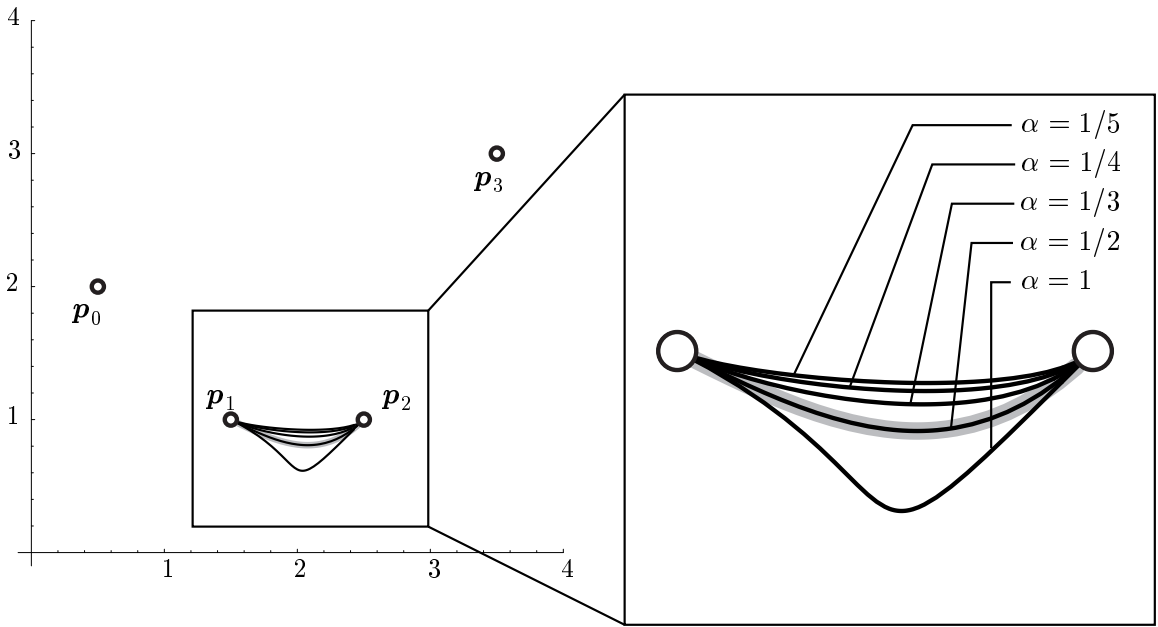


FIGURE 3.12: Interpolation of the target surface through points $(0.5, 2.0)$, $(1.5, 1.0)$, $(2.5, 1.0)$, $(3.5, 3.0)$ with Hermite polynomials and tangent scaling parameter α .

point \mathbf{p}_i , *viz.*,

$$\mathbf{s}'_{(-)}(\xi = 1) = \mathbf{s}'_{(+)}(\xi = 0). \quad (3.127)$$

The second derivatives of \mathbf{s} , representing the radius of curvature, will not, in general, be continuous at each point \mathbf{p}_i .

3.5.2 DEFORMABLE-RIGID INEQUALITY CONSTRAINT ELEMENT — VERSION 1

It may be shown by specialization of the derivation in SECTION A.5 that the element internal force vector is written

$$\underbrace{\delta^e \cdot \mathbf{F}^{int,e}}_{(\text{contact})} = \left\{ \begin{array}{c} \frac{\delta u_1}{\delta q_1} \\ \frac{\delta u_2}{\delta q_2} \\ \frac{\delta q_1}{\delta q_3} \\ \frac{\delta q_2}{\delta \lambda} \end{array} \right\}^T \left\{ \begin{array}{c} -n_1(\lambda + rg_n) \\ -n_2(\lambda + rg_n) \\ n_1(\lambda + rg_n) \\ n_2(\lambda + rg_n) \\ \zeta(\lambda + rg_n) \\ \boxed{g_n} \end{array} \right\}. \quad (3.128)$$

More detail regarding the definition of variables such as n_1 and ζ may be found by consulting Box A.3. In the case where the status is in gap instead of contact, the above entries are all zero except for the boxed quantity $[g_n]$. In the case of gap status, this boxed quantity becomes $-\lambda/r$ where $r > 0$.

Because the second variation is relatively complicated, the form but not the specific entries of the Hessian are provided here. These specific entries may be obtained in SECTION A.5, BOX A.6.

$$\underbrace{\delta^e \cdot K^e \Delta^e}_{(\text{contact})} = \left\{ \begin{array}{c} \delta u_1 \\ \delta u_2 \\ \hline \delta q_1 \\ \delta q_2 \\ \hline \delta q_3 \\ \hline \delta \lambda \end{array} \right\}^T \left\{ \begin{array}{cc|ccc|c} k_{11} & k_{12} & -k_{11} & -k_{12} & k_{15} & -\hat{n}_1 \\ k_{12} & k_{22} & -k_{12} & -k_{22} & k_{25} & -\hat{n}_2 \\ \hline -k_{11} & -k_{12} & k_{11} & k_{12} & -k_{15} & \hat{n}_1 \\ -k_{12} & -k_{22} & k_{12} & k_{22} & -k_{25} & \hat{n}_2 \\ \hline k_{15} & k_{25} & -k_{15} & -k_{25} & k_{55} & \zeta \\ \hline -\hat{n}_1 & -\hat{n}_2 & \hat{n}_1 & \hat{n}_2 & \zeta & \boxed{0} \end{array} \right\} \left\{ \begin{array}{c} \Delta u_1 \\ \Delta u_2 \\ \hline \Delta q_1 \\ \Delta q_2 \\ \hline \Delta q_3 \\ \hline \Delta \lambda \end{array} \right\}. \quad (3.129)$$

The above Hessian describes contact status. In the case of gap status, all entries in the Hessian are zero except for the boxed $\boxed{0}$ in Eq. (3.129). In the case of gap status, the boxed quantity becomes $-1/r$ where $r > 0$.

3.5.3 DEFORMABLE-RIGID INEQUALITY CONSTRAINT ELEMENT — VERSION 2

The version of deformable-rigid inequality constraint element for contact has another version if the rigid elements being used are of the embedded dynamics form. For this case, the first

variation is written

$$\underbrace{\delta^e \cdot \mathbf{F}^{int,e}}_{(contact)} = \left\{ \begin{array}{c} \delta u_1 \\ \delta u_2 \\ \hline \delta q_1 \\ \delta q_2 \\ \hline \delta q_3 \\ \hline \delta \lambda \\ \hline \delta \ddot{q}_1 \\ \delta \ddot{q}_2 \\ \hline \delta \ddot{q}_3 \end{array} \right\}^T \left\{ \begin{array}{c} -n_1(\lambda + rg_n) \\ -n_2(\lambda + rg_n) \\ \hline 0 \\ 0 \\ \hline 0 \\ \hline g_n \\ \hline n_1(\lambda + rg_n) \\ n_2(\lambda + rg_n) \\ \hline \zeta(\lambda + rg_n) \end{array} \right\}. \quad (3.130)$$

The second variation is written

$$\underbrace{\delta^e \cdot \mathbf{K}^e \Delta^e}_{(contact)} = \left\{ \begin{array}{c} \delta u_1 \\ \delta u_2 \\ \hline \delta q_1 \\ \delta q_2 \\ \hline \delta q_3 \\ \hline \delta \lambda \\ \hline \delta \ddot{q}_1 \\ \delta \ddot{q}_2 \\ \hline \delta \ddot{q}_3 \end{array} \right\}^T \left\{ \begin{array}{ccc|ccc|ccc} k_{11} & k_{12} & -k_{11} & -k_{12} & k_{15} & -\hat{n}_1 & 0 & 0 & 0 \\ k_{12} & k_{22} & -k_{12} & -k_{22} & k_{25} & -\hat{n}_2 & 0 & 0 & 0 \\ \hline 0 & 0 & 0 & 0 & 0 & 0 & 0 & 0 & 0 \\ 0 & 0 & 0 & 0 & 0 & 0 & 0 & 0 & 0 \\ 0 & 0 & 0 & 0 & 0 & 0 & 0 & 0 & 0 \\ \hline -\hat{n}_1 & -\hat{n}_2 & \hat{n}_1 & \hat{n}_2 & \zeta & \boxed{0} & 0 & 0 & 0 \\ -k_{11} & -k_{12} & k_{11} & k_{12} & -k_{15} & \hat{n}_1 & 0 & 0 & 0 \\ -k_{12} & -k_{22} & k_{12} & k_{22} & -k_{25} & \hat{n}_2 & 0 & 0 & 0 \\ \hline k_{15} & k_{25} & -k_{15} & -k_{25} & k_{55} & \zeta & 0 & 0 & 0 \end{array} \right\} \left\{ \begin{array}{c} \Delta u_1 \\ \Delta u_2 \\ \hline \Delta q_1 \\ \Delta q_2 \\ \hline \Delta q_3 \\ \hline \Delta \lambda \\ \hline \Delta \ddot{q}_1 \\ \Delta \ddot{q}_2 \\ \hline \Delta \ddot{q}_3 \end{array} \right\}. \quad (3.131)$$

The explanation of boxed quantities, $\boxed{(\bullet)}$, for Version 1 of the contact element applies here as well.

In FIG. 3.13, a rigid body is shown in its current configuration rotated 20 degrees with respect to the inertial reference frame. The rigid body has degrees of freedom q_1 and q_2 (translations) and q_3 (planar rotation). The position \mathbf{r}^{Ω_2} locates the rigid body mass center. A portion of the boundary of Ω_R defines the target contact surface \mathcal{C} . Points \mathbf{P}_i are used to interpolate the surface. Coordinates local to the rigid body frame, $c_1^{P_i}$ and $c_2^{P_i}$, locate a particular interpolation point \mathbf{P}_i . A portion of a deformable body finite element mesh is shown with the current position of a striker node located with φ^{P_1} with associated

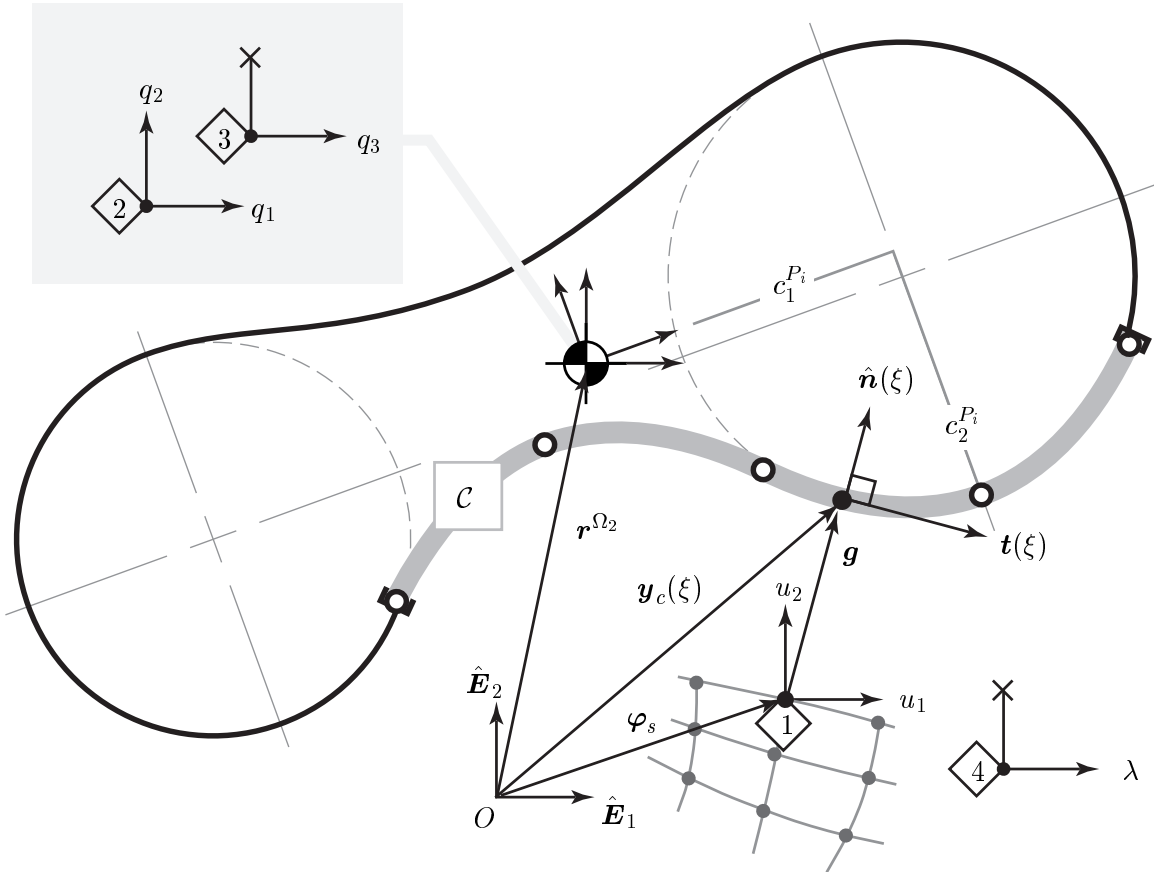


FIGURE 3.13: Two-dimensional contact element.

translational degrees of freedom u_1 and u_2 . The gap vector from the striker node to the target surface is denoted \mathbf{g} and the closest point projection is located in the inertial frame by the vector $\mathbf{y}_c(\xi)$.

The contact element implemented in TACT looks for the closest node on the target surface, then determines which facet the striker will be projected upon. Next the closest point projection to the Hermite-interpolated surface is found through the Newton scheme described through Eqs. (3.118)–(3.119).

CHAPTER 4

BIOMECHANICAL MODELS

4.1 OVERVIEW

The coupled deformable-rigid implementation is now applied to biomechanical models of human gait. Gait is selected over other forms of movement because it is the most common activity of humans. A typical human will take about one million gait cycles in a year [92, 104]. This million cycle number is an average used in many studies of arthroplasty wear [66, 77, 78].

The gait cycle projected into the sagittal plane is illustrated in FIG. 4.1. Though the beginning of a gait cycle is arbitrary in its designation, the end of one complete gait cycle necessarily occurs when the position of the body matches the configuration at the beginning of the gait cycle. Gait may be subdivided into four consecutive intervals, designated as right leg swing (RSW), left and right leg double-stance (DS), right leg stance (RST), and double-stance again, as shown in FIG. 4.1. It may be noted that right leg swing (RSW) is equivalent to left leg stance (LST). Similarly, (RST) is equivalent to (LSW). Walking at a typical 1.3 m/s (roughly 3 mph), the stance phases (both single and double) of gait account for 62% of the total gait cycle. The single-swing phase accounts for the remaining 38% of the cycle [97]. These percentages, however, depend on walking speed. A normal distribution of floor contact periods has been found to be stance for 60% and swing for 40% of the gait cycle. The stance is further decomposed into two 10% intervals of double-stance and one 40% interval of single-stance. Details may be found in [97].

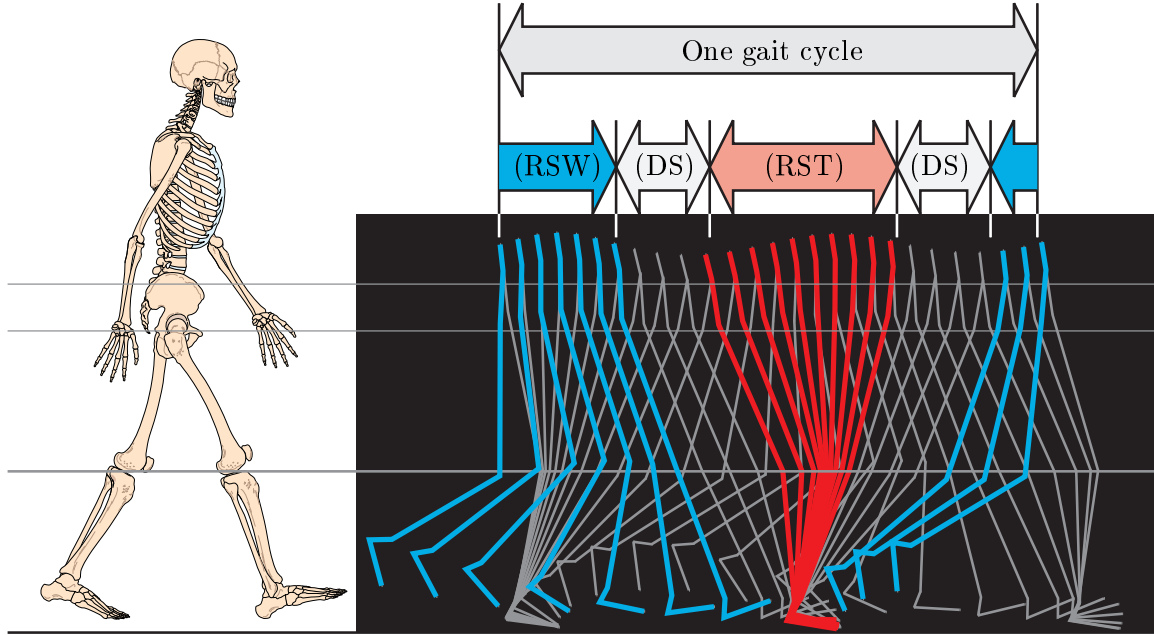


FIGURE 4.1: One complete human gait cycle and its subdivisions into (RSW) right leg swing, (DS) double-stance, (RST) right leg single-stance, (DS) double-stance.

We will model a ballistic gait cycle shown in FIG. 4.2, which represents a simplification of the human gait cycle shown in FIG. 4.1. The origins and variations of the ballistic gait model may be traced through Mochon [85]. The ballistic model in FIG. 4.2 has two rigid legs and a rigid head-arms-trunk (HAT). Revolute joints attach the stance leg to the ground, the HAT to the stance leg, and the swing leg to the HAT. The model moves in the sagittal plane, thus the model is two-dimensional. Most of the motion during gait occurs in the sagittal plane, though gait contains many features such as pelvic list and rotation which occur outside of this plane [57, 97].

4.2 MODEL CLASSIFICATION

We use four variations of a ballistic gait model, as summarized in TAB. 4.1. Among these four models, the two most defining features are (1) the presence or absence of a deformable hip joint, and (2) the presence or absence of muscles. Models that are composed of purely rigid bodies are designated **M1** and **M3**. Models that couple the rigid body dynamics of gait to the stress and deformation of a hip joint are labeled **M2** and **M4**. Models without

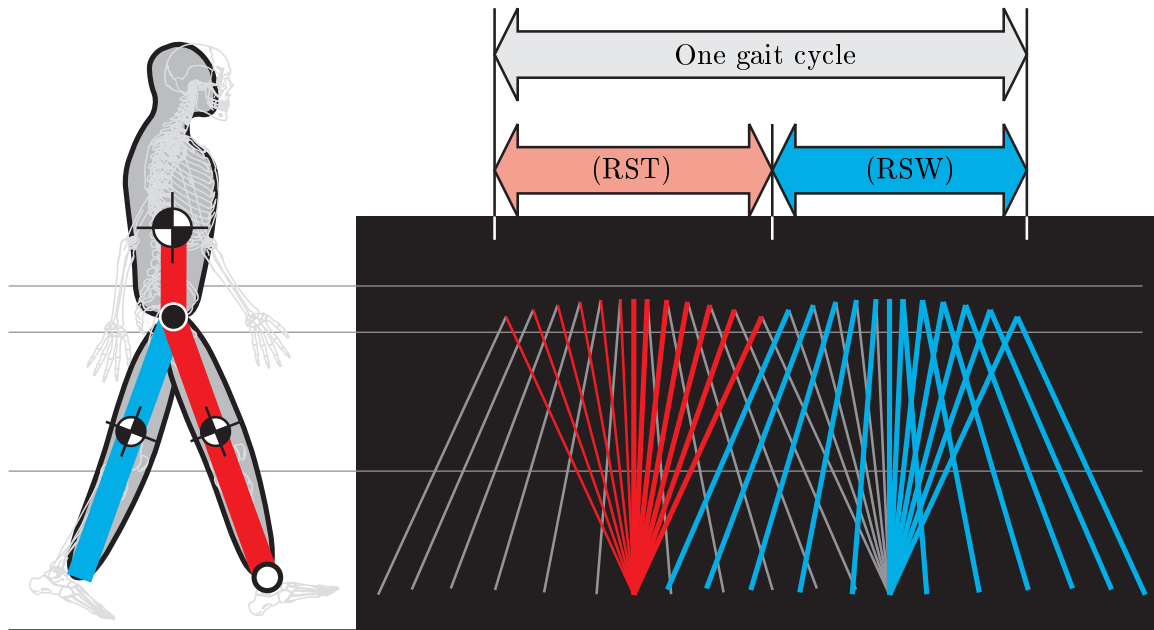


FIGURE 4.2: One complete ballistic gait cycle and its subdivisions into (RST) right leg single-stance, (RSW) right leg swing.

muscles are purely ballistic in the sense that they use only gravity and initial conditions to move through the gait cycle. These models are designated **M1** and **M2**. Models that use muscles, in addition to gravity and initial conditions, are designated **M3** and **M4**.

TABLE 4.1: Classification of the four gait models based on the presence or absence of a deformable hip joint, and the presence or absence of muscles.

	purely rigid	coupled rigid-deformable
no muscles	M1	M2
extensor and flexor groups	M3	M4

In addition to the two major differences, there are a few minor differences between the models. Each of these differences is noted in detail in the following sections. These differences include, for example, the use of certain elements types. To embed a deformable polyethylene mesh at the hip joint, constraint elements that interface between deformable and rigid domains must be used. These differences are important to note, should one seek

to reconstruct the models presented here. However, the differences are not central to the question of how gait dynamics and muscle forces cause stress and deformation in a joint. Therefore, these differences have been de-emphasized.

4.3 MODEL SIMILARITIES

We first describe the similarities of the four biomechanical models. The initial configuration, the manner in which initial velocities are determined, the anthropometric data, and the use of rigid body elements are all constant across models. Each of these model similarities is now discussed in detail.

4.3.1 SYMMETRY CONDITIONS

At the beginning of the ballistic gait cycle, the stance leg has an initial angular position measured from the vertical axis that is a reflection of the initial angular position of the swing leg. Here, we shall assume for all models that the initial angular position of the stance leg to be 20 degrees, labeled as q_3 in FIG. 4.3. See FIG. 4.4 for the sign convention. The swing leg, therefore, has an initial angular position of -20 degrees, labeled as q_6 in FIG. 4.3. At the end of the ballistic gait cycle, the stance leg has an angular position of -20 degrees; the swing leg has an angular position of 20 degrees. The exchanging of initial and final angular positions is referred to as the symmetry condition of ballistic gait. At the end of the ballistic gait cycle, the swing leg becomes the stance leg, and vice versa. Upon completion of two ballistic gait cycles, one complete cycle of gait is achieved (see FIG. 4.2).

The ballistic gait framework requires the appropriate initial velocities to be found so that the symmetry condition in the angular positions of the legs is satisfied. In this sense, the initial value problem of ballistic gait may be viewed as a two-point boundary value problem, where the initial and final configurations are known, but the gradients at these times (the velocities) are unknown.

To solve the two-point boundary value problem, we employ a shooting method. The shooting method attempts to satisfy the equations of motion by using initial and final configurations as knowns while trying to solve for the initial velocities, which are unknown.

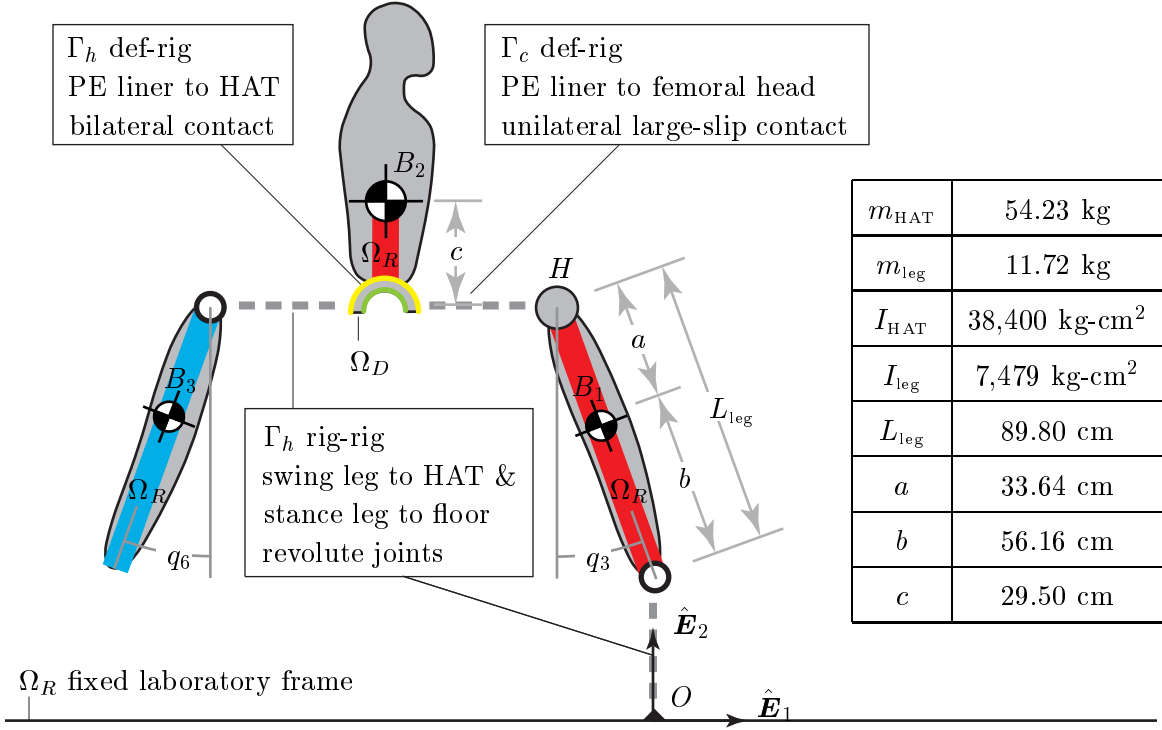


FIGURE 4.3: Geometry and mass properties for the coupled deformable-rigid ballistic gait model. Illustration of deformable Ω_D and rigid Ω_R bodies, as well as interfaces for bilateral Γ_h and unilateral Γ_c contact.

Reasonable guesses are provided for the initial velocities. With the guesses, the equation system is integrated forward in time to the end time. The degree of mismatch between the forward integrated, final configuration and the desired final configuration defines a residual. This residual is then driven to zero, satisfying the equations of motion of the dynamical system as well as the symmetry conditions of ballistic gait.

The shooting method is used to find the appropriate initial conditions for models **M1** and **M3**. Recall that **M1** is a purely rigid ballistic gait model without muscles; **M3** is a purely rigid ballistic gait model with muscles. The initial conditions are then used in forward dynamic simulations for all models **M1–M4**.

4.3.2 INITIAL CONDITIONS

The initial velocities for models **M1** and **M3** obtained from the shooting method that satisfy the ballistic gait symmetry condition are found to be identical. The initial conditions used

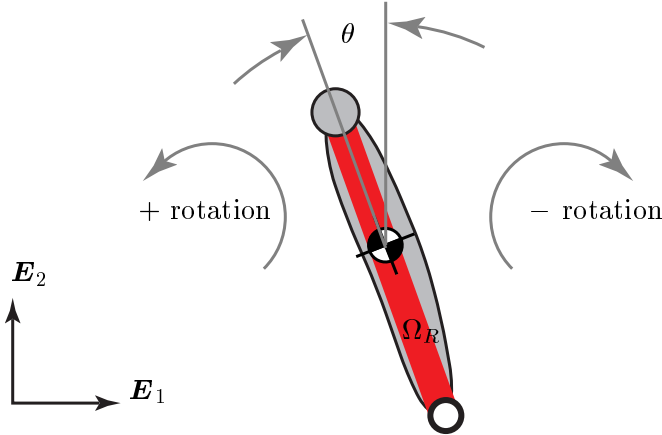


FIGURE 4.4: Convention for limb angles: Angles are measured in the sagittal plane. The vertical \mathbf{E}_2 axis represents zero degrees of rotation. Rotations that are counter-clock-wise from this axis are considered positive. Rotations that are clock-wise from this axis are considered negative.

for the forward dynamic time integration is given in TAB. 4.2.

TABLE 4.2: Initial conditions for the ballistic gait model shown in FIG. 4.2 following the convention for limb angles given in FIG. 4.4.

	stance leg	swing leg
initial angular position	20 deg 0.3491 rad	-20 deg -0.3491 rad
initial angular velocity	-90.9089 deg/s -1.58666 rad/s	-0.760229 deg/s -0.01326585 rad/s

Because the rigid body elements used in the ballistic gait model have translational degrees of freedom in addition to the rotational degree of freedom, the initial angular positions and velocities found in TAB. 4.2 must be used to find the corresponding initial positions and velocities of the leg and HAT mass centers. This is done with the following calculation. Consider the geometry of the model model shown in FIG. 4.3. Let point O be the origin where the stance leg is pinned to the ground. Let B_1 stand for the location of the stance leg mass center. Let B_2 stand for the location of the HAT mass center. Let H stand for the location of the hip axis. Let B_3 stand for the location of the swing leg mass center. The

position of the stance leg center of mass, \mathbf{r}^{OB_1} , is

$$\mathbf{r}^{OB_1} = \begin{Bmatrix} -b \sin q_3 \\ b \cos q_3 \end{Bmatrix} = \begin{Bmatrix} -19.2079 \\ 52.7731 \end{Bmatrix} \text{ cm.} \quad (4.1)$$

The position of the HAT center of mass, \mathbf{r}^{OB_2} , is given by

$$\mathbf{r}^{OB_2} = \begin{Bmatrix} -L_{\text{leg}} \sin q_3 \\ L_{\text{leg}} \cos q_3 \end{Bmatrix} + \begin{Bmatrix} 0 \\ c \end{Bmatrix} = \begin{Bmatrix} -30.7134 \\ 113.8844 \end{Bmatrix} \text{ cm.} \quad (4.2)$$

The position of the swing leg center of mass, \mathbf{r}^{OB_3} , is

$$\mathbf{r}^{OB_3} = \begin{Bmatrix} -L_{\text{leg}} \sin q_3 + a \sin q_6 \\ L_{\text{leg}} \cos q_3 - a \cos q_6 \end{Bmatrix} = \begin{Bmatrix} -42.219 \\ 52.7731 \end{Bmatrix} \text{ cm.} \quad (4.3)$$

Note that all of the foregoing position vectors are measured in the laboratory reference frame. The velocity of the stance leg center of mass, \mathbf{v}^{B_1} , is

$$\begin{aligned} \mathbf{v}^{B_1} &= \mathbf{v}^O + \boldsymbol{\omega}^{B_1} \times \mathbf{r}^{OB_1}, \\ &= \begin{Bmatrix} 0 \\ 0 \end{Bmatrix} + \begin{bmatrix} 0 & -\dot{q}_3 \\ \dot{q}_3 & 0 \end{bmatrix} \begin{Bmatrix} -b \sin q_3 \\ b \cos q_3 \end{Bmatrix}. \end{aligned} \quad (4.4)$$

Substituting the initial conditions and geometry for the stance leg gives

$$\mathbf{v}^{B_1} = \begin{Bmatrix} 83.733 \\ 30.4763 \end{Bmatrix} \text{ cm/s.} \quad (4.5)$$

Substituting the geometry of the stance leg and the initial conditions for the HAT, which for the ballistic gait model should coincide with the hip initial velocity, gives

$$\mathbf{v}^H = \mathbf{v}^{B_2} = \begin{Bmatrix} 0 \\ 0 \end{Bmatrix} + \begin{bmatrix} 0 & -\dot{q}_3 \\ \dot{q}_3 & 0 \end{bmatrix} \begin{Bmatrix} -L_{\text{leg}} \sin q_3 \\ L_{\text{leg}} \cos q_3 \end{Bmatrix} = \begin{Bmatrix} 133.889 \\ 48.7317 \end{Bmatrix} \text{ cm/s.} \quad (4.6)$$

Finally, substituting the initial conditions and geometry for the swing leg gives

$$\begin{aligned} \mathbf{v}^{B_3} &= \mathbf{v}^H + \boldsymbol{\omega}^{B_3} \times \mathbf{r}^{HB_3}, \\ &= \begin{Bmatrix} v_1^H \\ v_2^H \end{Bmatrix} + \begin{bmatrix} 0 & -\dot{q}_6 \\ \dot{q}_6 & 0 \end{bmatrix} \begin{Bmatrix} a \sin q_6 \\ -a \cos q_6 \end{Bmatrix} = \begin{Bmatrix} 133.47 \\ 48.8844 \end{Bmatrix} \text{ cm/s.} \end{aligned} \quad (4.7)$$

4.3.3 ANTHROPOMETRIC DATA

Satisfaction of the symmetry condition depends not only on the initial conditions, but also on the mass and inertia properties of the system. The same geometry, mass, and inertia are used for all ballistic gait models **M1–M4**.

From data in Winter (see TABLE 3.1, EXAMPLE 3.4, and EXAMPLE 3.6 in [117]), we assume our model to have a mass of 80 kg (784.8 N or 176 pounds). The HAT has a mass of 54.23 kg and inertia about the the mass center in the out-of-sagittal-plane direction of 38,400 kg·cm². Each leg (composed of the lower leg and thigh) has a mass of 11.72 kg and inertia about the mass center in the out-of-sagittal-plane direction of 7,479 kg·cm². We assume each leg to have a length of 89.80 cm and have a mass center located 56.16 cm from the distal end of the leg. The center of mass of the HAT is assumed to be 29.50 cm from the center of the hip. See FIG. 4.3 for an illustration of the model and the associated anthropometric quantities. Since the ballistic gait model has only the HAT and two legs (the feet are ignored), the total mass of the model is 77.67 kg (762 N or 171 pounds).

4.3.4 RIGID LIMB SEGMENTS AND ASSOCIATED INTERFACES

Rigid body elements, described in Eqs. (3.52)–(3.53) of SECTION 3.3, are used for all limb segments — the stance leg, the swing leg, and the HAT. No damping is used, thus $c = 0$ in the aforementioned equations. Mass and inertia properties are listed in FIG. 4.3. Gravity is taken to be 9.81 m/s², acting in the negative $\hat{\mathbf{E}}_2$ direction. Holonomic constraint elements, described in Eqs. (3.88)–(3.89) of SECTION 3.4, are used to create revolute joints between rigid body limb segments. The regularization parameter for the augmented Lagrange formulation is taken as $r = 1.0$.

4.4 MODEL DIFFERENCES

We now emphasize the distinction between purely rigid ballistic gait models and coupled ballistic gait models. The word “coupled” is used to indicate that both rigid and deformable bodies are used in the same model. In the coupled models (**M2** and **M4**), the revolute joint between the HAT and the stance leg of the purely rigid models (**M1** and **M3**), is replaced

with a deformable total hip arthroplasty, shown in FIG. 4.3.

4.4.1 DEFORMABLE HIP JOINT AND ASSOCIATED INTERFACES

To model the hip replacement, we embed the two-dimensional finite element mesh between the stance leg and HAT, shown in FIG. 4.3. The mesh, shown enlarged in FIG. 4.5, represents a sagittal cross section of the three dimensional Johnson & Johnson Professional, Inc. (JJPI) hip arthroplasty model used in Kurtz [66]. The JJPI total hip arthroplasty is composed of three main components — the acetabular cup, the liner, and the femoral head-stem. The cup is secured into the acetabulum either with screws, bone cement, or both. The liner is attached to the cup through locking mechanisms at the equatorial regions. The femoral head may rotate and (depending on the relative conformity of the liner inner radius and femoral head radius) translate in the cup. The femoral head is attached to the femoral stem, which is secured in the medulary canal of the femur. The acetabular cup and femoral head are made from chromium-cobalt. The liner is made from ultra-high-molecular-weight polyethylene (UHMWPE). Since chromium-cobalt is significantly stronger and deforms much less than UHMWPE, the acetabular shell and femoral head are assumed to be rigid bodies while the acetabular liner is assumed to be a deformable body.

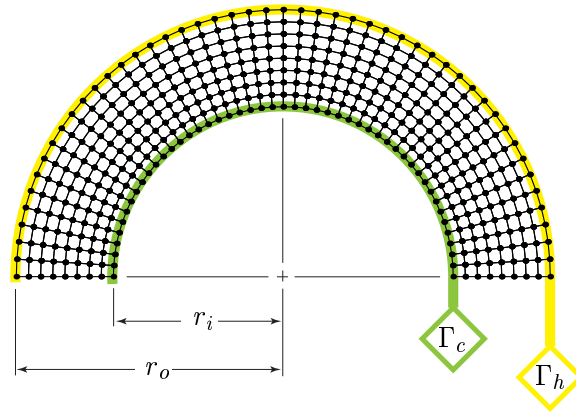


FIGURE 4.5: Sagittal plane representation of the finite element mesh from [66] used to model the Johnson & Johnson total hip arthroplasty.

The finite element mesh in FIG. 4.5 has 384 quadrilateral plane strain elements. A robust material law from Curnier [30], described in Eq. (2.18) of SECTION 2.2.4, is used with $E = 974$ MPa and $\nu = 0.46$. These material properties are identical to those used in

the hip arthroplasty studies of Kurtz [66, 67]. The inner radius has dimension $r_i = 1.4$ cm. The outer radius has dimension $r_o = 2.2$ cm.

Consider the nodes on the outer radius of the mesh, marked in FIG. 4.3 and FIG. 4.5 with yellow and labeled Γ_h . These nodes are constrained to represent perfectly conforming, persistent contact between the polyethylene liner and the acetabular shell. The acetabular shell is rigidly attached to the pelvis. The pelvis is included as part of the HAT rigid body. Therefore, motion of the outer radius of the polyethylene liner must be compatible with motion of the HAT. The compatibility is obtained through holonomic constraint elements, described in SECTION 3.4. Specifically, forty-nine deformable-rigid contact elements constrain each of the forty-nine nodes on the outer radius of the mesh to move with the motion of the HAT, through Eq. (3.61). The regularization parameter for the augmented Lagrangian formulation is taken as $r = 10.0$.

Though the nodes on the outer radius of the mesh are attached to the acetabular shell, the nodes on the inner radius of the mesh are not attached to the femoral head. Shown in FIG. 4.3 and FIG. 4.5 with green and labeled Γ_c , these nodes, in combination with Lagrange multiplier nodes and the nodes defining the shape of the femoral head, compose the forty-nine large-slip, unilateral contact elements. The unilateral contact law enforces the condition where (1) the femoral head and the inner surface of the UHMWPE liner can separate, touch, but not penetrate each other, and (2) where these two bodies can push but not pull on one another. Therefore, the gap between the two bodies must be non-negative, and the pressure between the two bodies must be non-positive. These interactions embody the unilateral contact law, described in SECTION 2.5, FIG. 2.8, and Eq. (2.98). The element used to provide unilateral, large-slip contact is described in SECTION 3.5. The regularization parameter for the augmented Lagrangian formulation is taken as $r = 2.0$. The tolerance for contact is taken as 1.0E-6.

4.4.2 MUSCLE EXTENSOR AND FLEXOR GROUPS

The effect of muscle force on joint stress and deformation is investigated by adding muscles to the coupled model. As a starting point, the rotational degree of freedom belonging to the HAT, defined as q_9 in FIG. 4.6(b), is added to model **M1**, shown in FIG. 4.6(a). Then, two

muscle groups are added to provide extension or flexion of the hip joint between the HAT and stance leg. Note that muscle origin and insertion locations depicted in FIG. 4.6(b) are conceptual and is not to scale.

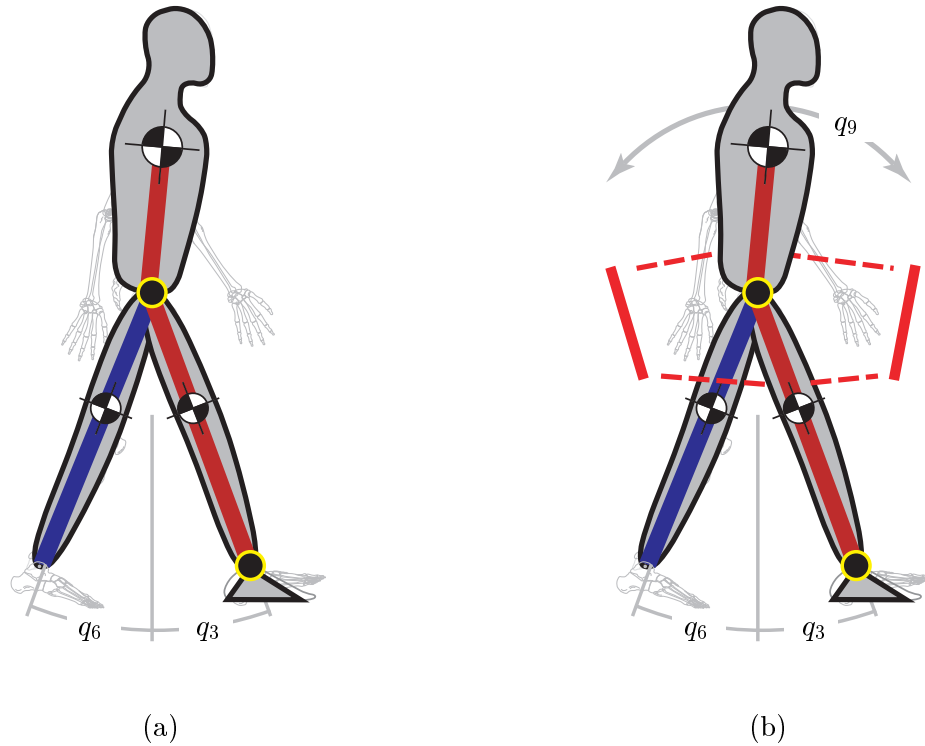


FIGURE 4.6: Large-scale view of a purely rigid ballistic gait model (a) without muscles and (b) with muscles.

A generalized extensor muscle is constructed to represent the muscles of the gluteus maximus. A generalized flexor muscle is constructed to represent the iliacus and psoas. These physiological muscles, based on the muscle anatomy in SIMM [34, 35], is shown in FIG. 4.7(a). The simplified extensor and flexor muscle groups are shown in FIG. 4.7(b). Each muscle in SIMM has an origin, insertion, and via points, which describe the path the muscle takes as it shortens or lengthens. The muscle elements developed in SECTION 3.4.6 only have an origin and insertion; they have no via point capabilities. The effect of via points is important to model. Ignoring them would cause artificial shortening of the muscle lever arms. With this in mind, we create origin and insertion locations of the simplified muscle groups, in FIG. 4.7(b), to reflect the path taken by the physiological model of the muscles, in FIG. 4.7(a).

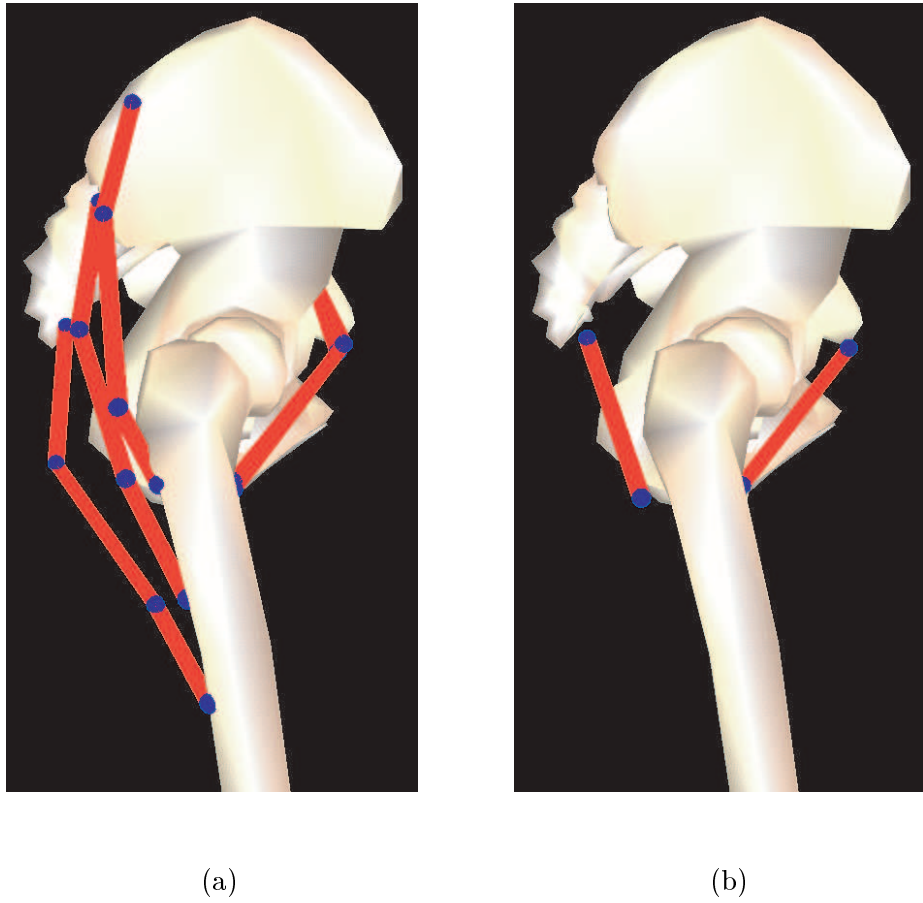


FIGURE 4.7: Sagittal view of (a) physiological extensor and flexor muscle groups and (b) simplified extensor and flexor muscles groups.

The location of the simplified extensor origin is the average location of the three proximal via points of the three gluteus maximus muscle groups. The location of the simplified extensor insertion is the average location of the three distal via points of the gluteus group. Similarly, the location of the simplified flexor origin is the average location of the proximal via points of the iliacus and psoas. The location of the simplified flexor insertion is the average location of the distal via points of the iliacus and psoas.

The extensor and flexor origins are defined in the HAT reference frame. The position vector from the HAT mass center to the extensor origin is given by

$$\mathbf{r}^{B_2 E_o} = \begin{Bmatrix} -6.920 \\ -28.09 \end{Bmatrix}_{(HAT)} \text{ cm.} \quad (4.8)$$

The position vector of the HAT mass center to the flexor origin is given by

$$\mathbf{r}^{B_2 F_o} = \begin{Bmatrix} 4.790 \\ -28.49 \end{Bmatrix}_{(HAT)} \text{ cm.} \quad (4.9)$$

The extensor and flexor insertions are defined in the stance leg reference frame. The position vector from the stance leg mass center to the extensor insertion is given by

$$\mathbf{r}^{B_1 E_i} = \begin{Bmatrix} -3.940 \\ 27.58 \end{Bmatrix}_{(\text{stance})} \text{ cm.} \quad (4.10)$$

The position vector from the stance leg mass center to the flexor insertion is given by

$$\mathbf{r}^{B_1 F_i} = \begin{Bmatrix} 0.1700 \\ 28.39 \end{Bmatrix}_{(\text{stance})} \text{ cm.} \quad (4.11)$$

The two simplified muscle elements are attached to the stance leg and HAT rigid bodies through deformable-rigid holonomic constraint elements, described in Eqs. (3.88)–(3.89) of SECTION 3.4. Four constraint elements fix the four muscle attachment sites (two origins, two insertions) to either the HAT (origins) or stance leg (insertions). The regularization parameter associated with the augmented Lagrangian formulation is taken as $r = 10.0$.

The objective of the muscles is to keep the HAT vertical through the duration of the ballistic gait simulation. To achieve this objective, the muscles must supply a force, which is unknown for now. The force is determined in the following manner. Starting from the purely rigid ballistic gait model **M1**, the HAT rotation degree of freedom, q_9 , is added to the equations of motion. The simplified extensor muscle is attached to the HAT and the stance leg. For now, there is no flexor muscle group. Generalized forces are added to the equation system using Eq. (2.32), representing either a push or a pull in the extensor muscle. A constraint equation is then added to the dynamical system, stating that $q_9 = 0$ for all time. The constraint equation, enforced with a standard Lagrange multiplier method, will yield a Lagrange multiplier λ that is related to the generalized force Q_i through

$$Q_i = \frac{\partial c_k(\mathbf{q})}{\partial q_i} \lambda_k, \quad (4.12)$$

where c_k is the k^{th} constraint equation. The generalized force terms will have a dependence on q_9 . The generalized force is related to the muscle force \mathbf{F} through

$$Q_i = \frac{\partial^N v_k^R}{\partial \dot{q}_i} F_k^R. \quad (4.13)$$

Refer to Eq. (2.29) in SECTION 2.3. This relationship may be used to find the magnitude F of the force vector \mathbf{F} ,

$$F = \frac{\frac{\partial c_k(\mathbf{q})}{\partial q_i} \lambda_k}{\frac{\partial^N v_s^R}{\partial \dot{q}_i} \hat{t}_s}, \quad (4.14)$$

where $\hat{\mathbf{t}}$ is the direction of the muscle force vector \mathbf{F} . This force magnitude F is precisely the amount of push or pull required in the extensor muscle to keep the HAT in the vertical position.

This force magnitude is shown in FIG. 4.8. The force is initially positive, at a value of 883 N, indicating the muscle is in tension, pulling the HAT in the positive rotation direction. Without the pulling of the extensors on the HAT, the HAT would fall forward. The required muscle force then decreases nearly linearly toward zero at midstance ($t = 0.30$ s). From midstance to the end of the simulation ($t = [0.30, 0.60]$ s), the force required in the muscle to keep the HAT vertical is actually negative, indicating the muscle must *push* against the HAT. Since muscles can pull but not push, we know that the results from the simulation with only the extensor muscle must be discarded for times $t > 0.30$ s.

Next, the extensor muscle is removed from the model. A flexor muscle is then added. With the same procedure as outlined above, the muscle force in the flexor required to keep the HAT vertical is found. This force magnitude, shown in FIG. 4.9 is found to be negative initially, indicating that the flexor must push on the HAT to keep it from falling forward at $t = 0$ s. This result is consistent with the previous result which used only an extensor, where the extensor provided the requisite pull to keep the HAT from falling forward. The difference in magnitudes between the extensors and flexors is due to the difference in moment arms of the two muscle groups. Continuing with the solitary flexor muscle, we see the necessary force decreases to zero at midstance. After midstance, the force required to keep the HAT increases nearly linearly to a peak magnitude of 1785 N. This positive number reflects a pulling force required in the flexors to keep the HAT from falling backward.

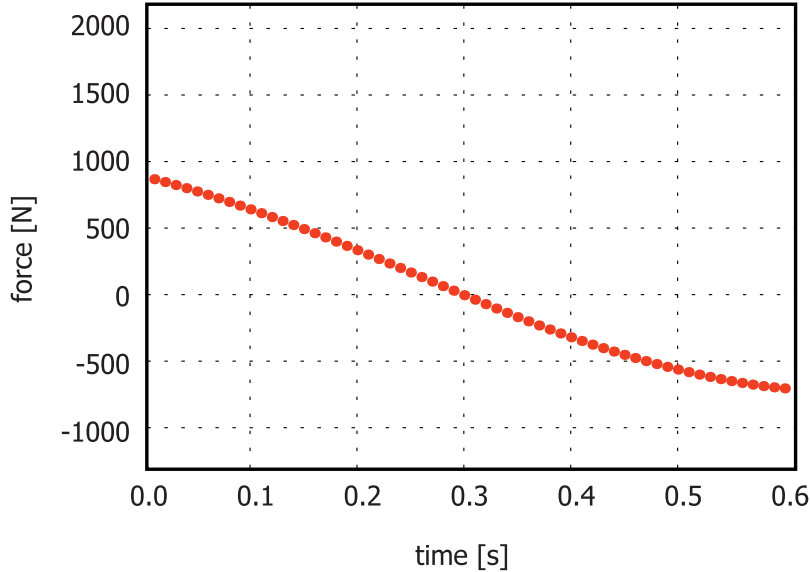


FIGURE 4.8: Extensor muscle force magnitude required to keep HAT vertical.

From a physioloical point of view, we know that muscles can provide a force only through contraction of the muscle fibers. Thus, the numerical result of a pushing force provided by the flexors during $t = [0.0, 0.3]$ seconds, and the pushing force provided by the extensors during $t = [0.3, 0.6]$ seconds is not realistic. Taking only the positive contributions of these muscles forces provides satisfaction of the vertical HAT angle constraint, while also satisfying the idea that muscles can produce forces through contraction of muscle fibers. The complementary contributions from the extensor and flexor muscle groups are shown in FIG. 4.10. This model uses no co-contraction of muscle groups. While co-contraction of muscles is commonly found during joint movement, there is some evidence to suggest that during the stance phase of gait, the extensors are active briefly, followed by a period of ballistic gait, followed by activation of the flexors [97]. The model employed here, therefore, may be a good first approximation of the muscle forces exerted while walking.

4.4.3 FORWARD INTEGRATION

Integration forward in time of the dynamical system is done in one of two ways. For the purely rigid models, **M1** and **M3**, the system is integrated with the explicit, fourth order accurate Runge-Kutta method in the rigid body dynamics program SMASH [60]. Results

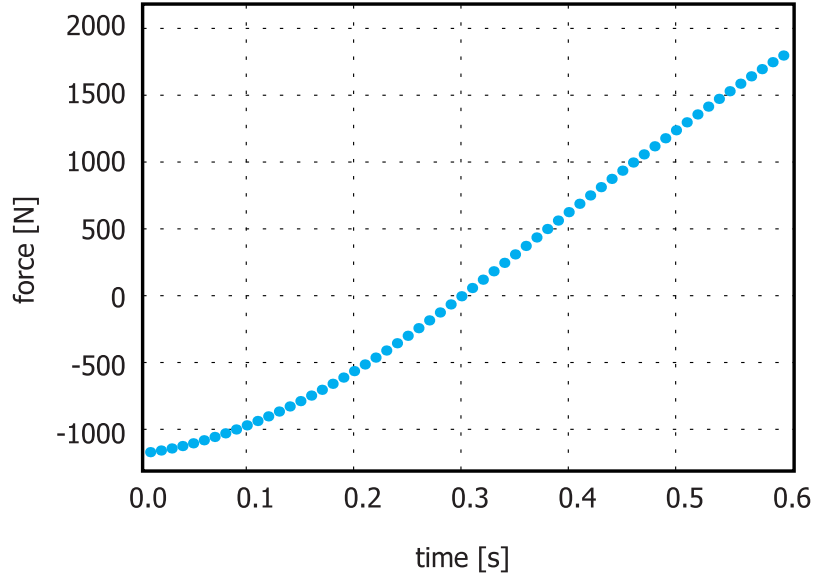


FIGURE 4.9: Flexor muscle force magnitude required to keep HAT vertical.

from SMASH are used as a baseline standard for the motion of the purely rigid ballistic gait models.

The coupled models, **M2** and **M4**, rely on new element technology, described in CHAPTER 3, which is built on top of the finite element code TACT [29]. To achieve sufficient high frequency damping, explained in SECTION 1.2.2, a damped Newmark time integrator is used in TACT. This integrator, though implicit and therefore more stable than explicit methods, is only first order accurate. As a result, comparisons of the kinematics between purely rigid and coupled deformable-rigid models may reflect differences in the time integrators.

For all simulations, a time step of $\Delta t = 0.01$ seconds is employed. Sixty time steps are used, for a total simulation time of 0.6 seconds. This time reflects the the duration of single leg stance, discussed in SECTION 4.1.

For the coupled models, quadratic convergence in each time step is obtained. When a tolerance of 1.0E-6 is used for the convergence norm, only six iterations are typically required. The algorithms described in BOX 3.1 and BOX 3.2 are used with a u-type formulation. Newmark parameters are set to $\beta = 0.3025$ and $\gamma = 0.6$, providing high frequency damping.

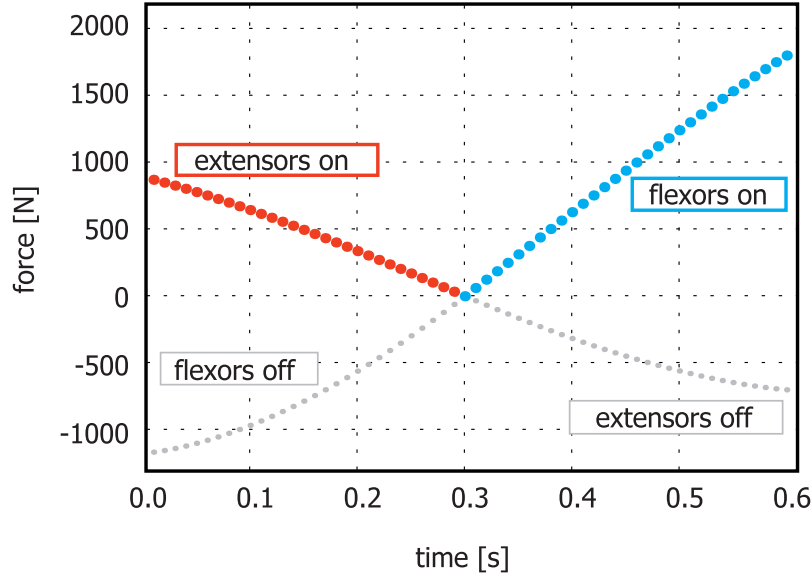


FIGURE 4.10: Complementary extensor and flexor muscle forces magnitudes required to keep HAT vertical.

4.5 MODEL VALIDATION

At this point, we have assembled all of the necessary information required for a forward dynamic simulation of (either purely rigid or coupled deformable-rigid) ballistic gait. We have built the ballistic gait model with geometry, mass, and inertia based on physiological data. We have found initial conditions which satisfy the symmetry condition of ballistic gait. We have developed rigid elements and rigid-rigid interface elements to describe limb segments and revolute joints, respectively. We have coupled a deformable hip arthroplasty to the ballistic gait model to investigate how gait dynamics causes stress and deformation in the joint. We have developed special bilateral and unilateral contact elements to model the physical interaction between rigid and deformable domains. Rudimentary extensor and flexor muscle groups have been added to allow the effects of muscle forces on joint stress and deformation to be investigated.

Before obtaining results from the coupled ballistic gait model, presented in CHAPTER 5, we are interested in knowing how well the deformable body mesh, in the absence of the rigid body dynamic coupling, can reproduce results from previous research.

Work by Bartel [15] provides both an analytical solution and finite element solution

to a rigid femoral head pushed statically into a deformable ultra-high-molecular-weight polyethylene (UHMWPE) liner. In his simulations, an external load of 3000 N, assumed to represent the peak hip reaction force during gait, is used. The polyethylene liner is assumed homogenous and isotropic, with $E = 1400$ MPa and $\nu = 0.3$.

Using the mesh shown in FIG. 4.5, the material law given in Eq. (2.18), the material properties and load from Bartel, we obtain results for maximum contact pressure and maximum displacement of the rigid femoral head as it indents into the deformable liner. This will be referred to as the validation study. We compare results from the validation study not only to those from Bartel, but also to results from Maxian [78] and Kurtz [67], mentioned in SECTION 1.2.1.

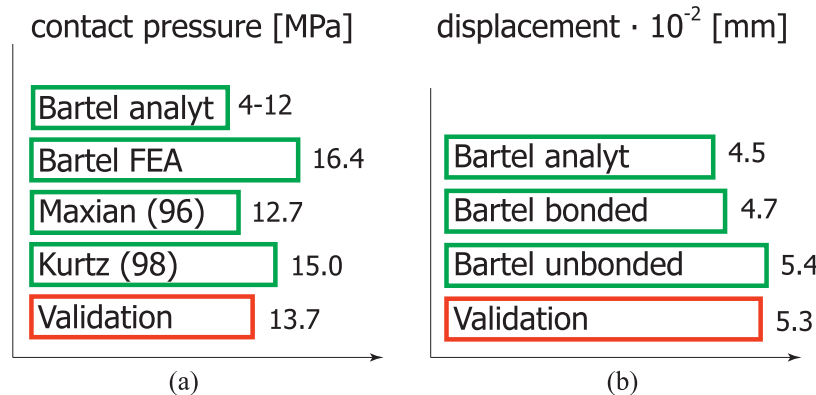


FIGURE 4.11: Comparison of (a) contact pressure and (b) maximum femoral head displacement results from Bartel [15], Maxian [78], and Kurtz [67] to the validation study.

From FIG. 4.11(a), we see that the maximum contact stress using the mesh in FIG. 4.5 agrees well with previously published results. Bartel, from his analytical model, reports maximum contact pressures within the range of 4–12 MPa. The broad range is caused by changes in conformity of the polyethylene liner with the acetabular shell and femoral head. See Bartel [15] for more details. The maximum contact pressure is found to be around 16.4 MPa.

Bartel's computational study, like the model in FIG. 4.5, uses a two dimensional, plane strain finite element mesh. The computational wear studies done by Maxian [78] and Kurtz [67] used three dimensional finite element meshes. Maxian reported a maximum contact pressure of approximately 12.7 MPa. Kurtz showed a maximum contact pressure

of roughly 15.0 MPa.

As shown in FIG. 4.11(a), the maximum contact pressure obtained in the validation study of 13.7 MPa fits well within the range of numbers found in previous research. This agreement provides confidence that the model used here provides reasonable results.

Furthermore, we look at the maximum displacement of the rigid femoral head as it pushes into the deformable liner. Bartel's analytical elasticity solution gives a maximum displacement of 4.5E-2 mm. Bartel's finite element models give maximum displacement within the range of 4.7E-2 to 5.4E-2 mm, if the interface between the liner and the acetabular shell is bonded or unbonded, respectively. The validation study gives a maximum displacement of 5.3E-2 mm. As shown in FIG. 4.11(b), the validation study displacement falls well within the range of results from Bartel.

The stress and deformation of the liner in the validation study will be compared to the results from the coupled ballistic gait models, presented in CHAPTER 5. FIGURE 4.12 shows the hydrostatic pressure from the validation study. The maximum hydrostatic pressure of approximately 6 MPa occurs directly above the applied 3000 N load. The pressure decreases symmetrically to zero toward either side of the mesh. FIGURE 4.13 shows the von Mises

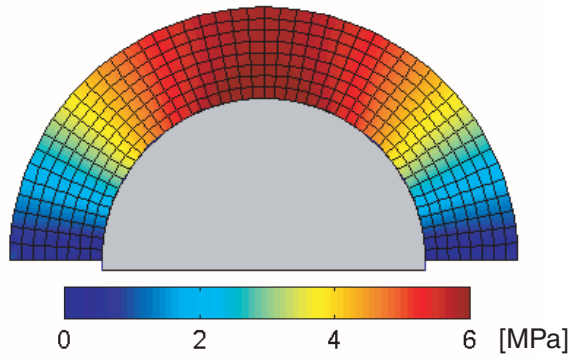


FIGURE 4.12: Hydrostatic pressure for hip arthroplasty using Bartel's inputs: Static applied load of 3000 N, $E = 1400$ MPa, and $\nu = 0.3$.

stress under the same loading conditions. A peak von Mises stress of about 10 MPa is observed directly under the applied load. The stress contour decreases to about 5 MPa at

the outer radius of the mesh on the centerline. Whereas the hydrostatic pressure appears

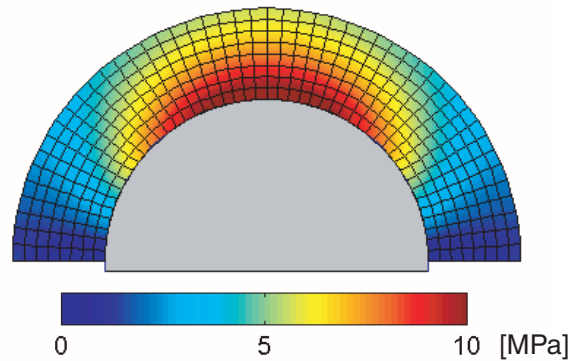


FIGURE 4.13: von Mises stress for hip arthroplasty using Bartel's inputs: Static applied load of 3000 N, $E = 1400$ MPa, and $\nu = 0.3$.

to have no radial variation, the von Mises stress displays a concentric ring pattern along the centerline of the mesh. The stress profiles are symmetric, as expected, because the loading condition, geometry, and boundary conditions are symmetric. The σ_{22} component of the Cauchy stress tensor is shown in FIG. 4.14. The contact pressure at the interface of the

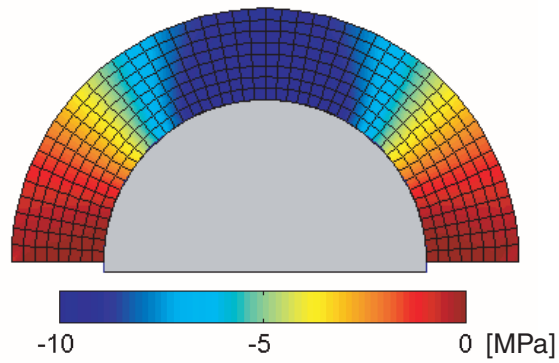


FIGURE 4.14: Stress component σ_{22} for hip arthroplasty using Bartel's inputs: Static applied load of 3000 N, $E = 1400$ MPa, and $\nu = 0.3$.

femoral head, polyethylene liner, is shown in FIG. 4.15. Taken together, FIGS. 4.14–4.15

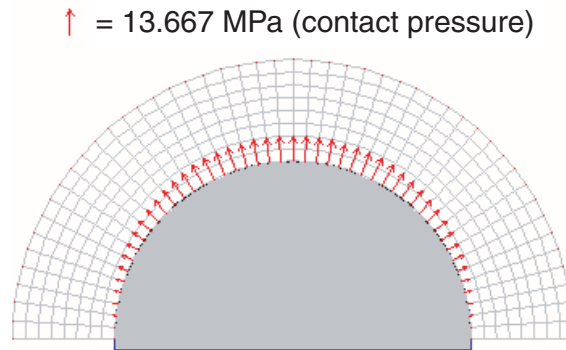


FIGURE 4.15: Contact pressure for hip arthroplasty using Bartel's inputs: Static applied load of 3000 N, $E = 1400 \text{ MPa}$, and $\nu = 0.3$.

show how the load applied to the femoral head is equilibrated through internal, elastic forces. The maximum contact pressure, noted as 13.7 MPa in FIG. 4.15, is found to exist at the centerline of the mesh. The pressure decreases to zero on either side of the mesh. The maximum and minimum strains occurring throughout the liner are shown in FIG. 4.16. The maximum strain is on the order of 0.8%. These compressive strains appear in a symmetric manner around the centerline. The maximum compressive strains have the same orientation as the contact pressures.

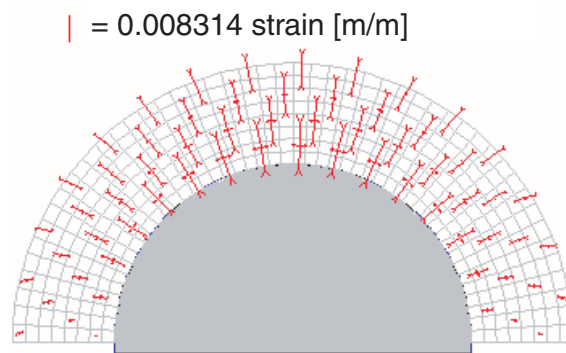


FIGURE 4.16: Maximum and minimum strain using Bartel's inputs: Static applied load of 3000 N, $E = 1400 \text{ MPa}$, and $\nu = 0.3$.

CHAPTER 5

RESULTS AND DISCUSSION

5.1 OVERVIEW

This chapter presents results from numerical simulations using the models described in CHAPTER 4. Recall that four biomechanical models were discussed, **M1–M4**. Models **M1** and **M2** were purely ballistic gait models; while models **M3** and **M4** used muscles to keep the head-arms-trunk (HAT) upright. Models **M1** and **M3** were constructed from purely rigid bodies, while models **M2** and **M4** had a deformable polyethylene finite element mesh at the HAT-stance leg hip joint. For these models, we are interested in measuring several items:

1. Compute the dynamics of the coupled model.
 - (a) Find position and velocity time histories for the stance leg, HAT, and swing leg.
 - (b) Compute the vertical and horizontal ground reaction force from the Lagrange multipliers enforcing contact between the stance leg and the ground.
2. Determine stress and deformation of the deformable joint.
 - (a) Find the hydrostatic pressure time history in the deformable polyethylene liner.
 - (b) Find the von Mises stress time history in the deformable polyethylene liner.
 - (c) Compute the maximum and minimum principal strains in the deformable polyethylene liner.

3. Determine forces at the interfaces between rigid and deformable domains.
 - (a) Compute the contact pressure between the rigid femoral head and the deformable polyethylene liner from the Lagrange multipliers of the inequality contact constraints.
 - (b) Compute the interface forces between the deformable polyethylene liner and the rigid bony foundation of the acetabulum from the Lagrange multipliers of the equality contact constraints.

Once the foregoing quantities are measured for each of the models, we are interested in discussing the following questions:

1. How do the dynamics of the coupled models compare with a purely rigid ballistic gait model?
2. How do the coupled models compare with experimental kinematic and ground reaction force data obtained from gait analysis data?
3. How realistic are the muscle forces used with models **M3** and **M4**?
4. How much of stress and motion in the joint is attributable to dynamics of human movement versus the contraction of muscles?

5.2 RESULTS

5.2.1 LARGE SCALE

FIGURE 5.1 shows the position and velocity for the two translational and one rotational degree of freedom for the stance leg. Two results are superposed in each of the six subplots. The solid red line depicts the results for the purely rigid ballistic gait model **M1**. The discrete blue circles depict the results from the coupled ballistic gait model **M2**.

The stance leg has an initial flexion angle of 20 degrees (FIG. 5.1(c)). This angle decreases to zero at midstance ($t = 0.3$ s). The stance leg then continues to extend to -20 degrees at the end of the stance phase ($t = 0.6$ s). At this point, the stance leg has the

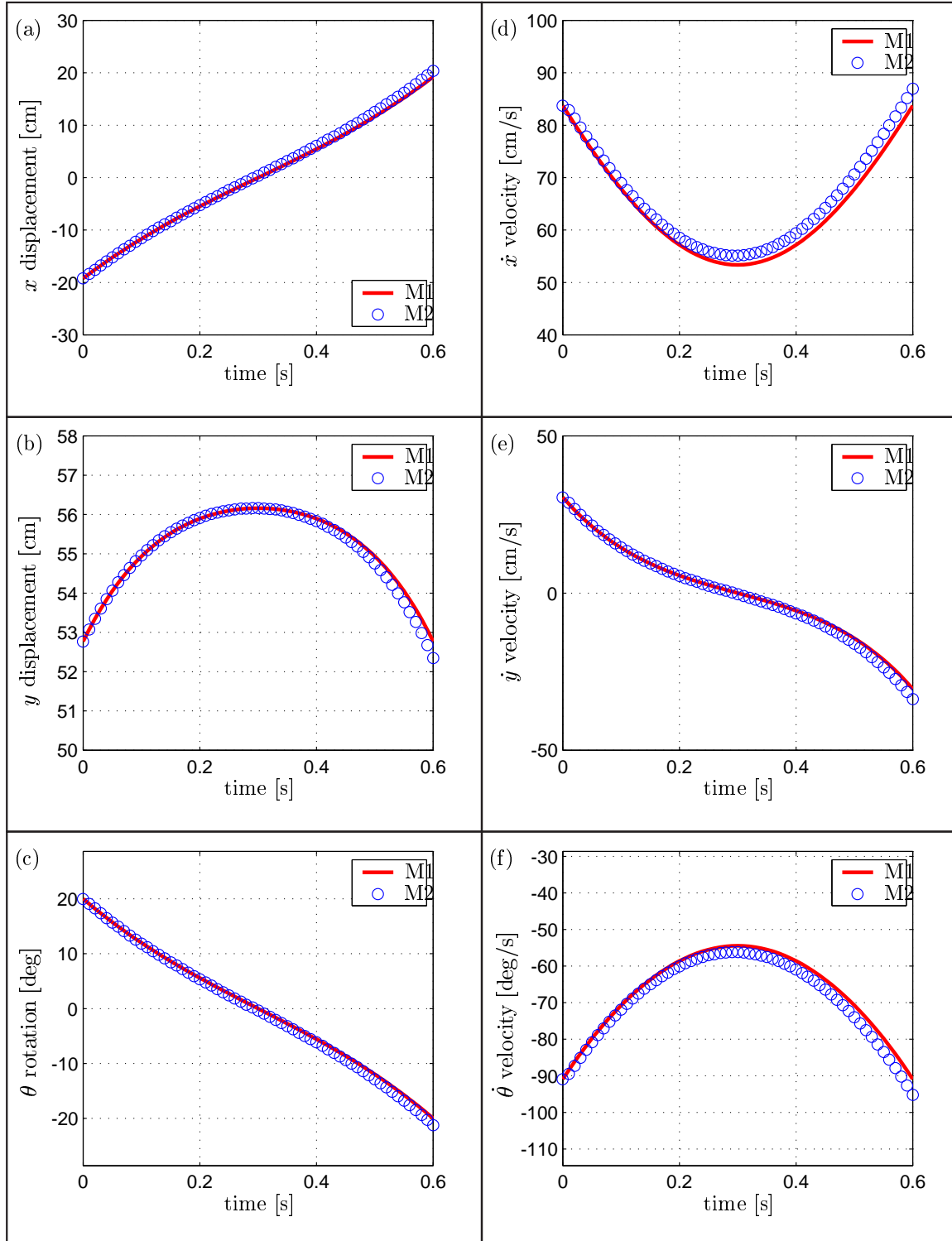


FIGURE 5.1: Comparison of the coupled ballistic gait model, **M2**, to the purely rigid ballistic gait model, **M1**. Position and velocity data for the stance leg: (a) x position, (b) y position, (c), θ angular rotation, (d) x velocity, (e), y velocity, (f) $\dot{\theta}$ angular velocity.

initial angular position that the swing leg had at the beginning of the simulation ($t = 0.0$ s), thereby satisfying the symmetry condition of the ballistic gait model.

The angular velocity of the stance leg begins at approximately -90 degrees per second, decreases to roughly -55 degrees per second at mid-stance, then regains its original value of about -90 degrees per second at the end of the cycle (FIG. 5.1(f)).

The rotation of the stance leg is the only true degree of freedom for this limb segment. The two translational degrees of freedom are constrained because the stance leg is pinned to the ground. The position of the stance leg mass center begins at approximately (-19, 53) cm from the origin, selected as the ankle of the stance leg (see FIG. 5.1(a), FIG. 5.1(b), and FIG. 4.3). The stance leg x position is directly over the origin at midstance and the exactly the distance from the origin to the leg mass center (56.16 cm). The motion continues from midstance to the end of the simulation in a manner symmetric to the first half of the cycle.

The velocity of the stance leg in the x direction ranges between approximately 55 cm per second at midstance to about 85 cm per second at the beginning and end of the stance cycle (FIG. 5.1(d)). The velocity of the stance leg in the y direction begins at roughly 30 cm per second, goes to zero at midstance, and finishes at about -30 cm per second at the end of the cycle (FIG. 5.1(e)).

FIGURE 5.2 shows the position and velocity for the two translational and one rotational degree of freedom for the HAT. As in FIG. 5.1, two results are superposed in each of the six subplots. The solid red line, indicated with **M1** in the legend, depicts the results for the purely rigid ballistic gait model. The discrete blue circles, indicated by **M2** in the legend, depict the results from the coupled ballistic gait model.

Since the rotational degrees of freedom are blocked in models **M1** and **M2** (the HAT rotational degree of freedom is allowed to move freely in models **M3** and **M4**), the angular positions and velocities are zero for all time, as they should be (FIG. 5.2(c) and (f)). The HAT is pinned to the stance leg at the right hip. Therefore, the translational positions and velocities of the HAT will follow the same trends as the stance leg (FIG. 5.2(a)-(b) and (d)-(f)).

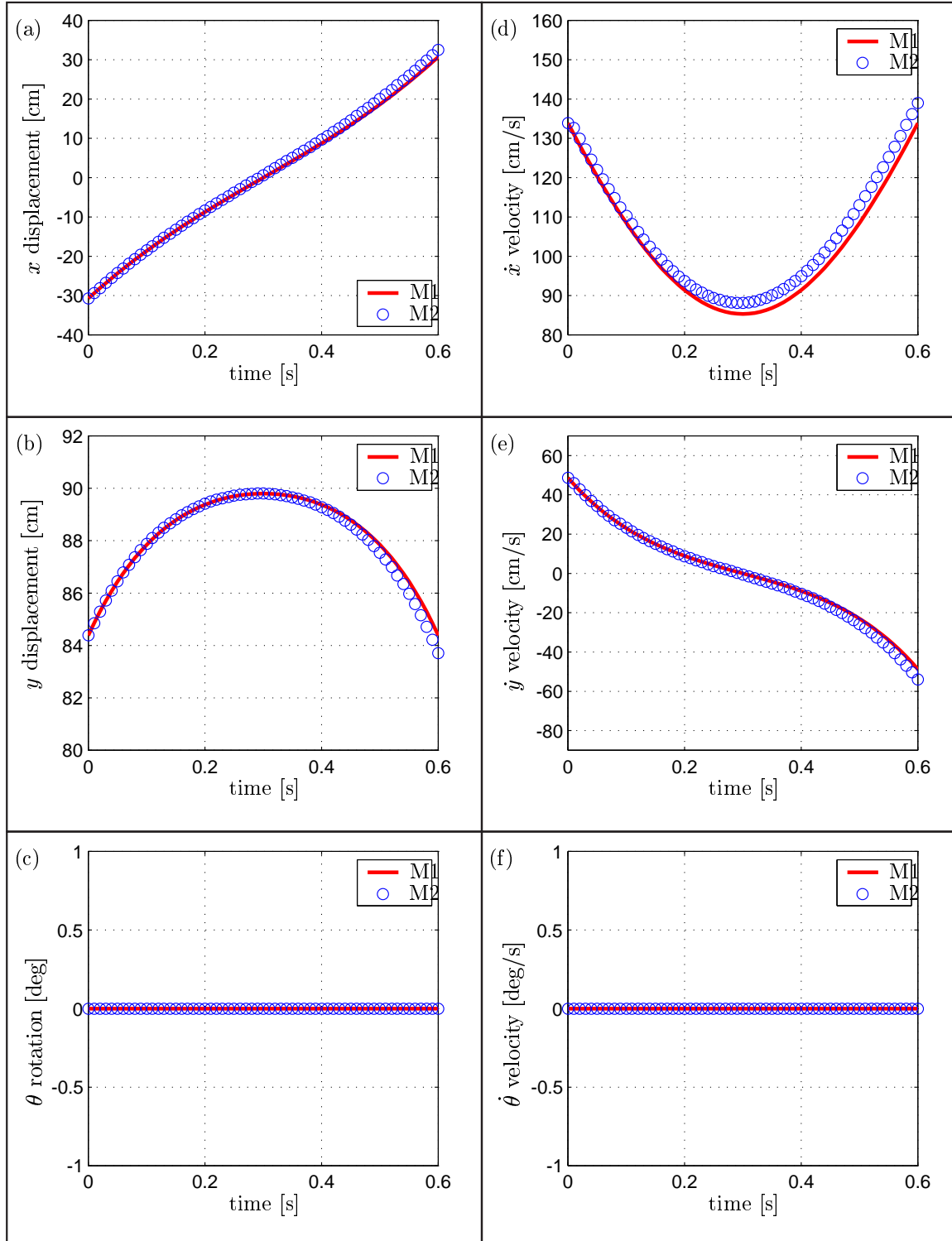


FIGURE 5.2: Comparison of the coupled ballistic gait model, **M2**, to the purely rigid ballistic gait model, **M1**. Position and velocity data for the HAT: (a) x position, (b) y position, (c), θ angular rotation, (d) x velocity, (e), y velocity, (f) $\dot{\theta}$ angular velocity.

FIGURE 5.3 shows the position and velocity for the two translational and one rotational degree of freedom for the swing leg. Just as before, two results are superposed in each of the six subplots. The swing leg has an initial flexion angle of -20 degrees (FIG. 5.3(c)). This angle increases to zero at midstance ($t = 0.3$ s). The swing leg then continues to flex to 20 degrees at the end of the stance phase ($t = 0.6$ s). At this point, the swing leg has the initial angular position that the stance leg had at the beginning of the simulation ($t = 0.0$ s), thus satisfying the symmetry condition of the ballistic gait model.

The angular velocity of the swing leg begins at approximately -0.76 degrees per second. Then, it increases to approximately 100 degrees per second at midstance. Finally, it decreases back to -0.76 degrees per second at the end of the cycle (FIG. 5.3(f)).

The rotation of the swing leg is the only true degree of freedom for this limb segment. The two translational degrees of freedom are constrained by the revolute joint connecting the swing leg to the HAT at the left hip. The position of the stance leg mass center begins at approximately (-42, 53) cm from the origin (FIG. 5.3(a) and (b)). Recall that the origin is selected as the ankle of the stance leg (see FIG. 4.3). The swing leg x position is directly over the origin at midstance and the y position is exactly the distance from the origin to the leg mass center (56.16 cm). Thus we observe that at midstance, the swing and the stance leg share the same positions. The swing leg motion continues from midstance to the end of the simulation in a fashion nearly symmetric with the first half of the cycle.

The velocity of the swing leg in the x direction ranges between approximately 133 cm per second at the beginning and end of the cycle to about about 148 cm per second at midstance (FIG. 5.3(d)). The velocity of the swing leg in the y direction begins at roughly 50 cm per second, goes to zero at midstance, and finishes at about -50 cm per second at the end of the cycle (FIG. 5.3(e)).

FIGURE 5.4 shows the horizontal and vertical ground reaction forces calculated from the ballistic gait models. These results come from the Lagrange multipliers enforcing the rigid-rigid pin joint between the stance leg and the ground. Two results are superposed in each of the two subplots. The solid red line, indicated with the **M1** in the legend, depicts the results for the purely rigid ballistic gait model. The discrete blue circles, indicated by **M2** in the legend, depict the results from the coupled ballistic gait model.

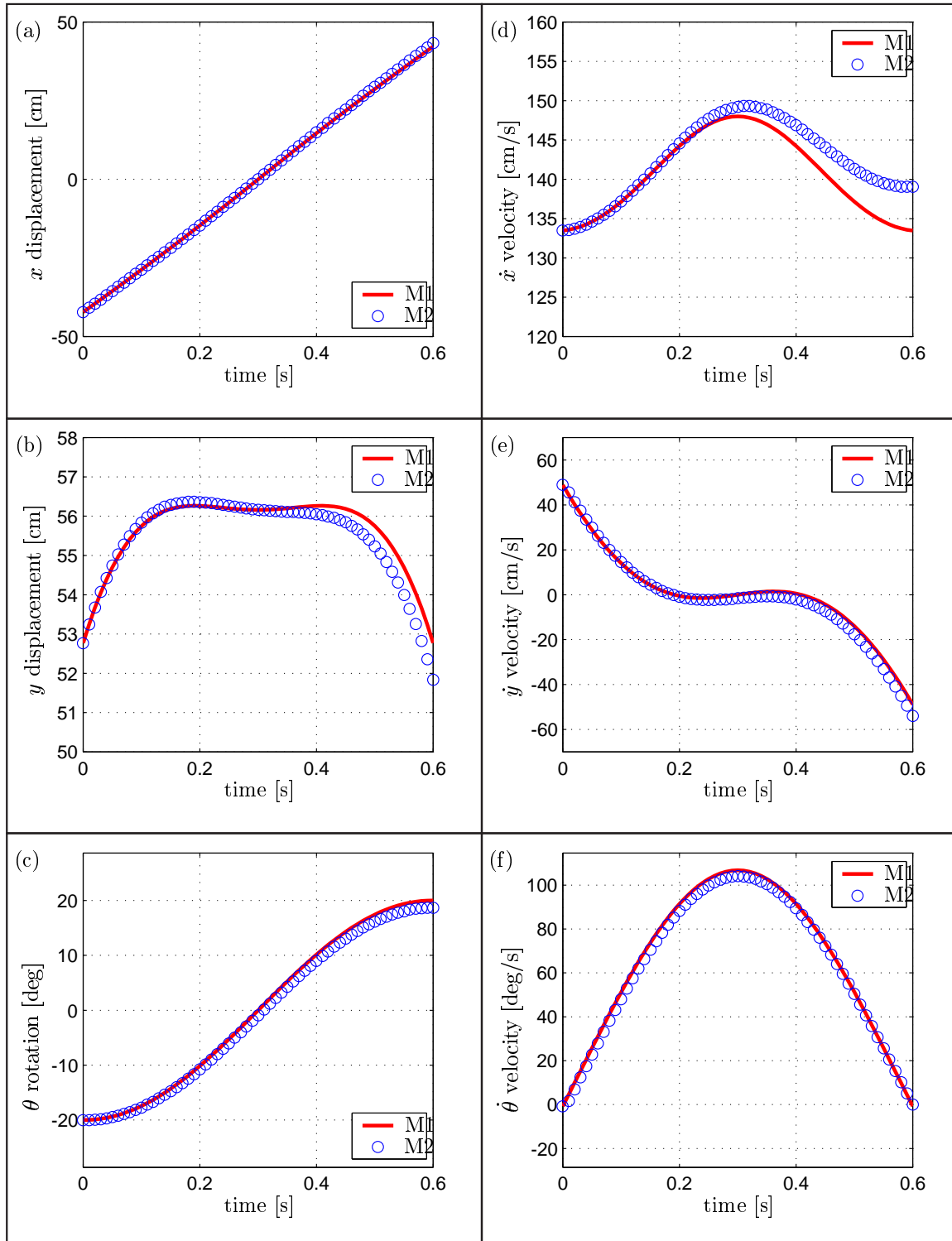


FIGURE 5.3: Comparison of the coupled ballistic gait model, **M2**, to the purely rigid ballistic gait model, **M1**. Position and velocity data for the swing leg: (a) x position, (b) y position, (c), θ angular rotation, (d) x velocity, (e), y velocity, (f) $\dot{\theta}$ angular velocity.

The horizontal reaction force at the beginning of the cycle is approximately -175 N (FIG. 5.4(a)). The force then decreases to zero at midstance. The reaction force then increases to about 175 N at the end of the cycle. The vertical reaction force begins and ends around 500 N (FIG. 5.4(b)). The force peaks at about 700 N at midstance. Body weight of 762 N is plotted in FIG. 5.4(b) for reference.

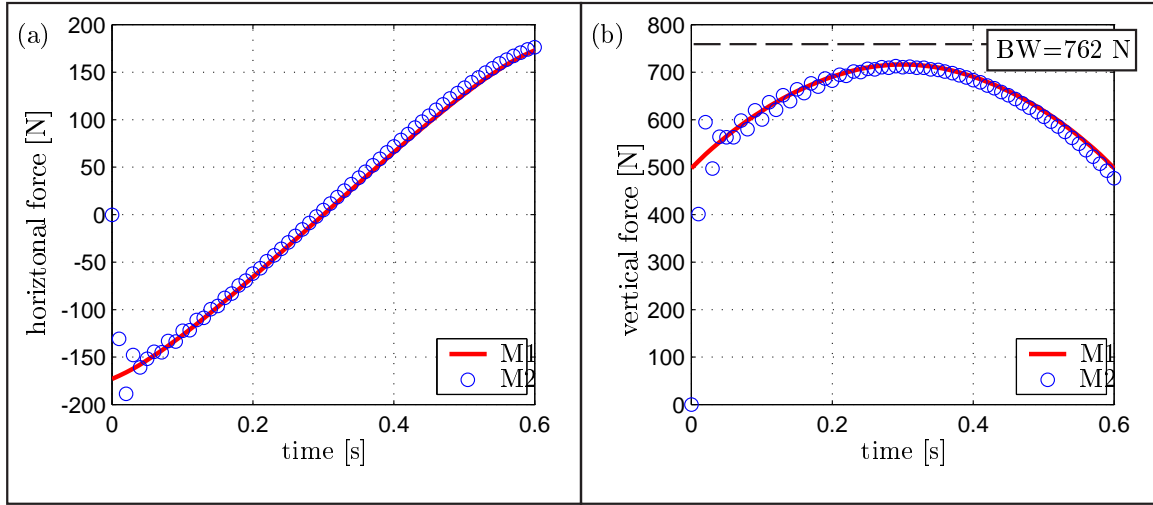


FIGURE 5.4: Comparison of the coupled ballistic gait model, **M2**, to the purely rigid ballistic gait model, **M1**. Ground reaction force between stance leg and floor: (a) horizontal reaction force, (b) vertical reaction force.

FIGURE 5.5 shows the position and velocity for the two translational and one rotational degree of freedom for the stance leg of the **M3** and **M4** models. In contrast to models **M1** and **M2**, these two models include muscle forces at the hip to keep the HAT vertical. Two results are superposed in each of the six subplots. The solid red line, indicated with **M3** in the legend, depicts the results for the purely rigid ballistic gait model with muscles. The discrete blue circles, indicated by **M4** in the legend, depict the results from the coupled ballistic gait model with muscles.

The stance leg has an initial flexion angle of 20 degrees (FIG. 5.5(c)). This angle decreases to zero at midstance ($t = 0.3$ s). The stance leg then continues to extend to -20 degrees at the end of the stance phase ($t = 0.6$ s). At this point, the stance leg has the initial angular position that the swing leg had at the beginning of the simulation ($t = 0.0$ s), thereby satisfying the symmetry condition of the ballistic gait model.

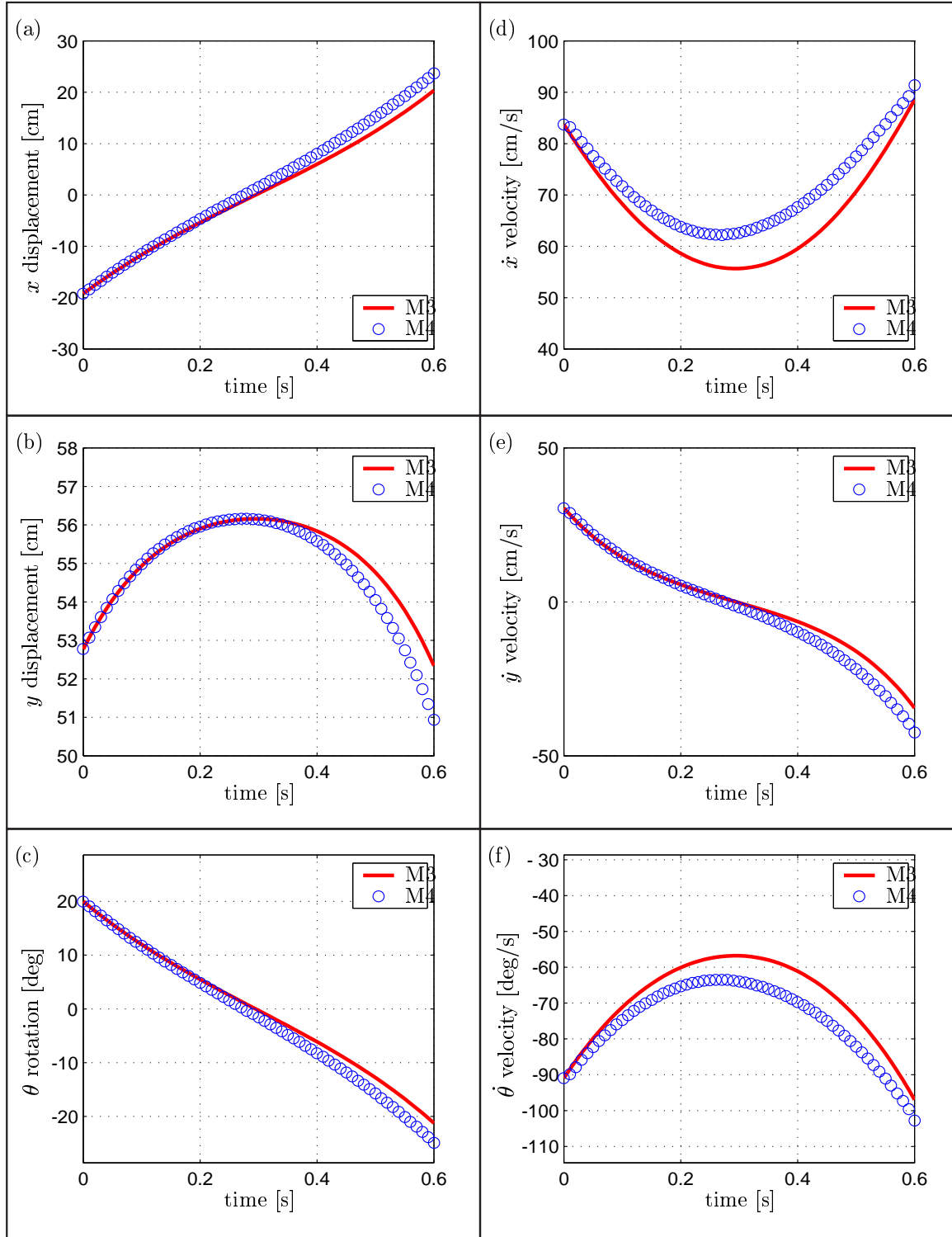


FIGURE 5.5: Comparison of the coupled ballistic gait model with muscles, **M4**, to the purely rigid ballistic gait model with muscles, **M3**. Position and velocity data for the stance leg: (a) x position, (b) y position, (c), θ angular rotation, (d) x velocity, (e), y velocity, (f) θ angular velocity.

The angular velocity of the stance leg begins at approximately -90 degrees per second, decreases to roughly -60 degrees per second at mid-stance, then tends toward -100 degrees per second at the end of the cycle (FIG. 5.5(f)).

The rotation of the stance leg is the only true degree of freedom for this limb segment. The two translational degrees of freedom are constrained because the stance leg is pinned to the ground. The position of the stance leg mass center begins at approximately (-19, 53) cm from the origin, selected as the ankle of the stance leg (see FIG. 5.5(a), FIG. 5.5(b), and FIG. 4.3). The stance leg x position is directly over the origin at midstance and the y position is exactly the distance from the origin to the leg mass center (56.16 cm). The motion continues in a symmetric fashion to the end of the gait cycle.

The velocity of the stance leg in the x direction ranges between approximately 55 cm per second at midstance to about 90 cm per second at the end of the stance cycle (FIG. 5.5(d)). The velocity of the stance leg in the y direction begins at roughly 30 cm per second, goes to zero at midstance, and finishes at about -30 cm per second at the end of the cycle (FIG. 5.5(b)).

FIGURE 5.6 shows the position and velocity for the two translational and one rotational degree of freedom for the HAT. As in FIG. 5.5, two results are superposed in each of the six subplots. The solid red line, indicated with **M3** in the legend, depicts the results for the purely rigid ballistic gait model. The discrete blue circles, indicated by **M4** in the legend, depict the results from the coupled ballistic gait model.

The HAT rotational degrees of freedom is now free to rotate in models **M3** and **M4**. We then added extensor and flexor muscles which attach to the HAT and stance leg. These muscles serve to extend and flex the stance hip joint. We have used the muscles to keep the HAT upright. See SECTION 4.4.2 for a full explanation of how muscles are included and used. Thus, we apply muscle forces that enforce zero angular position and velocity of the HAT.

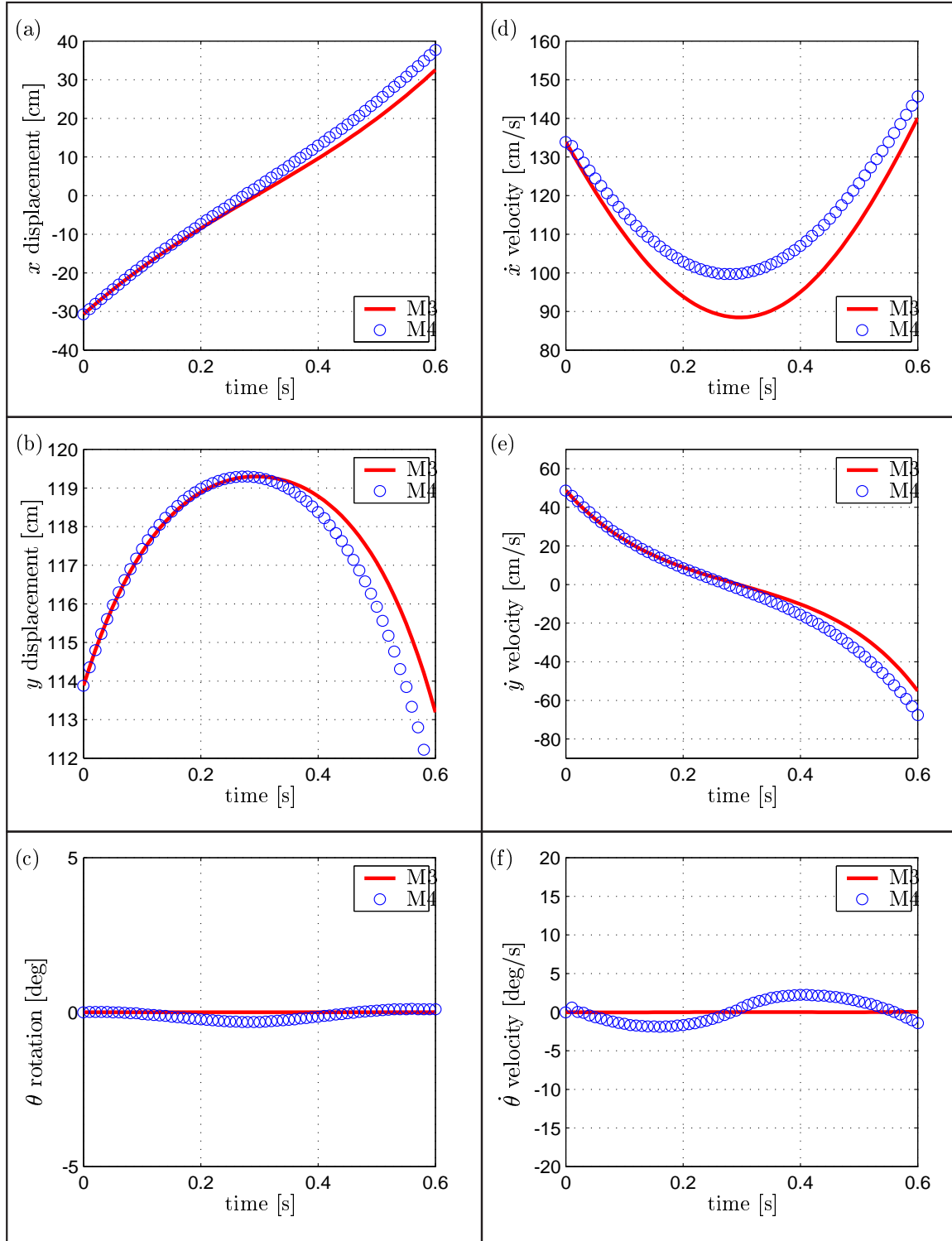


FIGURE 5.6: Comparison of the coupled ballistic gait model with muscles, **M4**, to the purely rigid ballistic gait model with muscles, **M3**. Position and velocity data for the HAT: (a) x position, (b) y position, (c), θ angular rotation, (d) x velocity, (e), y velocity, (f) $\dot{\theta}$ angular velocity.

FIGURE 5.7 shows the position and velocity for the two translational and one rotational degree of freedom for the swing leg. Just as before, two results are superposed in each of the six subplots. The swing leg has an initial flexion angle of -20 degrees (FIG. 5.7(c)). This angle increases to zero at midstance ($t = 0.3$ s). The swing leg then continues to flex to 20 degrees at the end of the stance phase ($t = 0.6$ s). At this point, the swing leg has the initial angular position that the stance leg had at the beginning of the simulation ($t = 0.0$ s), thus satisfying the symmetry condition of the ballistic gait model.

The angular velocity of the stance leg begins at approximately -0.76 degrees per second. Then, it increases to approximately 100 degrees per second at midstance. Finally, it decreases back to -0.76 degrees per second at the end of the cycle (FIG. 5.3(f)).

The rotation of the swing leg is the only true degree of freedom for this limb segment. The two translational degrees of freedom are constrained by the revolute joint connecting the swing leg to the HAT at the left hip. The position of the stance leg mass center begins at approximately (-42, 53) cm from the origin (FIG. 5.7(a) and (b)). Recall that the origin is selected as the ankle of the stance leg (see FIG. 4.3). The swing leg x position is directly over the origin at midstance and the y position is exactly the distance from the origin to the leg mass center (56.16 cm). Thus we observe that at midstance, the swing and the stance leg share the same positions. The swing leg motion continues from midstance to the end of the simulation in a fashion nearly symmetric with the first half of the cycle.

The velocity of the swing leg in the x direction ranges between approximately 133 cm per second at the beginning and end of the cycle to about about 150 cm per second at midstance for the purely rigid model (FIG. 5.7(d)). The coupled model reaches a peak of about 157 cm per second at midstance. Of all the kinematic measurements, the x velocity of the swing leg shows the most drift of the solution caused by the differences in the time integrators. The time integrators used for the purely rigid models and the coupled rigid-deformable models are discussed in SECTION 4.4.3. The velocity of the stance leg in the y direction begins at roughly 50 cm per second, goes to zero at midstance, and finishes at about -50 cm per second at the end of the cycle (FIG. 5.7(b)).

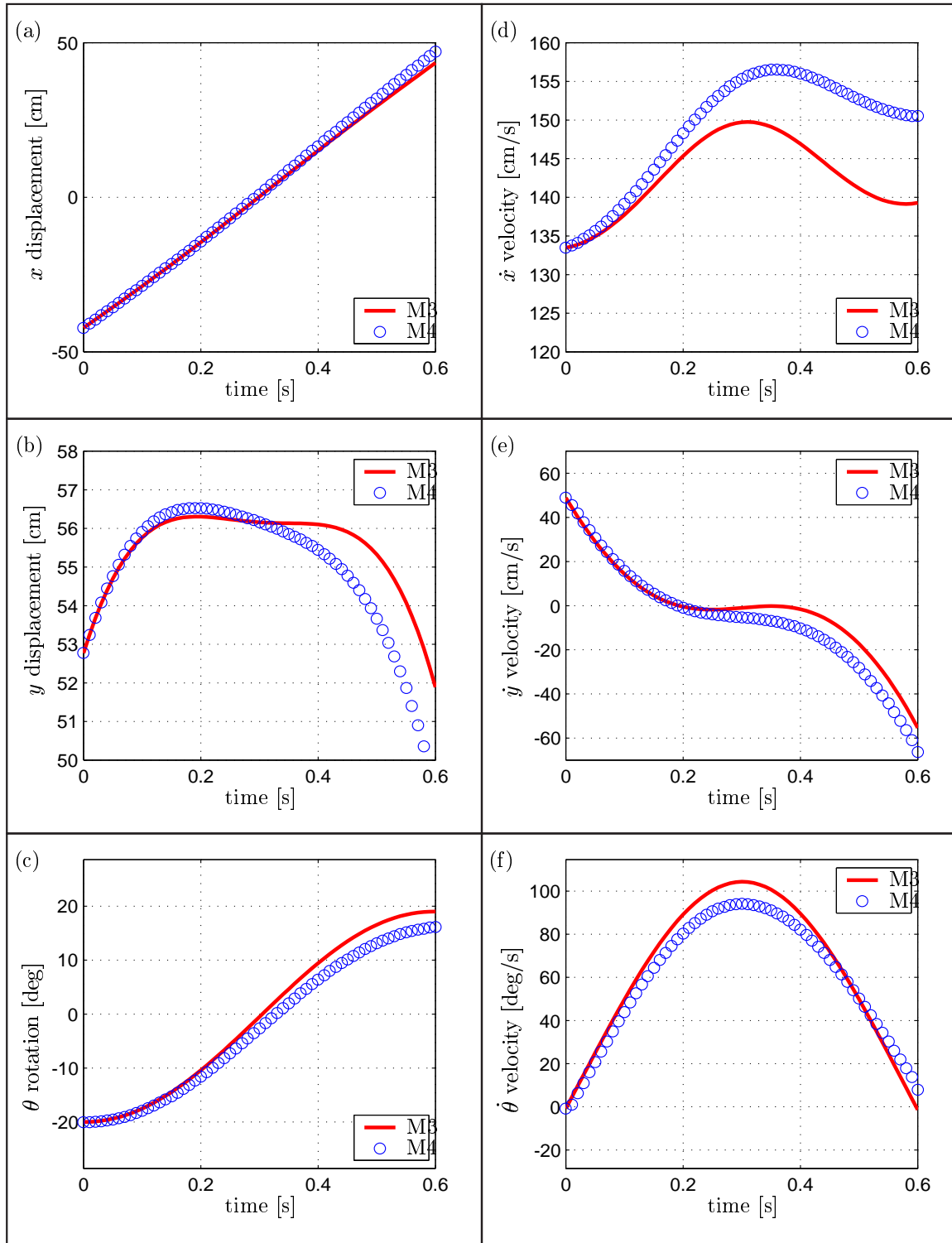


FIGURE 5.7: Comparison of the coupled ballistic gait model with muscles, **M4**, to the purely rigid ballistic gait model with muscles, **M3**. Position and velocity data for the swing leg: (a) x position, (b) y position, (c) θ angular rotation, (d) x velocity, (e), y velocity, (f) $\dot{\theta}$ angular velocity.

FIGURE 5.8 shows the horizontal and vertical ground reaction forces calculated from the ballistic gait models. These results come from the Lagrange multipliers enforcing the rigid-rigid pin joint between the stance leg and the ground. Two results are superposed in each of the two subplots. The solid red line, indicated with the **M3** in the legend, depicts the results for the purely rigid ballistic gait model. The discrete blue circles, indicated by **M4** in the legend, depict the results from the coupled ballistic gait model. The results are similar to results presented in FIG. 5.4, for models **M1** and **M2**.

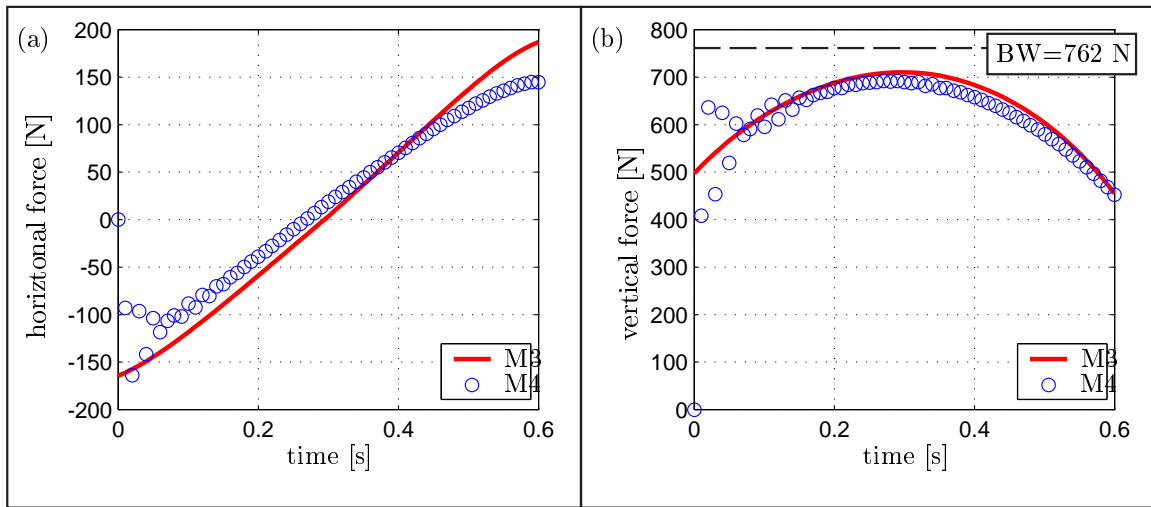


FIGURE 5.8: Comparison of the coupled ballistic gait model with muscles, **M4**, to the purely rigid ballistic gait model with muscles, **M3**. Ground reaction force between stance leg and floor: (a) horizontal reaction force, (b) vertical reaction force.

5.2.2 THE SMALL SCALE

During the ballistic gait cycle, the stance leg rotates relative to the head-arms-trunk (HAT) at the hip joint. In the purely rigid model, **M1** and **M3**, this hip is modeled as a revolute joint. In the coupled model, **M2** and **M4**, this revolute joint is replaced with a finite element mesh representing a sagittal cross-section of a total hip arthroplasty.

The coupled framework allows the joint stress and deformation to be obtained automatically from the same simulation used for the dynamic gait cycle. Consider the stress evolution shown in FIGS. 5.9–5.10.

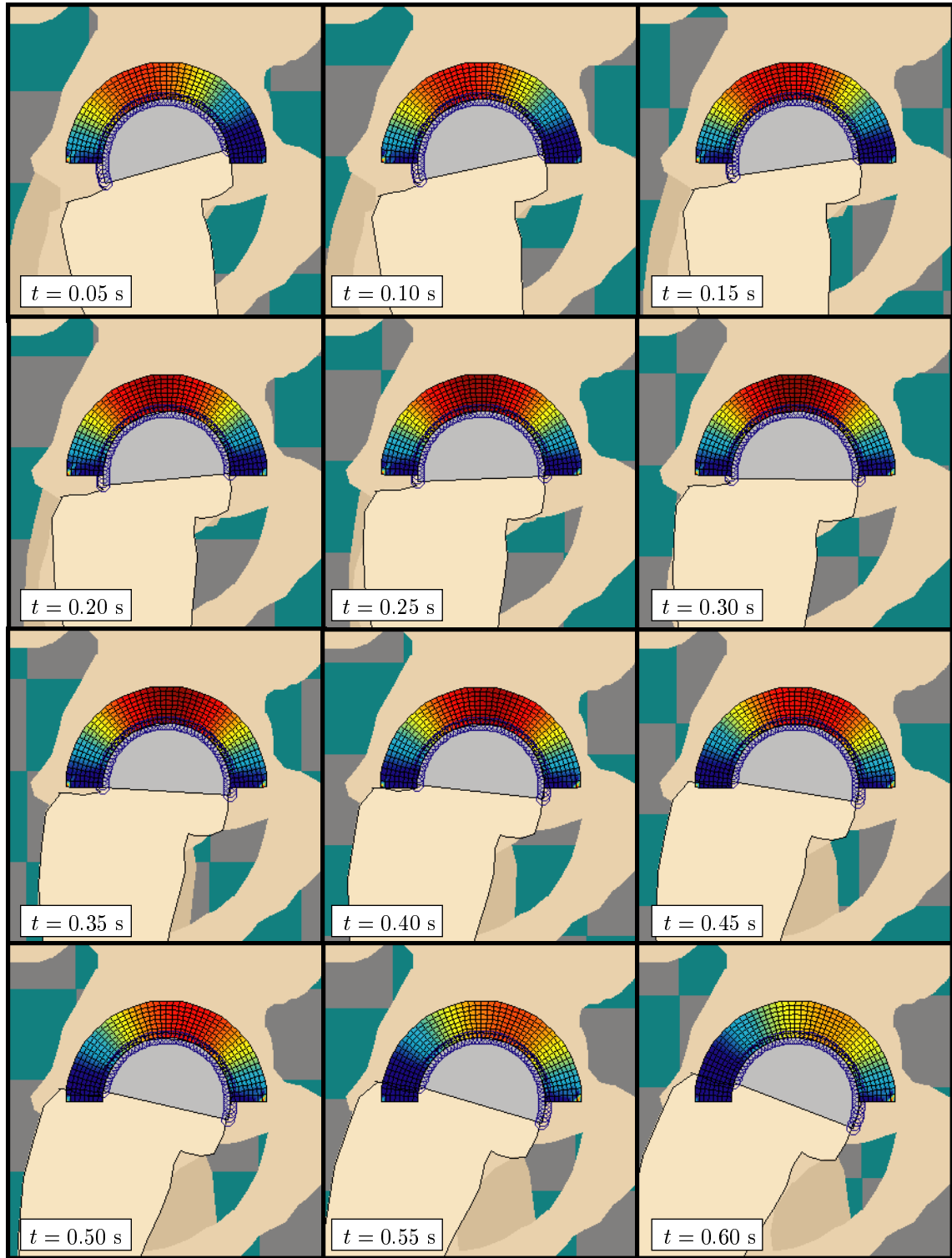


FIGURE 5.9: Hydrostatic pressure time evolution for the coupled ballistic gait model without muscles (**M2**). The scale for stress values appears in FIG. 5.11.

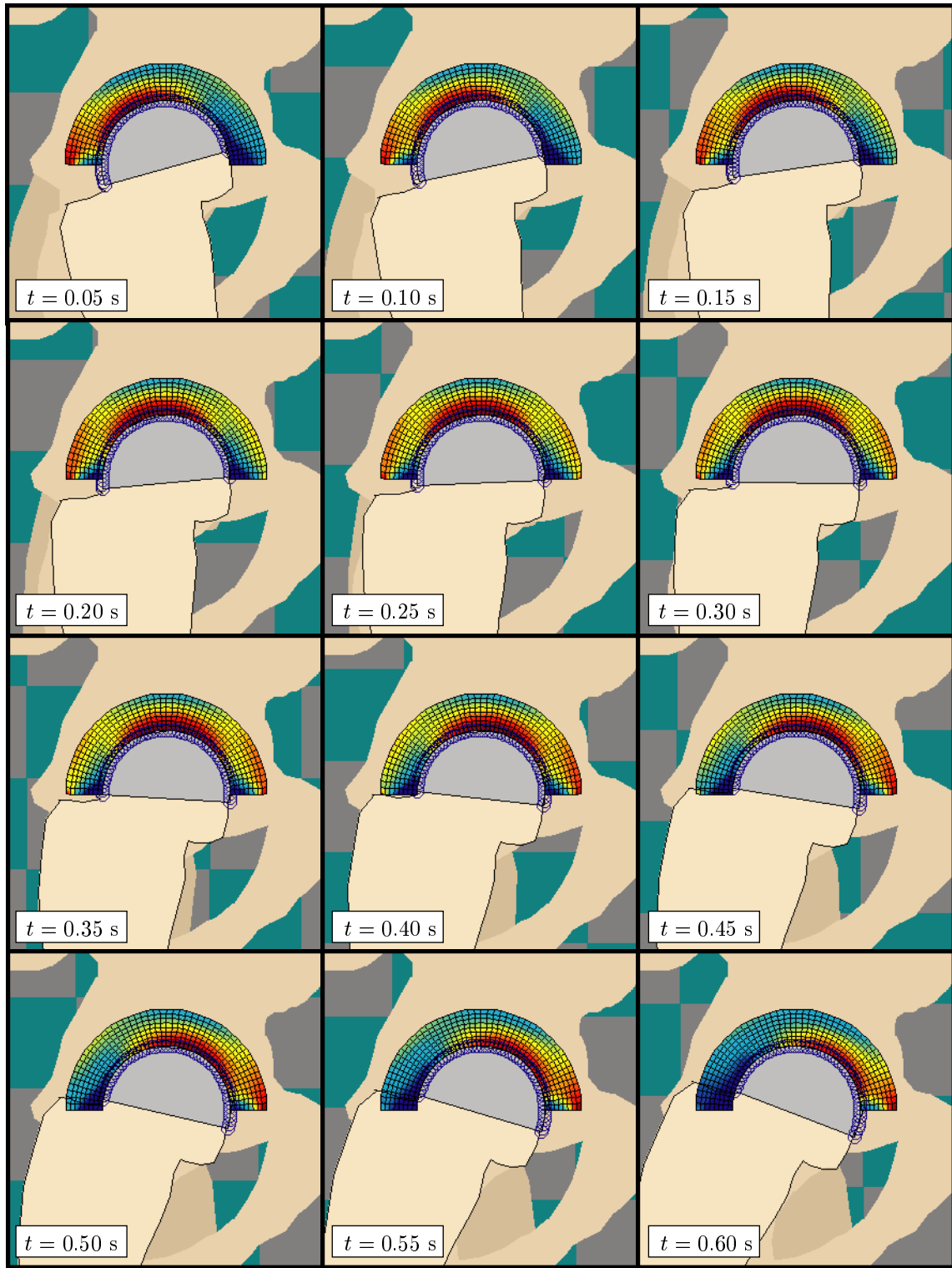


FIGURE 5.10: von Mises stress time evolution for the coupled ballistic gait model without muscles (**M2**). The scale for stress values appears in FIG. 5.12.

The evolution of stance in FIGS. 5.9–5.10 shows a peak in both hydrostatic and von Mises stress at midstance, $t = 0.3$ s. This peak corresponds to the peak in vertical ground reaction force (see FIG. 5.4). The midstance hydrostatic and von Mises stresses are plotted in FIGS. 5.11–5.12. The maximum hydrostatic pressure seen is approximately 2.0 MPa. The maximum hydrostatic pressure acts through the center of the polyethylene, with a slight hour-glass shape observed through the thickness. The stress decreases in a linear, symmetric manner toward the anterior and posterior sections of the liner to zero.

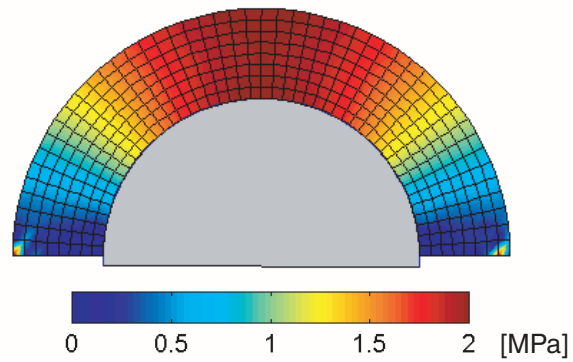


FIGURE 5.11: Hydrostatic pressure for the coupled ballistic gait model without muscles (**M2**) at $t = 0.30$ s.

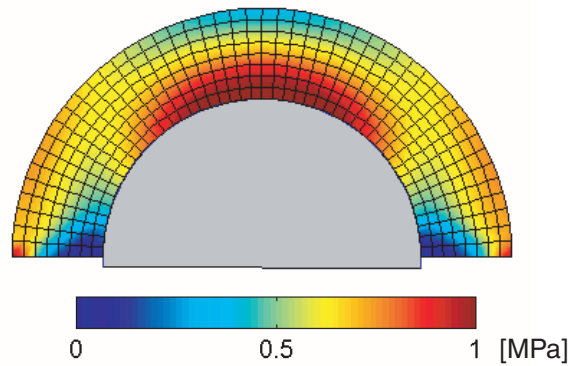


FIGURE 5.12: von Mises stress for the coupled ballistic gait model without muscles (**M2**) at $t = 0.30$ s.

This maximum von Mises stress is found to be on the order of 1 MPa, occurring at the femoral head interface on the inner radius of the polyethylene cup. Most of the cup experiences a 0.5–0.7 MPa von Mises stress, with two small regions of zero stress occurring at the far anterior and posterior sections. The femoral head, polyethylene liner interface is frictionless. It is important to note, however, that the von Mises stress need not be zero at this interface. Rather, the only stipulation on the stress results is that the shear force at that interface, obtained from contracting the stress tensor with the tangent unit vector, be identically zero.

The Cauchy stress σ_{22} component is plotted in FIG. 5.13. This stress component gives a good indication of the compressive stress felt in the vertical (y -axis) direction. A compressive stress of -2.5 to -2.0 MPa is shown directly above the femoral head at midstance.

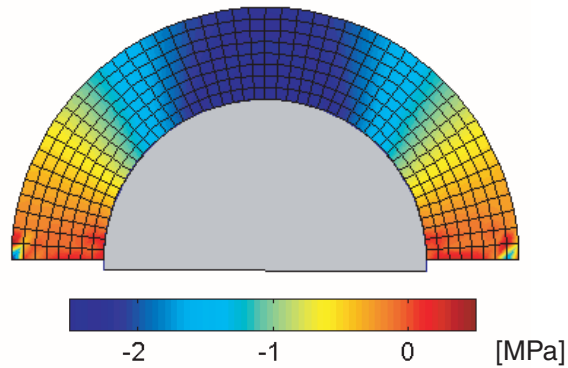


FIGURE 5.13: Stress component σ_{22} for coupled ballistic gait model without muscles at $t = 0.30$ s.

This result is in good agreement with the interface pressure and shear given in FIG. 5.14. The pressures on the inner radius have only a normal component because the interface is frictionless. In contrast, the boundary on the outer radius of the cup is fixed at all nodal points along the boundary, thus both normal and tangential contributions appear. The maximum contact pressure observed is 2.76 MPa, occurring at the centerline of the femoral head at midstance. The inner radius pressure and outer radius pressure-shear show the polyethylene liner to be compressed in the cranial direction. The outer radius result also

shows the cup is being pulled in toward the femoral head as the head tried to push up and through the liner.

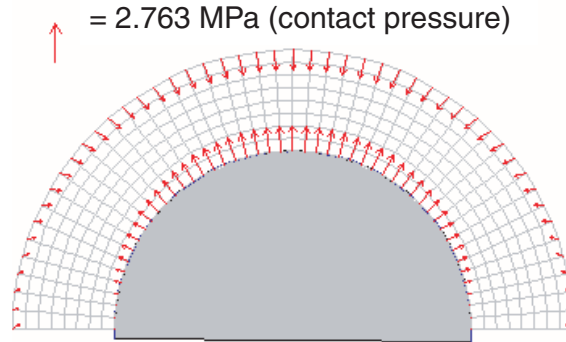


FIGURE 5.14: Inner radius contact pressure, outer radius contract pressure and shear for coupled ballistic gait model without muscles at $t = 0.30$ s.

FIGURE 5.15 shows the maximum and minimum strains in the polyethylene liner. The maximum and minimum strains represent the two eigenvalues of the Green-Lagrange strain tensor \mathbf{E} (see SECTION 2.2, Eq. (2.4), for a definition of \mathbf{E}). The axes on which the maximum and minimum strain occur is also shown. The maximum absolute value of approximately 1,200 micro-strain occurs at midstance just superior to the centerline of the femoral head.

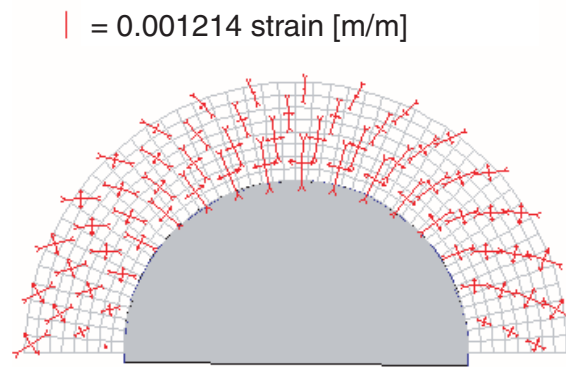


FIGURE 5.15: Maximum and minimum strain for coupled ballistic gait model without muscles at $t = 0.30$ s.

FIGURES. 5.16–5.17 show hydrostatic pressure and von Mises stress in the deformable polyethylene liner for various time steps in the simulation of the coupled ballistic gait model with muscles, model **M4**. Note that the flexor muscle comes within the field of view in these figures. The color of the muscle transitions from blue (zero force) to bright red (maximum force). See SECTION 4.4.2 for a discussion of the muscle forces used in the model.

The same stress scale for hydrostatic pressure, presented in FIG. 5.11, is used for FIG. 5.9 and FIG. 5.16. Similarly, the same stress scale for von Mises stress, presented in FIG. 5.12, is used for FIG. 5.16 and FIG. 5.17. As can be seen in FIGS. 5.16–5.17, the upper bound of the stress scale threshold is too low; much of the finite element mesh appears saturated.

The same stress scales used to create FIG. 5.9 and FIG. 5.10 (showing stress evolution for the ballistic gait model without muscles, **M2**) are used to create FIG. 5.16 and FIG. 5.17 for two reasons. First, using the same thresholding values reveal how significant muscle forces are to the determination of joint stress. Second, the same thresholding values expose that the maximum stress state in the ballistic gait model without muscles, **M2**, is actually the minimum stress state in the ballistic gait model with muscles, **M4**. This result occurs at $t = 0.30$ seconds. At this exact time, there are no muscle forces applied to the **M4** model — see FIG. 4.10. At all other times in the simulation, muscle forces from either extensor or flexor groups cause increased stress and deformation in the hip joint.

The effect of muscle on joint stress is most effectively shown through FIGS. 5.20–5.21. Shown in FIG. 5.20 is the maximum contact pressure between the femoral head the polyethylene liner as a function of time. The pressures are obtained from the Lagrange multipliers enforcing large-slip, unilateral contact, representing the tractions, divided by the tributary area of each finite element facet. The maximum contact pressure from the ballistic gait model with muscles, **M4**, is shown in red and labeled (a). The maximum contact pressures from the ballistic gait model without muscles, **M2**, is shown in blue and labeled (b). Here we clearly see that the maximum contact pressure for the model without muscles is actually the minimum contact pressure for the model with muscles. This result makes sense as we would expect that turning off the muscle forces in model **M4** would tend toward the result from model **M2**, which lacks muscles.

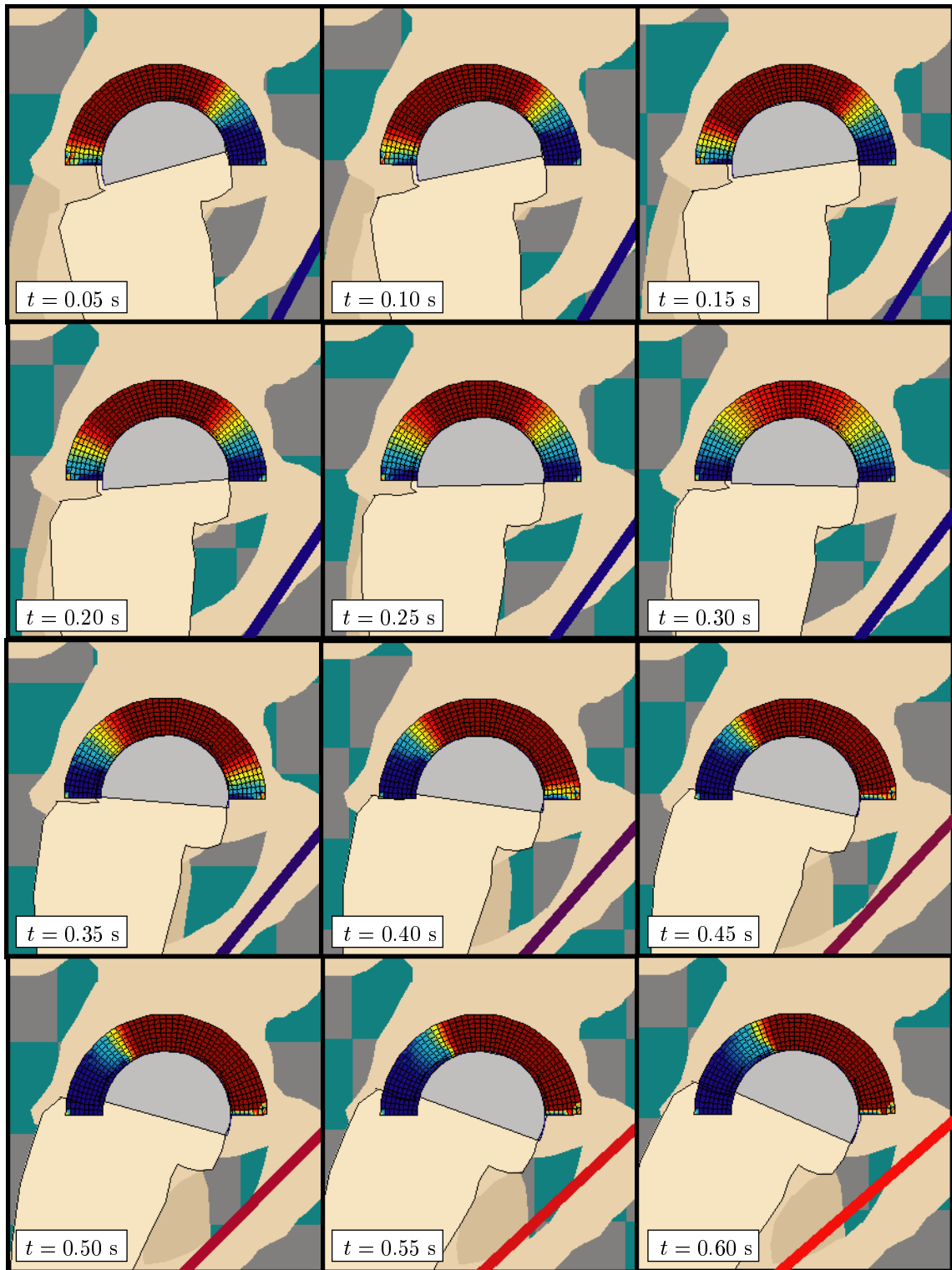


FIGURE 5.16: Hydrostatic pressure time evolution for the coupled ballistic gait model with muscles (**M4**). The scale for stress values appears in FIG. 5.11.



FIGURE 5.17: von Mises stress time evolution for the coupled ballistic gait model with muscles (**M4**). The scale for stress values appears in FIG. 5.12.

5.3 DISCUSSION

Before considering the results from a biomechanical point-of-view, we discuss some of the numerical aspects of the results. In all simulations, rigid body dynamics govern the motion of the stance leg, the swing leg, and the HAT. Nonlinear elastostatics govern the stress and deformation of the deformable finite element mesh. Revolute joints pin the stance leg to the ground and the HAT to the swing leg. These revolute joints are created by holonomic rigid–rigid constraint elements. The deformable mesh moves in the HAT reference frame, and is connected at each node on the outer radius of the mesh to the HAT mass center through deformable–rigid constraint elements. The rigid femoral head of the stance leg and the deformable polyethylene mesh interact through large-slip, unilateral contact. The dynamic motion of the rigid bodies as well as the deformation of the polyethylene hip are fully coupled. Generalized coordinates, displacements, and Lagrange multipliers enforcing the interface constraints are obtained simultaneously using consistent linearization and a Generalized Newton-Raphson Method (GNRM). The equations of motion and equations of constraint are integrated forward in time. At each time step, inertial, gravitational, and internal forces are balanced.

Observe in FIG. 5.4 the high frequency oscillations in the ground reaction forces at the beginning of the simulation. These oscillations are a manifestation of the infinite frequencies associated with the algebraic constraints on the dynamic system. The infinite frequencies, discussed in SECTION 1.2.2, are seen to be well controlled by the damped Newmark time integration scheme ($\beta = 0.3025$ and $\gamma = 0.6$). At approximately 0.05 s, the high frequency oscillations have been effectively damped out, leaving the desired low frequency response.

Though the agreement between the purely rigid and the coupled results is quite good, the agreement is not perfect. The deviations are caused by the differences in accuracy of the two time integrators used to obtain these results. For models composed of purely rigid bodies, **M1** and **M3**, the rigid body dynamics code SMASH was used [60]. This code uses an explicit, fourth order accurate Runge-Kutta time integration scheme. For models composed of both rigid and deformable bodies, **M2** and **M4**, the coupled finite element code TACT, with the elements developed in CHAPTER 3, was used. This code uses the Newmark algorithm for time integration. The parameters $\beta = 0.3025$ and $\gamma = 0.6$ are used

to obtain high frequency damping. With these parameters, the Newmark algorithm, though implicit and unconditionally stable in the linear regime, is only first order accurate.

The HHT- α might be a suitable alternative to the damped Newmark, as it offers not only high frequency dissipation but also second order accuracy [54]. Use of the HHT- α for time integration of differential-algebraic equations was advocated by Cardona, Geradin, and co-workers [21, 40, 41]. Bauchau *et al.* later showed HHT- α (in addition to the trapezoidal rule) to be weakly unstable in the presence of infinite frequencies associated with the Lagrange multipliers [16]. See SECTION 1.2.2 for more detail. We have observed the damped Newmark method, in combination with the elimination of inertial and time derivative terms on the (high stiffness, low density) deformable domain, provides good results for the short time scales of interest here. We refer to this implementation as embedded dynamics. See SECTION 3.3.4 for more details.

Now consider the results from a biomechanical point-of-view. The ground reaction forces agree well with results from other ballistic gait models. This agreement provides confidence that the ballistic model is implemented correctly. The simple ballistic gait model described by Mochon [85] produces a peak vertical ground reaction force of approximately 90% body weight at midstance. Mochon calculates a horizontal ground reaction force of 10% body weight at the beginning of stance, identically zero at midstance, and approximately 20% body weight at the end of stance. The corresponding numbers found from the ballistic gait model (FIG. 5.4) give a peak vertical ground reaction force of 92% body weight. The horizontal ground reaction force starts at approximately 23% body weight, goes through zero at midstance, and increases again to 23% body weight at the end of stance.

Though there is good agreement between the results of ballistic gait models, there is only fair agreement between results from ballistic gait models and clinical data. FIGURE 5.18 shows vertical ground reaction forces from FIG. 5.4 and clinical force plate data. As walking speed increases, the the force magnitude increases and contact time decreases. Therefore, it is necessary to compare the ballistic gait model ground reaction forces in the context of walking speed. The hip of the ballistic gait model moves in the horizontal direction two times the sine of the initial leg angle times the leg length ($2 \cdot \sin(20^\circ) \cdot 89.8 \text{ cm} = 61.4258 \text{ cm}$). This distance is traversed in 0.6 seconds, the simulation time. Therefore the ballistic gait

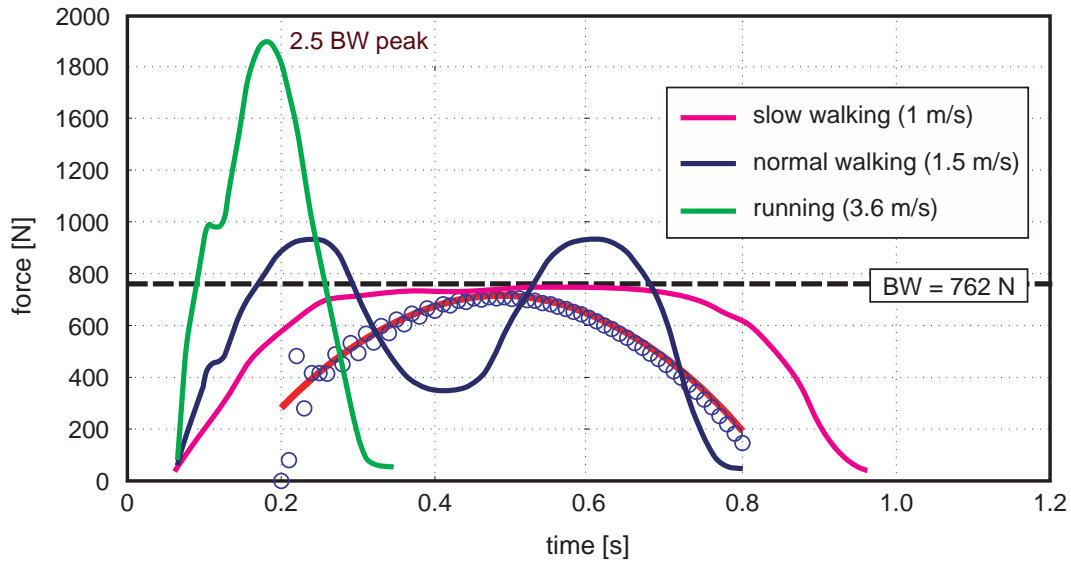


FIGURE 5.18: Comparison of vertical ground reaction force as a function of walking speed, adapted from Perry [97], to vertical ground reaction force from the ballistic gait model M1.

model has a walking speed of $(0.6142 \text{ cm}/0.60 \text{ s}) / 100 \text{ cm} = 1.0238 \text{ m/s}$. Note that this speed is the average of the HAT velocity time history in the x direction, shown in FIG. 5.2(d). The calculated average walking speed corresponds to slow walking in FIG. 5.18.

In the context of this walking speed, we see the ballistic gait model nearly predicts the peak vertical ground reaction force at midstance of one body weight (1 BW). However, the shape of the ground reaction force plot from the ballistic gait model does not predict the rise to and fall from the peak midstance values. Moreover, the ballistic gait model, by its design, cannot account for the ground reaction force occurring during the double stance phases of gait, as observed in FIG. 5.18 at time 0.05 to 0.20 s and 0.80 to 1.00 s, after heel strike and before toe off, respectively. The lack of a double stance phase of gait in the ballistic model may be seen by comparing FIG. 4.2 to FIG. 4.1.

Mochon observed the shortcomings of a simplified ballistic gait model in [85], stating:

“In conclusion, we can say that the simple model presented in this section predicts reasonably well the range of times of swing and angle movements of the limbs, but it fails to give an accurate description of the vertical [ground reaction] force.”

The simple model Mochon refers to is a ballistic gait model with a rigid stance leg, point mass at the hip describing the HAT, and a rigid swing leg. Only the swing leg has a knee. There are two minor differences between Mochon's first simple model and the purely rigid ballistic gait model, **M1**, shown in FIG. 4.2:

1. Mochon's swing leg has a knee; his stance leg does not. In contrast, the ballistic gait models developed in CHAPTER 4, **M1–M4**, do not have knees.
2. Mochon's HAT is represented by a point force at the hip. The ballistic gait models **M1–M4** have a rigid body representing the HAT. Thus, in addition to the weight of the HAT felt at the hip, the dynamics of the HAT are considered.

Mochon obtained better agreement of vertical ground reaction force with clinical data by adding pelvic tilt and ankle dorsi-plantar flexion to his first ballistic gait model. These additions allowed Mochon to obtain the bi-modal appearance of the vertical ground reaction force, shown in FIG. 5.18, normal walking (1.5 m/s). The systematic improvements made to Mochon's models allowed him to conclude [85]:

- “... the mechanism responsible for the first maximum [in vertical ground reaction force] immediately after toeing off is the pelvic tilt.”
- “... ankle angle movement is the mechanism responsible for the second maximum appearing in the vertical [ground reaction] force just before heel strike.”

In addition to ground reaction force, consider the kinematics of gait. The symmetry condition of ballistic gait applies to the angular positions but not the angular velocities of the stance and swing legs. Juxtaposing FIG. 5.1(c) with FIG. 5.3(c), we see that the stance leg end configuration matches the swing leg initial configuration, and vice versa. Comparing the angular velocities of the two legs, FIG. 5.1(f) and FIG. 5.3(f), we see the same type of symmetry condition is not achieved. The symmetry condition is not applied to the velocities because velocity discontinuities occur physically as the leg changes status from stance to swing to stance, and so on. The discontinuities of velocities is perhaps most easily seen by considering the foot just as it completes the swing phase. Just before heel strike, the foot has a nonzero translational and angular velocity. These velocities abruptly go to zero as the

foot transitions from heel strike to a stationary configuration persisting through the stance phase of gait. In the ballistic gait models, the legs comprise all the structures from the foot to the hip. Since the leg is rigid, a velocity discontinuity at the foot must necessarily mean a discontinuity in the velocity of the legs.

In more sophisticated models, where multiple rigid body segments are used to construct the legs, only the foot would be expected to exhibit this velocity discontinuity. Away from the foot, the trajectories of the lower limb and thigh should become smooth. In a model significantly more refined than the ballistic gait model, the velocity discontinuities would begin to appear as sharp but continuous changes. Since the limb positions observed clinically are not only continuous, but also smooth, one would expect the velocity time histories to be continuous. Although continuous, the velocity time histories may not be smooth, resulting in discontinuities in the accelerations. Acceleration discontinuities may result from forces instantly applied to or released from the dynamic system. Since integration is an operation which smooths, one would expect integration of the governing second order differential equations (see Box 2.3), even in the presence of instantaneously applied forces, to produce smooth velocity and position time histories.

FIGURE 5.19 shows the stance and swing leg angles from the model **M1** plotted over experimentally obtained clinical thigh angles from Winter [117]. The ballistic gait model closely predicts the maximum angle (25 degrees) and minimum angle (-18 degrees) of the thigh. Though the curves follow the same trend, significant differences are seen in the swing phase of gait (0.9–1.4 seconds in FIG. 5.19). The ballistic gait model could better match during the swing phase if a knee were included. The presence of a swing leg knee would allow the leg to bend, producing an increase in the thigh angles at an earlier time in the gait cycle.

Models **M1** and **M2** lack control systems, such as muscles, and are therefore driven solely by the effects of gravity and the initial trajectories of the limb segments. The purely rigid model and the coupled model have identical geometry, mass, and initial conditions. The key difference between the two models is the description of the hip joint connecting the stance leg and the HAT. The purely rigid model has a revolute joint. The coupled model has a total hip arthroplasty composed of a rigid femoral head and acetabular liner articulating

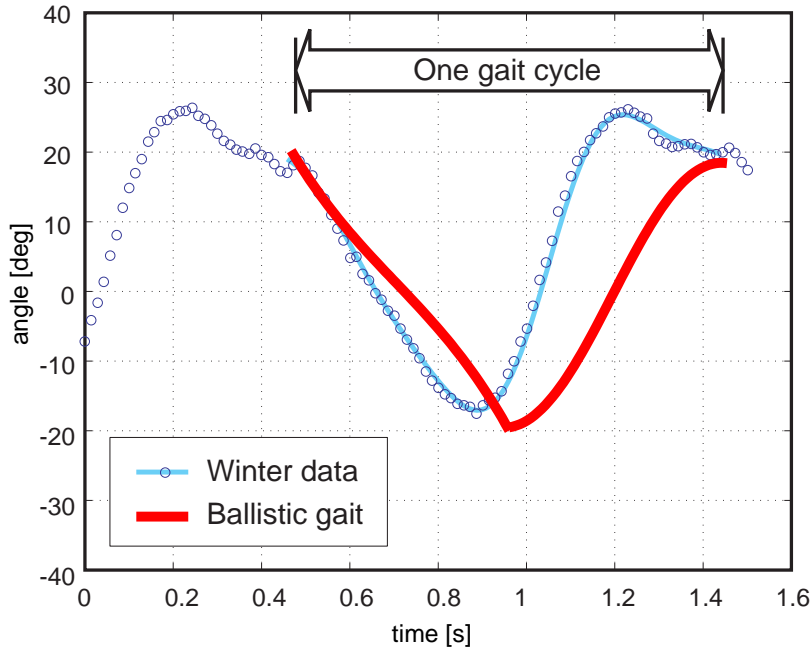


FIGURE 5.19: Comparison of clinical thigh angle measured in a gait laboratory by Winter [117] compared to leg angle calculated from the ballistic gait model **M1**.

a deformable ultra-high-molecular-weight-polyethylene (UHMWPE) liner. Based on the results, we can make the conclusion:

- The similarity in the state time histories of the purely rigid ballistic gait model, **M1**, and the coupled ballistic gait model, **M2**, suggest that the deformation of the joint plays a minor role in the dynamics of gait.

This conclusion is made in the context of having a coupled model with a stiff yet deformable material (UHMWPE, $E = 974$ MPa, $\nu = 0.46$) at the hip joint. There may be less similarity between the results from the purely rigid model and the results from the coupled model if the material used for the joint, such as cartilage, is more compliant. A joint that is several orders of magnitude less stiff than UHMWPE arthroplasty might produce deformations large enough to influence the dynamics of the gait cycle.

As we consider the results for the coupled ballistic gait model **M2**, we see that the stresses are significantly lower than those obtained by Bartel [15], Maxian [78], Kurtz [67], and the validation study, discussed in SECTION 4.5. Referring to FIG. 4.11, we see the maximum contact pressures to be in the range of 10–16 MPa. In contrast, the maximum

contact pressure from the coupled ballistic gait model, **M2**, produces a maximum contact pressure of 2.76 MPa, shown in FIG. 5.14. Thus, the contact pressures obtained from the purely ballistic gait model are 3.6–5.8 times lower than what we would expect to see physiologically.

The studies mentioned in SECTION 4.5 use a static load to represent the hip contact force, which accounts for the effects of inertia, gravity, and muscles. Load magnitudes on the order of 3000 N, used in Bartel [15], Kurtz [67] and the validation study (in SECTION 4.5), are justified from experimental data, such as that from Bergmann [18]. With a telemeterized hip prosthesis, Bergmann’s subjects, walking between 0.28–1.39 m/s, produced a hip reaction force of 2.8–4.8 times body weight, respectively. For the 762 N model discussed in CHAPTER 4, the hip force would correspond to 2134–3658 N.

Critically absent from models **M1** and **M2** is the effect of muscle contraction on the joint. The absence of such muscle forces results in joint stress and deformation that are too low to be considered physiologically meaningful. This shortcoming of ballistic gait motivates the subsequent investigation where extensor and flexor muscles are added to the ballistic gait model.

Considering FIG. 5.2(c) and (f), we conclude that the muscle forces we have used as inputs for the model, shown in FIG. 4.10, keep the HAT upright as desired. Keeping the HAT upright with muscles in models **M3** and **M4** produces kinematics that are very similar to those produced by models **M1** and **M2** (models without muscles and blocked HAT rotation). This similarity is expected as we are attempting to achieve the same kinematics across all models. Differences will be observed at the reaction force at the hip. The extensors and flexors are turned on to produce the correct resultant moment which keeps the HAT upright. This resultant moment is generated by a muscle force and lever arm defined by the origin and insertion of each muscle group. The contraction force of the muscles compresses the HAT and stance leg together. This compressive force will be manifest as increased stress and deformation in the polyethylene liner as the internal forces now must balance muscle forces in addition to the gravity and inertial forces.

Shown in green in FIG. 5.20 is the range of contact pressures expected during toe-off. Contact pressures within this range have been reported by Bartel [15], Maxian [78], and

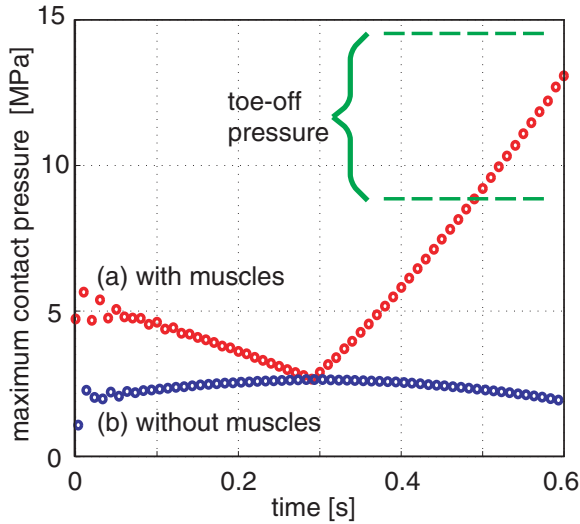


FIGURE 5.20: Comparison maximum contact pressure for the coupled ballistic gait model (a) with muscles, and (b) without muscles.

Kurtz [67]. See SECTION 4.5 for more detail. Comparing the contact pressures obtained from model **M4** with the expected physiological contact pressures, we can conclude that muscle forces must be included in the gait model to obtain meaningful stress and deformation results. This conclusion is further reinforced by the results shown in FIG. 5.21. Here, the resultant hip force as a percentage of body weight is plotted over the gait cycle. Clinical data from Bergmann's telemeterized hip prosthesis are superposed in green [18]. The toe-off peak around 300% body weight is absent in both models, **M2** and **M4**. The coupled ballistic gait model with muscles, **M4**, however, does begin to approximate the clinical hip reaction force near the end of the gait cycle.

The simplicity of the walking model limits its ability to produce physiological results. Aside from the limitations inherent to a simple ballistic gait model (namely, the lack of pelvic list, knee joints, and ankle flexion, discussed in SECTION 5.2.1), limitations of the muscle model are present. These muscle limitations take four forms.

1. Model **M4** lacks hip abductor muscles; it has only extensor and flexor muscles. The abductor muscles have been shown experimentally to produce a hip reaction force of 1.8–2.7 times body weight during one-legged stance [83]. The hip abductors act in the frontal plane, balancing the moment caused by gravity on the HAT and swing leg.

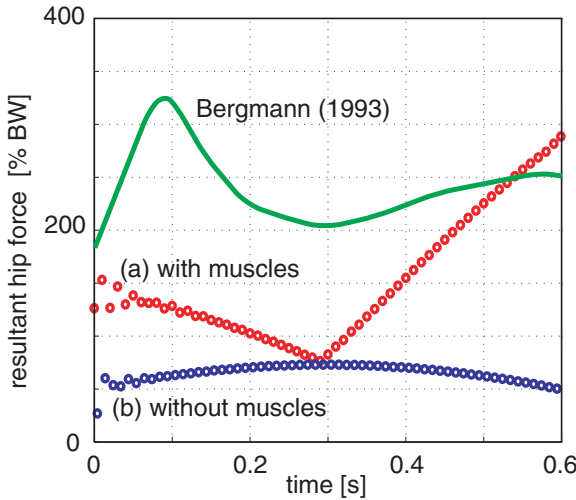


FIGURE 5.21: Comparison maximum contact pressure for the coupled ballistic gait model (a) with muscles, and (b) without muscles.

Because the models used here are only two dimensional, it is difficult to account for muscle forces acting outside of the sagittal plane. Therefore, we see that the planar assumption of the model ultimately limits the representation of muscles.

2. The extensor muscles are lumped into one generalized extensor group with a single origin and single insertion, as described in SECTION 4.4.2. The same lumping procedure is used for the flexors. Having only one flexor muscle and one extensor muscle severely oversimplifies the geometry and complexity of the musculoskeletal system.
3. Keeping the HAT upright during the entire gait cycle was the objective set for the determination of the muscle forces. This objective seems, in part, reasonable as we know the HAT remains nearly upright during walking. However, such a simple objective may ultimately not be appropriate to capture the complexity of the neuromuscular system. Other objective functions, such as minimizing muscle stress or minimizing muscle work, may produce more clinically accurate results.
4. The internal forces in the muscles are completely specified through boundary schedules present in the input file. Thus the muscles present here operate more like an actuator than a true muscle. Incorporating force-length and force-velocity relationships, as well as activation dynamics, would yield a model with muscles that are more realistic.

Despite the shortcomings listed above, it is important to emphasize first that the limitations of the ballistic gait model in no way translate into limitations on the coupled deformable-rigid framework developed in CHAPTERS 2–3. The lack of agreement between the simulations and the experimental results is due to simplifications of the underlying ballistic gait model, not in the formulation or implementation of the finite element tools used to construct the model.

Additionally, the shortcomings may be tempered by the fact that the coupled ballistic gait model represents, to our knowledge, the first time a biomechanical model has been proposed which fully couples the dynamics of gait with the deformation of the joint. Many biomechaical models consider rigid body gait analysis. Other biomechanical models consider deformable joints. The coupled ballistic gait model represents the fusion of these two approaches.

The results from this section help answer the first question raised in the introduction of CHAPTER 5, regarding the relative weight that should be given to either gait dynamics or muscle force in the determination of joint stress and deformation. Based on the results shown FIGS. 5.20–5.21, we make the following conclusion:

- For slow gait, which is modeled here at approximately 1 m/s, the effects of muscles forces are far greater than the dynamics of gait on the resulting stress and deformation at the hip.

In addition to answering this question, we hoped to shed light on the relative merits of the coupled framework compared to an uncoupled approach. The uncoupled approach consists of performing the rigid body dynamic analysis and calculating the reaction forces, say at the revolute hip joint. Then, these reaction forces obtained from the purely dynamics model are applied, perhaps in a distributed parabolic fashion, to a static joint model.

A resounding theme found in the results from the coupled models with (**M4**) and without (**M2**) muscles was that deformations of the stiff, polyethylene joint were too small to influence the dynamics of the gait simulation. Therefore, such results suggest that the uncoupled approach is satisfactory for hip arthroplasty wear studies. A few caveats are in order, however.

First, recall that slow gait was modeled. As the gait speed increases, or as the activity

changes from gait to running or falling, the inertial forces of the activity will play a larger role. The increased inertial forces from rigid bodies will be felt through increased internal forces and deformations in the deformable bodies. If the deformations become large enough, they may change the dynamics of the system.

Second, recall the deformable joint was modeled with stiff polyethylene. If the joint were composed of cartilage, which is known to be many times more compliant than polyethylene, the deformations observed in the coupled system may be significantly higher. Therefore, the uncoupled approach may no longer remain valid for models with soft joints.

Finally, the results from the coupled ballistic gait models provide some validation for the uncoupled approach adopted by Maxian [78] and by Kurtz [67]. Both research groups have provided valuable insights on the wear of total hip arthroplasty. However, such studies has been based on an uncoupled approach where a joint load is statically applied to a deformable polyethylene mesh. There was always a tacit assumption underlying such models — the assumption that the coupling between the dynamics of gait and the deformation of the joint was weak enough to justify a purely static analysis. The results from the coupled ballistic gait models confirm this assumption.

CHAPTER 5 has presented results from a novel biomechanical model, which, for the first time, fully couples joint deformation with limb dynamics. As a consequence, the framework presented here allows changes in gait to be automatically reflected in joint stress and deformation. Similarly, joint deformations, if large enough to alter the positions of the mass centers of the attached rigid bodies, affect the dynamics of the rigid body model. The coupling is exactly enforced through augmented Lagrange multipliers. The solution of both primal and dual variables simultaneously allows the entire coupled system to be solved in a single analysis.

CHAPTER 6

CONCLUSIONS

6.1 REVIEW

The main goal of this thesis work was to construct a computational biomechanical model of a diarthrodial joint undergoing finite deformation in a dynamic simulation of human gait.

This was accomplished through the development of several elements including rigid elements and those designed to couple rigid and deformable domains. The implementation grew from a finite element code which uses standard deformable finite elements as its main element type. The code was then expanded to include rigid finite elements, as well as holonomic and nonholonomic interface elements.

The implementation of rigid bodies resulted in modular elements that can be assembled through a connectivity array just like traditional finite elements. In this sense, a rigid element is included in a finite element analysis just as if it were any other type of finite element. The clear distinction from deformable elements is that rigid elements only have inertial and external force terms — there are no internal force terms by virtue of the rigid assumption.

An embedded time stepping implementation was developed, which allows the rigid body velocity and accelerations to be included as element degrees of freedom. The time stepping algorithm is then included as additional element equations. The embedded rigid body dynamics, in conjunction with elastostatics from standard finite element codes, can be used to solve the coupled deformable-rigid problems in a compact, nonlinear, elliptic setting.

TABLE 6.1: Summary of elements developed for the finite element implementation.

Element Type	Form
Rigid	Standard Embedded
Equality Constraints	Deformable-Deformable Deformable-Rigid Deformable-Rigid Embedded Rigid-Rigid Rigid-Rigid Embedded
Contact (Inequality Constraints)	Deformable-Rigid Deformable-Rigid Embedded
Muscle	Rigid-Rigid Embedded Dashpot Deformable-Deformable Spring Deformable-Deformable Force Actuator Deformable-Deformable-Rigid Moment Actuator

Holonomic constraint elements used to produce deformable-deformable, deformable-rigid, or rigid-rigid connections were constructed. Unilateral, large-slip contact elements were developed to allow smooth, frictionless interactions between dynamic, rigid bodies and deformable bodies. Forms compatible with standard and embedded dynamics approaches were developed. Rudimentary muscle elements were developed to provide geometrically nonlinear stiffness, damping, and actuation between bodies.

In total, 13 elements were coded: two rigid elements, five equality constraint elements, two contact (inequality constraint) elements, and four muscle elements (see TAB. 6.1).

These developments in the computational setting allowed a biomechanical model to be developed that uniquely combined the dynamics of gait with the stress and motion of a deformable joint. The unified approach integrates the link between motion that we might observe in a gait laboratory and joint stress that we cannot readily ascertain. Lagrange multipliers provide for reaction forces at interfaces between all types of bodies. These data provide quantities such as ground reaction force. Because ground reaction forces can be

easily measured in a gait laboratory with the use of force plate transducers, they may serve as a benchmark for the calculated ground reaction forces and to validate computational models. Moreover, the Lagrange multipliers provide interface pressure and shear in the nonholonomic case. These quantities are useful for engineers seeking to improve the design of arthroplasty.

The biomechanical models presented in CHAPTER 4 produced many results. Extracted from CHAPTER 5, these results are briefly summarized:

- The coupled ballistic gait models can predict experimentally measured thigh motion. However, such models do not accurately predict clinical ground reaction forces. See SECTION 6.2 for detail on the limitations of the model.
- The ballistic gait model, with contributions from inertial and gravity forces alone, does not produce stress or a hip resultant load which matches clinical data. The effects of muscles must be included to accurately portray the stress and deformation of the polyethylene liner.
- There is a small or perhaps negligible effect of joint deformation on the dynamic ballistic gait model. This conclusion rests on having a stiff (UHMWPE, $E = 974$ MPa, $\nu = 0.46$) deformable body at joint.
- The minimal effect that polyethylene deformation has on the dynamics of gait supports the uncoupled approaches (such as those by Maxian [78] or Kurtz [67]) to determine arthroplasty stress and deformation. Such approaches however, unlike the one described here, cannot account for motion of rigid body modes in a quasi-static framework.
- Muscle forces have a significantly greater effect than gait dynamics on the stress and deformation of the joint at slow walking speeds (under 1 m/s). The relative contribution from the inertial and gravity forces may outweigh the effects of musculoskeletal forces during other forms of movement, such as running or falling.

6.2 LIMITATIONS

- The time integration scheme for the coupled formulation developed in TACT is only first order accurate. Using trapezoidal rule, which is the second order variant of the Newmark method, resulted in the excitation of the infinite frequencies associated with the constraint equations. A time integrator that both damps out high frequencies and has higher order accuracy would represent an improvement upon the current implementation.
- The deformable-rigid contact element is two dimensional. Formulating the element in three dimensions while accounting for the dynamics of the target surface will greatly complicate the implementation, especially in the terms involving rotations.
- The embedded dynamics framework should be used only when the dynamics of the deformable domain are deemed to be insignificant compared to the dynamics of the rigid domain. Such a case may arise when the deformable domain has very high stiffness and very low mass. The associated high frequency contributions to a coupled system are likely unimportant and may serve only to impose unrealistically small time step restrictions and ultimately pollute the solution.
- The deformable body domain can be considered to be dynamic (hyperbolic) in the coupled framework. The deformable domain only must be considered elliptic for the embedded formulation. For a system composed of rigid and deformable bodies, where the deformable body has either low stiffness, or high mass (or both) the dynamics of both the rigid and deformable domains should be considered. In this case, the embedded formulation should be avoided entirely, and the time stepping algorithm should be applied to both (deformable and rigid) governing sets of equations, as described in CHAPTERS 2–3.
- The ballistic gait model models used in CHAPTER 4 cannot predict the bi-modal shape of vertical ground reaction force during normal speed gait. Improvements to the ballistic gait model, including pelvic list and ankle flexion, are required to achieve the bi-modal vertical reaction force.

- The models with muscles have only hip extensor and flexor muscles. The effect of hip abduction muscles is not considered. Taking hip abduction into account would increase the hip reaction force and bring the hip contact stress results into agreement with clinical data.
- The geometry of the muscles has a single, lumped extensor muscle and a single, lumped flexor muscle. There are no via points to the muscles. Adding a greater number of muscles with via point capabilities would enhance the fidelity of the muscle model to the underlying anatomy.
- The muscle model contraction mechanism is oversimplified. The implementation here works more like an actuator than a true muscle. Including force-length, force-velocity, and activation dynamics would better represent the muscle physiology.

6.3 APPLICATION

The coupled framework developed in this thesis may help lay the ground work for new and innovative research in biomechanics, especially as it relates to determining joint stress and deformation using clinical gait data. New clinically relevant questions may be explored using the coupled technology, such as:

- Do people alter their locomotion strategy to minimize joint stress?

For example, a person who is observed to limp may have a joint injury. The limping gait data might be used as kinematic inputs to a coupled model, and joint stress and deformation may be obtained from the coupled approach. Furthermore, one may ask:

- How do activities other than gait, such as running, stair climbing, or jumping alter states of stress and deformation at the joint?

The coupled framework developed here is extensible to activities other than walking. Only the dynamic model need change, either through increased number of rigid bodies or through changes in the initial conditions. Finally, in a world where MRI data is being used more extensively to noninvasively visualize the inner structures of the human body, one may be inclined to ask:

- Can MRI data be used in conjunction with clinically-obtained gait data to provide designers with the parameters needed to produce a custom fit joint replacement?

One might envision using MRI scans of a patient's bone geometry for development of the arthroplasty design, to assure good fit and compatibility. Then the design geometry and material properties may be used as model inputs for a deformable finite element joint model. In conjunction, the individual's gait patterns may be used to build a rigid body limb dynamics model. Finally, the large and small scale models may then be used with the coupled framework proposed here to evaluate the performance of the proposed joint replacement.

6.4 FUTURE WORK

Fruitful areas of future work include the continued bridging of length scales — the large length scale composed of rigid links used to model limb segments, and the small length scale composed of finite element joint models. Although the jump from two to three dimensions sounds appealing, perhaps more ground could be gained by retaining the two dimensional (sagittal plane) setting, but adding more sophistication in other areas. For example, activation dynamics, force-length, and force-velocity relationships could be added to the muscle model. Additional joint segments could be added. These two enhancements might well represent the most tractable next steps.

APPENDIX A

FORMULATION DETAILS

A.1 OVERVIEW

APPENDIX A contains details of the formulation in CHAPTER 2. These details are ultimately necessary for successful implementation of the formulation into a finite element code.

APPENDIX A first records the linearization procedure of the internal force operator appearing in the weak form of the initial boundary value problem (see Box 2.2) as it applies to the context of finite element analysis (see SECTION 3.2). Next, results from rigid body dynamics pertaining to differentiation appear. The first and second variations of generalized, three-dimensional equality constraints are subsequently derived. The first and second variations of the inequality rigid-deformable contact constraint are then shown. Finally, the first and second variations of the fully coupled deformable domain, rigid domain, equality and inequality constrained problem are presented in indicial notation.

A.2 DEFORMABLE BODY DYNAMICS DETAILS

The internal force derives from the operator $\mathcal{N}(\delta\mathbf{u}; \mathbf{u})$, which is linear in $\delta\mathbf{u}$ but in general nonlinear in \mathbf{u} and possibly $\dot{\mathbf{u}}$ as well. The directional derivative at $\mathbf{u} \in \mathcal{S}$ in the direction of $\Delta\mathbf{u} \in \mathcal{V}$ takes the form

$$\boxed{\mathbf{D}_u \mathcal{N}(\delta\mathbf{u}; \mathbf{u}) = \int_{\Omega} \delta u_{i,J} \left(\delta_{ik} S_{JL} + F_{iI} F_{kK} C_{IJKL} + F_{iI} \dot{F}_{kK} V_{IJKL} \right) \Delta u_{k,L} d\Omega}. \quad (\text{A.1})$$

This result may be shown with the following derivation:

$$\mathbf{D}_u \mathcal{N}(\delta \mathbf{u}; \mathbf{u}) = \mathbf{D}_u \left[\int_{\Omega} \delta u_{i,J} F_{iI} S_{IJ} d\Omega \right], \quad (\text{A.2})$$

$$= \int_{\Omega} \mathbf{D}_u (\delta u_{i,J} F_{iI} S_{IJ}) d\Omega, \quad (\text{A.3})$$

$$= \int_{\Omega} \mathbf{D}_u \delta u_{i,J} F_{iI} S_{IJ} + \delta u_{i,J} \mathbf{D}_u F_{iI} S_{IJ} + \delta u_{i,J} F_{iI} \mathbf{D}_u S_{IJ} d\Omega, \quad (\text{A.4})$$

$$= \int_{\Omega} 0 + \delta u_{i,J} \Delta u_{i,I} S_{IJ} + \delta u_{i,J} F_{iI} \frac{\partial S_{IJ}}{\partial E_{KL}} \mathbf{D}_u E_{KL} \\ + \delta u_{i,J} F_{iI} \frac{\partial S_{IJ}}{\partial \dot{E}_{KL}} \mathbf{D}_u \dot{E}_{KL} d\Omega, \quad (\text{A.5})$$

$$= \int_{\Omega} \delta u_{i,J} \Delta u_{i,L} S_{LJ} + \delta u_{i,J} F_{iI} C_{IJKL} \cdot \frac{1}{2} (\Delta u_{k,K} F_{kL} + F_{kK} \Delta u_{k,L}) \\ + \delta u_{i,J} F_{iI} V_{IJKL} \cdot \frac{1}{2} (\dot{F}_{kK} \Delta u_{k,L} + \Delta u_{k,K} \dot{F}_{k,L}) d\Omega. \quad (\text{A.6})$$

Using properties of the Kronecker delta, symmetry of the Piola-Kirchhoff II stress tensor, and minor symmetry of the constitutive elasticity tensor (endowed by symmetry of \mathbf{E}), and minor symmetry of the constitutive viscoelasticity tensor (endowed by symmetry of $\dot{\mathbf{E}}$), *viz.*, ($\Delta u_{i,L} = \delta_{ik} \Delta u_{k,L}$, $S_{LJ} = S_{JL}$, $C_{IJKL} = C_{IJKL}$, and $V_{IJKL} = V_{IJKL}$) we have

$$\mathbf{D}_u \mathcal{N}(\delta \mathbf{u}; \mathbf{u}) = \int_{\Omega} \delta u_{i,J} \delta_{ik} \Delta u_{k,L} S_{JL} + \delta u_{i,J} F_{iI} C_{IJKL} F_{kK} \Delta u_{k,L} \\ + \delta u_{i,J} F_{iI} V_{IJKL} \dot{F}_{kK} \Delta u_{k,L} d\Omega, \quad (\text{A.7})$$

$$= \int_{\Omega} \delta u_{i,J} \left(\delta_{ik} S_{JL} + F_{iI} F_{kK} C_{IJKL} + F_{iI} \dot{F}_{kK} V_{IJKL} \right) \Delta u_{k,L} d\Omega, \quad (\text{A.8})$$

which is the desired result.

If the internal force operator has dependence on $\dot{\mathbf{u}}$ as well, then another directional derivative must be taken. The directional derivative at $\dot{\mathbf{u}}$ in the direction $\Delta \dot{\mathbf{u}}$ takes the form

$$\mathbf{D}_{\dot{\mathbf{u}}} \mathcal{N}(\delta \mathbf{u}; \mathbf{u}) = \int_{\Omega} \delta u_{i,J} F_{iI} F_{kK} V_{IJKL} \Delta \dot{u}_{k,L} d\Omega. \quad (\text{A.9})$$

This result is shown through the following derivation:

$$\mathbf{D}_{\dot{u}} \mathcal{N}(\delta \mathbf{u}; \mathbf{u}) = \mathbf{D}_{\dot{u}} \left[\int_{\Omega} \delta u_{i,J} F_{iI} S_{IJ} d\Omega \right], \quad (\text{A.10})$$

$$= \int_{\Omega} \mathbf{D}_{\dot{u}} (\delta u_{i,J} F_{iI} S_{IJ}) d\Omega, \quad (\text{A.11})$$

$$= \int_{\Omega} \mathbf{D}_{\dot{u}} \delta u_{i,J} F_{iI} S_{IJ} + \delta u_{i,J} \mathbf{D}_{\dot{u}} F_{iI} S_{IJ} + \delta u_{i,J} F_{iI} \mathbf{D}_{\dot{u}} S_{IJ} d\Omega, \quad (\text{A.12})$$

$$= \int_{\Omega} 0 + 0 + \delta u_{i,J} F_{iI} \frac{\partial S_{IJ}}{\partial E_{KL}} \mathbf{D}_{\dot{u}} E_{KL} \\ + \delta u_{i,J} F_{iI} \frac{\partial S_{IJ}}{\partial \dot{E}_{KL}} \mathbf{D}_{\dot{u}} \dot{E}_{KL} d\Omega, \quad (\text{A.13})$$

$$= \int_{\Omega} 0 + \delta u_{i,J} F_{iI} V_{IJKL} \mathbf{D}_{\dot{u}} \dot{E}_{KL} d\Omega, \quad (\text{A.14})$$

$$= \int_{\Omega} \delta u_{i,J} F_{iI} V_{IJKL} \cdot \frac{1}{2} (\Delta \dot{u}_{k,K} F_{kL} + F_{kK} \Delta \dot{u}_{k,L}) d\Omega. \quad (\text{A.15})$$

Employing minor symmetry of the viscous tangent, $V_{IJKL} = V_{IJKL}$, endowed by virtue of symmetry in $\dot{\mathbf{E}}$, we have

$$\mathbf{D}_{\dot{u}} \mathcal{N}(\delta \mathbf{u}; \mathbf{u}) = \int_{\Omega} \delta u_{i,J} F_{iI} V_{IJKL} F_{kK} \Delta \dot{u}_{k,L} d\Omega, \quad (\text{A.16})$$

which is the desired result.

A.3 RIGID BODY DYNAMICS DETAILS

Considering any vector $\mathbf{r}(\mathbf{q}, t)$ as a function of generalized coordinates \mathbf{q} and time t .

$$\mathbf{r} = \mathbf{r}(\mathbf{q}, t), \quad (\text{A.17})$$

$$d\mathbf{r} = \mathbf{v} dt = \sum_{r=1}^n \frac{\partial \mathbf{r}}{\partial q_r} dq_r + \frac{\partial \mathbf{r}}{\partial t} dt, \quad (\text{A.18})$$

and

$$\mathbf{v} = \sum_{r=1}^n \frac{\partial \mathbf{r}}{\partial q_r} \dot{q}_r + \frac{\partial \mathbf{r}}{\partial t}, \quad (\text{A.19})$$

which is homogeneous in $\dot{\mathbf{q}}$, thus

$$\boxed{\frac{\partial \mathbf{v}}{\partial \dot{\mathbf{q}}} = \frac{\partial \mathbf{r}}{\partial \mathbf{q}}}. \quad (\text{A.20})$$

Note also that this relationship is useful for writing variations of position to a point \mathbf{r} or variations of an angular position of a body $\boldsymbol{\theta}^B$ in terms of variations of the generalized coordinates \mathbf{q} as

$$\delta\mathbf{r} = \sum_{r=1}^n \frac{\partial\mathbf{v}}{\partial\dot{q}_r} \delta q_r, \quad (\text{A.21})$$

$$\delta\boldsymbol{\theta}^B = \sum_{r=1}^n \frac{\partial\boldsymbol{\omega}^B}{\partial\dot{q}_r} \delta q_r. \quad (\text{A.22})$$

Consider next rigid body Ω_R with mass center G located by the vector ${}^N\mathbf{r}^G$ in the inertial frame N . Let Ω_R have an angular velocity ${}^N\boldsymbol{\omega}^{\Omega_R}$. Let the vector \mathbf{p} be fixed in the body Ω_R , originate at the mass center, and terminate at some point C in Ω_R . The velocity of point C in the inertial frame may be written

$${}^N\mathbf{v}^C = {}^N\mathbf{v}^G + {}^N\boldsymbol{\omega}^{\Omega_R} \times \mathbf{r}^{GC}, \quad (\text{A.23})$$

which is equivalent to

$$\dot{\mathbf{p}} = \dot{\mathbf{r}} + \boldsymbol{\omega} \times \mathbf{p} = \dot{\mathbf{r}} - \mathbf{p} \times \boldsymbol{\omega}. \quad (\text{A.24})$$

The cross product has been rewritten as the skew matrix product, for vectors $\mathbf{w} \in \mathbb{R}^3$, $\mathbf{a} \in \mathbb{R}^3$, and matrix $\mathbf{W} \in so(3)$

$$\mathbf{w} \times \mathbf{a} = \hat{\mathbf{W}}\mathbf{a} = \begin{bmatrix} 0 & -w_3 & w_2 \\ w_3 & 0 & -w_1 \\ -w_2 & w_1 & 0 \end{bmatrix} \begin{Bmatrix} a_1 \\ a_2 \\ a_3 \end{Bmatrix}. \quad (\text{A.25})$$

Thus $\dot{\mathbf{p}} = \dot{\mathbf{r}} - \hat{\mathbf{P}}\boldsymbol{\omega}$ which is linear in $\boldsymbol{\omega}$. Finally this leads to a relationship for $\partial\mathbf{p}/\partial\boldsymbol{\theta}$

$$\boxed{\frac{\partial\mathbf{p}}{\partial\boldsymbol{\theta}} = \frac{\partial\dot{\mathbf{p}}}{\partial\boldsymbol{\omega}} = \frac{\partial}{\partial\boldsymbol{\omega}} (\dot{\mathbf{r}} - \hat{\mathbf{P}}\boldsymbol{\omega}) = -\hat{\mathbf{P}}}. \quad (\text{A.26})$$

which will be useful when derivatives with respect to the $\boldsymbol{\theta}$ variable are required.

A.4 EQUALITY CONSTRAINT DETAILS

In what follows, the first and second variations are derived in an abstract setting for holonomic constraints between two bodies. Three special cases may be extracted from the general derivation (a) deformable-deformable, (b) deformable-rigid, and (c) rigid-rigid. These three cases will be abbreviated (D–D), (D–R), and (R–R), respectively.

Consider the two bodies Ω_1 and Ω_2 shown in FIG. A.1. Body Ω_1 contains points \mathbf{A}_1 and \mathbf{B}_1 . The vector $\mathbf{u} \in \mathbb{R}^3$ locates point \mathbf{A}_1 from the origin O . The vector $\mathbf{p} \in \mathbb{R}^3$ locates point \mathbf{B}_1 from point \mathbf{A}_1 . Analogous statements may be made for Ω_2 , \mathbf{A}_2 , \mathbf{B}_2 , \mathbf{r} , and \mathbf{z} .

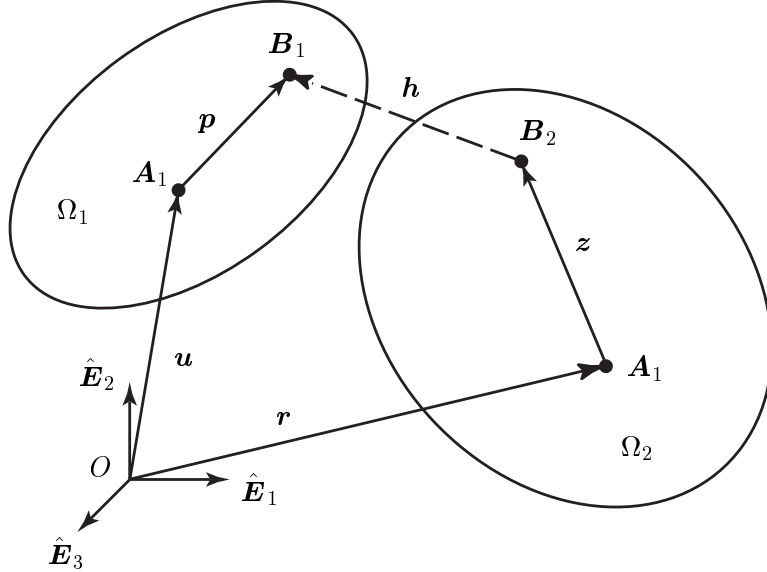


FIGURE A.1: Generalization of constraint equation \mathbf{h} between two bodies, which are either deformable or rigid, depending on the formulation type: deformable-deformable, deformable-rigid, or rigid-rigid.

While vectors \mathbf{u} and \mathbf{r} will be assumed to be unknown variables, the vectors \mathbf{p} and \mathbf{z} will be assumed to be nonlinear functions of unknown variables $\psi \in \mathbb{R}^3$ and $\theta \in \mathbb{R}^3$, respectively. The vectors ψ and θ are meant to abstractly represent the rotations of bodies Ω_1 and Ω_2 respectively. The vectors \mathbf{u} , \mathbf{p} , \mathbf{r} , and \mathbf{z} take on the the following meanings for each of the three special cases as indicated in TAB. A.1.

The constraint equation $\mathbf{h} \in \mathbb{R}^3$ takes the general form

$$\boxed{\mathbf{h} = \mathbf{u} + \mathbf{p} - \mathbf{r} - \mathbf{z} = \mathbf{0}}. \quad (\text{A.27})$$

The unknown variables are assumed to be \mathbf{u} , ψ , \mathbf{r} , and θ and abbreviated as the state vector $\mathbf{s} = \langle \mathbf{u}, \psi, \mathbf{r}, \theta \rangle^T$. The variation $\delta\mathbf{h} = \nabla_s \mathbf{h} \delta\mathbf{s}$ is then

$$\delta\mathbf{h} = \mathbf{1} \delta\mathbf{u} + \frac{\partial \mathbf{p}}{\partial \psi} \delta\psi - \mathbf{1} \delta\mathbf{r} - \frac{\partial \mathbf{z}}{\partial \theta} \delta\theta. \quad (\text{A.28})$$

	(D-D)	(D-R)	(R-R)
\mathbf{u}	\mathbf{u}^{P_1}	\mathbf{u}^{P_1}	\mathbf{r}^{G_1}
\mathbf{r}	\mathbf{u}^{0P_2}	\mathbf{r}^{G_2}	\mathbf{r}^{G_2}
\mathbf{p}	—	—	\mathbf{z}^{P_1}
\mathbf{z}	—	\mathbf{z}^{P_2}	\mathbf{z}^{P_2}
ψ	—	—	$\boldsymbol{\theta}^{\Omega_1}$
$\boldsymbol{\theta}$	—	$\boldsymbol{\theta}^{\Omega_2}$	$\boldsymbol{\theta}^{\Omega_2}$

TABLE A.1: Correspondence of vectors \mathbf{u} , \mathbf{p} , \mathbf{r} , and \mathbf{z} in the generalized equality constraint derivation to the special cases of deformable-deformable, deformable-rigid, and rigid-rigid.

From the result in Eq. (A.26), the following relationships hold:

$$\frac{\partial \mathbf{p}}{\partial \psi} = -\hat{\mathbf{P}}, \quad (\text{A.29})$$

$$\frac{\partial \mathbf{z}}{\partial \boldsymbol{\theta}} = -\hat{\mathbf{Z}}, \quad (\text{A.30})$$

where the hat notation represents a skew-symmetric matrix of a vector such that

$$\text{skew}(\mathbf{w}) = \hat{\mathbf{W}} = \begin{bmatrix} 0 & -w_3 & w_2 \\ w_3 & 0 & -w_1 \\ -w_2 & w_1 & 0 \end{bmatrix} \quad \forall \mathbf{w} \in \mathbb{R}^3. \quad (\text{A.31})$$

Equation (A.28) is then written $\delta \mathbf{h} = \mathbf{1} \delta \mathbf{u} - \hat{\mathbf{P}} \delta \psi + \mathbf{1} \delta \mathbf{r} + \hat{\mathbf{Z}} \delta \boldsymbol{\theta}$; or, in matrix form as

$$\left\{ \delta \mathbf{h} \right\} = \underbrace{\left[\mathbf{1} \mid -\hat{\mathbf{P}} \mid -\mathbf{1} \mid \hat{\mathbf{Z}} \right]}_{[\nabla_s \mathbf{h}]} \left\{ \begin{array}{l} \delta \mathbf{u} \\ \delta \psi \\ \delta \mathbf{r} \\ \delta \boldsymbol{\theta} \end{array} \right\}. \quad (\text{A.32})$$

A.4.1 FIRST VARIATION

From SECTION 2.4, the variation of the constraint potential is $\delta\mathcal{W}_h = (\boldsymbol{\lambda} + r\mathbf{h}) \cdot \nabla_s \mathbf{h} \delta s + \mathbf{h} \cdot \delta \boldsymbol{\lambda}$. Expanding $\delta\mathcal{W}_h$ gives

$$\delta\mathcal{W}_h = (\boldsymbol{\lambda} + r\mathbf{h}) \cdot \nabla_s \mathbf{h} \delta s + \mathbf{h} \cdot \delta \boldsymbol{\lambda} = (\lambda_k + rh_k) \frac{\partial h_k}{\partial s_i} \delta s_i + h_k \delta \lambda_k, \quad (\text{A.33})$$

$$= \delta s^T [\nabla_s \mathbf{h}]^T (\boldsymbol{\lambda} + r\mathbf{h}) + \delta \boldsymbol{\lambda}^T \mathbf{h}, \quad (\text{A.34})$$

$$= \begin{Bmatrix} \delta \mathbf{u} \\ \delta \boldsymbol{\psi} \\ \delta \mathbf{r} \\ \delta \boldsymbol{\theta} \end{Bmatrix}_{(1 \times 12)}^T \begin{Bmatrix} \mathbf{1} \\ -\hat{\mathbf{P}}^T \\ -\mathbf{1} \\ \hat{\mathbf{Z}}^T \end{Bmatrix}_{(12 \times 3)} \begin{Bmatrix} \boldsymbol{\lambda} + r\mathbf{h} \\ | \\ | \\ | \end{Bmatrix}_{(3 \times 1)} + \begin{Bmatrix} \delta \boldsymbol{\lambda} \\ (1 \times n_{\text{he}}) \end{Bmatrix}^T \begin{Bmatrix} \mathbf{h} \\ (n_{\text{he}} \times 1) \end{Bmatrix}. \quad (\text{A.35})$$

Using the substitution $\hat{\mathbf{W}}^T = -\hat{\mathbf{W}}$ for any skew-symmetric matrix $\hat{\mathbf{W}}$ and taking the inner product on the augmented multiplier $(\boldsymbol{\lambda} + r\mathbf{h})$, the first variation may be stated

$$\boxed{\delta\mathcal{W}_h = \begin{Bmatrix} \delta \mathbf{u} \\ \delta \boldsymbol{\psi} \\ \delta \mathbf{r} \\ \hline \delta \boldsymbol{\theta} \\ \hline \delta \boldsymbol{\lambda} \end{Bmatrix}^T \begin{Bmatrix} \boldsymbol{\lambda} + r\mathbf{h} \\ \hat{\mathbf{P}}(\boldsymbol{\lambda} + r\mathbf{h}) \\ -(\boldsymbol{\lambda} + r\mathbf{h}) \\ \hline -\hat{\mathbf{Z}}(\boldsymbol{\lambda} + r\mathbf{h}) \\ \hline \mathbf{h} \end{Bmatrix}}. \quad (\text{A.36})$$

Expanded, the first variation has the form given in Box A.1.

A.4.2 THE SECOND VARIATION

The second variation is given by

$$\begin{aligned} \Delta\delta\mathcal{W}_h &= \underbrace{\delta s^T [\nabla_s \{[\nabla_s \mathbf{h}]^T \{\boldsymbol{\lambda} + r\mathbf{h}\}\}] \Delta s}_{\phi_{11}} + \underbrace{\delta s^T [\nabla_\lambda \{[\nabla_s \mathbf{h}]^T \{\boldsymbol{\lambda} + r\mathbf{h}\}\}] \Delta \boldsymbol{\lambda}}_{\phi_{12}} \\ &\quad + \underbrace{\delta \boldsymbol{\lambda}^T [\nabla_s \mathbf{h}] \Delta s}_{\phi_{21}} + \underbrace{\delta \boldsymbol{\lambda}^T [\nabla_\lambda \mathbf{h}] \Delta \boldsymbol{\lambda}}_{\phi_{22}}. \end{aligned} \quad (\text{A.38})$$

Box A.1: First variation of the generalized equality constraint in expanded form.

$$\delta \mathcal{W}_h = \left\{ \begin{array}{c} \delta u_1 \\ \delta u_2 \\ \delta u_3 \\ \hline \delta \psi_1 \\ \delta \psi_2 \\ \delta \psi_3 \\ \hline \delta r_1 \\ \delta r_2 \\ \delta r_3 \\ \hline \delta \theta_1 \\ \delta \theta_2 \\ \delta \theta_3 \\ \hline \delta \lambda_1 \\ \delta \lambda_2 \\ \delta \lambda_3 \end{array} \right\}^T \left\{ \begin{array}{c} \lambda_1 + rh_1 \\ \lambda_2 + rh_2 \\ \lambda_3 + rh_3 \\ \hline -p_3(\lambda_2 + rh_2) + p_2(\lambda_3 + rh_3) \\ p_3(\lambda_1 + rh_1) - p_1(\lambda_3 + rh_3) \\ -p_2(\lambda_1 + rh_1) + p_1(\lambda_2 + rh_2) \\ \hline -(\lambda_1 + rh_1) \\ -(\lambda_2 + rh_2) \\ -(\lambda_3 + rh_3) \\ \hline z_3(\lambda_2 + rh_2) - z_2(\lambda_3 + rh_3) \\ -z_3(\lambda_1 + rh_1) + z_1(\lambda_3 + rh_3) \\ z_2(\lambda_1 + rh_1) - z_1(\lambda_2 + rh_2) \\ \hline h_1 \\ h_2 \\ h_3 \end{array} \right\} \quad (\text{A.37})$$

Simplification of these ϕ_{ij} terms is carried out as follows: The ϕ_{11} term may be expanded to be

$$\phi_{11} = \underbrace{\delta \mathbf{s}^T \left[\nabla_{s[1]} \left\{ [\nabla_s \mathbf{h}]^T \{ \boldsymbol{\lambda} + r \mathbf{h} \} \right\} \right] \Delta \mathbf{s}}_{\phi_{11,a}} + \underbrace{\delta \mathbf{s}^T \left[[\nabla_s \mathbf{h}]^T [\nabla_s \mathbf{h}] r \right] \Delta \mathbf{s}}_{\phi_{11,b}}. \quad (\text{A.39})$$

The notation gets a bit heavy here because there are numerous derivative operations being made. The gradient ∇_s is distributed on the $\{ [\nabla_s \mathbf{h}]^T \{ \boldsymbol{\lambda} + r \mathbf{h} \} \}$ vector in ϕ_{11} , resulting in two separate derivatives. The first derivative is on the $[\nabla_s \mathbf{h}]^T$ term, shown in $\phi_{11,a}$ with the $\nabla_{s[1]}$ notation. The second derivative is on the $\{ \boldsymbol{\lambda} + r \mathbf{h} \}$ term, shown in $\phi_{11,b}$ with the derivative already taken. In the $\phi_{11,a}$ term, $\{ \boldsymbol{\lambda} + r \mathbf{h} \}$ is held constant. To avoid confusion while taking this derivative, we let $\mathbf{c} = \{ \boldsymbol{\lambda} + r \mathbf{h} \}$ to evoke the notion that vector \mathbf{c} is held constant.

The $\phi_{11,a}$ term is obtained via the following manipulations:

$$\phi_{11,a} = \delta \mathbf{s}^T \left[\nabla_{s[1]} \left\{ [\nabla_s \mathbf{h}]^T \{ \mathbf{c} \} \right\} \right] \Delta \mathbf{s}, \quad (\text{A.40})$$

$$= \delta \mathbf{s}^T \nabla_s \begin{bmatrix} \mathbf{1} \\ \hat{\mathbf{P}} \\ -\mathbf{1} \\ -\hat{\mathbf{Z}} \end{bmatrix} \{ \mathbf{c} \} \Delta \mathbf{s} = \delta \mathbf{s}^T \nabla_s \begin{bmatrix} \mathbf{c} \\ \hat{\mathbf{P}}\mathbf{c} \\ -\mathbf{c} \\ -\hat{\mathbf{Z}}\mathbf{c} \end{bmatrix} \Delta \mathbf{s}. \quad (\text{A.41})$$

Now the \mathbf{c} terms have no dependence on \mathbf{s} (for the time being) because the \mathbf{c} term is being held constant. Thus only the $\hat{\mathbf{P}}\mathbf{c}$ and $-\hat{\mathbf{Z}}\mathbf{c}$ terms have a non-zero gradient. Furthermore, $\hat{\mathbf{P}}$ has dependence only on $\boldsymbol{\psi}$; it has no dependence on \mathbf{u} , \mathbf{r} , or $\boldsymbol{\theta}$. Also, $\hat{\mathbf{Z}}$ has dependence only on $\boldsymbol{\theta}$; it has no dependence on \mathbf{u} , $\boldsymbol{\psi}$, or \mathbf{r} . To calculate $\nabla_s \{ \hat{\mathbf{P}}\mathbf{c} \}$, consider the following manipulations:

$$\delta \mathbf{s}^T \left[\frac{\partial}{\partial \boldsymbol{\psi}} \{ \hat{\mathbf{P}}\mathbf{c} \} \right] \Delta \mathbf{s} = \delta \boldsymbol{\psi}^T \left[\frac{\partial}{\partial \boldsymbol{\psi}} \{ \mathbf{p} \times \mathbf{c} \} \right] \Delta \boldsymbol{\psi}, \quad (\text{A.42})$$

$$= \delta \boldsymbol{\psi}^T \left[\frac{\partial}{\partial \boldsymbol{\psi}} \{ -\mathbf{c} \times \mathbf{p} \} \right] \Delta \boldsymbol{\psi}, \quad (\text{A.43})$$

$$= \delta \boldsymbol{\psi}^T \left[\frac{\partial}{\partial \boldsymbol{\psi}} \{ -\hat{\mathbf{C}}\mathbf{p} \} \right] \Delta \boldsymbol{\psi}, \quad (\text{A.44})$$

$$= \delta \boldsymbol{\psi}^T \left[-\hat{\mathbf{C}} \frac{\partial \mathbf{p}}{\partial \boldsymbol{\psi}} \right] \Delta \boldsymbol{\psi}, \quad (\text{A.45})$$

$$= \delta \boldsymbol{\psi}^T \left[\hat{\mathbf{C}} \hat{\mathbf{P}} \right] \Delta \boldsymbol{\psi}. \quad (\text{A.46})$$

To calculate $\nabla_s \{-\hat{\mathbf{Z}}\mathbf{c}\}$, consider the following manipulations:

$$\delta s^T \left[\frac{\partial}{\partial \boldsymbol{\theta}} \{-\hat{\mathbf{Z}}\mathbf{c}\} \right] \Delta s = \delta \boldsymbol{\theta}^T \left[\frac{\partial}{\partial \boldsymbol{\theta}} \{-\mathbf{z} \times \mathbf{c}\} \right] \Delta \boldsymbol{\theta}, \quad (\text{A.47})$$

$$= \delta \boldsymbol{\theta}^T \left[\frac{\partial}{\partial \boldsymbol{\theta}} \{\mathbf{c} \times \mathbf{z}\} \right] \Delta \boldsymbol{\theta}, \quad (\text{A.48})$$

$$= \delta \boldsymbol{\theta}^T \left[\frac{\partial}{\partial \boldsymbol{\theta}} \{\hat{\mathbf{C}}\mathbf{z}\} \right] \Delta \boldsymbol{\theta}, \quad (\text{A.49})$$

$$= \delta \boldsymbol{\theta}^T \left[\hat{\mathbf{C}} \frac{\partial \mathbf{z}}{\partial \boldsymbol{\theta}} \right] \Delta \boldsymbol{\theta}, \quad (\text{A.50})$$

$$= \delta \boldsymbol{\theta}^T \left[-\hat{\mathbf{C}}\hat{\mathbf{Z}} \right] \Delta \boldsymbol{\theta}. \quad (\text{A.51})$$

Thus the $\phi_{11.a}$ term may be written out

$$\phi_{11.a} = \begin{Bmatrix} \delta \mathbf{u} \\ \delta \psi \\ \delta \mathbf{r} \\ \delta \boldsymbol{\theta} \end{Bmatrix}^T \begin{bmatrix} \mathbf{0} & \mathbf{0} & \mathbf{0} & \mathbf{0} \\ \mathbf{0} & (\widehat{\boldsymbol{\lambda} + r\mathbf{h}})\hat{\mathbf{P}} & \mathbf{0} & \mathbf{0} \\ \mathbf{0} & \mathbf{0} & \mathbf{0} & \mathbf{0} \\ \mathbf{0} & \mathbf{0} & \mathbf{0} & -(\widehat{\boldsymbol{\lambda} + r\mathbf{h}})\hat{\mathbf{Z}} \end{bmatrix} \begin{Bmatrix} \Delta \mathbf{u} \\ \Delta \psi \\ \Delta \mathbf{r} \\ \Delta \boldsymbol{\theta} \end{Bmatrix}. \quad (\text{A.52})$$

The $\phi_{11.b}$ term results in the outer product of $[\nabla_s \mathbf{h}]^T [\nabla_s \mathbf{h}]$ multiplied by the scalar r .

This outer product is represented

$$r \begin{bmatrix} \mathbf{1} & \hat{\mathbf{P}}^T & -\mathbf{1} & -\hat{\mathbf{Z}}^T \end{bmatrix} \begin{bmatrix} \mathbf{1} \\ \hat{\mathbf{P}} \\ -\mathbf{1} \\ -\hat{\mathbf{Z}} \end{bmatrix}^T \begin{bmatrix} r\mathbf{1} & r\hat{\mathbf{P}}^T & -r\mathbf{1} & -r\hat{\mathbf{Z}}^T \\ r\hat{\mathbf{P}} & r\hat{\mathbf{P}}\hat{\mathbf{P}}^T & -r\hat{\mathbf{P}} & -r\hat{\mathbf{P}}\hat{\mathbf{Z}}^T \\ -r\mathbf{1} & -r\hat{\mathbf{P}}^T & r\mathbf{1} & r\hat{\mathbf{Z}}^T \\ -r\hat{\mathbf{Z}} & -r\hat{\mathbf{Z}}\hat{\mathbf{P}}^T & r\hat{\mathbf{Z}} & r\hat{\mathbf{Z}}\hat{\mathbf{Z}}^T \end{bmatrix} \quad (\text{A.53})$$

With regard to the ϕ_{12} term, carrying through the differentiation with respect to $\boldsymbol{\lambda}$ gives the identity matrix $\mathbf{1}$ where the column vector $\{\boldsymbol{\lambda} + r\mathbf{h}\}$ was, prior to differentiation. The $[\nabla_s \mathbf{h}]^T$ matrix post-multiplied with the (3×3) identity matrix gives the (12×3) $[\nabla_s \mathbf{h}]^T$ matrix back again.

The ϕ_{21} term is already simplified, and equal to the transpose of the $[\nabla_s \mathbf{h}]^T$ term found in the first variation. The ϕ_{22} term equals zero since \mathbf{h} has no dependence on $\boldsymbol{\lambda}$.

After simplification, the second variation may then be written compactly as

$$\Delta\delta\mathcal{W}_h = \left\{ \begin{array}{c} \delta\mathbf{u} \\ \delta\psi \\ \delta\mathbf{r} \\ \delta\boldsymbol{\theta} \\ \hline \delta\lambda \end{array} \right\}^T \left[\begin{array}{cccc|c} r\mathbf{1} & -r\hat{\mathbf{P}} & -r\mathbf{1} & r\hat{\mathbf{Z}} & 1 \\ r\hat{\mathbf{P}} & \mathbf{T}_{22} & -r\hat{\mathbf{P}} & r\hat{\mathbf{P}}\hat{\mathbf{Z}} & \hat{\mathbf{P}} \\ -r\mathbf{1} & r\hat{\mathbf{P}} & r\mathbf{1} & -r\hat{\mathbf{Z}} & -1 \\ -r\hat{\mathbf{Z}} & r\hat{\mathbf{Z}}\hat{\mathbf{P}} & r\hat{\mathbf{Z}} & \mathbf{T}_{44} & -\hat{\mathbf{Z}} \\ \hline 1 & -\hat{\mathbf{P}} & -1 & \hat{\mathbf{Z}} & 0 \end{array} \right] \left\{ \begin{array}{c} \Delta\mathbf{u} \\ \Delta\psi \\ \Delta\mathbf{r} \\ \Delta\boldsymbol{\theta} \\ \hline \Delta\lambda \end{array} \right\}, \quad (\text{A.54})$$

where

$$\mathbf{T}_{22} = [\widehat{\lambda + rh}] - r\hat{\mathbf{P}}, \quad (\text{A.55})$$

$$\mathbf{T}_{44} = [-\widehat{\lambda + rh}] - r\hat{\mathbf{Z}} \hat{\mathbf{Z}}. \quad (\text{A.56})$$

Expanded, the second variation has the form given in Box A.2, where the substitutions are made for c , k , f , and m . The c substitutions are

$$c_1 = \lambda_1 + rh_1, \quad c_2 = \lambda_2 + rh_2, \quad c_3 = \lambda_3 + rh_3. \quad (\text{A.57})$$

The k substitutions are

$$\begin{aligned} k_{11} &= -c_2 p_2 - c_3 p_3 + r(p_2^2 + p_3^2), & k_{12} &= c_2 p_1 - r p_1 p_2, \\ k_{21} &= c_1 p_2 - r p_1 p_2, & k_{22} &= -c_1 p_1 - c_3 p_3 + r(p_1^2 + p_3^2), \\ k_{31} &= c_1 p_3 - r p_1 p_3, & k_{32} &= c_2 p_3 - r p_2 p_3, \\ k_{13} &= c_3 p_1 - r p_1 p_3, \\ k_{23} &= c_3 p_2 - r p_2 p_3, \\ k_{33} &= -c_1 p_1 - c_2 p_2 + r(p_1^2 + p_2^2). \end{aligned} \quad (\text{A.58})$$

The f substitutions are

$$\begin{aligned} f_{11} &= -r(p_2 z_2 + p_3 z_3), & f_{12} &= r p_2 z_1, & f_{13} &= r p_3 z_1, \\ f_{21} &= r p_1 z_2, & f_{22} &= -r(p_1 z_1 + p_3 z_3), & f_{23} &= r p_3 z_2, \\ f_{31} &= r p_1 z_3, & f_{32} &= r p_2 z_3, & f_{33} &= -r(p_1 z_1 + p_2 z_2). \end{aligned} \quad (\text{A.59})$$

The m substitutions are

$$\begin{aligned}
 m_{11} &= c_2 z_2 + c_3 z_3 + r(z_2^2 + z_3^2), & m_{12} &= -c_2 z_1 - r z_1 z_2, \\
 m_{21} &= -c_1 z_2 - r z_1 z_2, & m_{22} &= c_1 z_1 + c_3 z_3 + r(z_1^2 + z_3^2), \\
 m_{31} &= -c_1 z_3 - r z_1 z_3, & m_{32} &= -c_2 z_3 - r z_2 z_3, \\
 m_{13} &= -c_3 z_1 - r z_1 z_3, \\
 m_{23} &= -c_3 z_2 - r z_2 z_3, \\
 m_{33} &= c_1 z_1 + c_2 z_2 + r(z_1^2 + z_2^2).
 \end{aligned} \tag{A.60}$$

Box A.2: Second variation of the generalized equality constraint in expanded form.

$$\Delta\delta\mathcal{W}_h = \left(\begin{array}{c} \delta u_1 \\ \delta u_2 \\ \delta u_3 \\ \hline \delta\psi_1 \\ \delta\psi_2 \\ \delta\psi_3 \\ \hline \delta r_1 \\ \delta r_2 \\ \delta r_3 \\ \hline \delta\theta_1 \\ \delta\theta_2 \\ \delta\theta_3 \\ \hline \delta\lambda_1 \\ \delta\lambda_2 \\ \delta\lambda_3 \end{array} \right)^T \left[\begin{array}{ccc|ccc|ccc|ccc|ccc} r & 0 & 0 & 0 & rp_3 & -rp_2 & -r & 0 & 0 & 0 & -rz_3 & rz_2 & 1 & 0 & 0 \\ 0 & r & 0 & -rp_3 & 0 & rp_1 & 0 & -r & 0 & rz_3 & 0 & -rz_1 & 0 & 1 & 0 \\ 0 & 0 & r & rp_2 & -rp_1 & 0 & 0 & 0 & -r & -rz_2 & rz_1 & 0 & 0 & 0 & 1 \\ \hline 0 & -rp_3 & rp_2 & k_{11} & k_{12} & k_{13} & 0 & rp_3 & -rp_2 & f_{11} & f_{12} & f_{13} & 0 & -p_3 & p_2 \\ rp_3 & 0 & -rp_1 & k_{21} & k_{22} & k_{23} & -rp_3 & 0 & rp_1 & f_{21} & f_{22} & f_{23} & p_3 & 0 & -p_1 \\ -rp_2 & rp_1 & 0 & k_{31} & k_{32} & k_{33} & rp_2 & -rp_1 & 0 & f_{31} & f_{32} & f_{33} & -p_2 & p_1 & 0 \\ \hline -r & 0 & 0 & 0 & -rp_3 & rp_2 & r & 0 & 0 & 0 & rz_3 & -rz_2 & -1 & 0 & 0 \\ 0 & -r & 0 & rp_3 & 0 & -rp_1 & 0 & r & 0 & -rz_3 & 0 & rz_1 & 0 & -1 & 0 \\ 0 & 0 & -r & -rp_2 & rp_1 & 0 & 0 & 0 & r & rz_2 & -rz_1 & 0 & 0 & 0 & -1 \\ \hline 0 & rz_3 & -rz_2 & f_{11} & f_{21} & f_{31} & 0 & -rz_3 & rz_2 & m_{11} & m_{12} & m_{13} & 0 & z_3 & -z_2 \\ -rz_3 & 0 & rz_1 & f_{12} & f_{22} & f_{32} & rz_3 & 0 & -rz_1 & m_{21} & m_{22} & m_{23} & -z_3 & 0 & z_1 \\ rz_2 & -rz_1 & 0 & f_{13} & f_{23} & f_{33} & -rz_2 & rz_1 & 0 & m_{31} & m_{32} & m_{33} & z_2 & -z_1 & 0 \\ \hline 1 & 0 & 0 & 0 & p_3 & -p_2 & -1 & 0 & 0 & 0 & -z_3 & z_2 & 0 & 0 & 0 \\ 0 & 1 & 0 & -p_3 & 0 & p_1 & 0 & -1 & 0 & z_3 & 0 & -z_1 & 0 & 0 & 0 \\ 0 & 0 & 1 & p_2 & -p_1 & 0 & 0 & 0 & -1 & -z_2 & z_1 & 0 & 0 & 0 & 0 \end{array} \right] \left(\begin{array}{c} \Delta u_1 \\ \Delta u_2 \\ \Delta u_3 \\ \hline \Delta\psi_1 \\ \Delta\psi_2 \\ \Delta\psi_3 \\ \hline \Delta r_1 \\ \Delta r_2 \\ \Delta r_3 \\ \hline \Delta\theta_1 \\ \Delta\theta_2 \\ \Delta\theta_3 \\ \hline \Delta\lambda_1 \\ \Delta\lambda_2 \\ \Delta\lambda_3 \end{array} \right) \quad (A.61)$$

A.5 CONTACT MECHANICS DETAILS

Consider unilateral contact between a deformable body and a rigid body, shown in FIG. A.2.

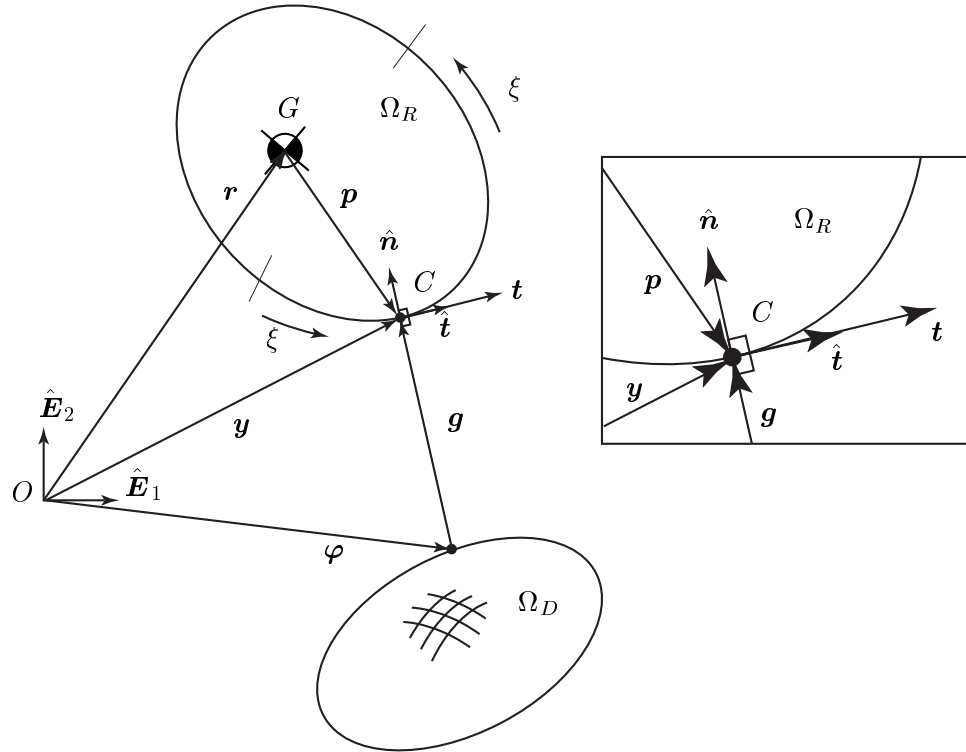


FIGURE A.2: Vector nomenclature for contact between rigid and deformable bodies.

The rigid body Ω_R has mass center at current time located by \mathbf{r} in the $\hat{\mathbf{E}}$ basis. The vector \mathbf{p} is directed from the mass center to the contact point C . The boundary of the rigid body $\partial\Omega_R$ is parameterized by ξ . The contact point C is found on the boundary $\partial\Omega_R$ through the closest point projection \mathbf{y} of the striker point located in the current configuration located on $\partial\Omega_D$ by φ . The gap vector \mathbf{g} originates at this point and terminates at C . At point C , a tangent vector \mathbf{t} and unit normal vector $\hat{\mathbf{n}}$ are made. The out-of-plane direction (or bi-normal direction) $\hat{\mathbf{e}}_3$ is constructed from $\hat{\mathbf{e}}_3 = \hat{\mathbf{t}} \times \hat{\mathbf{n}}$. Note that $\hat{\mathbf{t}} = \mathbf{t} / \| \mathbf{t} \|$.

We assume two-dimensional space for rigid-deformable contact. Thus bodies Ω_D and Ω_R can translate in the $\hat{\mathbf{E}}_1$ and $\hat{\mathbf{E}}_2$ directions. The rigid body also has one rotation in the $\hat{\mathbf{E}}_3$ direction. This assumption is made so that the problem is tractable. As will be seen, the description of large-slip bilateral contact between a rigid body and a deformable body

is quite involved. Many of the complications and nonlinearities arise from the rotation of the rigid body.

The dependence of ξ and other variables is important to note because derivatives of these quantities will be taken as precursors to constructing the first and second variations of contact potential. For the rigid body

$$\mathbf{q} = \begin{cases} \mathbf{r} \\ \boldsymbol{\theta} \end{cases} \quad \begin{array}{l} \text{translation,} \\ \text{rotation,} \end{array} \quad \begin{array}{l} \mathbf{r} = r_1 \hat{\mathbf{E}}_1 + r_2 \hat{\mathbf{E}}_2, \\ \boldsymbol{\theta} = \theta \hat{\mathbf{E}}_3. \end{array} \quad (\text{A.62})$$

For the deformable body

$$\boldsymbol{\varphi} = \boldsymbol{\varphi}(\mathbf{u}) = \mathbf{u} + \mathbf{X}. \quad (\text{A.63})$$

For the closest-point projection

$$\xi = \xi(\mathbf{u}, \mathbf{r}, \boldsymbol{\theta}), \quad (\text{A.64})$$

$$\mathbf{y} = \mathbf{y}(\mathbf{r}, \boldsymbol{\theta}, \xi(\mathbf{u}, \mathbf{r}, \boldsymbol{\theta})), \quad (\text{A.65})$$

$$\mathbf{g} = \mathbf{g}(\mathbf{u}, \mathbf{r}, \boldsymbol{\theta}, \xi(\mathbf{u}, \mathbf{r}, \boldsymbol{\theta})) = \mathbf{y}(\mathbf{r}, \boldsymbol{\theta}, \xi(\mathbf{u}, \mathbf{r}, \boldsymbol{\theta})) - \boldsymbol{\varphi}(\mathbf{u}), \quad (\text{A.66})$$

$$\mathbf{p} = \mathbf{p}(\boldsymbol{\theta}, \xi(\mathbf{u}, \mathbf{r}, \boldsymbol{\theta})), \quad \text{thus} \quad \mathbf{y}(\mathbf{r}, \boldsymbol{\theta}, \xi(\mathbf{u}, \mathbf{r}, \boldsymbol{\theta})) = \mathbf{r} + \mathbf{p}(\boldsymbol{\theta}, \xi(\mathbf{u}, \mathbf{r}, \boldsymbol{\theta})), \quad (\text{A.67})$$

and the direction vectors associated with the projection

$$\mathbf{t} = \mathbf{t}(\boldsymbol{\theta}, \xi(\mathbf{u}, \mathbf{r}, \boldsymbol{\theta})) \quad (\text{tangent direction}), \quad (\text{A.68})$$

$$\hat{\mathbf{n}} = \hat{\mathbf{n}}(\boldsymbol{\theta}, \xi(\mathbf{u}, \mathbf{r}, \boldsymbol{\theta})) \quad (\text{normal direction}), \quad (\text{A.69})$$

$$\hat{\mathbf{e}}_3 = \hat{\mathbf{t}} \times \hat{\mathbf{n}} = \hat{\mathbf{E}}_3 = \hat{\mathbf{E}}_1 \times \hat{\mathbf{E}}_2 \quad (\text{bi-normal direction}). \quad (\text{A.70})$$

A.5.1 SOME PRELIMINARY RESULTS

TENSOR RELATIONSHIPS For vectors $\mathbf{a}, \mathbf{b}, \mathbf{c}, \mathbf{d} \in \mathbb{R}^3$,

$$\boxed{\begin{aligned} [\mathbf{a} \otimes \mathbf{b}] \cdot \mathbf{c} &= (\mathbf{a} \cdot \mathbf{d})(\mathbf{b} \cdot \mathbf{c}) \\ [\mathbf{a} \otimes \mathbf{b}] [\mathbf{c} \otimes \mathbf{d}] &= [\mathbf{a} \otimes \mathbf{d}] (\mathbf{b} \cdot \mathbf{c}) \end{aligned}}. \quad (\text{A.71})$$

Let a vector \mathbf{v} have dependence on another vector \mathbf{a} such that $\mathbf{v} = \mathbf{v}(\mathbf{a})$. The variation of the normed vector \mathbf{v} in the direction \mathbf{a} is given by

$$\delta \left(\frac{\mathbf{v}}{\|\mathbf{v}\|} \right) = \frac{1}{\|\mathbf{v}\|} \left[\mathbf{1} - \left(\frac{\mathbf{v}}{\|\mathbf{v}\|} \otimes \frac{\mathbf{v}}{\|\mathbf{v}\|} \right) \right] \frac{\partial \mathbf{v}}{\partial \mathbf{a}} \delta \mathbf{a}. \quad (\text{A.72})$$

This result is obtained first by noting

$$\delta \parallel \mathbf{v} \parallel = \delta \sqrt{\mathbf{v} \cdot \mathbf{v}} = \delta(\mathbf{v} \cdot \mathbf{v})^{1/2} = \frac{\mathbf{v}}{\parallel \mathbf{v} \parallel} \frac{\partial \mathbf{v}}{\partial \mathbf{a}} \delta \mathbf{a}. \quad (\text{A.73})$$

Recalling the quotient rule for products of derivatives

$$\left(\frac{f(x)}{g(x)} \right)' = \frac{g(x)f'(x) - f(x)g'(x)}{[g(x)]^2} \quad g(x) \neq 0, \quad (\text{A.74})$$

gives

$$\delta \left(\frac{\mathbf{v}}{\parallel \mathbf{v} \parallel} \right) = \frac{\frac{\partial \mathbf{v}}{\partial \mathbf{a}} \delta \mathbf{a} \parallel \mathbf{v} \parallel - \mathbf{v} \frac{\mathbf{v}}{\parallel \mathbf{v} \parallel} \frac{\partial \mathbf{v}}{\partial \mathbf{a}} \delta \mathbf{a}}{\parallel \mathbf{v} \parallel^2}, \quad (\text{A.75})$$

which can further be simplified to give the claimed result.

Next consider any vector $\mathbf{v} \in \mathbb{R}^3$ described in the $\{\hat{\mathbf{t}}, \hat{\mathbf{n}}, \hat{\mathbf{e}}_3\}$ basis. Consider

$$[\mathbf{1} - \hat{\mathbf{t}} \otimes \hat{\mathbf{t}}] \mathbf{v} = \mathbf{v} - (\mathbf{v} \cdot \hat{\mathbf{t}}) \hat{\mathbf{t}}, \quad (\text{A.76})$$

$$= (\mathbf{v} \cdot \hat{\mathbf{t}}) \hat{\mathbf{t}} + (\mathbf{v} \cdot \hat{\mathbf{n}}) \hat{\mathbf{n}} + (\mathbf{v} \cdot \hat{\mathbf{e}}_3) \hat{\mathbf{e}}_3 - (\mathbf{v} \cdot \hat{\mathbf{t}}) \hat{\mathbf{t}}, \quad (\text{A.77})$$

$$= [\hat{\mathbf{n}} \otimes \hat{\mathbf{n}} + \hat{\mathbf{e}}_3 \otimes \hat{\mathbf{e}}_3] \mathbf{v}. \quad (\text{A.78})$$

Since this relationship must hold for all $\mathbf{v} \in \mathbb{R}^3$, then

$$[\mathbf{1} - \hat{\mathbf{t}} \otimes \hat{\mathbf{t}}] = [\hat{\mathbf{n}} \otimes \hat{\mathbf{n}} + \hat{\mathbf{e}}_3 \otimes \hat{\mathbf{e}}_3]. \quad (\text{A.79})$$

Furthermore, the cross product of $\hat{\mathbf{e}}_3$ with a vector $\mathbf{v} \in \mathbb{R}^3$ will be a useful result:

$$\hat{\mathbf{e}}_3 \times \mathbf{v} = \hat{\mathbf{e}}_3 \times ((\mathbf{v} \cdot \hat{\mathbf{t}}) \hat{\mathbf{t}} + (\mathbf{v} \cdot \hat{\mathbf{n}}) \hat{\mathbf{n}} + (\mathbf{v} \cdot \hat{\mathbf{e}}_3) \hat{\mathbf{e}}_3), \quad (\text{A.80})$$

which gives

$$\hat{\mathbf{e}}_3 \times (\bullet) = [\hat{\mathbf{n}} \otimes \hat{\mathbf{t}} - \hat{\mathbf{t}} \otimes \hat{\mathbf{n}}] (\bullet). \quad (\text{A.81})$$

Let the skew matrices be written as

$$\widehat{\mathbf{P}} = \text{skew}(\mathbf{p}), \quad [\widehat{\mathbf{P}}] = \begin{bmatrix} 0 & -p_3 & p_2 \\ p_3 & 0 & -p_1 \\ -p_2 & p_1 & 0 \end{bmatrix}. \quad (\text{A.82})$$

Similarly, $\widehat{\mathbf{T}} = \text{skew}(\mathbf{t})$, $\widehat{\mathbf{N}} = \text{skew}(\hat{\mathbf{n}})$. Note the double hat $(\widehat{\bullet})$ represents the skew matrix form from a unit vector.

GEOMETRICAL RELATIONSHIPS The inner product of $\hat{\mathbf{n}}$ with itself is

$$\hat{\mathbf{n}} \cdot \hat{\mathbf{n}} = 1, \quad (\text{A.83})$$

$$\delta(\hat{\mathbf{n}} \cdot \hat{\mathbf{n}}) = 0, \quad (\text{A.84})$$

$$\implies \delta\hat{\mathbf{n}} \cdot \hat{\mathbf{n}} = 0. \quad (\text{A.85})$$

The projection \mathbf{y} has a slope along the ξ axis which is identically the tangent vector \mathbf{t}

$$\frac{\partial \mathbf{y}}{\partial \xi} = \mathbf{t}, \quad \mathbf{y} = \mathbf{r} + \mathbf{p} \implies \frac{\partial \mathbf{p}}{\partial \xi} = \mathbf{t}. \quad (\text{A.86})$$

The tangent vector \mathbf{t} and the normal unit vector $\hat{\mathbf{n}}$ are always orthogonal.

$$\mathbf{t} \cdot \hat{\mathbf{n}}. \quad (\text{A.87})$$

Because they are orthogonal for any \mathbf{t} and for any $\hat{\mathbf{n}}$, then they are equal to a constant (zero in this case) for all \mathbf{t} and for all $\hat{\mathbf{n}}$. Variations of a constant are equal to zero, thus

$$\delta(\mathbf{t} \cdot \hat{\mathbf{n}}) = 0, \quad (\text{A.88})$$

which expanded is

$$\delta\mathbf{t} \cdot \hat{\mathbf{n}} + \mathbf{t} \cdot \delta\hat{\mathbf{n}} = 0. \quad (\text{A.89})$$

DERIVATIVES ON ξ The gradient of ξ with respect to the state variables \mathbf{u} , \mathbf{r} , and $\boldsymbol{\theta}$ will all be calculated from the orthogonality of the tangent \mathbf{t} and the gap vector \mathbf{g} , *i.e.*, $(\mathbf{t} \cdot \mathbf{g}) = 0$. Because these two vectors are orthogonal for any \mathbf{t} and for any \mathbf{g} , their inner product is always equal to a constant (zero in this case). Variations of a constant are equal to zero, thus

$$\delta(\mathbf{t} \cdot \mathbf{g}) = \delta\mathbf{t} \cdot \mathbf{g} + \mathbf{t} \cdot \delta\mathbf{g} = 0. \quad (\text{A.90})$$

Variations are now taken in turn, first with \mathbf{u} , then with \mathbf{r} , and finally with $\boldsymbol{\theta}$.

$$\delta_u(\mathbf{t} \cdot \mathbf{g}) = \delta_u \mathbf{t} \cdot \mathbf{g} + \mathbf{t} \cdot \delta_u \mathbf{g} = 0, \quad (\text{A.91})$$

$$0 = \left[\frac{\partial \mathbf{t}}{\partial \xi} \frac{\partial \xi}{\partial \mathbf{u}} \right] \delta \mathbf{u} \cdot \mathbf{g} + \mathbf{t} \cdot \delta_u (\mathbf{y} - \boldsymbol{\varphi}), \quad (\text{A.92})$$

$$= \left[\mathbf{t}_{,\xi} \frac{\partial \xi}{\partial \mathbf{u}} \right] \delta \mathbf{u} \cdot \mathbf{g} + \mathbf{t} \cdot \left(\left[\frac{\partial \mathbf{y}}{\partial \xi} \frac{\partial \xi}{\partial \mathbf{u}} \right] - \frac{\partial \boldsymbol{\varphi}}{\partial \mathbf{u}} \right) \delta \mathbf{u}, \quad (\text{A.93})$$

$$= \left[\mathbf{t}_{,\xi} \frac{\partial \xi}{\partial \mathbf{u}} \right] \delta \mathbf{u} \cdot \mathbf{g} + \mathbf{t} \cdot \left(\left[\mathbf{t} \frac{\partial \xi}{\partial \mathbf{u}} \right] - \mathbf{1} \right) \delta \mathbf{u}, \quad (\text{A.94})$$

$$= (\mathbf{t}_{,\xi} \cdot \mathbf{g}) \left(\frac{\partial \xi}{\partial \mathbf{u}} \cdot \delta \mathbf{u} \right) + (\mathbf{t} \cdot \mathbf{t}) \left(\frac{\partial \xi}{\partial \mathbf{u}} \cdot \delta \mathbf{u} \right) - \mathbf{t} \cdot \mathbf{1} \delta \mathbf{u}. \quad (\text{A.95})$$

Since this relationship must hold for all $\delta \mathbf{u}$, it follows that

$$\frac{\partial \xi}{\partial \mathbf{u}} = \frac{\mathbf{t}}{\mathbf{t} \cdot \mathbf{t} + \mathbf{t}_{,\xi} \cdot \mathbf{g}}. \quad (\text{A.96})$$

Since the quantity in the denominator will show up repeatedly, it is convenient to make the following abbreviation

$$\boxed{\alpha = \frac{1}{\mathbf{t} \cdot \mathbf{t} + \mathbf{t}_{,\xi} \cdot \mathbf{g}}}. \quad (\text{A.97})$$

Making the substitution for α gives

$$\boxed{\frac{\partial \xi}{\partial \mathbf{u}} = \alpha \mathbf{t}}. \quad (\text{A.98})$$

Similarly, taking the variation with respect to \mathbf{r} gives

$$\delta_r(\mathbf{t} \cdot \mathbf{g}) = \delta_r \mathbf{t} \cdot \mathbf{g} + \mathbf{t} \cdot \delta_r \mathbf{g} = 0, \quad (\text{A.99})$$

$$0 = \left[\frac{\partial \mathbf{t}}{\partial \xi} \frac{\partial \xi}{\partial \mathbf{r}} \right] \delta \mathbf{r} \cdot \mathbf{g} + \mathbf{t} \cdot \delta_r (\mathbf{y} - \boldsymbol{\varphi}), \quad \text{recall } \mathbf{y} = \mathbf{r} + \mathbf{p}, \quad (\text{A.100})$$

$$= \left[\mathbf{t}_{,\xi} \frac{\partial \xi}{\partial \mathbf{r}} \right] \delta \mathbf{r} \cdot \mathbf{g} + \mathbf{t} \cdot \left(\frac{\partial \mathbf{y}}{\partial \mathbf{r}} + \left[\frac{\partial \mathbf{p}}{\partial \xi} \frac{\partial \xi}{\partial \mathbf{r}} \right] \right) \delta \mathbf{r}, \quad (\text{A.101})$$

$$= \left[\mathbf{t}_{,\xi} \frac{\partial \xi}{\partial \mathbf{r}} \right] \delta \mathbf{r} \cdot \mathbf{g} + \mathbf{t} \cdot \left(\mathbf{1} + \left[\mathbf{t} \frac{\partial \xi}{\partial \mathbf{r}} \right] \right) \delta \mathbf{r}, \quad (\text{A.102})$$

$$= (\mathbf{t}_{,\xi} \cdot \mathbf{g}) \left(\frac{\partial \xi}{\partial \mathbf{r}} \cdot \delta \mathbf{r} \right) + \mathbf{t} \cdot \mathbf{1} \delta \mathbf{r} + (\mathbf{t} \cdot \mathbf{t}) \left(\frac{\partial \xi}{\partial \mathbf{r}} \cdot \delta \mathbf{r} \right), \quad (\text{A.103})$$

Since this relationship must hold for all $\delta \mathbf{r}$, it follows that

$$\frac{\partial \xi}{\partial \mathbf{r}} = \frac{-\mathbf{t}}{\mathbf{t} \cdot \mathbf{t} + \mathbf{t}_{,\xi} \cdot \mathbf{g}}, \quad (\text{A.104})$$

or compactly

$$\boxed{\frac{\partial \xi}{\partial \mathbf{r}} = -\alpha \mathbf{t}}. \quad (\text{A.105})$$

Note the symmetry $\delta \mathbf{u} = -\delta \mathbf{r}$. Finally, taking the variation with respect to $\boldsymbol{\theta}$ gives

$$\delta_\theta(\mathbf{t} \cdot \mathbf{g}) = \delta_\theta \mathbf{t} \cdot \mathbf{g} + \mathbf{t} \cdot \delta_\theta \mathbf{g} = 0, \quad (\text{A.106})$$

$$0 = \left[\frac{\partial \mathbf{t}}{\partial \boldsymbol{\theta}} + \frac{\partial \mathbf{t}}{\partial \xi} \frac{\partial \xi}{\partial \boldsymbol{\theta}} \right] \delta \boldsymbol{\theta} \cdot \mathbf{g} + \mathbf{t} \cdot \delta_\theta(\mathbf{y} - \boldsymbol{\varphi}), \quad \text{recall } \mathbf{y} = \mathbf{r} + \mathbf{p}, \quad (\text{A.107})$$

$$= \left[\frac{\partial \dot{\mathbf{t}}}{\partial \boldsymbol{\omega}} + \mathbf{t}_{,\xi} \frac{\partial \xi}{\partial \boldsymbol{\theta}} \right] \delta \boldsymbol{\theta} \cdot \mathbf{g} + \mathbf{t} \cdot \left(\frac{\partial \mathbf{p}}{\partial \boldsymbol{\theta}} + \left[\frac{\partial \mathbf{p}}{\partial \xi} \frac{\partial \xi}{\partial \boldsymbol{\theta}} \right] \right) \delta \boldsymbol{\theta}, \quad (\text{A.108})$$

$$= \left[-\hat{\mathbf{T}} + \mathbf{t}_{,\xi} \frac{\partial \xi}{\partial \boldsymbol{\theta}} \right] \delta \boldsymbol{\theta} \cdot \mathbf{g} + \mathbf{t} \cdot (-\hat{\mathbf{P}}) \delta \boldsymbol{\theta} + \mathbf{t} \cdot \left[\mathbf{t} \frac{\partial \xi}{\partial \boldsymbol{\theta}} \right] \delta \boldsymbol{\theta}, \quad (\text{A.109})$$

$$= (\hat{\mathbf{T}}\mathbf{g}) \cdot \delta \boldsymbol{\theta} + (\mathbf{t}_{,\xi} \cdot \mathbf{g}) \left(\frac{\partial \xi}{\partial \boldsymbol{\theta}} \cdot \delta \boldsymbol{\theta} \right) + (\hat{\mathbf{P}}\mathbf{t}) \cdot \delta \boldsymbol{\theta} + (\mathbf{t} \cdot \mathbf{t}) \left(\frac{\partial \xi}{\partial \boldsymbol{\theta}} \cdot \delta \boldsymbol{\theta} \right). \quad (\text{A.110})$$

Since this relationship must hold for all $\delta \boldsymbol{\theta}$, it follows that

$$\frac{\partial \xi}{\partial \boldsymbol{\theta}} = \frac{-(\hat{\mathbf{T}}\mathbf{g} + \hat{\mathbf{P}}\mathbf{t})}{\mathbf{t} \cdot \mathbf{t} + \mathbf{t}_{,\xi} \cdot \mathbf{g}}, \quad (\text{A.111})$$

or compactly

$$\frac{\partial \xi}{\partial \boldsymbol{\theta}} = -\alpha(\hat{\mathbf{T}}\mathbf{g} + \hat{\mathbf{P}}\mathbf{t}). \quad (\text{A.112})$$

Since we are considering planar rotation, $\boldsymbol{\theta} = \theta \hat{\mathbf{e}}_3$, this relationship can further be rewritten by first decomposing \mathbf{p} into its normal and tangential components then crossing this result with the tangent vector, *viz.*,

$$\hat{\mathbf{P}}\mathbf{t} = \mathbf{p} \times \mathbf{t}, \quad (\text{A.113})$$

$$= (p_n \hat{\mathbf{n}} + p_t \hat{\mathbf{t}}) \times \| \mathbf{t} \| \hat{\mathbf{t}}, \quad (\text{A.114})$$

$$= -\| \mathbf{t} \| (\mathbf{p} \cdot \hat{\mathbf{n}}) \hat{\mathbf{e}}_3, \quad (\text{A.115})$$

and

$$\hat{\mathbf{T}}\mathbf{g} = \mathbf{t} \times \mathbf{g}, \quad (\text{A.116})$$

$$= \| \mathbf{t} \| \hat{\mathbf{t}} \times g_n \hat{\mathbf{n}}, \quad (\text{A.117})$$

$$= \| \mathbf{t} \| g_n \hat{\mathbf{e}}_3. \quad (\text{A.118})$$

These two simplifications and the abbreviation

$$\boxed{\beta = \|\mathbf{t}\| (g_n - \mathbf{p} \cdot \hat{\mathbf{n}})}, \quad (\text{A.119})$$

make Eq. (A.112) become

$$\boxed{\frac{\partial \xi}{\partial \boldsymbol{\theta}} = -\alpha \beta \hat{\mathbf{e}}_3}. \quad (\text{A.120})$$

Three additional simplifications resulting from planar rotation will be used later. These are

$$\hat{\mathbf{P}} \hat{\mathbf{n}} = \mathbf{p} \times \hat{\mathbf{n}}, \quad (\text{A.121})$$

$$= (p_n \hat{\mathbf{n}} + p_t \hat{\mathbf{t}}) \times \hat{\mathbf{n}}, \quad (\text{A.122})$$

$$= (\mathbf{p} \cdot \hat{\mathbf{t}}) \hat{\mathbf{e}}_3, \quad (\text{A.123})$$

and

$$\hat{\mathbf{P}} \hat{\mathbf{e}}_3 = \mathbf{p} \times \hat{\mathbf{e}}_3, \quad (\text{A.124})$$

$$= (p_n \hat{\mathbf{n}} + p_t \hat{\mathbf{t}}) \times \hat{\mathbf{e}}_3, \quad (\text{A.125})$$

$$= (\mathbf{p} \cdot \hat{\mathbf{n}}) \hat{\mathbf{t}} - (\mathbf{p} \cdot \hat{\mathbf{t}}) \hat{\mathbf{n}}, \quad (\text{A.126})$$

and the signed curvature $\tilde{\kappa}$ in

$$\boxed{\tilde{\kappa} = \frac{\mathbf{t}_{,\xi} \cdot \hat{\mathbf{n}}}{\mathbf{t} \cdot \mathbf{t}}}. \quad (\text{A.127})$$

VARIATION OF THE TANGENT VECTOR \mathbf{t} The variation of the tangent vector is important because it is used in deriving the expression for the variation of the unit normal vector $\hat{\mathbf{n}}$, which in turn is necessary to construct the variations contributing to the contact potential.

The variation of the tangent vector is given by

$$\delta \mathbf{t} = \left[\frac{\partial \mathbf{t}}{\partial \xi} \frac{\partial \xi}{\partial \mathbf{u}} \right] \delta \mathbf{u} + \left[\frac{\partial \mathbf{t}}{\partial \xi} \frac{\partial \xi}{\partial \mathbf{r}} \right] \delta \mathbf{r} + \left[\frac{\partial \mathbf{t}}{\partial \boldsymbol{\theta}} + \frac{\partial \mathbf{t}}{\partial \xi} \frac{\partial \xi}{\partial \boldsymbol{\theta}} \right] \delta \boldsymbol{\theta}. \quad (\text{A.128})$$

Substituting from Eqs. (A.98), (A.105), and (A.120) gives

$$\delta \mathbf{t} = \alpha [\mathbf{t}_{,\xi} \otimes \mathbf{t}] \delta \mathbf{u} - \alpha [\mathbf{t}_{,\xi} \otimes \mathbf{t}] \delta \mathbf{r} - [\hat{\mathbf{T}}] \delta \boldsymbol{\theta} - \alpha \beta [\mathbf{t}_{,\xi} \otimes \hat{\mathbf{e}}_3] \delta \boldsymbol{\theta}, \quad (\text{A.129})$$

$$= \alpha [\mathbf{t}_{,\xi} \otimes \mathbf{t}] \delta \mathbf{u} - \alpha [\mathbf{t}_{,\xi} \otimes \mathbf{t}] \delta \mathbf{r} - \mathbf{t} \times \hat{\mathbf{e}}_3 \delta \theta - \alpha \beta [\mathbf{t}_{,\xi} \otimes \hat{\mathbf{e}}_3] \hat{\mathbf{e}}_3 \delta \theta, \quad (\text{A.130})$$

$$= \alpha [\mathbf{t}_{,\xi} \otimes \mathbf{t}] \delta \mathbf{u} - \alpha [\mathbf{t}_{,\xi} \otimes \mathbf{t}] \delta \mathbf{r} + \|\mathbf{t}\| \hat{\mathbf{n}} \delta \theta - \alpha \beta \mathbf{t}_{,\xi} \delta \theta, \quad (\text{A.131})$$

or finally

$$\boxed{\delta \mathbf{t} = \alpha [\mathbf{t}_{,\xi} \otimes \mathbf{t}] \delta \mathbf{u} - \alpha [\mathbf{t}_{,\xi} \otimes \mathbf{t}] \delta \mathbf{r} + [\|\mathbf{t}\| \hat{\mathbf{n}} - \alpha \beta \mathbf{t}_{,\xi}] \delta \theta}. \quad (\text{A.132})$$

VARIATION OF THE UNIT TANGENT VECTOR $\hat{\mathbf{t}}$ The variation of the unit tangent vector $\hat{\mathbf{t}} = \mathbf{t} / \|\mathbf{t}\|$ is a bit more complicated than the variation of the tangent vector \mathbf{t} because the denominator depends on \mathbf{u} , \mathbf{r} , and $\boldsymbol{\theta}$ as well. The variation of the unit tangent vector is given by

$$\delta \hat{\mathbf{t}} = \delta \left(\frac{\mathbf{t}}{\|\mathbf{t}\|} \right). \quad (\text{A.133})$$

Using Eq. (A.72) and Eq. (A.79) in turn give

$$\delta \hat{\mathbf{t}} = \frac{1}{\|\mathbf{t}\|} [\mathbf{1} - \hat{\mathbf{t}} \otimes \hat{\mathbf{t}}] \delta \mathbf{t}, \quad (\text{A.134})$$

$$\begin{aligned} &= \frac{1}{\|\mathbf{t}\|} [\hat{\mathbf{n}} \otimes \hat{\mathbf{n}} + \hat{\mathbf{e}}_3 \otimes \hat{\mathbf{e}}_3] [\alpha \mathbf{t}_{,\xi} \otimes \mathbf{t}] (\delta \mathbf{u} - \delta \mathbf{r}) \\ &\quad + \frac{1}{\|\mathbf{t}\|} [\hat{\mathbf{n}} \otimes \hat{\mathbf{n}} + \hat{\mathbf{e}}_3 \otimes \hat{\mathbf{e}}_3] (\|\mathbf{t}\| \hat{\mathbf{n}} - \alpha \beta \mathbf{t}_{,\xi}) \delta \theta, \end{aligned} \quad (\text{A.135})$$

$$= \alpha (\mathbf{t}_{,\xi} \cdot \hat{\mathbf{n}}) [\hat{\mathbf{n}} \otimes \hat{\mathbf{t}}] (\delta \mathbf{u} - \delta \mathbf{r}) + \frac{1}{\|\mathbf{t}\|} (\|\mathbf{t}\| \hat{\mathbf{n}} - \alpha \beta (\mathbf{t}_{,\xi} \cdot \hat{\mathbf{n}}) \hat{\mathbf{n}}) \delta \theta, \quad (\text{A.136})$$

$$= \alpha (\mathbf{t}_{,\xi} \cdot \hat{\mathbf{n}}) [\hat{\mathbf{n}} \otimes \hat{\mathbf{t}}] (\delta \mathbf{u} - \delta \mathbf{r}) + (1 - \tilde{\kappa} \alpha \beta \|\mathbf{t}\|) \hat{\mathbf{n}} \delta \theta. \quad (\text{A.137})$$

$$(\text{A.138})$$

Consider now simplification of the coefficient of the $\delta \theta$ variation

$$1 - \tilde{\kappa} \alpha \beta \|\mathbf{t}\| = 1 - \frac{\tilde{\kappa} \|\mathbf{t}\| (g_n - \mathbf{p} \cdot \hat{\mathbf{n}}) \|\mathbf{t}\|}{\mathbf{t} \cdot \mathbf{t} + \mathbf{t}_{,\xi} \cdot \mathbf{g}}, \quad (\text{A.139})$$

$$= \frac{\mathbf{t} \cdot \mathbf{t} + \mathbf{t}_{,\xi} \cdot \hat{\mathbf{n}} g_n - \tilde{\kappa} (\mathbf{t} \cdot \mathbf{t}) g_n + \tilde{\kappa} (\mathbf{t} \cdot \mathbf{t}) (\mathbf{p} \cdot \hat{\mathbf{n}})}{\mathbf{t} \cdot \mathbf{t} + \mathbf{t}_{,\xi} \cdot \hat{\mathbf{n}} g_n}, \quad (\text{A.140})$$

$$= \frac{\mathbf{t} \cdot \mathbf{t} + \mathbf{t}_{,\xi} \cdot \hat{\mathbf{n}} g_n - \mathbf{t}_{,\xi} \cdot \hat{\mathbf{n}} g_n + (\mathbf{t}_{,\xi} \cdot \hat{\mathbf{n}}) (\mathbf{p} \cdot \hat{\mathbf{n}})}{\mathbf{t} \cdot \mathbf{t} + \mathbf{t}_{,\xi} \cdot \hat{\mathbf{n}} g_n}, \quad (\text{A.141})$$

$$= \frac{1 + \tilde{\kappa} (\mathbf{p} \cdot \hat{\mathbf{n}})}{1 + \tilde{\kappa} g_n}, \quad (\text{A.142})$$

which when substituted finally gives

$$\boxed{\delta \hat{\mathbf{t}} = \alpha (\mathbf{t}_{,\xi} \cdot \hat{\mathbf{n}}) [\hat{\mathbf{n}} \otimes \hat{\mathbf{t}}] \delta \mathbf{u} - \alpha (\mathbf{t}_{,\xi} \cdot \hat{\mathbf{n}}) [\hat{\mathbf{n}} \otimes \hat{\mathbf{t}}] \delta \mathbf{r} + \left(\frac{1 + \tilde{\kappa} (\mathbf{p} \cdot \hat{\mathbf{n}})}{1 + \tilde{\kappa} g_n} \right) \hat{\mathbf{n}} \delta \theta}. \quad (\text{A.143})$$

VARIATION OF THE UNIT NORMAL VECTOR $\hat{\mathbf{n}}$ The variation of the unit normal vector $\delta\hat{\mathbf{n}}$ will be important for the second variation. Perhaps surprisingly, it is not necessary for the first variation because the terms which are eventually multiplied with $\delta\hat{\mathbf{n}}$ turn out to be parallel to $\hat{\mathbf{n}}$. As already noted in Eq. (A.85), $\delta\hat{\mathbf{n}} \cdot \hat{\mathbf{n}} = 0$, thus the variation of the normal vector makes no contribution to the first variation. This claim is shown in Eq. (A.143).

The cross product of the bi-normal $\hat{\mathbf{e}}_3$ with the unit tangent vector $\hat{\mathbf{t}}$ is used to make the unit normal vector $\hat{\mathbf{n}} = \hat{\mathbf{e}}_3 \times \hat{\mathbf{t}}$. Using this construction and results from Eq. (A.72) gives $\delta\hat{\mathbf{n}} = \delta(\hat{\mathbf{e}}_3 \times \hat{\mathbf{t}}) = \hat{\mathbf{e}}_3 \times \delta\hat{\mathbf{t}}$. Note this expression describes the special case of planar rotation about the $\hat{\mathbf{e}}_3$ axis. In this special case, the variation of this unit vector is zero, $\delta\hat{\mathbf{e}}_3 = \mathbf{0}$. Substituting for $\delta\hat{\mathbf{t}}$ from Eq. (A.143)

$$\delta\hat{\mathbf{n}} = \hat{\mathbf{e}}_3 \times \underbrace{\left(\alpha(\mathbf{t}_{,\xi} \cdot \hat{\mathbf{n}})[\hat{\mathbf{n}} \otimes \hat{\mathbf{t}}](\delta\mathbf{u} - \delta\mathbf{r}) + \left(\frac{1 + \bar{\kappa}(\mathbf{p} \cdot \hat{\mathbf{n}})}{1 + \bar{\kappa}g_n} \right) \hat{\mathbf{n}} \delta\theta \right)}_{\delta\hat{\mathbf{t}}}, \quad (\text{A.144})$$

and then using the cross product result from Eq. (A.81) gives

$$\begin{aligned} \delta\hat{\mathbf{n}} &= \alpha(\mathbf{t}_{,\xi} \cdot \hat{\mathbf{n}}) [\hat{\mathbf{n}} \otimes \hat{\mathbf{t}} - \hat{\mathbf{t}} \otimes \hat{\mathbf{n}}] [\hat{\mathbf{n}} \otimes \hat{\mathbf{t}}] (\delta\mathbf{u} - \delta\mathbf{r}) \\ &\quad + [\hat{\mathbf{n}} \otimes \hat{\mathbf{t}} - \hat{\mathbf{t}} \otimes \hat{\mathbf{n}}] \left(\frac{1 + \bar{\kappa}(\mathbf{p} \cdot \hat{\mathbf{n}})}{1 + \bar{\kappa}g_n} \right) \hat{\mathbf{n}} \delta\theta, \end{aligned} \quad (\text{A.145})$$

$$= -\bar{\kappa} \alpha[\mathbf{t} \otimes \hat{\mathbf{t}}](\delta\mathbf{u} - \delta\mathbf{r}) - \left(\frac{1 + \bar{\kappa}(\mathbf{p} \cdot \hat{\mathbf{n}})}{1 + \bar{\kappa}g_n} \right) \hat{\mathbf{t}} \delta\theta, \quad (\text{A.146})$$

which finally gives

$$\boxed{\delta\hat{\mathbf{n}} = -\bar{\kappa} \alpha[\mathbf{t} \otimes \hat{\mathbf{t}}] \delta\mathbf{u} + \bar{\kappa} \alpha[\mathbf{t} \otimes \hat{\mathbf{t}}] \delta\mathbf{r} - \left(\frac{1 + \bar{\kappa}(\mathbf{p} \cdot \hat{\mathbf{n}})}{1 + \bar{\kappa}g_n} \right) \hat{\mathbf{t}} \delta\theta}. \quad (\text{A.147})$$

VARIATION OF THE GAP DISTANCE g_n The variation of the normal gap distance g_n is

$$\delta g_n = \delta(\mathbf{y} - \boldsymbol{\varphi}) \cdot \hat{\mathbf{n}} + (\mathbf{y} - \boldsymbol{\varphi}) \cdot \delta\hat{\mathbf{n}}. \quad (\text{A.148})$$

This expression may be simplified further by noting the vector $(\mathbf{y} - \boldsymbol{\varphi})$ is always parallel to $\hat{\mathbf{n}}$ by construction and from Eq. (A.85), $\delta\hat{\mathbf{n}} \cdot \hat{\mathbf{n}} = 0$ implies any vector parallel to $\hat{\mathbf{n}}$ dotted with $\delta\hat{\mathbf{n}}$ is zero, thus

$$\delta g_n = \delta(\mathbf{y} - \boldsymbol{\varphi}) \cdot \hat{\mathbf{n}} + \underbrace{(\mathbf{y} - \boldsymbol{\varphi})}_{\parallel \hat{\mathbf{n}}} \cdot \delta\hat{\mathbf{n}}, \quad (\text{A.149})$$

$$\delta g_n = \delta(\mathbf{y} - \boldsymbol{\varphi}) \cdot \hat{\mathbf{n}}. \quad (\text{A.150})$$

Next the chain rule is used to find an expression for δg_n in terms of $\delta \mathbf{u}, \delta \mathbf{r}, \delta \boldsymbol{\theta}$:

$$\delta g_n = \left(\left[\frac{\partial \mathbf{y}}{\partial \xi} \frac{\partial \xi}{\partial \mathbf{u}} - \frac{\partial \boldsymbol{\varphi}}{\partial \mathbf{u}} \right] \delta \mathbf{u} + \left[\frac{\partial \mathbf{y}}{\partial \mathbf{r}} + \frac{\partial \mathbf{y}}{\partial \xi} \frac{\partial \xi}{\partial \mathbf{r}} \right] \delta \mathbf{r} + \left[\frac{\partial \mathbf{y}}{\partial \boldsymbol{\theta}} + \frac{\partial \mathbf{y}}{\partial \xi} \frac{\partial \xi}{\partial \boldsymbol{\theta}} \right] \delta \boldsymbol{\theta} \right) \cdot \hat{\mathbf{n}}. \quad (\text{A.151})$$

Substituting \mathbf{t} from Eq. (A.86) and $\partial \boldsymbol{\varphi}/\partial \mathbf{u} = \mathbf{1}$ gives

$$\delta g_n = \left(\left[\mathbf{t} \frac{\partial \xi}{\partial \mathbf{u}} - \mathbf{1} \right] \delta \mathbf{u} + \left[\frac{\partial \mathbf{y}}{\partial \mathbf{r}} + \mathbf{t} \frac{\partial \xi}{\partial \mathbf{r}} \right] \delta \mathbf{r} + \left[\frac{\partial \mathbf{y}}{\partial \boldsymbol{\theta}} + \mathbf{t} \frac{\partial \xi}{\partial \boldsymbol{\theta}} \right] \delta \boldsymbol{\theta} \right) \cdot \hat{\mathbf{n}}. \quad (\text{A.152})$$

Note that the projection may be written as either

$$\mathbf{y} = \boldsymbol{\varphi}(\mathbf{u}) + \mathbf{g}(\mathbf{u}, \mathbf{r}, \boldsymbol{\theta}, \xi(\mathbf{u}, \mathbf{r}, \boldsymbol{\theta})), \quad \text{or} \quad \mathbf{y} = \mathbf{r} + \mathbf{p}(\boldsymbol{\theta}, \xi(\mathbf{u}, \mathbf{r}, \boldsymbol{\theta})), \quad (\text{A.153})$$

thus

$$\frac{\partial \mathbf{y}}{\partial \mathbf{r}} = \mathbf{1}, \quad \text{and} \quad \frac{\partial \mathbf{y}}{\partial \boldsymbol{\theta}} = \frac{\partial \mathbf{p}}{\partial \boldsymbol{\theta}} + \frac{\partial \mathbf{p}}{\partial \xi} \frac{\partial \xi}{\partial \boldsymbol{\theta}}. \quad (\text{A.154})$$

Substituting these two expressions gives

$$\delta g_n = \left(\left[\mathbf{t} \frac{\partial \xi}{\partial \mathbf{u}} - \mathbf{1} \right] \delta \mathbf{u} + \left[\mathbf{1} + \mathbf{t} \frac{\partial \xi}{\partial \mathbf{r}} \right] \delta \mathbf{r} + \left[\frac{\partial \mathbf{p}}{\partial \boldsymbol{\theta}} + \frac{\partial \mathbf{p}}{\partial \xi} \frac{\partial \xi}{\partial \boldsymbol{\theta}} + \mathbf{t} \frac{\partial \xi}{\partial \boldsymbol{\theta}} \right] \delta \boldsymbol{\theta} \right) \cdot \hat{\mathbf{n}}. \quad (\text{A.155})$$

The vector \mathbf{r} has no dependence on ξ . Therefore the relationship $\mathbf{y} = \mathbf{r} + \mathbf{p}$ may be used to show that the tangent vector \mathbf{t} may be derived from \mathbf{p} through

$$\mathbf{t} = \frac{\partial \mathbf{y}}{\partial \xi} = \frac{\partial}{\partial \xi}(\mathbf{r} + \mathbf{p}) = \frac{\partial \mathbf{p}}{\partial \xi}. \quad (\text{A.156})$$

Note \mathbf{r} has no dependence on ξ . Substituting this expression gives

$$\delta g_n = \left(\left[\mathbf{t} \frac{\partial \xi}{\partial \mathbf{u}} - \mathbf{1} \right] \delta \mathbf{u} + \left[\mathbf{1} + \mathbf{t} \frac{\partial \xi}{\partial \mathbf{r}} \right] \delta \mathbf{r} + \left[\frac{\partial \mathbf{p}}{\partial \boldsymbol{\theta}} + 2\mathbf{t} \frac{\partial \xi}{\partial \boldsymbol{\theta}} \right] \delta \boldsymbol{\theta} \right) \cdot \hat{\mathbf{n}}. \quad (\text{A.157})$$

Next using Eq. (A.71) as

$$[\mathbf{a} \otimes \mathbf{b}] \mathbf{c} \cdot \mathbf{d} = (\mathbf{a} \cdot \mathbf{d})(\mathbf{b} \cdot \mathbf{c}), \quad (\text{A.158})$$

$$\left[\mathbf{t} \otimes \frac{\partial \xi}{\partial (\bullet)} \right] \delta(\bullet) \cdot \hat{\mathbf{n}} = \underbrace{(\mathbf{t} \cdot \hat{\mathbf{n}})}_{= \mathbf{0}} \left(\frac{\partial \xi}{\partial (\bullet)} \cdot \delta(\bullet) \right), \quad (\text{A.159})$$

gives

$$\delta g_n = \left([-\mathbf{1}] \delta \mathbf{u} + [\mathbf{1}] \delta \mathbf{r} + \left[\frac{\partial \mathbf{p}}{\partial \boldsymbol{\theta}} \right] \delta \boldsymbol{\theta} \right) \cdot \hat{\mathbf{n}}, \quad (\text{A.160})$$

$$= (\delta \mathbf{r} - \hat{\mathbf{P}} \delta \boldsymbol{\theta} - \delta \mathbf{u}) \cdot \hat{\mathbf{n}}, \quad (\text{A.161})$$

$$= -\hat{\mathbf{n}} \cdot \delta \mathbf{u} + \hat{\mathbf{n}} \cdot \delta \mathbf{r} - \hat{\mathbf{P}} \hat{\mathbf{e}}_3 \delta \theta \cdot \hat{\mathbf{n}}, \quad (\text{A.162})$$

$$= -\hat{\mathbf{n}} \cdot \delta \mathbf{u} + \hat{\mathbf{n}} \cdot \delta \mathbf{r} - ((\mathbf{p} \cdot \hat{\mathbf{n}}) \hat{\mathbf{t}} - (\mathbf{p} \cdot \hat{\mathbf{t}}) \hat{\mathbf{n}}) \cdot \hat{\mathbf{n}} \delta \theta, \quad (\text{A.163})$$

which finally gives

$$\boxed{\delta g_n = -\hat{\mathbf{n}} \cdot \delta \mathbf{u} + \hat{\mathbf{n}} \cdot \delta \mathbf{r} + (\mathbf{p} \cdot \hat{\mathbf{t}}) \delta \theta}. \quad (\text{A.164})$$

The variation of the gap distance may also be written as

$$\delta g_n = \underbrace{\langle -\hat{\mathbf{n}}, \hat{\mathbf{n}}, (\mathbf{p} \cdot \hat{\mathbf{t}}) \rangle}_{\langle \nabla_s g_n \rangle} \begin{Bmatrix} \delta \mathbf{u} \\ \delta \mathbf{r} \\ \delta \boldsymbol{\theta} \end{Bmatrix} = \begin{Bmatrix} \delta \mathbf{u} \\ \delta \mathbf{r} \\ \delta \boldsymbol{\theta} \end{Bmatrix}^T \underbrace{\begin{Bmatrix} -\hat{\mathbf{n}} \\ \hat{\mathbf{n}} \\ (\mathbf{p} \cdot \hat{\mathbf{t}}) \end{Bmatrix}}_{\langle \nabla_s g_n \rangle^T}, \quad (\text{A.165})$$

as a precursor to implementing the first variation on an element level.

VARIATION OF THE PROJECTION FROM MASS CENTER VECTOR \mathbf{p} The variation of the vector locating the projection of the contact point from the mass center vector is required for proper linearization of the tangent matrices involving the $\delta \boldsymbol{\theta}$ equations. Recall \mathbf{p} may be constructed from \mathbf{y} and \mathbf{r} as $\mathbf{p} = \mathbf{y} - \mathbf{r}$ thus

$$\delta \mathbf{p} = \delta \mathbf{y} - \delta \mathbf{r}, \quad (\text{A.166})$$

$$= \frac{\partial \mathbf{y}}{\partial \xi} \frac{\partial \xi}{\partial \mathbf{u}} \delta \mathbf{u} + \left[\frac{\partial \mathbf{y}}{\partial \mathbf{r}} + \frac{\partial \mathbf{y}}{\partial \xi} \frac{\partial \xi}{\partial \mathbf{r}} \right] \delta \mathbf{r} + \left[\frac{\partial \mathbf{y}}{\partial \boldsymbol{\theta}} + \frac{\partial \mathbf{y}}{\partial \xi} \frac{\partial \xi}{\partial \boldsymbol{\theta}} \right] \delta \boldsymbol{\theta} - \mathbf{1} \delta \mathbf{r}. \quad (\text{A.167})$$

Substituting

$$\frac{\partial \mathbf{y}}{\partial \xi} = \mathbf{t}, \quad \frac{\partial \mathbf{y}}{\partial \mathbf{r}} = \mathbf{1}, \quad \frac{\partial \mathbf{y}}{\partial \boldsymbol{\theta}} = \frac{\partial \mathbf{p}}{\partial \boldsymbol{\theta}} = \frac{\partial \dot{\mathbf{p}}}{\partial \boldsymbol{\omega}} = -\hat{\mathbf{P}}, \quad (\text{A.168})$$

and $\partial \xi / \partial \mathbf{u}$, $\partial \xi / \partial \mathbf{r}$, and $\partial \xi / \partial \boldsymbol{\theta}$ from Eqs. (A.98), (A.105), and (A.120), respectively gives

$$\delta \mathbf{p} = \alpha [\mathbf{t} \otimes \mathbf{t}] \delta \mathbf{u} - \alpha [\mathbf{t} \otimes \mathbf{t}] \delta \mathbf{r} - [\hat{\mathbf{P}} + \alpha \beta \mathbf{t} \otimes \hat{\mathbf{e}}_3] \delta \boldsymbol{\theta}, \quad (\text{A.169})$$

$$= \alpha [\mathbf{t} \otimes \mathbf{t}] \delta \mathbf{u} - \alpha [\mathbf{t} \otimes \mathbf{t}] \delta \mathbf{r} - \hat{\mathbf{P}} \hat{\mathbf{e}}_3 \delta \theta - \alpha \beta [\mathbf{t} \otimes \hat{\mathbf{e}}_3] \hat{\mathbf{e}}_3 \delta \theta, \quad (\text{A.170})$$

or finally

$$\boxed{\delta \mathbf{p} = \alpha [\mathbf{t} \otimes \mathbf{t}] \delta \mathbf{u} - \alpha [\mathbf{t} \otimes \mathbf{t}] \delta \mathbf{r} + ((\mathbf{p} \cdot \hat{\mathbf{t}}) \hat{\mathbf{n}} - (\alpha \beta \| \mathbf{t} \| + \mathbf{p} \cdot \hat{\mathbf{n}}) \hat{\mathbf{t}}) \delta \theta}. \quad (\text{A.171})$$

A.5.2 THE FIRST VARIATION

From SECTION 2.5, the variation of the contact potential $\delta\mathcal{W}_g$ has two forms, depending on whether contact or gap status is encountered. The contact case is considered first. Recall the state variable \mathbf{s} contains displacements and rotations, $\mathbf{s} = \langle \mathbf{u}, \mathbf{r}, \theta \rangle^T$. The variation of the contact potential is then written

$$\begin{aligned} \delta\mathcal{W}_g &= (\lambda + rg_n) \nabla_s g_n \delta\mathbf{s} + g_n \delta\lambda, \\ \text{(contact)} \end{aligned} \quad (\text{A.172})$$

$$= \delta\mathbf{s}^T \langle \nabla_s g_n \rangle^T (\lambda + rg_n) + \delta\lambda g_n, \quad (\text{A.173})$$

$$= \left\{ \begin{array}{c} \delta\mathbf{u} \\ \delta\mathbf{r} \\ \delta\theta \end{array} \right\}_{(1 \times 5)}^T \left\{ \begin{array}{c} -\hat{\mathbf{n}} \\ \hat{\mathbf{n}} \\ (\mathbf{p} \cdot \hat{\mathbf{t}}) \end{array} \right\}_{(5 \times 1)}^{(1 \times 1)} (\lambda + rg_n) + \left\{ \begin{array}{c} \delta\lambda \end{array} \right\}_{(1 \times 1)}^T \left\{ \begin{array}{c} g_n \end{array} \right\}_{(1 \times 1)}. \quad (\text{A.174})$$

The the first variation may be stated

$$\delta\mathcal{W}_g_{\text{(contact)}} = \left\{ \begin{array}{c} \delta\mathbf{u} \\ \delta\mathbf{r} \\ \frac{\delta\theta}{\delta\lambda} \end{array} \right\}^T \left\{ \begin{array}{c} -\hat{\mathbf{n}} (\lambda + rg_n) \\ \hat{\mathbf{n}} (\lambda + rg_n) \\ \frac{(\mathbf{p} \cdot \hat{\mathbf{t}}) (\lambda + rg_n)}{g_n} \end{array} \right\}. \quad (\text{A.175})$$

Expanded, the first variation has the form given in Box A.3, which represents Eq. (2.104) in explicit form. Note that in Box A.3, the expression for $(\mathbf{p} \cdot \hat{\mathbf{t}})$ has been expressed in terms of the components of the normal vector $\hat{\mathbf{n}}$ instead of the normalized tangent vector $\hat{\mathbf{t}}$ using $(\mathbf{p} \cdot \hat{\mathbf{t}}) = \hat{\mathbf{P}}\hat{\mathbf{n}} \cdot \hat{\mathbf{e}}_3$ from Eq. (A.123). We abbreviate this quantity as

$$\zeta = (\mathbf{p} \cdot \hat{\mathbf{t}}) = \hat{\mathbf{P}}\hat{\mathbf{n}} \cdot \hat{\mathbf{e}}_3 = (n_2 p_1 - n_1 p_2). \quad (\text{A.176})$$

The variation of the contact potential $\delta\mathcal{W}_g$ has a much simpler form in the case of gap. It is written in Box A.4 simply by inspection of Eq. (2.105).

Box A.3: First variation of the generalized contact constraint with contact status in expanded form.

$$\delta \mathcal{W}_g \begin{cases} \text{(contact)} \end{cases} = \left\{ \frac{\delta u_1}{\delta r_1}, \frac{\delta u_2}{\delta r_2}, \frac{\delta r_1}{\delta \theta}, \frac{\delta r_2}{\delta \lambda} \right\}^T \left\{ \begin{array}{c} -n_1(\lambda + rg_n) \\ -n_2(\lambda + rg_n) \\ n_1(\lambda + rg_n) \\ n_2(\lambda + rg_n) \\ \zeta(\lambda + rg_n) \\ g_n \end{array} \right\} \quad (\text{A.177})$$

Box A.4: First variation of the generalized contact constraint with gap status in expanded form.

$$\delta \mathcal{W}_g \begin{cases} \text{(gap)} \end{cases} = \left\{ \frac{\delta u_1}{\delta r_1}, \frac{\delta u_2}{\delta r_2}, \frac{\delta r_1}{\delta \theta}, \frac{\delta r_2}{\delta \lambda} \right\}^T \left\{ \begin{array}{c} 0 \\ 0 \\ 0 \\ 0 \\ 0 \\ \frac{-\lambda}{r} \end{array} \right\}, \quad r > 0 \quad (\text{A.178})$$

A.5.3 THE SECOND VARIATION

Differentiating Eq. (A.175) with the state vector $\mathbf{s} = \langle \mathbf{u}, \mathbf{r}, \theta \rangle^T$ and the Lagrange multiplier λ gives the second variation

$$\begin{aligned} \Delta\delta\mathcal{W}_g &= \underbrace{\delta\mathbf{s}^T [\nabla_s \{(\nabla_s g_n)^T (\lambda + rg_n)\}] \Delta\mathbf{s}}_{\phi_{11}} \\ &+ \underbrace{\delta\mathbf{s}^T [\nabla_\lambda \{(\nabla_s g_n)^T (\lambda + rg_n)\}] \Delta\lambda}_{\phi_{12}} \\ &+ \underbrace{\delta\lambda^T (\nabla_s g_n) \Delta\mathbf{s}}_{\phi_{21}} + \underbrace{\delta\lambda^T (\nabla_\lambda g_n) \Delta\lambda}_{\phi_{22}}. \end{aligned} \quad (\text{A.179})$$

Simplification of these ϕ_{ij} terms is carried out as follows: The ϕ_{11} term may be expanded to be

$$\phi_{11} = \underbrace{\delta\mathbf{s}^T [\nabla_{s[1]} \{(\nabla_s g_n)^T (\lambda + rg_n)\}] \Delta\mathbf{s}}_{\phi_{11.a}} + \underbrace{\delta\mathbf{s}^T [\langle \nabla_s g_n \rangle^T \langle \nabla_s g_n \rangle r] \Delta\mathbf{s}}_{\phi_{11.b}}. \quad (\text{A.180})$$

The gradient ∇_s is distributed on the $\{(\nabla_s g_n)^T (\lambda + rg_n)\}$ vector in ϕ_{11} , resulting in two separate derivatives. The first derivative is on the $(\nabla_s g_n)^T$ term, shown in $\phi_{11.a}$ with the $\nabla_{s[1]}$ notation. The second derivative is on the $(\lambda + rg_n)$ term, shown in $\phi_{11.b}$, with the derivative already taken. In the $\phi_{11.a}$ term, $(\lambda + rg_n)$ is held constant. To avoid confusion while taking this derivative, we let $c = (\lambda + rg_n)$ to evoke the notion that the scalar c is held constant.

The $\phi_{11.a}$ term is obtained through the following manipulations:

$$\phi_{11.a} = \delta\mathbf{s}^T [\nabla_{s[1]} \{(\nabla_s g_n)^T (c)\}] \Delta\mathbf{s}, \quad (\text{A.181})$$

$$= \delta\mathbf{s}^T \nabla_s \left[\begin{Bmatrix} -\hat{\mathbf{n}} \\ \hat{\mathbf{n}} \\ (\mathbf{p} \cdot \hat{\mathbf{t}}) \end{Bmatrix} (c) \right] \Delta\mathbf{s}. \quad (\text{A.182})$$

Simplification of the above result requires finding the derivatives of two types of terms: $[\nabla_s \hat{\mathbf{n}}]$ and $[\nabla_s (\mathbf{p} \cdot \hat{\mathbf{t}})]$. The variation of Eq. (A.182) is lengthy and therefore broken down into several smaller steps. We begin with the first row of equations. The first row terms contributing to the Hessian are found by substituting from Eq. (A.147). The [11] term is

found to be

$$[11] \quad \delta \mathbf{u}^T(c) [-\nabla_u \hat{\mathbf{n}}] \Delta \mathbf{u} = \delta \mathbf{u}^T [(\lambda + rg_n) \tilde{\kappa} \alpha [\mathbf{t} \otimes \hat{\mathbf{t}}]] \Delta \mathbf{u}, \quad (\text{A.183})$$

the [12] term

$$[12] \quad \delta \mathbf{u}^T(c) [-\nabla_r \hat{\mathbf{n}}] \Delta \mathbf{r} = \delta \mathbf{u}^T [-(\lambda + rg_n) \tilde{\kappa} \alpha [\mathbf{t} \otimes \hat{\mathbf{t}}]] \Delta \mathbf{r}, \quad (\text{A.184})$$

and finally the [13] term

$$\begin{aligned} [13] \quad & \delta \mathbf{u}^T(c) [-\nabla_\theta \hat{\mathbf{n}}] \Delta \theta \\ &= \delta \mathbf{u}^T \left\{ (\lambda + rg_n) \left(\frac{1 + \tilde{\kappa}(\mathbf{p} \cdot \hat{\mathbf{n}})}{1 + \tilde{\kappa}g_n} \right) \hat{\mathbf{t}} \right\} \Delta \theta. \end{aligned} \quad (\text{A.185})$$

The second row terms are simply negative the first row. The third row gets complicated because both \mathbf{p} and $\hat{\mathbf{t}}$ depend on the variables $\mathbf{u}, \mathbf{r}, \boldsymbol{\theta}$. Consider the derivative of a vector

$$\frac{d}{dt}(\mathbf{a} \cdot \mathbf{b}) = \frac{d\mathbf{a}}{dt} \cdot \mathbf{b} + \mathbf{a} \cdot \frac{d\mathbf{b}}{dt} \quad \forall \quad \mathbf{a}, \mathbf{b} \in \mathbb{R}^3. \quad (\text{A.186})$$

This leads to

$$\delta \mathbf{s}^T(c) [\nabla_s(\mathbf{p} \cdot \hat{\mathbf{t}})] \Delta \mathbf{s} = \delta \mathbf{s}^T(c) [\hat{\mathbf{t}}^T \nabla_s \mathbf{p} + \mathbf{p}^T \nabla_s \hat{\mathbf{t}}] \Delta \mathbf{s}. \quad (\text{A.187})$$

Carrying out the derivatives term by term and substituting from both Eq. (A.143) for $\delta \hat{\mathbf{t}}$ and Eq. (A.171) for $\delta \mathbf{p}$ gives the third row contributions to the Hessian. The [31] term is found to be

$$\begin{aligned} [31] \quad & \delta \theta(c) \left[\hat{\mathbf{t}}^T [\alpha \mathbf{t} \otimes \mathbf{t}] + \mathbf{p}^T \alpha (\mathbf{t}_{,\xi} \cdot \hat{\mathbf{n}}) [\hat{\mathbf{n}} \otimes \hat{\mathbf{t}}] \right] \Delta \mathbf{u} \\ &= \delta \theta(c) [\alpha([\mathbf{t} \otimes \mathbf{t}] \hat{\mathbf{t}})^T + \alpha(\mathbf{t}_{,\xi} \cdot \hat{\mathbf{n}})([\hat{\mathbf{t}} \otimes \hat{\mathbf{n}}] \mathbf{p})^T] \Delta \mathbf{u}, \end{aligned} \quad (\text{A.188})$$

$$= \delta \theta(c) [\alpha([\mathbf{t} \otimes \mathbf{t}] \hat{\mathbf{t}})^T + \alpha([\mathbf{t}_{,\xi} \otimes \hat{\mathbf{n}}] \mathbf{p})^T] \Delta \mathbf{u}, \quad (\text{A.189})$$

$$= \delta \theta(c) \left[\frac{(\mathbf{t} \cdot \mathbf{t})(\hat{\mathbf{t}} \cdot \hat{\mathbf{t}}) \hat{\mathbf{t}}^T + (\mathbf{t}_{,\xi} \cdot \hat{\mathbf{n}})(\mathbf{p} \cdot \hat{\mathbf{n}}) \hat{\mathbf{t}}^T}{\mathbf{t} \cdot \mathbf{t} + \mathbf{t}_{,\xi} \cdot \mathbf{g}} \right] \Delta \mathbf{u}, \quad (\text{A.190})$$

which finally gives

$$[31] \quad \delta \theta(\lambda + rg_n) \left[\frac{1 + \tilde{\kappa}(\mathbf{p} \cdot \hat{\mathbf{n}})}{1 + \tilde{\kappa}g_n} \right] \hat{\mathbf{t}}^T \Delta \mathbf{u}. \quad (\text{A.191})$$

The [32] term is found in a similar fashion used for the [31] term. By symmetry of the ∇_u terms with the $-\nabla_r$ terms on \mathbf{t} and \mathbf{p} , the [32] term may be written by inspection as

$$[32] \quad \delta \theta(-\lambda + rg_n) \left[\frac{1 + \tilde{\kappa}(\mathbf{p} \cdot \hat{\mathbf{n}})}{1 + \tilde{\kappa}g_n} \right] \hat{\mathbf{t}}^T \Delta \mathbf{u}. \quad (\text{A.192})$$

Finally, the [33] term is found through the following manipulations

$$\begin{aligned} [33] \quad \delta\theta(c) & \left[\hat{\mathbf{t}}^T ((\mathbf{p} \cdot \hat{\mathbf{t}})\hat{\mathbf{n}} - (\alpha\beta \| \mathbf{t} \| + \mathbf{p} \cdot \hat{\mathbf{n}})\hat{\mathbf{t}}) + \mathbf{p}^T \left(\frac{1 + \tilde{\kappa}(\mathbf{p} \cdot \hat{\mathbf{n}})}{1 + \tilde{\kappa}g_n} \right) \hat{\mathbf{n}} \right] \Delta\theta \\ & = \delta\theta(c) [-\alpha\beta \| \mathbf{t} \| + \mathbf{p} \cdot \hat{\mathbf{n}} + (1 - \tilde{\kappa}\alpha\beta \| \mathbf{t} \|)(\mathbf{p} \cdot \hat{\mathbf{n}})] \Delta\theta, \end{aligned} \quad (\text{A.193})$$

$$= \delta\theta [-\alpha\beta \| \mathbf{t} \| - \tilde{\kappa}\alpha\beta \| \mathbf{t} \| \mathbf{p} \cdot \hat{\mathbf{n}}] \Delta\theta, \quad (\text{A.194})$$

$$= \delta\theta \left[\frac{-(\mathbf{t} \cdot \mathbf{t})(g_n - \mathbf{p} \cdot \hat{\mathbf{n}})(1 + \tilde{\kappa}\mathbf{p} \cdot \hat{\mathbf{n}})}{\mathbf{t} \cdot \mathbf{t} + \mathbf{t} \cdot \hat{\mathbf{n}}g_n} \right] \Delta\theta, \quad (\text{A.195})$$

$$= \delta\theta \left[\frac{-(g_n - \mathbf{p} \cdot \hat{\mathbf{n}})(1 + \tilde{\kappa}(\mathbf{p} \cdot \hat{\mathbf{n}}))}{1 + \tilde{\kappa}g_n} \right] \Delta\theta, \quad (\text{A.196})$$

which finally gives

$$[33] \quad \delta\theta \left[-(\lambda + rg_n)(g_n - \mathbf{p} \cdot \hat{\mathbf{n}}) \frac{1 + \tilde{\kappa}(\mathbf{p} \cdot \hat{\mathbf{n}})}{1 + \tilde{\kappa}g_n} \right] \Delta\theta. \quad (\text{A.197})$$

The $\phi_{11.b}$ term results from the outer product of $\langle \nabla_s g_n \rangle^T \langle \nabla_s g_n \rangle$ multiplied by the scalar r . This outer product is represented

$$\begin{bmatrix} r & \langle & -\hat{\mathbf{n}} & \hat{\mathbf{n}} & \hat{\mathbf{P}}\hat{\mathbf{n}} & \rangle \\ -\hat{\mathbf{n}} & \left[\begin{array}{ccc} r\hat{\mathbf{n}} \otimes \hat{\mathbf{n}} & -r\hat{\mathbf{n}} \otimes \hat{\mathbf{n}} & -r\hat{\mathbf{n}} \otimes \hat{\mathbf{P}}\hat{\mathbf{n}} \\ -r\hat{\mathbf{n}} \otimes \hat{\mathbf{n}} & r\hat{\mathbf{n}} \otimes \hat{\mathbf{n}} & r\hat{\mathbf{n}} \otimes \hat{\mathbf{P}}\hat{\mathbf{n}} \\ -r\hat{\mathbf{P}}\hat{\mathbf{n}} \otimes \hat{\mathbf{n}} & r\hat{\mathbf{P}}\hat{\mathbf{n}} \otimes \hat{\mathbf{n}} & r\hat{\mathbf{P}}\hat{\mathbf{n}} \otimes \hat{\mathbf{P}}\hat{\mathbf{n}} \end{array} \right] \\ \hat{\mathbf{n}} & \end{bmatrix} \quad (\text{A.198})$$

When specialized for planar rotation, the $\phi_{11.b}$ term becomes

$$\phi_{11.b} = \begin{Bmatrix} \delta\mathbf{u} \\ \delta\mathbf{r} \\ \delta\theta \end{Bmatrix}^T \begin{bmatrix} r\hat{\mathbf{n}} \otimes \hat{\mathbf{n}} & -r\hat{\mathbf{n}} \otimes \hat{\mathbf{n}} & -r\zeta\hat{\mathbf{n}} \\ -r\hat{\mathbf{n}} \otimes \hat{\mathbf{n}} & r\hat{\mathbf{n}} \otimes \hat{\mathbf{n}} & r\zeta\hat{\mathbf{n}} \\ -r\zeta\hat{\mathbf{n}}^T & r\zeta\hat{\mathbf{n}}^T & r\zeta^2 \end{bmatrix} \begin{Bmatrix} \Delta\mathbf{u} \\ \Delta\mathbf{r} \\ \Delta\theta \end{Bmatrix}, \quad (\text{A.199})$$

where $\zeta = (n_2 p_1 - n_1 p_2)$ from Eq. (A.176).

The ϕ_{21} term is already simplified, and equal to the $\langle \nabla_s g_n \rangle$ term found in the first variation. The ϕ_{22} term equals zero since g_n has no dependence λ .

Written compactly in tensor notation, the complete tangent for the case of contact is written in Box A.5 Expanded, the Hessian takes the explicit form for two dimensional contact as shown in Box A.6.

Box A.5: Second variation of the generalized inequality contact constraint in tensor form.

$$\Delta\delta\mathcal{W}_g \underset{\text{(contact)}}{=} \begin{Bmatrix} \delta\mathbf{u} \\ \hline \delta\mathbf{r} \\ \hline \delta\theta \\ \hline \delta\lambda \end{Bmatrix}^T \begin{bmatrix} \tilde{\lambda}\tilde{\kappa}\alpha[\mathbf{t}\otimes\mathbf{t}] & -\tilde{\lambda}\tilde{\kappa}\alpha[\mathbf{t}\otimes\mathbf{t}] & -\tilde{\lambda}(\tilde{\kappa}\alpha\beta\|\mathbf{t}\|-1)\hat{\mathbf{t}} & -\hat{\mathbf{n}} \\ +r[\hat{\mathbf{n}}\otimes\hat{\mathbf{n}}] & -r[\hat{\mathbf{n}}\otimes\hat{\mathbf{n}}] & -r\zeta\hat{\mathbf{n}} & \\ \hline -\tilde{\lambda}\tilde{\kappa}\alpha[\mathbf{t}\otimes\mathbf{t}] & \tilde{\lambda}\tilde{\kappa}\alpha[\mathbf{t}\otimes\mathbf{t}] & \tilde{\lambda}(\tilde{\kappa}\alpha\beta\|\mathbf{t}\|-1)\hat{\mathbf{t}} & \hat{\mathbf{n}} \\ -r[\hat{\mathbf{n}}\otimes\hat{\mathbf{n}}] & +r[\hat{\mathbf{n}}\otimes\hat{\mathbf{n}}] & +r\zeta\hat{\mathbf{n}} & \\ \hline -\tilde{\lambda}(\tilde{\kappa}\alpha\beta\|\mathbf{t}\|-1)\hat{\mathbf{t}}^T & \tilde{\lambda}(\tilde{\kappa}\alpha\beta\|\mathbf{t}\|-1)\hat{\mathbf{t}}^T & -\tilde{\lambda}(g_n - \mathbf{p}\cdot\hat{\mathbf{n}})\left(\frac{1+\tilde{\kappa}\mathbf{p}\cdot\hat{\mathbf{n}}}{1+\tilde{\kappa}g_n}\right) & \zeta \\ -r\zeta\hat{\mathbf{n}}^T & +r\zeta\hat{\mathbf{n}}^T & +r\zeta^2 & \\ \hline -\hat{\mathbf{n}}^T & \hat{\mathbf{n}}^T & \zeta & 0 \end{bmatrix} \begin{Bmatrix} \Delta\mathbf{u} \\ \hline \Delta\mathbf{r} \\ \hline \Delta\theta \\ \hline \Delta\lambda \end{Bmatrix} \quad (\text{A.200})$$

where

$$\begin{aligned} \tilde{\lambda} &= \lambda + rg_n & \alpha &= \frac{1}{\mathbf{t}\cdot\mathbf{t}(1+\tilde{\kappa}g_n)} & \zeta &= \mathbf{p}\cdot\hat{\mathbf{t}} \\ \tilde{\kappa} &= \frac{\mathbf{t}\cdot\hat{\mathbf{n}}}{\mathbf{t}\cdot\mathbf{t}} & \beta &= \|\mathbf{t}\|(g_n - \mathbf{p}\cdot\hat{\mathbf{n}}) \end{aligned}$$

Box A.6: Second variation of the generalized inequality contact constraint in expanded form.

$$\begin{aligned} \Delta\delta\mathcal{W}_g &= \\ (\text{contact}) \end{aligned}$$

$$\left\{ \begin{array}{c} \delta u_1 \\ \delta u_2 \\ \hline \delta r_1 \\ \delta r_2 \\ \hline \delta \theta \\ \hline \delta \lambda \end{array} \right\}^T \left[\begin{array}{cc|cc|cc|c} b t_1^2 + r \hat{n}_1^2 & b t_1 t_2 + r \hat{n}_1 \hat{n}_2 & -b t_1^2 - r \hat{n}_1^2 & -b t_1 t_2 - r \hat{n}_1 \hat{n}_2 & -c \hat{t}_1 - r \zeta \hat{n}_1 & -\hat{n}_1 & \Delta u_1 \\ b t_1 t_2 + r \hat{n}_1 \hat{n}_2 & b t_2^2 + r \hat{n}_2^2 & -b t_1 t_2 - r \hat{n}_1 \hat{n}_2 & -b t_2^2 - r \hat{n}_2^2 & -c \hat{t}_2 - r \zeta \hat{n}_2 & -\hat{n}_2 & \Delta u_2 \\ \hline -b t_1^2 - r \hat{n}_1^2 & -b t_1 t_2 - r \hat{n}_1 \hat{n}_2 & b t_1^2 + r \hat{n}_1^2 & b t_1 t_2 + r \hat{n}_1 \hat{n}_2 & c \hat{t}_1 + r \zeta \hat{n}_1 & \hat{n}_1 & \Delta r_1 \\ -b t_1 t_2 - r \hat{n}_1 \hat{n}_2 & -b t_2^2 - r \hat{n}_2^2 & b t_1 t_2 + r \hat{n}_1 \hat{n}_2 & b t_2^2 + r \hat{n}_2^2 & c \hat{t}_2 + r \zeta \hat{n}_2 & \hat{n}_2 & \Delta r_2 \\ \hline -c \hat{t}_1 - r \zeta \hat{n}_1 & -c \hat{t}_2 - r \zeta \hat{n}_2 & c \hat{t}_1 + r \zeta \hat{n}_1 & c \hat{t}_2 + r \zeta \hat{n}_2 & -\tilde{\lambda} \vartheta + r \zeta^2 & \zeta & \Delta \theta \\ \hline -\hat{n}_1 & -\hat{n}_2 & \hat{n}_1 & \hat{n}_2 & \zeta & 0 & \Delta \lambda \end{array} \right] \quad (\text{A.201})$$

where

$$\begin{aligned} \tilde{\lambda} &= (\lambda + rg_n) & \alpha &= \frac{1}{\mathbf{t} \cdot \mathbf{t} (1 + \tilde{\kappa} g_n)} & \zeta &= (n_2 p_1 - n_1 p_2) \\ b &= \tilde{\lambda} \tilde{\kappa} \alpha & \beta &= \| \mathbf{t} \| (g_n - \mathbf{p} \cdot \hat{\mathbf{n}}) & \vartheta &= (g_n - \mathbf{p} \cdot \hat{\mathbf{n}}) \left(\frac{1 + \tilde{\kappa} \mathbf{p} \cdot \hat{\mathbf{n}}}{1 + \tilde{\kappa} g_n} \right) \\ c &= \tilde{\lambda} (\tilde{\kappa} \alpha \beta \| \mathbf{t} \| - 1) & \tilde{\kappa} &= \frac{\mathbf{t} \cdot \xi \cdot \hat{\mathbf{n}}}{\mathbf{t} \cdot \mathbf{t}} \end{aligned}$$

Box A.7: Second variation of the generalized contact constraint with gap status in expanded form.

$$\Delta\delta\mathcal{W}_g = \begin{Bmatrix} \delta u_1 \\ \delta u_2 \\ \delta r_1 \\ \delta r_2 \\ \delta\theta \\ \hline \delta\lambda \end{Bmatrix}^T \left[\begin{array}{cc|c} 0 & 0 & 0 & 0 & 0 & 0 \\ 0 & 0 & 0 & 0 & 0 & 0 \\ 0 & 0 & 0 & 0 & 0 & 0 \\ 0 & 0 & 0 & 0 & 0 & 0 \\ 0 & 0 & 0 & 0 & 0 & 0 \\ \hline 0 & 0 & 0 & 0 & 0 & 0 \\ 0 & 0 & 0 & 0 & 0 & -\frac{1}{r} \end{array} \right] \begin{Bmatrix} \Delta u_1 \\ \Delta u_2 \\ \Delta r_1 \\ \Delta r_2 \\ \Delta\theta \\ \hline \Delta\lambda \end{Bmatrix} \quad (\text{A.202})$$

The second variation of the contact potential $\Delta\delta\mathcal{W}_g$ has a much simpler form in the case of gap. It is simply written in Box A.7 by inspection of Eq. (2.110).

A.6 FULLY COUPLED SYSTEM DETAILS

Equation (2.112), expanded in indicial notation, is written as

$$\begin{aligned} \delta\mathcal{W} = & \delta u_i [\mathbf{F}^{\text{iner}} + \mathbf{F}^{\text{int}} - \mathbf{F}^{\text{ext}}]_i^{\Omega_D} + \delta u_i ((\lambda_h)_\alpha + r_h h_\alpha) \frac{\partial h_\alpha}{\partial u_i} + \delta u_i \underbrace{((\lambda_g)_\nu + r_g g_\nu)}_{=0 \text{ if gap}} \frac{\partial g_\nu}{\partial u_i} \\ & + \delta q_k [\mathbf{F}^{\text{iner}} - \mathbf{F}^{\text{ext}}]_k^{\Omega_R} + \delta q_k ((\lambda_h)_\alpha + r_h h_\alpha) \frac{\partial h_\alpha}{\partial q_k} + \delta q_k \underbrace{((\lambda_g)_\nu + r_g g_\nu)}_{=0 \text{ if gap}} \frac{\partial g_\nu}{\partial q_k} \\ & + \delta(\lambda_h)_\alpha h_\alpha + \delta(\lambda_g)_\nu \underbrace{(g_\nu)}_{=0 \text{ if gap}} - \delta(\lambda_g)_\nu \underbrace{\left(\frac{(\lambda_g)_\nu}{r_g} \right)}_{=0 \text{ if contact}} . \end{aligned} \quad (\text{A.203})$$

Equations (2.116) and (2.125), expanded in indicial notation, is written as

$$\begin{aligned}
\Delta \delta \mathcal{W} = & \delta u_i \left\{ \underbrace{\left[\mathbf{M}_{im} \frac{\partial a_m}{\partial u_j} + \mathbf{D}_{im} \frac{\partial v_m}{\partial u_j} + \mathbf{K}_{ij} \right]}_{=K_{\Omega_D}^*}^{\Omega_D} + ((\lambda_h)_\alpha + r_h h_\alpha) \frac{\partial^2 h_\alpha}{\partial u_i \partial u_j} + r_h \frac{\partial h_\alpha}{\partial u_i} \frac{\partial h_\alpha}{\partial u_j} \right. \\
& \quad \left. + \underbrace{((\lambda_g)_\nu + r_g g_\nu) \frac{\partial^2 g_\nu}{\partial u_i \partial u_j} + r_g \frac{\partial g_\nu}{\partial u_i} \frac{\partial g_\nu}{\partial u_j}}_{=0 \text{ if gap}} \right\} \Delta u_j \\
& + \delta u_i \left\{ ((\lambda_h)_\alpha + r_h h_\alpha) \frac{\partial^2 h_\alpha}{\partial u_i \partial q_l} + r_h \frac{\partial h_\alpha}{\partial u_i} \frac{\partial h_\alpha}{\partial q_l} + \underbrace{((\lambda_g)_\nu + r_g g_\nu) \frac{\partial^2 g_\nu}{\partial u_i \partial q_l} + r_g \frac{\partial g_\nu}{\partial u_i} \frac{\partial g_\nu}{\partial q_l}}_{=0 \text{ if gap}} \right\} \Delta q_l \\
& + \delta u_i \left\{ \frac{\partial h_\alpha}{\partial u_i} \frac{\partial (\lambda_h)_\alpha}{\partial (\lambda_h)_\beta} \right\} \Delta (\lambda_h)_\beta + \underbrace{\delta u_i \left\{ \frac{\partial g_\nu}{\partial u_i} \frac{\partial (\lambda_g)_\nu}{\partial (\lambda_g)_\eta} \right\} \Delta (\lambda_g)_\eta}_{=0 \text{ if gap}} \\
& + \delta q_k \left\{ ((\lambda_h)_\alpha + r_h h_\alpha) \frac{\partial^2 h_\alpha}{\partial q_k \partial u_j} + r_h \frac{\partial h_\alpha}{\partial q_k} \frac{\partial h_\alpha}{\partial u_j} + \underbrace{((\lambda_g)_\nu + r_g g_\nu) \frac{\partial^2 g_\nu}{\partial q_k \partial u_j} + r_g \frac{\partial g_\nu}{\partial q_k} \frac{\partial g_\nu}{\partial u_j}}_{=0 \text{ if gap}} \right\} \Delta u_j \\
& + \delta q_k \left\{ \underbrace{\left[\mathbf{M}_{kn} \frac{\partial a_n}{\partial u_l} + \mathbf{D}_{kn} \frac{\partial v_n}{\partial u_l} + \mathbf{K}_{kl} \right]}_{=K_{\Omega_R}^*}^{\Omega_R} + ((\lambda_h)_\alpha + r_h h_\alpha) \frac{\partial^2 h_\alpha}{\partial q_k \partial q_l} + r_h \frac{\partial h_\alpha}{\partial q_k} \frac{\partial h_\alpha}{\partial q_l} \right. \\
& \quad \left. + \underbrace{((\lambda_g)_\nu + r_g g_\nu) \frac{\partial^2 g_\nu}{\partial q_k \partial q_l} + r_g \frac{\partial g_\nu}{\partial q_k} \frac{\partial g_\nu}{\partial q_l}}_{=0 \text{ if gap}} \right\} \Delta q_l \\
& + \delta q_k \left\{ \frac{\partial h_\alpha}{\partial q_k} \frac{\partial (\lambda_h)_\alpha}{\partial (\lambda_h)_\beta} \right\} \Delta (\lambda_h)_\beta + \underbrace{\delta q_k \left\{ \frac{\partial g_\nu}{\partial q_k} \frac{\partial (\lambda_g)_\nu}{\partial (\lambda_g)_\eta} \right\} \Delta (\lambda_g)_\eta + \delta (\lambda_h)_\alpha \left\{ \frac{\partial h_\alpha}{\partial u_i} \right\} \Delta u_j}_{=0 \text{ if gap}} \\
& + \delta (\lambda_h)_\alpha \left\{ \frac{\partial h_\alpha}{\partial q_l} \right\} \Delta q_l + \delta (\lambda_g)_\nu \underbrace{\left\{ \frac{\partial g_\nu}{\partial u_j} \right\} \Delta u_j}_{=0 \text{ if gap}} + \delta (\lambda_g)_\nu \underbrace{\left\{ \frac{\partial g_\nu}{\partial q_l} \right\} \Delta q_l}_{=0 \text{ if gap}} - \frac{\delta (\lambda_g)_\nu}{r_g} \underbrace{\left\{ \frac{\partial (\lambda_g)_\nu}{\partial (\lambda_g)_\eta} \right\} \Delta (\lambda_g)_\eta}_{=0 \text{ if contact}}
\end{aligned} \tag{A.204}$$

where

$$i, j, m = 1 \dots \dim[\mathbf{u}], \quad (\text{A.205})$$

$$k, l, n = 1 \dots \dim[\mathbf{q}], \quad (\text{A.206})$$

$$\alpha, \beta = 1 \dots \dim[\mathbf{h}], \quad (\text{A.207})$$

$$\nu, \eta = 1 \dots \dim[\mathbf{g}], \quad (\text{A.208})$$

$$r_g > 0, \quad (\text{A.209})$$

$$r_h \geq 0. \quad (\text{A.210})$$

APPENDIX B

FINITE ELEMENT VALIDATION

B.1 OVERVIEW

This appendix summarizes the test cases run to validate the finite element implementations discussed in CHAPTER 3. While numerous validations were undertaken, this appendix contains only the essential studies. The order of presentation here follows the order the elements appear in Chapter 3.

B.2 RIGID BODY ELEMENTS

The addition of the equations of motion for the standard rigid body dynamics element, SECTION 3.3.3, amounts to simply adding residual and Hessian terms, Eqs. (3.45)–(3.48), to the time stepping algorithm used for elastodynamics, Box 3.1, with the modifications listed in Box 3.2. This element was implemented and validated in TACT. However, the element was not used in the simulations presented in CHAPTER 4. Instead, the embedded form of the rigid element was used. Therefore, only the validation of this element is included here.

B.2.1 EMBEDDED DYNAMICS, THE RIGID ELEMENT — VERSION 2

Consider the finite element implementation a two dimensional rigid body element, discussed in SECTION 3.3.4 (see also FIG 3.2). Let the rigid body have mass $m = 5$ kg, and out-of-

plane principal moment of inertia $I_{33} = 1.04167 \text{ kg}\cdot\text{m}^2$. Gravity, $g = 9.81 \text{ m/s}^2$, acts in the $-\hat{\mathbf{E}}_2$ direction. The respective initial position and velocity are

$$\begin{Bmatrix} q_1 \\ q_2 \\ q_3 \end{Bmatrix} = \begin{Bmatrix} 3 \text{ m} \\ 4 \text{ m} \\ \pi \text{ rad} \end{Bmatrix}, \quad \begin{Bmatrix} \dot{q}_1 \\ \dot{q}_2 \\ \dot{q}_3 \end{Bmatrix} = \begin{Bmatrix} 30\sqrt{2} \text{ m/s} \\ 30\sqrt{2} \text{ m/s} \\ -0.1\pi \text{ rad/s} \end{Bmatrix}. \quad (\text{B.1})$$

An external force and moment are applied to the mass center as

$$\begin{Bmatrix} F_1 \\ F_2 \\ M_3 \end{Bmatrix} = \begin{Bmatrix} 2.5 \text{ N} \\ 4.905 t \text{ N} \\ 39.4784 \sin(2\pi t) \text{ Nm} \end{Bmatrix}. \quad (\text{B.2})$$

The closed-form solution for the q evolution is

$$\begin{Bmatrix} q_1(t) \\ q_2(t) \\ q_3(t) \end{Bmatrix} = \begin{Bmatrix} 0.25t^2 + \dot{q}_{1|0}t + q_{1|0} \text{ m} \\ g(-1/60t^3 + 0.5t^2) + \dot{q}_{2|0}t + q_{2|0} \text{ m} \\ -\sin(2\pi t)/I_{33} + (q_{3|0} + 2\pi/I_{33})t + q_{3|0} \text{ rad} \end{Bmatrix}. \quad (\text{B.3})$$

TACT is run with 200 time steps, each time step $\Delta t = 0.05 \text{ s}$. Two iterations are required at each time step. Newmark parameters are chosen as $\beta = 1/4$, $\gamma = 1/2$. The comparison of the TACT results to the closed-form solution appear in FIG. B.1.

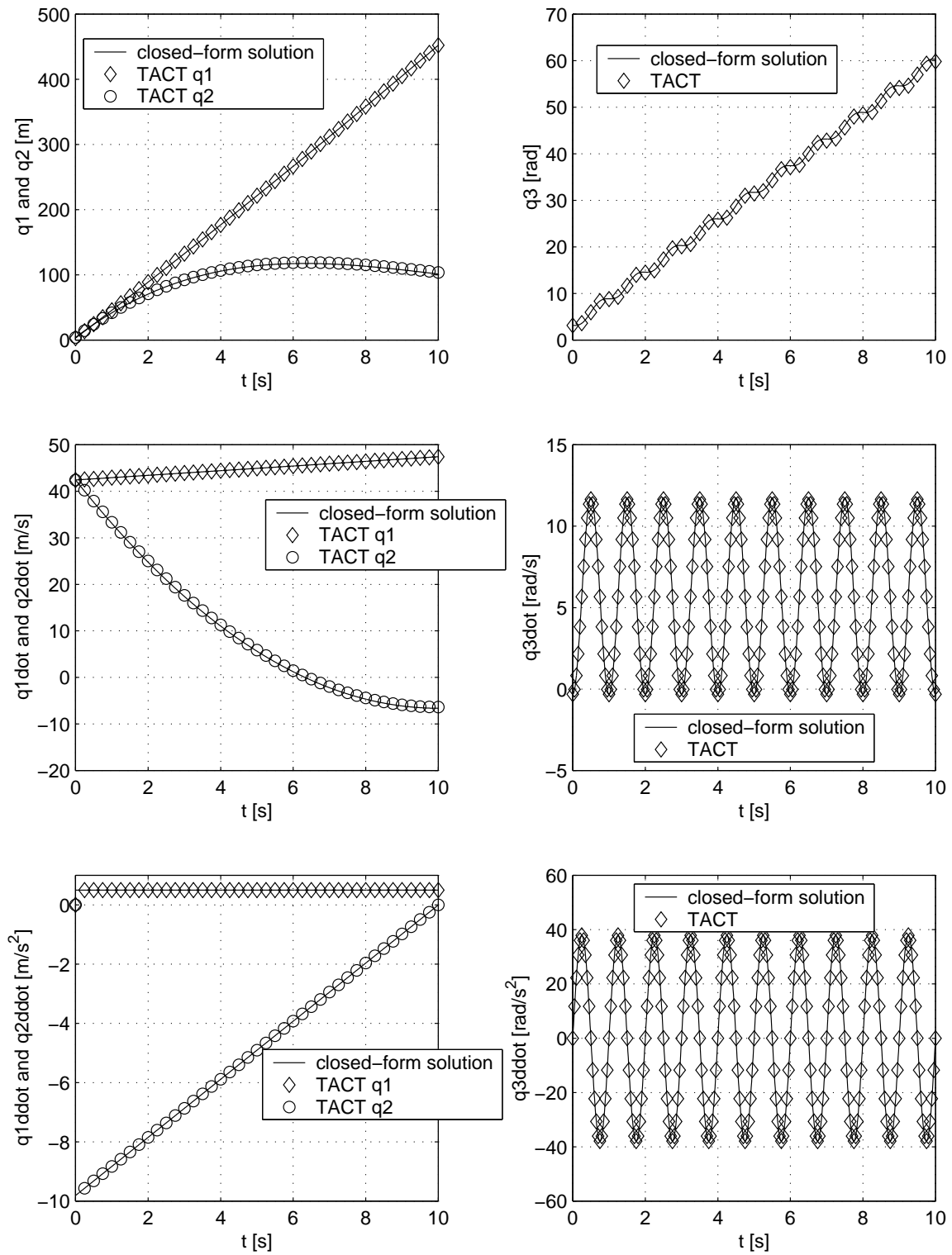


FIGURE B.1: Comparision of position and rotation time history, and their derivatives, using the Embedded Dynamic Rigid Element — Version 2, from TACT to closed-form solution.

B.3 EQUALITY CONSTRAINT ELEMENTS

The validation of equality constraints between two deformable bodies, discussed in SECTION 3.4.1, is straight forward. The resulting motion should be identical to the motion were the two elements connected through the element connectivity of the finite element mesh. The main difference between a constraint between two nodes versus element connectivity between two nodes is that the former provides the force, via Lagrange multipliers, required to keep the two nodes joined. The deformable–deformable constraint elements were not used in the simulations described in CHAPTER 4. However, several deformable–rigid and rigid–rigid constraint elements were used. Therefore, we include a validation study of each of these types of elements. We begin by presenting the rigid–rigid constraint, discussed in SECTIONS 3.4.4–3.4.5. Then, the study is extended to include a deformable finite element, to validate the deformable–rigid element, discussed in SECTIONS 3.4.2–3.4.3.

B.3.1 RIGID–RIGID EQUALITY CONSTRAINT ELEMENT — VERSION 2

Consider a rigid double pendulum moving in a plane with large rotation. Let each link of the pendulum have a mass, $m = 2$ kg, length $l = 0.50$ m, and out-of-plane principal moment of inertia $I_{33} = 0.0416667$ kg·m². Gravity, $g = 9.81$ m/s², acts in the $-\hat{\mathbf{E}}_2$ direction. The respective initial position and velocity are

$$\begin{Bmatrix} q_3 \\ q_6 \end{Bmatrix} = \begin{Bmatrix} \pi/4 \text{ rad} \\ \pi/3 \text{ rad} \end{Bmatrix}, \quad \begin{Bmatrix} \dot{q}_3 \\ \dot{q}_6 \end{Bmatrix} = \begin{Bmatrix} -1.0 \text{ rad/s} \\ 2.0 \text{ rad/s} \end{Bmatrix}. \quad (\text{B.4})$$

Note that only the rotational values are included. The translational values, for implementation in TACT, are uniquely determined from the configuration of the system as well as the initial conditions on the rotational variables. There are no external forces. The rigid body dynamics program SMASH [60] is used as the validation standard to which the TACT implementation is compared.

SMASH is set up so that two planar rods, each with three degrees of freedom, are constrained to create a double pendulum. The first rod is constrained to the laboratory reference frame. The second rod is constrained to the free end of the first rod. SMASH, like TACT, uses Lagrange multipliers to enforce the constraints. SMASH is run for 3.0 seconds,

with time steps $\Delta t=0.010$ s. SMASH uses a fourth-order accurate, explicit Runge-Kutta time stepping scheme.

TACT is run with 300 time steps, each time step $\Delta t = 0.010$ s. Four iterations, with quadratic rates of convergence, are required at each time step. Newmark parameters are chosen as $\beta = 0.3025$, $\gamma = 0.6$. This damped Newmark scheme is used to eliminate high frequency pollution from the constraints. See CHAPTER 1 for a discussion of time stepping algorithms in the presence of constraints. Interestingly, choosing Newmark parameters as $\beta = 1/4$, $\gamma = 1/2$ caused the high frequencies of the constraints to become excited, leading to a divergence of the simulation. A regularization parameter, $r = 1.0$, was used with the augmented Lagrange multipliers. The embedded formulation, as noted in CHAPTER 3, leads to a mildly non-symmetric Hessian.

The comparison of the TACT results to the SMASH solution appear in FIGS. B.2–B.3.

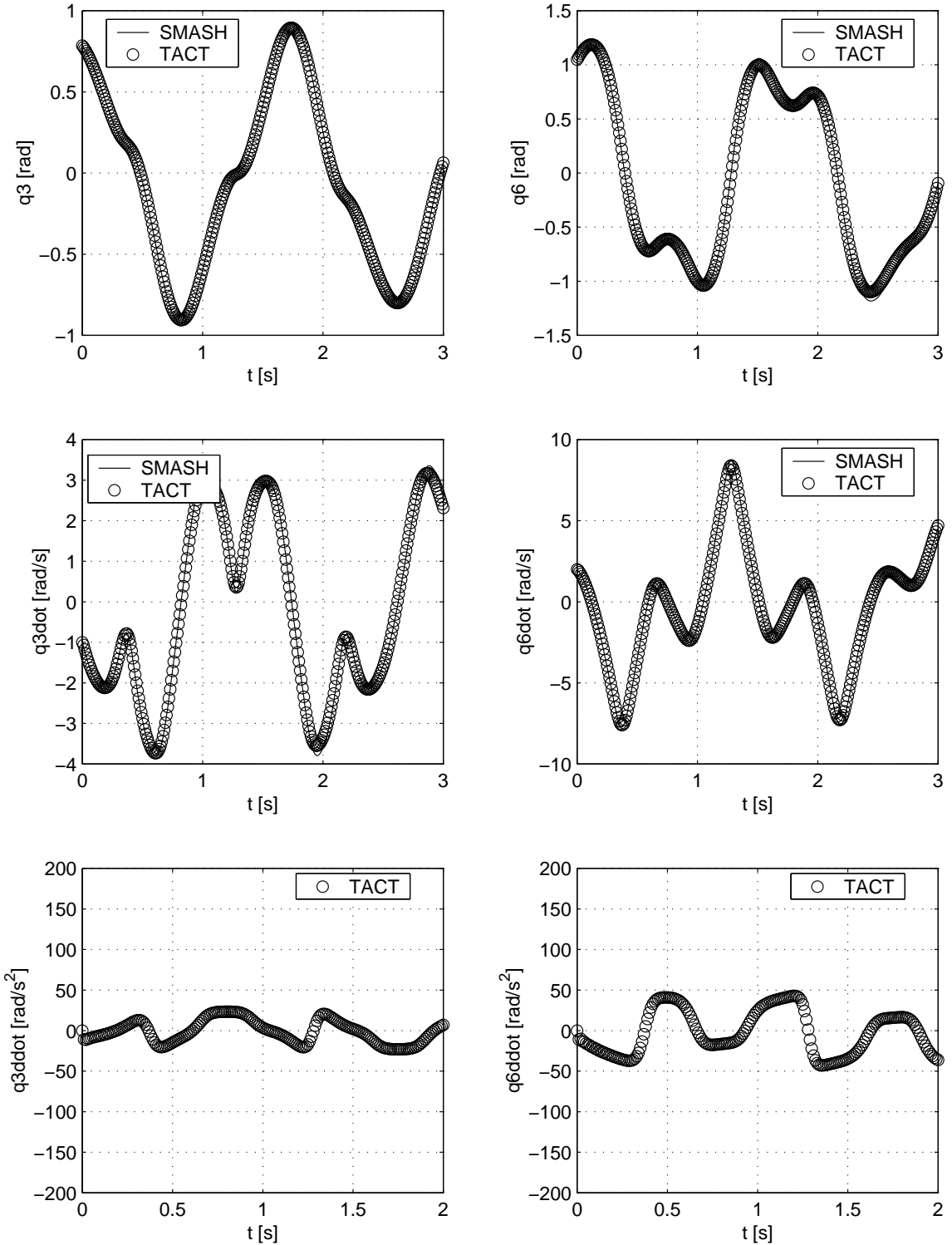


FIGURE B.2: Comparision of position and rotation time history, and their derivatives, using the Embedded Dynamic Rigid Element and Rigid–Rigid Equality Constraint Element — Version 2, from TACT to dynamic solution from SMASH. Note that SMASH does not report second derivative information, thus only the TACT data is shown for accelerations.

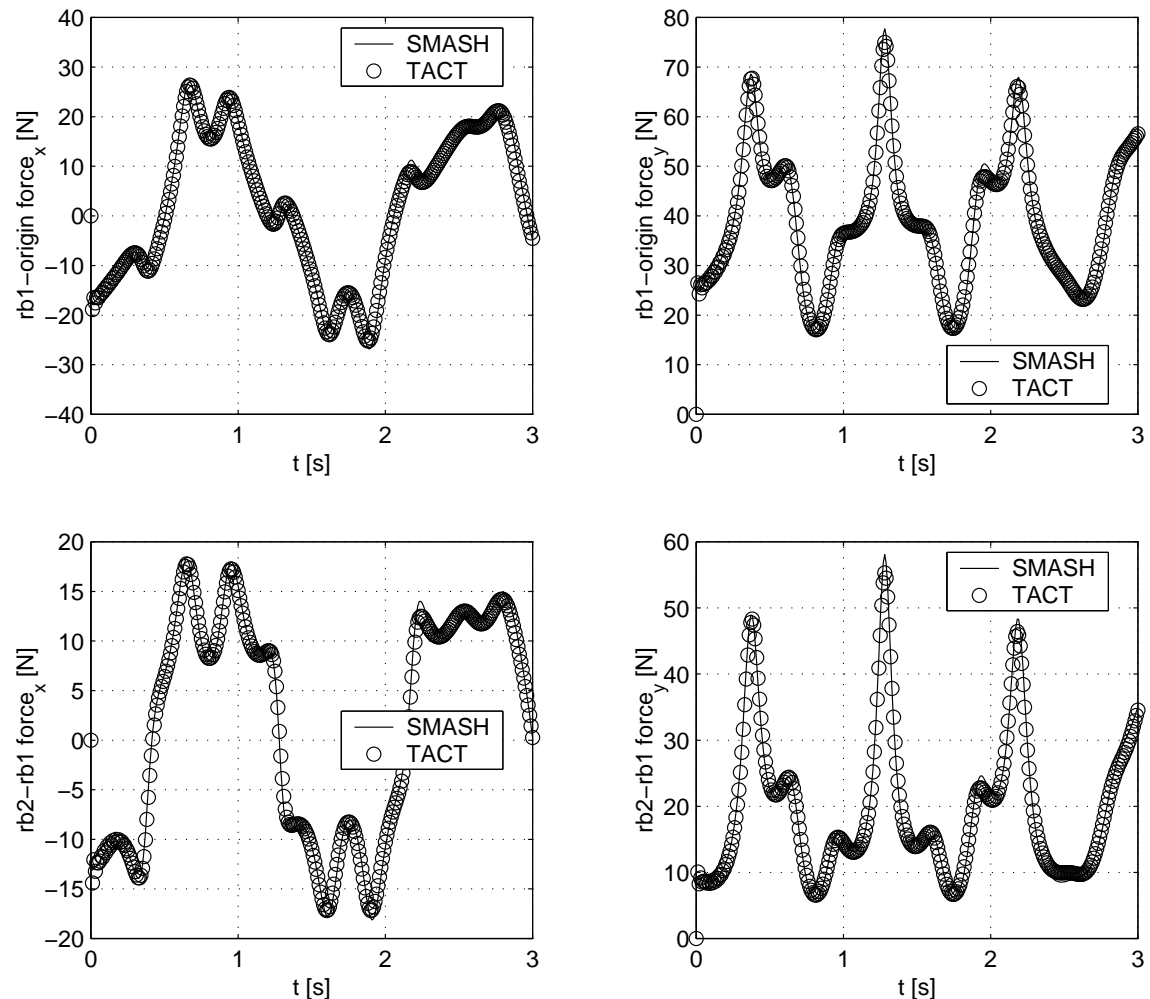


FIGURE B.3: Comparision of constraint forces using the Embedded Dynamic Rigid Element and Rigid-Rigid Equality Constraint Element — Version 2, from TACT to dynamic solution from SMASH.

B.3.2 DEFORMABLE-RIGID EQUALITY CONSTRAINT ELEMENT — VERSION 2

The same simulation described in the previous section is now augmented to validate the deformable-rigid equality constraint element. A single, quadrilateral finite element, of dimension 0.5 m by 0.5 m, is attached to the free end of the second rigid body of the double pendulum. The free end of the second rod bisects and its long axis is perpendicular to one edge of the finite element. The two nodes along this side attach, via two deformable-rigid constraint elements, to the second rigid link. As with the rigid-rigid constraint elements, the deformable-rigid constraint elements use a regularization parameter, $r = 1.0$, with the augmented Lagrange multipliers. Experience showed that non-zero regularization parameters were necessary to avoid zero pivots while solving the equations. The deformable element has no mass and no dynamics associated with it. The element is strictly an elastic, structural element. As a result, the presence of the deformable element at the end of the double rigid pendulum should not change the evolution of the system from the results previously obtained, presented in FIGS. B.2–B.3. Indeed this is the case. Results from the deformable-rigid interface are obtained via the Lagrange multipliers. These multipliers represent the force on the nodes of the finite element. As previously, TACT is run with 300 time steps, each time step $\Delta t = 0.010$ s. Four iterations, with quadratic rates of convergence, are required at each time step. Newmark parameters are chosen as $\beta = 0.3025$, $\gamma = 0.6$. The time history of the state variables as well as the rigid-rigid Lagrange multipliers are identical to those presented in FIGS. B.2–B.3. Figure B.4 shows the reaction forces at the deformable-rigid interface.

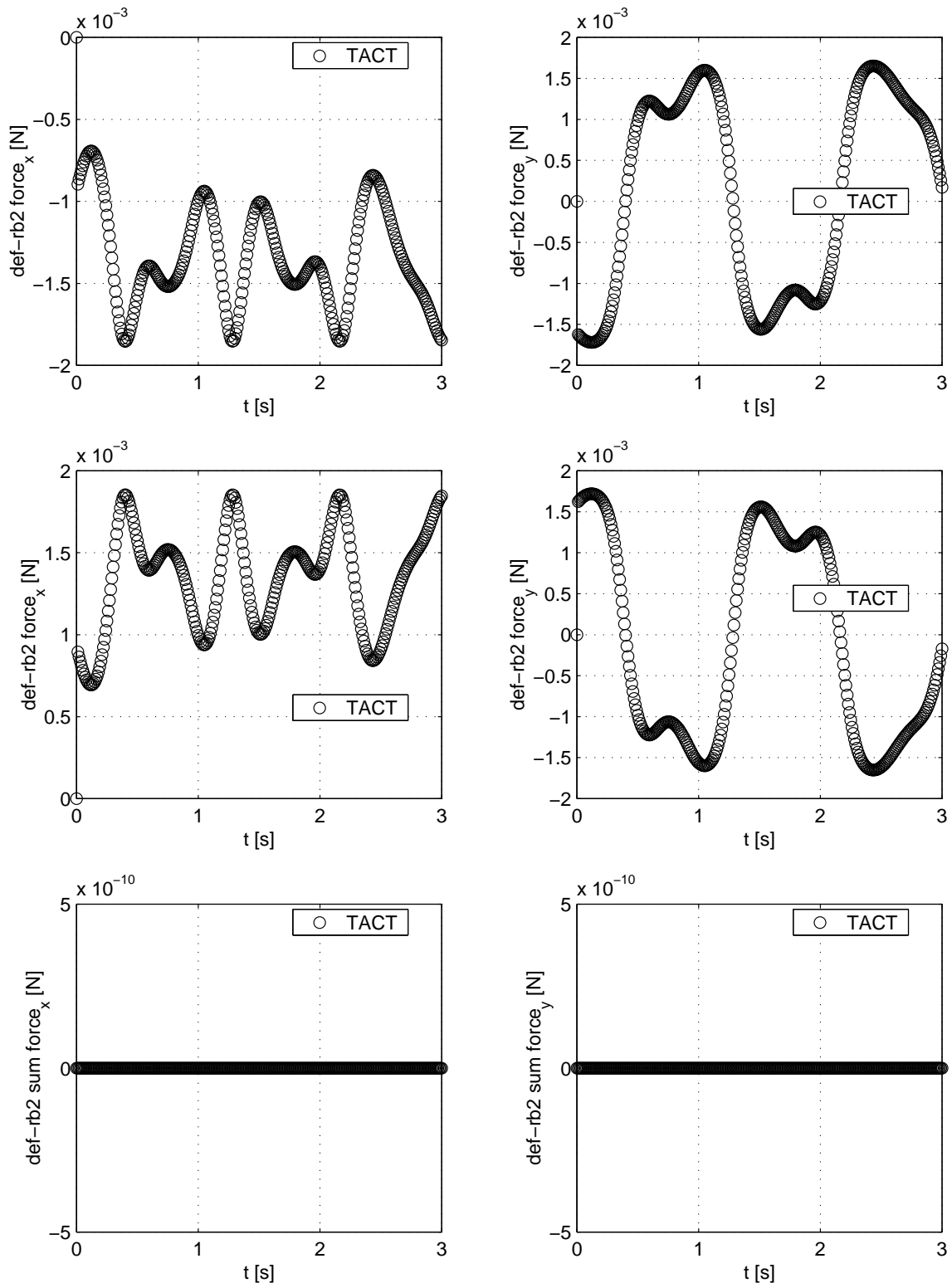


FIGURE B.4: Reaction forces from the Lagrange multipliers at the deformable–rigid interface. Note that the forces sum to zero.

B.3.3 MUSCLE ACTUATOR ELEMENT

There are essentially three components to the muscle element discussed in SECTION 3.4.6: A spring, a dashpot, and an actuator. We first validate the dashpot (FIG. 3.8). Validation of the spring (FIG. 3.6 with actuation $a = 0$) follows exactly along the same lines as the dashpot. Then we demonstrate a validation study of the actuator element (FIG. 3.6 with stiffness $k = 0$, or alternatively FIG. 3.7, where the moment m is specified).

Consider a muscle model composed of a single dashpot with viscous damping $c = 50$ N-s/m (see FIG. 3.8). Attached to the end of the dashpot is a point mass, $m = 4$ kg. Gravity, $g = 10$ m/s², acts in the $-\hat{\mathbf{E}}_2$ direction. One end of the dashpot is fixed at the origin. The other end of the dashpot fixes to the point mass. The point mass has an initial position and velocity of

$$\begin{Bmatrix} q_1 \\ q_2 \end{Bmatrix} = \begin{Bmatrix} 0 \text{ m} \\ 2 \text{ m} \end{Bmatrix}, \quad \begin{Bmatrix} \dot{q}_1 \\ \dot{q}_2 \end{Bmatrix} = \begin{Bmatrix} 0 \text{ m/s} \\ 0 \text{ m/s} \end{Bmatrix}. \quad (\text{B.5})$$

The simulation in TACT uses 100 time steps, with $\Delta t = 0.100$ s. Newmark parameters are chosen as $\beta = 1/4$, $\gamma = 1/2$. Five iterations is typically required for quadratic convergence. Iterations reflect the geometric (rotational) nonlinearity that must be resolved. Figure B.5 shows the result with TACT compared to integration of the equations of motion with MATLAB ODE45.

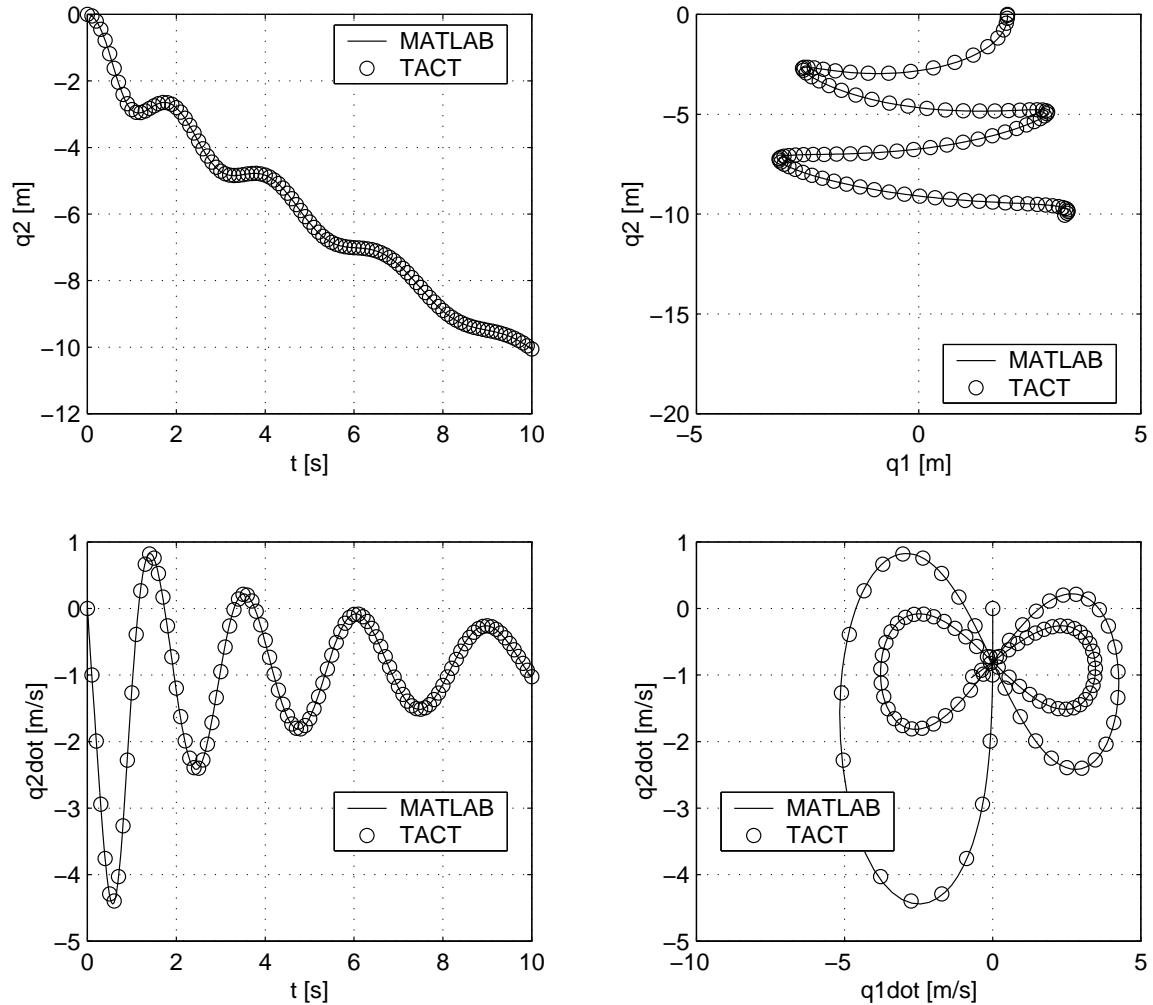


FIGURE B.5: Comparison of time and velocity time history of results obtained with TACT with results obtained from integration of the equations of motion with MATLAB ODE45.

Validation of the actuator (see FIG. 3.7) is done by using a double pendulum, and attaching via deformable–rigid constraints, two actuator elements between the two links of the double pendulum. Each rigid body link has mass $m = 2$ kg, out-of-plane principal moment of inertia $I_{33} = 0.04167$ kg·m², and length $l = 0.50$ m. The first rigid body link, body B_1 , attaches to the reference frame at point P_1 , located at $\langle 0.25, 0 \rangle$ m. Body B_1 hangs vertically below point P_1 in its initial configuration so that its mass center is located at $\langle 0.25, -0.25 \rangle$ m at $t = 0$. A rigid–rigid constraint creates a pin joint between body B_1 and body B_2 , the second rigid link. The pin joint initially is located at $\langle 0.25, -0.50 \rangle$ m. Body B_2 hangs vertically below point P_1 in its initial configuration so that its mass center is located at $\langle 0.25 - 0.75 \rangle$ m at $t = 0$. Two actuator elements attach B_1 to B_2 at points located in the respective body’s reference frame. In the initial configuration, one actuator has end points located at $\langle 0.0, -0.25 \rangle$ m and $\langle 0.0 - 0.75 \rangle$ m; the other actuator has end points located at $\langle 0.50, -0.25 \rangle$ m and $\langle 0.50, -0.75 \rangle$ m, when measured in the global reference frame. The actuation on the left-hand-side element is set to zero for all time. The actuation on the right-hand-side element is set so that the the resultant moment produced by the actuator is equal to the square of the time, $m = t^2$. Rigid–rigid constraint elements connect body B_1 to the reference frame, and body B_2 to body B_1 . Four deformable–rigid constraint elements join the four end points of the actuator elements to the rigid body elements. The regularization parameter used for the augmented multiplier, for both the rigid–rigid and deformable–rigid constraint elements, is taken to be $r = 1.0$. All initial velocities of the rigid bodies are set to zero. Gravity, $g = 9.81$ m/s², acts in the $-\hat{\mathbf{E}}_2$ direction. TACT is run with 40 time steps, each time step $\Delta t = 0.050$ s. Four iterations are typically required at each time step. Quadratic convergence is obtained for each time step. Newmark parameters are chosen as $\beta = 0.3025$, $\gamma = 0.6$. Because the double pendulum only has two free degrees of freedom, only the rotation results are presented. The translation of the mass centers of each body is obtained from the angular data and the geometry. Results from TACT are validated against a dynamics model developed in SMASH. The

Figure B.6 shows the result with TACT compared to the same simulation run in SMASH [60].

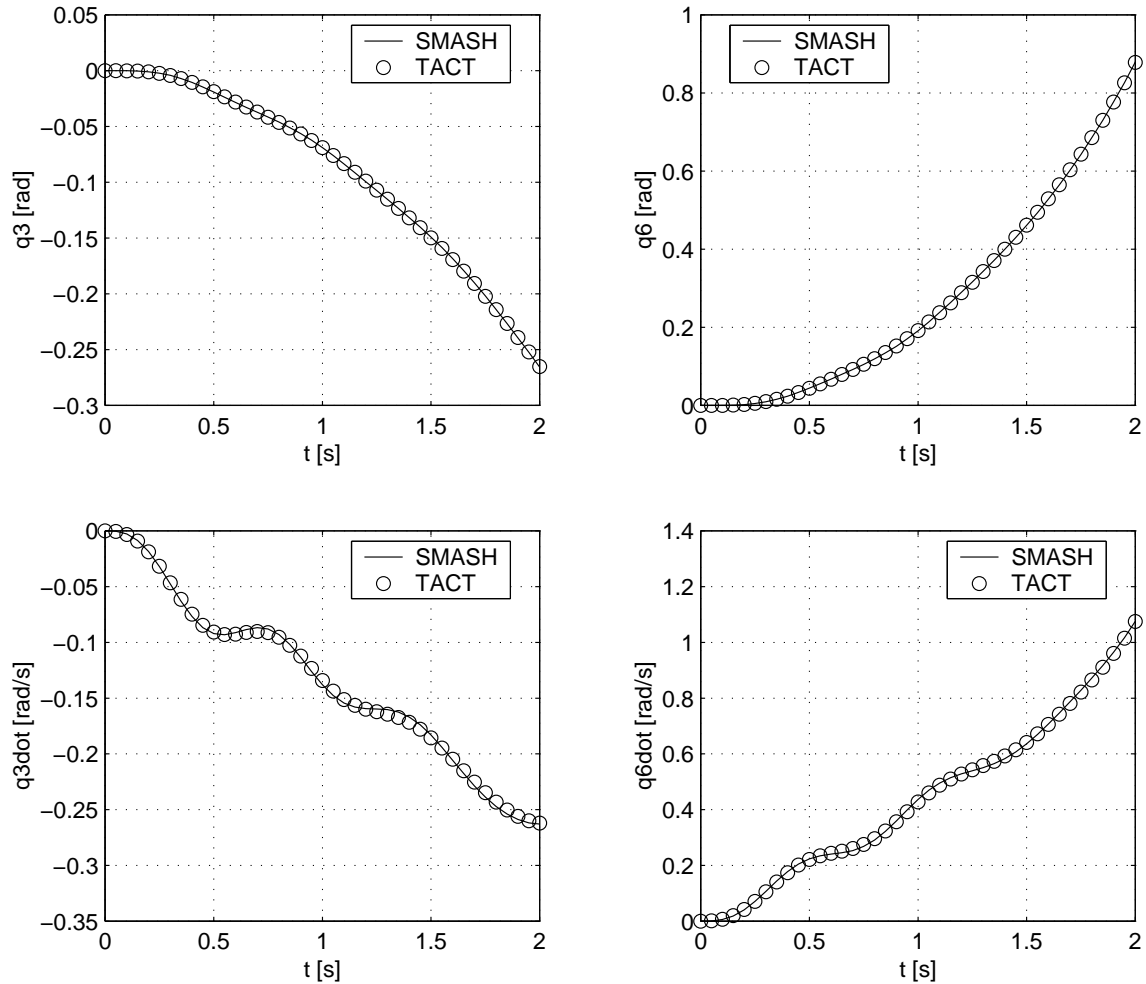


FIGURE B.6: Comparison of angular position and velocity time history results from TACT with results from SMASH.

B.4 INEQUALITY CONSTRAINT ELEMENTS

B.4.1 DEFORMABLE-RIGID INEQUALITY CONSTRAINT ELEMENT — VERSION 2

Finally we validate the contact element discussed in SECTION 3.5. The element is shown in FIG. 3.13. The governing residual and Hessian terms appear in Eqs. 3.130–3.131. We first establish that the embedded form of the inequality contact constraint element obtains static Hertz contact solutions. Consider a rigid, infinite cylinder pushed into an elastic half-space. From the theory of elasticity solution of Landau and Lifshitz [69], who present a solution to the contact problem originally posed by Hertz in 1882, the contact pressure field p is given by

$$p(x) = \frac{2P}{\pi a} \sqrt{1 - \frac{x^2}{a^2}}. \quad (\text{B.6})$$

Here P is load applied to the rigid indentor. The origin of the x -axis rests at the centerline of the circular indentor. The contact area a (or length per unit depth) is given by

$$a = \sqrt{\frac{4(1 - \nu^2)PR}{E\pi}}. \quad (\text{B.7})$$

Here, R is the radius of curvature of the rigid indentor, E is the modulus of elasticity, and ν is the Poisson ratio. Combining these two equations gives an expression for the contact pressure p in terms of E , ν , P , and x ,

$$p(x) = \frac{E}{2(1 - \nu^2)R} \sqrt{\frac{4(1 - \nu^2)PR}{E\pi} - x^2}. \quad (\text{B.8})$$

The elastic half-space is approximated by a circular, symmetric finite element mesh composed of 1560 elements, shown in FIG. B.7

A single rigid body dynamics element is used to model the rigid indentor. Because this is a static simulation, the equations describing the dynamics of the rigid body are effectively shut off through setting those equations to zero through homogeneous essential boundary conditions. The force P is applied to the mass center of the rigid body. The indentor has a radius $R = 100$ cm. Contact elements, created with twenty-one facets, describe the circular boundary of the rigid body. The radius of the finite element mesh used to model the elastic half space was taken as 8 cm. The nonlinear Kirchhoff-St.Venant material model

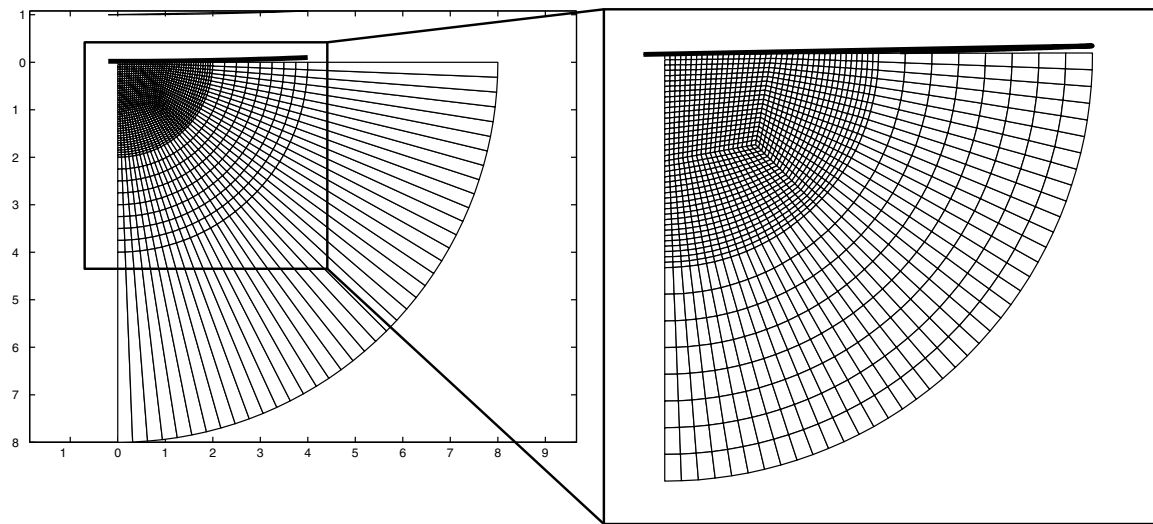


FIGURE B.7: Finite element mesh used to validate the Hertz contact problem.

with $E = 100$ dN/cm (modulus per unit depth) and $\nu = 0.3$. The solution is obtained for ten load increments, $P = [0.1, 1.0]$ dN. Quadratic convergence is obtained for each load increment.

Figure B.8 shows agreement between the finite element implementation and the analytical solution for ten different load cases.

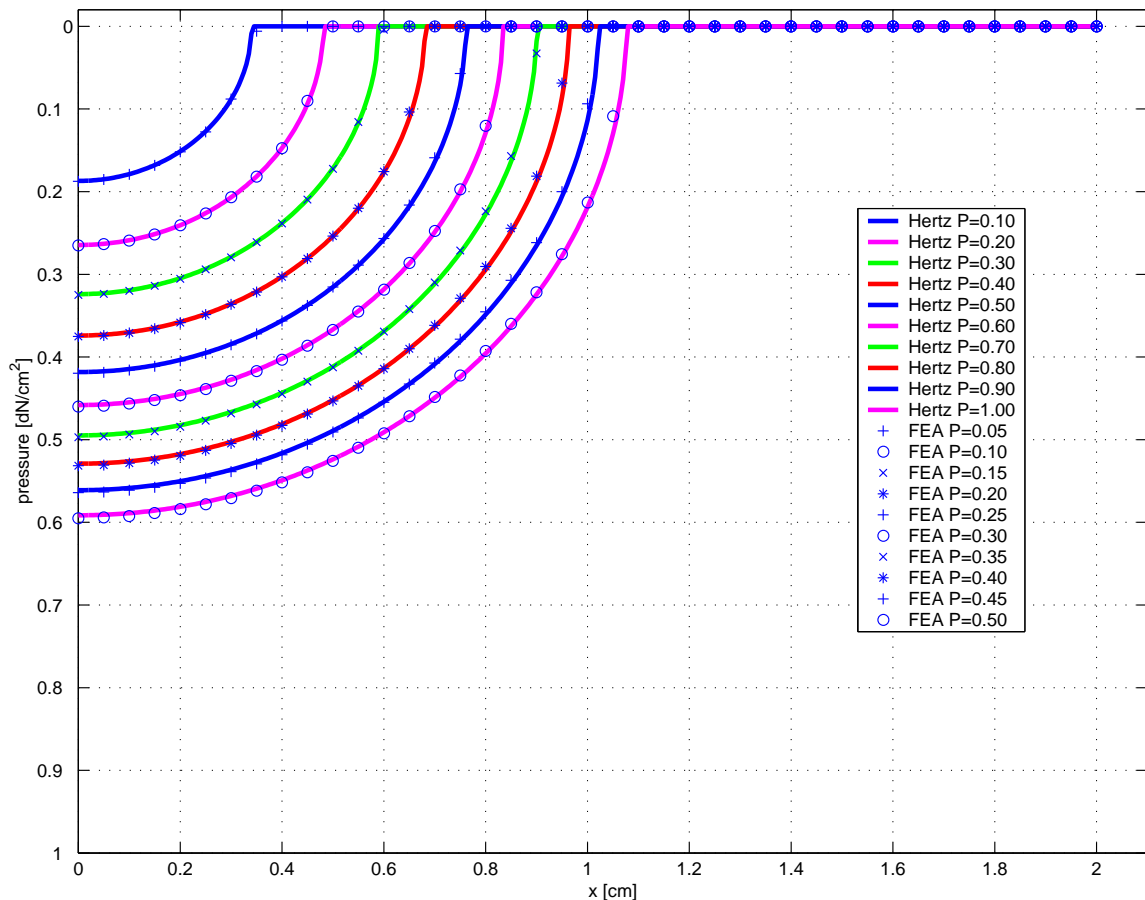


FIGURE B.8: Validation of the contact implementation with the analytical contact solution. Note the FEA load is half of the analytical load because symmetry conditions in the simulation were used.

A second study involving the same mesh and indentor as before is used now for a dynamics simulation. Here the equations associated with the dynamics of the rigid indentor are active. The elastic-half space has no mass, so effectively it acts as a spring which catches and repels a mass that flies into it. The rigid indentor has a new initial configuration which is raised so there is a 1 cm gap between the contact boundary of the indentor and the surface of the elastic half-space.

The indentor is assumed to have a mass $m = 5.10\text{E-}4 \text{ dN}\cdot\text{s}^2/\text{cm}$. Gravity, $g = 9.81 \text{ m/s}^2$, acts in the $-\hat{\mathbf{E}}_2$ direction. Thus the total gravitational force is $5.0031\text{E-}2 \text{ dN}$. TACT is run with 500 time steps, $\Delta t = 0.001 \text{ s}$. Newmark parameters are chosen as $\beta = 0.3025$, $\gamma = 0.6$. This damped Newmark scheme is used to eliminate high frequency pollution from the constraints. Quadratic convergence is obtained at each time step. Only two iterations are required when there is a gap between the indentor and the elastic half-space. Up to nine iterations are required when the two bodies come into contact.

Figure B.9 shows the position, velocity, and acceleration of the mass center of the indentor. Note that the attenuation in the mass center height is due to the damping properties of the Newmark time integrator when $\beta = 0.3025$, $\gamma = 0.6$.

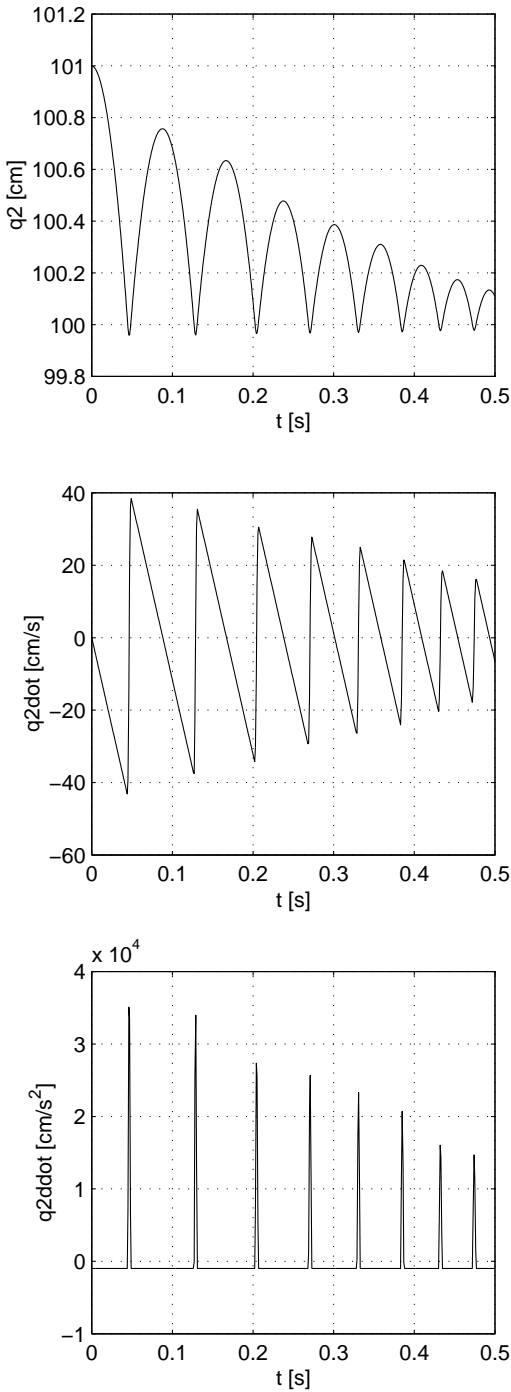


FIGURE B.9: Position, velocity, and acceleration time history of the indenter center of mass. The vertical degree of freedom is q_2 .

BIBLIOGRAPHY

- [1] H.J. Agins, N.W. Alcock, and M. et al. Bansal. Metallic wear in failed titanium-alloy total hip replacements: A histological and quantitative analysis. *The Journal of Bone and Joint Surgery*, 70A:347–356, 1988.
- [2] P. Alart and A. Curnier. A mixed formulation for frictional contact problems prone to Newton-like solution methods. *Computer Methods in Applied Mechanics and Engineering*, 92:353–375, 1991.
- [3] R. McN. Alexander. Simple models of human movement. *App Mech Rev*, 48:461–469, 1995.
- [4] J.A.C. Ambrósio. Dynamics of structures undergoing gross motion and nonlinear deformations: A multibody approach. *Computers and Structures*, 59:1001–1012, 1996.
- [5] M. Anantharaman and M. Hiller. Numerical simulation of mechanical systems using methods for differential-algebraic equations. *International Journal for Numerical Methods in Engineering*, 32:1531–1542, 1991.
- [6] T.P. Andriacchi. Dynamics of pathological motion: Applied to the anterior cruciate deficient knee. *Journal of Biomechanics*, 23:99–105, 1990.
- [7] T.P. Andriacchi. Dynamics of knee malalignment. *Orthop Clin North America*, 25:395–403, 1994.
- [8] T.P. Andriacchi, R.N. Natarajan, and D.E. Hurwitz. Musculoskeletal dynamics, locomotion, and clinical applications. In V.C. Mow and W.C. Hayes, editors, *Basic Orthopaedic Biomechanics*, pages 37–68, Philadelphia, 1997. Lippincott–Raven.
- [9] Ansys Inc., Canonsburg, PA. <http://www.ansys.com>. March 2000.
- [10] F. Armero and E. Petőcz. A new class of conserving algorithms for dynamic contact problems. In *ECCOMAS 96*, pages 861–867, Paris, 1996. John Wiley & Sons.

- [11] F. Armero and E. Petőcz. On the formulation of stable time-stepping algorithms for contact problems. In *COMPLAS V*, Barcelona, 1997. CIMNE.
- [12] The Arthritis Foundation. Facts and Tactics, <http://www.arthritis.org/facts/>. 1998.
- [13] P. Aspenberg, Y. Kadoya, and H. Kobayashi, A. Ohashi. Wear and osteolysis in total joint replacements. *Acta Orthopaedica Scandinavica*, 69:435–436, 1998.
- [14] R.L. Barrack, A. Folgueras, B. Munn, D. Tvetden, and P. Sharkey. Pelvic lysis and polyethylene wear at 5–8 years in an uncemented total hip. *Clinical Orthopaedics and Related Research*, 335:211–217, 1997.
- [15] D.L. Bartel, A.H. Burstein, M.D. Toda, and D.L. Edwards. The effect of conformity and plastic thickness on contact stresses in metal-backed plastic implants. *Journal of Biomechanical Engineering*, 107:193–199, 1985.
- [16] O.A. Bauchau, G. Bamilano, and N.J. Theron. Numerical integration of nonlinear elastic mult-body systems. *International Journal for Numerical Methods in Engineering*, 38:2727–2751, 1995.
- [17] T. Belytschko and T.J.R. Hughes. *Computational Methods for Transient Analysis*, pages 67–155. North-Holland, Amsterdam, 1983.
- [18] G. Bergmann, F. Graichen, and A. Rohlmann. Hip joint loading during walking and running, measured in two patients. *Journal of Biomechanics*, 26:969–990, 1993.
- [19] A. Cardona and M. Geradin. Time integration of the equations of motion in mechanism analysis. *Computers and Structures*, 33:801–820, 1989.
- [20] A. Cardona and M. Geradin. A superelement formulation for mechanism analysis. *Computer Methods in Applied Mechanics and Engineering*, 100:1–29, 1992.
- [21] A. Cardona, M. Geradin, and D.B. Doan. Rigid and flexible joint modelling in multibody dynamics using finite elements. *Computer Methods in Applied Mechanics and Engineering*, 89:395–418, 1991.
- [22] P. Chabrand and F. Dubois. Numerical methods for dealing with frictional contact in finite elastoplastic deformation. In M. Raous, editor, *Contact Mechanics*, pages 159–168, New York, 1995. Plenum Press.
- [23] S.H. Chan and I.S. Tuba. A finite element method for contact problems in solid bodies. *Int. J. Mech. Sci.*, 13:615–639, 1971.

- [24] A.J. Chen. *Energy-momentum conserving methods for three dimensional dynamic nonlinear multibody systems*. PhD thesis, Stanford University, 1997.
- [25] P.G. Ciarlet. *Mathematical Elasticity, Volume I: Three Dimensional Elasticity*. North-Holland, Amsterdam, 1988.
- [26] G.K. Cole, B.M. Nigg, A.J. van den Bogert, and K.G.M. Gerritsen. Lower extremity joint loading during impact in running. *Clinical Biomechanics*, 11:181–193, 1996.
- [27] J.P. Collier, M.B. Mayor, R.E. Jensen, V.A. Suprenant, H.P. Suprenant, J.L. McNamara, and L. Belec. Mechanisms of failure of modular prosthesis. *Clinical Orthopaedics and Related Research*, 285:129–139, 1992.
- [28] J.R. Cournoyer, J.A. Ochoa, and S.M. Surtz. Relative motion at the backside of a metal-backed acetabular component under quasistatic and dynamic loading. *Transactions of the Orthopaedic Research Society*, 22:839, 1997.
- [29] A. Curnier. Tact: A contact analysis program. In F. Maceri and G. Del Piero, editors, *Unilateral Problems in Structural Analysis – 2, CISM 304*, pages 97–116, Wien, 1985. Springer-Verlag.
- [30] A. Curnier. *Computational Methods in Solid Mechanics*. Kluwer Academic Publishers, Dordrecht, 1994.
- [31] A. Curnier. Personal communication. 1998.
- [32] A. Curnier and P. Alart. A generalized Newton method for contact problems with friction. *Méch. Théor. Appl., Suppl.*, 7(1):67–82, 1988.
- [33] A. Curnier, Q-C. He, and A. Klarbring. Continuum mechanics modelling of large deformation contact with friction. In M. Raous, editor, *Contact Mechanics*, pages 145–158, New York, 1995. Plenum Press.
- [34] S.L. Delp and J.P. Loan. A software system to develop and analyze models of musculoskeletal structures. *Computers in Biology and Medicine*, 25:21–34, 1995.
- [35] S.L. Delp, J.P. Loan, M.G. Hoy, F.E. Zajac, E.L. Topp, and J.M. Rosen. An interactive graphics based model of the lower extremity to study orthopedic surgical procedures. *IEEE Trans Biomed Engng*, 37:757–767, 1990.
- [36] T.C. Doehring, H.E. Rubash, and D.E. Dore. Micromotion measurements with hip center and modular neck length alterations. *Clinical Orthopaedics and Related Research*, 362:230–239, 1999.

- [37] P.A. Dowdy, C.H. Rorabeck, and R.B. Bourne. Uncemented total hip arthroplasty in patients 50 years of age or younger. *Journal of Arthroplasty*, 12:853–862, 1997.
- [38] Center for Disease Control and Prevention. Vital and health statistics, series 10, no. 193. 1994.
- [39] A. Francavilla and O.C. Zienkiewicz. A note on numerical computation of elastic contact problems. *International Journal for Numerical Methods in Engineering*, 9:913–924, 1975.
- [40] M. Geradin and A. Cardona. Time integration of the equations of motion in mechanism analysis. *Computers and Structures*, 33:801–820, 1988.
- [41] M. Geradin and A. Cardona. A superelement formulation for mechanism analysis. *Computer Methods in Applied Mechanics and Engineering*, 100:1–29, 1992.
- [42] K.G.M. Gerritsen, A.J. van den Bogert, and B.M. Nigg. Direct dynamics simulation of the impact phase in heel-toe running. *Journal of Biomechanics*, 28:661–668, 1995.
- [43] G.M.L. Gladwell. *Contact problems in the classical theory of elasticity*. Sijhoff and Noordhoff, Alphen aan den Rijn, 1980.
- [44] M. Glowinski, R. Vidrascu and P. LeTallec. Augmented Lagrangian techniques for solving frictionless contact problems in finite elasticity. In *Finite element method for Nonlinear Problems Europe-US Symposium*, Berlin and Heidelberg, 1986. Springer-Verlag.
- [45] M.E. Gurton. *An Introduction to Continuum Mechanics*. Academic Press, San Diego, 1981.
- [46] J.O. Hallquist, G.L. Goudreau, and D.J. Benson. Sliding interfaces with contact-impact in large-scale Lagrangian computations. *Computer Methods in Applied Mechanics and Engineering*, 51:107–137, 1985.
- [47] J.H. Heegaard. *Large slip contact in biomechanics: kinematics and stress analysis of the patello-femoral joint*. PhD thesis, École Polytechnique Fédérale de Lausanne, Lausanne, Switzerland, 1993.
- [48] J.H. Heegaard and A. Curnier. An augmented Lagrangian method for discrete large-slip contact problems. *International Journal for Numerical Methods in Engineering*, 36:569–593, 1993.
- [49] J.H. Heegaard and A. Curnier. Geometric properties of 2d and 3d unilaterial large slip contact operators. *Computer Methods in Applied Mechanics and Engineering*, 131:263–286, 1996.
- [50] J.H. Heegaard, C.B. Hovey, and M.L. Kaplan. Fast convergent solvers for augmented lagrangian equations in contact mechanics. 10th International Conference on Computational Engineering Science, 6-9 October, 1998, Atlanta, GA.

- [51] H. Hertz. Über die berührung fester elastischer körper. *Journal für Mathematic*, BD.XCII Heft 2, Berlin, 1881.
- [52] H.M. Hilber, T.J.R. Hughes, and R.L. Taylor. Improved numerical dissipation for time integration algorithms in structural dynamics. *Earthquake Engineering and Structural Dynamics*, 5:282–292, 1977.
- [53] HKS Inc., Pawtucket, RI. <http://www.abaqus.com>. March 2000.
- [54] T.J.R. Hughes. *The Finite Element Method – Linear Static and Dynamic Finite Element Analysis*. Prentice-Hall, New Jersey, 1987.
- [55] T.J.R. Hughes, R.L. Taylor, J.L. Sackman, A. Curnier, and W. Kanoknukulchai. A finite element method for a class of contact-impact problems. *Computer Methods in Applied Mechanics and Engineering*, 8:249–276, 1976.
- [56] O.L. Huk, M. Bansal, F. Betts, C.M. Rimnac, J.R. Lieberman, M.H. Huo, and E.A. Salvati. Polyethylene and metal debris generated by non-articulating surfaces of modular acetabular components. *The Journal of Bone and Joint Surgery*, 76B:568–574, 1994.
- [57] V.T. Inman, H.J. Ralston, and F. Todd. *Human Walking*. Williams and Wilkins, Baltimore, second edition, 1994.
- [58] K.L. Johnson. *Contact mechanics*. Cambridge University Press, Cambridge, 1985.
- [59] T.R. Kane and D.A. Levinson. *Dynamics: Theory and applications*. McGraw-Hill, New York, 1985.
- [60] M.L. Kaplan and J.H. Heegaard. *SMASH users manual*. Stanford University, 2000.
- [61] N. Kikuchi and J.T. Oden. *Contact problems in elasticity: A study of variational inequalities and finite element methods*. SIAM, Philadelphia, 1988.
- [62] A. Klarbring. Quadratic programs in frictionless elastic contact problems. *Int. J. Engng. Sci.*, 24:1207–1217, 1986.
- [63] A. Klarbring. Mathematical programming and augmented Lagrangian methods for frictional contact problems. In A. Curnier, editor, *Contact Mechanics International Symposium*, pages 409–422. PPUR, 1992.
- [64] S.M. Kurtz, D.L. Bartel, and A.A. Edidin. The effect of gaps on contact stress and relative motion in a metal-backed acetabular component. *Transactions of the Orthopaedic Research Society*, 19:243, 1994.

- [65] S.M. Kurtz, S.M. Gabriel, and D.L. Bartel. The effect of non-conformity between metal backing and polyethylene inserts in acetabular components for total hip arthroplasty. *Transactions of the Orthopaedic Research Society*, 18:434, 1993.
- [66] S.M. Kurtz, J.A. Ochoa, C.B. Hovey, and C.V. White. Simulation of initial frontside and backside wear rates in a modular acetabular component with multiple screw holes. *Journal of Biomechanics*, 32:967–976, 1999.
- [67] S.M. Kurtz, J.A. Ochoa, C.V. White, S. Srivastav, and J. Cournoyer. Backside nonconformity and locking restraints affect liner/shell load transfer mechanisms and relative motion in modular acetabular components for total hip replacement. *Journal of Biomechanics*, 31:431–437, 1998.
- [68] C. Lanczos. *The variational principles of mechanics*. Dover, New York, fourth edition, 1970.
- [69] L.D. Landau and E.M. Lifshitz. *Theory of Elasticity*. Pergamon Press, Oxford, 1986.
- [70] J.A. Landers and R.L. Taylor. *An augmented Langrangian formulation for the finite element solution of contact problems*. Technical Report UCB/SESM-85-09, Department of Civil Engineering, University of California at Berkeley, 1985.
- [71] Lawrence Livermore National Laboratories, Lawrence, CA. <http://www.llnl.gov/eng/mdg/codes/manuals>. March 2000.
- [72] J.R. Lieberman, R.M. Kay, W.P. Hamlet, S-H. Park, and J.M. Kabo. Wear of the polyethylene liner-metallic shell interface in modular acetabular components. *Journal of Arthroplasty*, 11:602–608, 1996.
- [73] LMS International, Leuven, Belgium. <http://www.cadsi.com>. March 2000.
- [74] L.E. Malvern. *Introduction to the Mechanics of a Continuous Medium*. Prentice-Hall, New Jersey, 1969.
- [75] J.E. Marsden and T.J.R. Hughes. *Mathematical Foundations of Elasticity*. Dover, New York, 1983.
- [76] T.A. Maxian, T.D. Brown, D.R. Peterson, and J.J. Callaghan. Adaptive finite element modeling of long-term polyethylene wear in total hip arthroplasty. *Journal of Orthopaedic Research*, 14:668–675, 1996.
- [77] T.A. Maxian, T.D. Brown, D.R. Peterson, and J.J. Callaghan. The Frank Stinchfield Award. three-dimensional sliding/contact computational simulation of total hip wear. *Clinical Orthopaedics and Related Research*, 333:41–50, 1996.

- [78] T.A. Maxian, T.D. Brown, D.R. Peterson, and J.J. Callaghan. A sliding-distance-coupled finite element formulation for polyethylene wear in total hip arthroplasty. *Journal of Biomechanics*, 29:687–692, 1996.
- [79] T.A. Maxian, T.D. Brown, D.R. Peterson, H.A. McKellop, B.L. Lu, and J.J. Callaghan. Finite element analysis of acetabular wear. *Clinical Orthopaedics and Related Research*, 344:111–117, 1997.
- [80] T. McGeer. Passive dynamic walking. *International Journal of Robotics Research*, 9:62–82, 1990.
- [81] T. McGeer. Dynamics and control of bipedal locomotion. *Journal of Theoretical Biology*, 163:277–314, 1993.
- [82] D.J. McGill and W.W. King. *An introduction to dynamics*. PWS-Kent, Boston, second edition, 1989.
- [83] R.D. McLeish and J. Charnley. Abduction forces in the one-legged stance. *Journal of Biomechanics*, 3:191–209, 1970.
- [84] Mechanical Dynamics Inc., Ann Arbor, MI. <http://www.adams.com>. March 2000.
- [85] S. Mochon. A mathematical model of human walking. In S. Childress, editor, *Some Mathematical Questions in Biology*, volume 14, Lectures on Mathematics in the Life Sciences, pages 193–214, Toronto, 1981. American Mathematical Society.
- [86] J.-J. Moreau. Quadratic programming in mechanics: Dynamics of one-sided constraints. *SIAM Journal on Control*, 4:153–158, 1966.
- [87] MSC.Software, Palo Alto, CA. <http://www.marc.com>. March 2000.
- [88] MSC.Working Knowledge, San Mateo, CA. <http://www.workingmodel.com>. March 2000.
- [89] S. Nasser, P.A. Campbell, D. Kilgus, N. Kossovsky, and H.C. Amstutz. Cementless total joint arthroplasty prostheses with titanium-alloy articular surfaces. *Clinical Orthopaedics and Related Research*, 261:171–181, 1990.
- [90] National Institute of Arthritis National Institute of Heath, Musculoskeletal, and Skin Diseases. Congressional Justification – FY98. Annual Scientific Advances and Initiatives, 1998.
- [91] R.R. Neptune and M.L. Hull. Evaluation of performance criteria for simulation of submaximal steady-state cycling using a forward dynamic model. *Journal of Biomechanical Engineering*, 120:334–341, 1998.

- [92] M.R. Northfield, T.P. Schmalzried, G. Belcher, and H.C. Amstutz. Quantitative assessment of activity in joint replacement patients. *Transactions of the Orthopaedic Research Society*, 40:680, 1994.
- [93] J.T. Oden and E.B. Pires. Nonlocal and nonlinear friction laws and variational principles for contact problems in elasticity. *Journal of Applied Mechanics*, 50:67–76, 1983.
- [94] R.W. Ogden. *Nonlinear Elastic Deformations*. Ellis Horwood, Chichester, 1984.
- [95] M.G. Pandy, F.E. Zajac, E. Sim, and S.M. Levine. An optimal control model for maximum-height human jumping. *Journal of Biomechanics*, 23:1185–1198, 1990.
- [96] R.E. Perez, J.A. Rodriguez, R.G. Deshmukh, and C.S. Ranawat. Polyethylene wear and periprosthetic osteolysis in metal-backed acetabular components with cylindrical liners. *Journal of Arthroplasty*, 13:1–7, 1998.
- [97] J.P. Perry. *Gait analysis — Normal and pathological function*. SLACK Incorporated, New Jersey, 1992.
- [98] G. Pietrzak. *Continuum mechanics modelling and augmented Lagragian formulation of large deformation frictional contact problems*. PhD thesis, École Polytechnique Fédérale de Lausanne, Lausanne, Switzerland, 1997.
- [99] G. Pietrzak and A. Curnier. Continuum mechanics modelling and augmented Langrangian formulation of multibody, large deformation frictional contact problems. In D.R.J. Owen, E. Onate, and E. Hinton, editors, *Computational Plasticity: Fundamentals and applications I*, pages 873–878, Barcelona, 1997. CIMNE.
- [100] D. Pioletti, L. Rakotomanana, C. Gilliéron, P.F. Leyvraz, and J.F. Benvenuti. Nonlinear viscoelasticity of the ACL: Experiments and theory. In J. Middleton, M.L. Jones, and G.N. Pande, editors, *Computer Methods in Biomechanics and Biomedical Engineering*, pages 271–280, The Netherlands, 1996. Gordon and Breach.
- [101] R. Rabevala. *Étude d'une Loi de Comportement Visco-Élastique*. Thèse de Docteur-Ingénieur, École Polytechnique Fédérale de Lausanne, Lausanne, Switzerland, 1990.
- [102] D.W. Risher, L.M. Schutte, and C.F. Runge. The use of inverse dynamics solutions in direct dynamics simulations. *Journal of Biomechanical Engineering*, 119:417–422, 1997.
- [103] Samtech Inc., Angleur-Liege, Belgium. <http://www.samcef.com>. March 2000.

- [104] T.P. Schmalzried, E.S. Szuszczewicz, M.R. Northfield, K.H. Akizuki, R.E. Frankel, G. Belcher, and H.C. Amstutz. Quantitative assessment of walking activity after total hip or knee replacement. *The Journal of Bone and Joint Surgery*, 80A:54–59, 1998.
- [105] A. Signorini. Sopra alcune questioni di elastostatica. *Atti Soc. Ital. per il Progesso delle Scienze*, 1933.
- [106] J.C. Simo and T.A. Laursen. An augmented Lagrangian treatment of contact problems involving friction. *Computers and Structures*, 42:97–116, 1992.
- [107] J.C. Simo and N. Tarnow. The discrete energy-momentum method. Conserving algorithms for nonlinear dynamics. *ZAMP*, 43:737–792, 1992.
- [108] J.C. Simo and K. Wong. Unconditionally stable algorithms for rigid body dynamics that exactly preserve energy and momentum. *International Journal for Numerical Methods in Engineering*, 31:19–52, 1991.
- [109] T. Spaggele, A. Kistner, and A. Gollhofer. Modelling, simulation and optimisation of a human vertical jump. *Journal of Biomechanics*, 32:521–530, 1999.
- [110] Structural Research and Analysis Corporation, Los Angeles, CA. <http://www.cosmosm.com>. March 2000.
- [111] C.J. Sychterz, K.H. Moon, Y. Hashimoto, K.M. Terefenko, C.A.Jr. Engh, and T.W. Bauer. Wear of polyethylene cups in total hip arthroplasty. *The Journal of Bone and Joint Surgery*, 78A:1193–1200, 1996.
- [112] R.L. Taylor and P. Papadopoulos. On a finite element method for dynamic contact/impact problems. *International Journal for Numerical Methods in Engineering*, 36:2123–2140, 1993.
- [113] K. Tetsworth and D. Paley. Malalignment and degenerative arthropathy. *Orthop Clin North America*, 25:367–377, 1994.
- [114] TNO Inc., Delft, The Netherlands. <http://www.madymo.com>. March 2000.
- [115] A.G. Urquhart, D.D. Dlima, E. Vennwatson, C.W. Colwell, and R.H. Walker. Polyethylene wear after total hip arthroplasty: The effect of a modular femoral-head with an extended flange-reinforced neck. *The Journal of Bone and Joint Surgery*, 80A:1641–1647, 1998.
- [116] V.G. Williams, L.A. Whiteside, S.E. White, and D.S. McCarthy. Fixation of ultrahigh-molecular-weight polyethylene liners to metal-backed acetabular cups. *Journal of Arthroplasty*, 12:25–31, 1997.

- [117] D.A. Winter. *Biomechanics of Human Movement*. John Wiley & Sons, New York, second edition, 1990.
- [118] P. Wriggers. Finite element algorithms for contact problems. *Archives of Computational Methods in Engineering*, 2:1–49, 1995.
- [119] P. Wriggers and J.C. Simo. A note on the tangent stiffness for fully nonlinear contact problems. *Comm. Num. Meth.*, 1:199–203, 1985.
- [120] P. Wriggers, T. Vu Van, and E. Stein. Finite element formulation of large deformation impact-contact problems with friction. *Computers and Structures*, 37:319–331, 1990.
- [121] I.C. Wright, R.R. Neptune, A.J. van den Bogert, and B.M. Nigg. Passive regulation of impact forces in heel-toe running. *Clinical Biomechanics*, 13:521–531, 1998.
- [122] G.T. Yamaguchi and F.E. Zajac. Restoring unassisted natural gait to paraplegics via functional neuromuscular stimulation: A computer-simulation study. *IEEE Transactions on Biomedical Engineering*, 37:886–902, 1990.